VIETNAM ATOMIC ENERGY INSTITUTE

The ANNUAL REPORT for 2018

SCIENCE AND TECHNICS PUBLISHING HOUSE

VIETNAM ATOMIC ENERGY INSTITUTE

The
ANNUAL REPORT
for 2018

SCIENCE AND TECHNICS PUBLISHING HOUSE

The VINATOM Annual Report for 2018 has been prepared as an account of works carried out at VINATOM for the period 2018. Many results presented in the report have been obtained in collaboration with scientists from national and overseas universities and research institutions.

The ANNUAL REPORT for 2018

Edited by
Vietnam Atomic Energy Institute
59 Ly Thuong Kiet, Ha Noi, Vietnam

President: Dr. Tran Chi Thanh
Tel: +84-4-39423434
Fax: +84-4-39424133

This report is available from:
Dept. of Planning and R&D Management
Vietnam Atomic Energy Institute
59 Ly Thuong Kiet, Ha Noi,Vietnam
Tel: +84-4-39423591
Fax: +84-4-39424133
E-mail: hq.vinatom@hn.vnn.vn
infor.vinatom@hn.vnn.vn

Preface

The research and development (R&D) activities of Vietnam Atomic Energy Institute (VINATOM) during the period from the 1st January 2018 to 31st December 2018 are presented in this publication. Our report mainly focuses on the following subject categories:

1. Nuclear Physics, Reactor Physics
2. Research Reactor, Nuclear Power Technology, Nuclear Safety, Nuclear Power Economy
3. Instrumentation, Nuclear Electronics
4. Industrial Applications
5. Applications in Ecology, Environment and Geology
6. Applications in Biology, Agriculture and Medicine
7. Radiation Safety and Radioactive Waste Management
8. Radiation Technology
9. Radiochemistry and Materials Science

By the 31st December 2018, the total number of personnel working at VINATOM is 745, including 570 permanent employees and 175 contract staff members. Regarding to the finance, our Institute was funded 179,670,000,000 VND by the government for FY 2018. The international support of about ….USD was committed to the VINATOM's operating projects related to equipment, human resources training, and expert services. In terms of doctoral training at VINATOM, 4 PhDs candidates fulfilled the dissertations and were awarded their full doctorate degrees.

We sincerely thank those making great contribution and giving concern to the publication. The report is expected to offer all readers an insight into VINATOM's accomplishments in R&D activities of 2018. We highly appreciate your continued trust, cooperation and support.

Dr. Tran Chi Thanh,

Chief Editor of VINATOM Annual Report 2018

President of VINATOM

CONTENTS

1. CONTRIBUTIONS

1.1- Nuclear Physics, Reactor Physics

R-MATRIX METHOD AND THE NONLOCAL NUCLEON OPTICAL POTENTIAL

Doan Thi Loan, Dao Tien Khoa and Nguyen Hoang Phuc

Institute for Nuclear Science and Technology, Vietnam Atomic Energy Institute
179 Hoang Quoc Viet, Ha Noi, Vietnam

Project information:

- **Code:** CS/18/04-01
- **Managerial Level:** Institute
- **Allocated Fund:** 60,000,000 VND
- **Implementation time:** 12 months (Jan 2018- Dec 2018)
- **Contact email:** loandoan87@gmail.com
- **Paper published in related to the project:**

1. D.T. Loan et al., 2018. *R*-matrix method and the nonlocal nucleon optical potential. *The 5th Vietnam Conference on Nuclear Science and Technology for Young Researchers.* Hanoi, Vietnam October 2018 (in Vietnamese).
2. D. T. Loan et al., 2018. *R*-matrix method and the nonlocal nucleon optical potential. *Communication in Physics 28*, 4 (2018), pp. 323-336.

A

Abstract: The calculable *R*-matrix method is applied to solve the Schrodinger equation in the optical model (OM) analysis of the elastic nucleon-nucleus scattering using a nonlocal nucleon optical potential (OP). The phenomenological nonlocal nucleon OP proposed by Perey and Buck (PB), and the two recent versions of the PB parametrization were used in the present OM study of the elastic nucleon scattering on ^{40}Ca, ^{48}Ca, ^{90}Zr and ^{208}Pb targets at different energies. The comparison of the OM results given by the calculable *R*-matrix method with those given by other methods confirms that the *R*-matrix method is an efficient tool for the OM study of the elastic nucleon-nucleus scattering using a nonlocal nucleon OP.

Keywords: *Nonlocality, nucleon optical potential, R-matrix.*

1. INTRODUCTION

The nucleon-nucleus scattering remains an important experiment of the modern nuclear physics to investigate the nucleon-nucleus interaction as well as the structure of the target nucleus. The key quantity needed for the description of the nucleon-nucleus scattering at both low and high energies is the nucleon optical potential (OP). Over the years, for the simplicity of the numerical calculation, the OP was mainly assumed in the local form for the OM analysis of the elastic nucleon-nucleus scattering. However, it is well known that the nucleon OP is nonlocal in the coordinate space due to the Pauli principle and multichannel coupling. The nonlocality of the nucleon OP has a physical origin and it is of importance to implement the use of the nonlocal OP in the OM studies of the nucleon-nucleus scattering. In general, solving the OM equation with a nonlocal OP readily leads to an integro-differential equation, which is more complicated than a standard differential equation with a local potential. For the nucleon-nucleus scattering problem, the use of the nonlocal OP leads to an explicit angular-momentum dependence of the integral equation for the scattering wave function.

In the present work, we apply the calculable *R*-matrix method [1] to solve the OM equation involving the *nonlocal* nucleon OP. The calculable *R*-matrix method was applied [1,2] to include the Lagrange mesh and Gauss-Legendre quadrature integration that significantly simplify the numerical calculation. Therefore, the aim of the present work is to explore the applicability of the calculable *R*-matrix method in the OM calculation of the elastic nucleon-nucleus scattering using a nonlocal nucleon OP. For the nonlocal nucleon OP, we have chosen the PB [3] and TPM [4] potentials to study the elastic nucleon scattering on ^{40}Ca, ^{48}Ca, ^{90}Zr, and ^{208}Pb targets at energies of 14.6 MeV to 40 MeV. More recently, an energy dependence of the nonlocal OP was introduced explicitly into the imaginary parts of the PB and TPM potentials, dubbed as PB-E and TPM-E potentials, whose parameters were fitted to the best OM description of the nucleon elastic scattering data on ^{40}Ca, ^{90}Zr and ^{208}Pb targets at energies $E \approx$ 5-45 MeV [5]. The OM results obtained with the calculable *R*-matrix method are compared with those obtained with other methods given by the computer codes NLOM [6], NLAT [7], and DWBA98 [8].

2. THEORETICAL FRAMEWORK

We give here a brief introduction into the OM calculation with a nucleon OP that contains a nonlocal central term [3-5]. In this case, the scattering wave function of the incident nucleon is obtained by solving the following Schrodinger equation

$$\left[-\frac{\hbar^2}{2\mu}\nabla^2 + V_C(\boldsymbol{r}) + V_{SO}(\boldsymbol{r})\boldsymbol{l}.\boldsymbol{\sigma}\right]\chi(\boldsymbol{k},\boldsymbol{r}) + \int V(\boldsymbol{r},\boldsymbol{r}')\chi(\boldsymbol{k},\boldsymbol{r}')d\boldsymbol{r}' = E\chi(\boldsymbol{k},\boldsymbol{r}) \qquad (1)$$

Here $V_C(r)$ and $V_{so}(r)$ are the Coulomb and spin-orbit potentials, respectively, which are assumed to be local, and $V(r,r')$ is the nonlocal central potential. The nonlocal potential in PB type was parametrized in the following form

$$V(\boldsymbol{r},\boldsymbol{r}') = U\left(\frac{|\boldsymbol{r}+\boldsymbol{r}'|}{2}\right)H\left(\frac{|\boldsymbol{r}-\boldsymbol{r}'|}{\beta}\right)$$

where β is the range of the nonlocality. The function $H(|\boldsymbol{r}-\boldsymbol{r}'|/\beta)$ was chosen in the Gaussian form and the function $U\left(|\boldsymbol{r}+\boldsymbol{r}'|/2\right)$ was chosen in the Woods-Saxon form [3].

The main principle of solving the Schrodinger Eq. (1) using the calculable *R*-matrix method is the division of the configuration space at the channel radius *a* into an internal region and an external region. The channel radius *a* is chosen large enough so that the nuclear potential is negligible in the external region. In the present work, a = 15 *fm* was chosen for all the OM calculations using the *R*-matrix method. In the internal region, the radial component $\psi_{lj}(r)$ of the wave function is expanded over some finite basis of *N* linearly independent functions $\varphi_n(r)$ with the corresponding coefficients c_n. The internal and external parts of the radial wave function can be connected at the boundary $r = a$ through the continuity condition $\psi_{lj}^{\mathrm{ext}}(a) = \psi_{lj}^{\mathrm{int}}(a)$. This leads to the definition of the *R*-matrix at a given energy *E* as

$$\psi_{lj}(a) = R_{lj}(E)\left[a\psi'_{lj}(a) - B\psi_{lj}(a)\right], \qquad (2)$$

where *B* is the dimensionless boundary paramete. The Schrödinger equation in the internal region can be approximated by an inhomogeneous Bloch- Schrödinger equation Eq. (1) can then be rewritten as

$$\left\{-\frac{\hbar^2}{2\mu}\left[\frac{d^2}{dr^2}-\frac{l(l+1)}{r^2}\right]+V_C(r)+A_{lj}V_{SO}(r)-\mathrm{E}+\mathcal{L}\right\}\sum_{i=1}^{N}c_n\varphi_n(r)$$
$$+\int v_l(r,r')\sum_{i=1}^{N}c_n\varphi_n(r')dr'=\mathcal{L}\psi_{lj}^{\mathrm{ext}}(r). \tag{3}$$

The Bloch operator ensures the continuity of the derivative of the wave function [1,2]. Using the boundary condition (2), we obtain the calculable *R*-matrix

$$R_{lj}(E)=\frac{\hbar^2}{2\mu a}\sum_{i,n=1}^{N}\varphi_i(a)(C^{-1})_{in}\varphi_n(a), \tag{4}$$

where the matrix elements C_{in} (E) are determined by projecting the left-hand side of Eq. (3) on $\varphi_i(r)$ and integrating over *r* variable. For the convenience in the calculation of $C_{in}(E)$, the modified Lagrange functions are chosen as the basis functions $\varphi_n(r)$ (see the explicit expressions in Ref. [1]). Using the Gauss-Legendre quadrature, the calculation is simplified significantly since the integrals including local potential and nonlocal central potential are determined by the values of these potentials at mesh points given by the solutions of the Legendre polynomial.

It is obvious that external wave functions contain the partial-wave elements S_{lj} of the scattering matrix and internal wave functions which include the *R*-matrix component $R_{\mathrm{lj}}(E)$. Through the continuity condition of the scattering wave function, the relationship between S_{lj} and $R_{\mathrm{lj}}(E)$ is obtained as

$$S_{lj}=\exp(2i\phi_l)\frac{1-L_l^*R_{lj}(E)}{1-L_l}R_{lj}(E), \tag{5}$$

The differential scattering cross section for the elastic nucleon scattering is then readily obtained from the partial-wave elements of the scattering matrix (5).

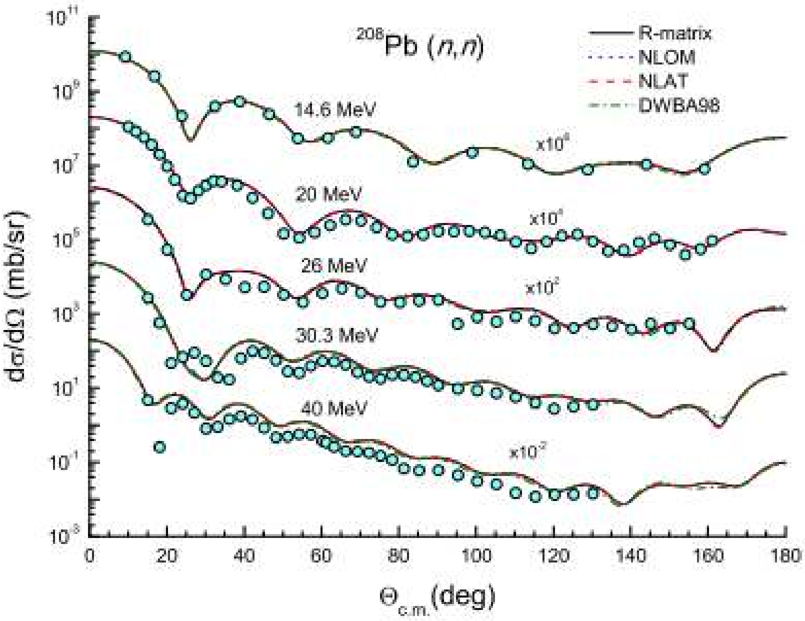

Figure 1: OM descriptions of the neutron elastic scattering on 208Pb target at 14.6, 20, 26, 30.3 and 40 MeV given by the calculable *R*-matrix method and other methods using the nonlocal PB potential [3]. The experimental data were taken from Refs. [9–13].

1. RESULTS AND DISCUSSION:

In the present work, we have tested the reliability of the calculable *R*-matrix method by comparing the OM results given by the *R*-matrix method with three other methods used in codes NLOM [6], NLAT [7], and DWBA98 [8]. Fig. 1 presents the OM descriptions of the neutron elastic scattering on ^{208}Pb target at the energies of 14.6, 20, 26, 30.3, and 40 MeV given by the four different methods of solving Eq. (7), using the same nonlocal PB potential [3]. One can see that all the considered methods give nearly the same differential scattering cross sections over the whole angular range, which are indistinguishable in the logarithmic scale. The comparison of the OM results given by the calculable *R*-matrix method [1] with those given by the three other methods [6–8] confirms that the calculable *R*-matrix method is an efficient, alternative method to treat the nonlocality of the nucleon OP.

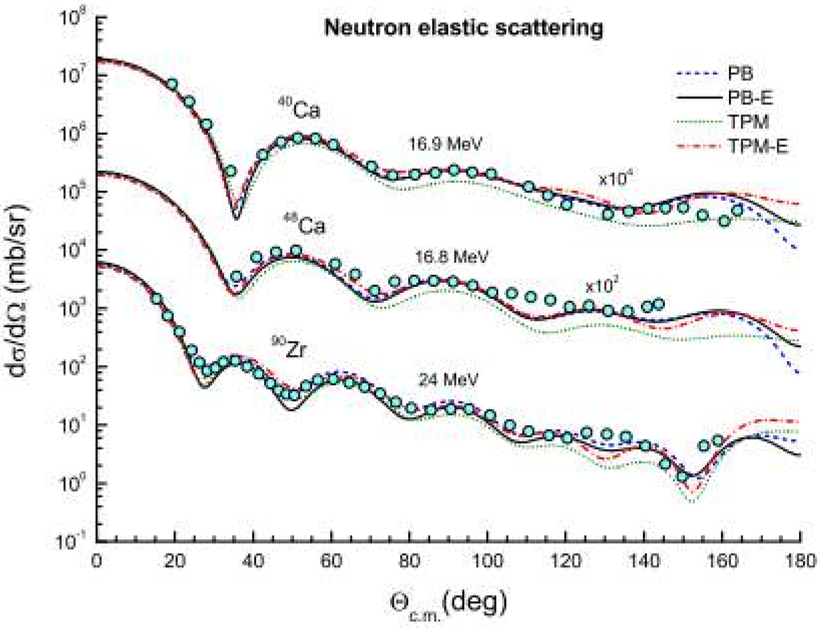

Figure 2: OM descriptions of the neutron elastic scattering on ^{40}Ca, ^{48}Ca, and ^{90}Zr targets at the energies of 16.9, 16.8, and 24 MeV respectively by the calculable *R*-matrix method using the nonlocal PB and TPM potential [3] and its energy dependent version [5]. The experimental data were taken from Refs. [14–16].

The OM results obtained with the calculable *R*-matrix method for the neutron elastic scattering on ^{40}Ca, ^{48}Ca, and ^{90}Zr targets at the energies of 16.8 to 24 MeV using the original PB, TPM potentials and their energy dependent PB-E, TPM-E versions are compared with the data in Fig. 2. One can see that the energy dependent PB-E and TPM-E nonlocal potentials give a better OM description of the data compared to the original PB and TPM potential.

REFERENCE

[1] P. Descouvemont and D. Baye, *Rep. Prog. Phys*. 2010 73, 36301.

[2] P. Descouvemont, *Comp. Phys. Comm.* 2016, 200, 199.

[3] F. Perey and B. Buck, *Nucl. Phys*. 1962, 32, 353-380.

[4] Y. Tian, D.Y. Pang, and Z.Y. Ma*, Int. J. Mod. Phy*s. *E* 24, 1550006 (2015).

[5] A. E. Lovell, P. L. Bacq, P. Capel, F. M. Nunes, and L. J. Titus, *Phys. Rev. C*, **96** (2017) 051601(R).

[6] B. T. Kim and T. Udagawa, *Phys. Rev. C.* 1990, 42, 1147.

[7] L. J. Titus, A. Ross, and F. M. Nunes, *Comp. Phys. Comm.* 2016, 207**,** 499.

[8] J. Raynal, Computing as a Language of Physics, IAEA, Vienna (1972) p.75; Notes on DWBA98 code (unpublished).

[9] L. F. Hansen, F. S. Dietrich, B. A. Pohl, C. H. Poppe, and C. Wong, *Phys. Rev. C.* 1985, 31, 111.

[10] R. W. Finlay, J. R. M. Annand, T. S. Cheema, J. Rapaport, and F. S. Dietrich, *Phys. Rev. C.* 1984, 30, 796.

[11] J. Rapaport, T. S. Cheema, D. E. Bainum, R. W. Finlay, and J. D. Carlson, *Nucl. Phys. A*. 1979, 313, 1.

[12] R. P. DeVito, Sam M. Austin, W. Sterrenburg, and U. E. P. Berg, *Phys. Rev. Lett.*1981, 47, 628.

[13] R. P. DeVito, D. T. Khoa, S. M. Austin, U. E. P. Berg, and B. M. Loc, *Phys. Rev. C*. 2012, 85, 024619.

[14] G. M. Honoré, W. Tornow, C. R. Howell, R. S. Pedroni, R. C. Byrd, R. L. Walter, and J. P. Delaroche, *Phys. Rev. C*. 1986, 33, 1129.

[15] J. M. Mueller *et. al*, *Phys. Rev. C.* 2011, 83, 064605.

1.2- Research Reactor, Nuclear Power Technology, Nuclear Safety, Nuclear Power Economy

STUDY AND TESTING OF SILICON TRANSMUTATION DOPING IN DALAT NUCLEAR RESEARCH REACTOR

Pham Quang Huy, Luong Ba Vien, Le Vinh Vinh, Huynh Ton Nghiem, Nguyen Kien Cuong, Nguyen Manh Hung, Nguyen Minh Tuan, Tran Quoc Duong, Vo Doan Hai Dang and, Nguyen Tien Vu

Dalat Nuclear Research Institute, Vietnam Atomic Energy Institute
01 Nguyen Tu Luc, Dalat, Lam Dong Province, Vietnam

Project information:

- **Code:** 33/2014/TT-BKHCN
- **Managerial Level:** Ministry
- **Allocated Fund:** 1,040,000,000 VND
- **Implementation time:** 42 months (Jan 2016- Jun 2019)
- **Contact email:** huypq.re@dnri.vn
- **Paper published in related to the project:**

1. Trang The Dat, Nguyen Nhi Dien, Pham Quang Huy, Tran Quoc Duong, “A design of irradiation channel for silicon transmutation doping experiment at the Dalat Research Reactor”, *The 5th Vietnam Conference on Nuclear Science and Technology for Young Researchers.* Hanoi, Vietnam October 2018 (in Vietnamese).
2. Pham Quang Huy, Nguyen Nhi Dien, Nguyen Kien Cuong, Tran Quoc Duong, Vo Doan Hai Dang, Trang The Dat, “Design of an irradiation using screen method for silicon transmutation doping at the Dalat Research Reactor”. *Vietnam Conference on Nuclear Science and Technology 13,* Ha Long, August 2019.
3. Pham Quang Huy, Nguyen Nhi Dien, Nguyen Kien Cuong, Tran Quoc Duong, Vo Doan Hai Dang, Trang The Dat, “Design of an irradiation using screen method for silicon transmutation doping at the Dalat Research Reactor”, *Nuclear Science and Technology* (accepted).

Abstract: The neutron transmutation doping of silicon (NTD-Si) at research reactors has been implemented effectively in many countries to produce high-quality semiconductors. In Vietnam, some silicon ingots were irradiated on the Dalat Nuclear Research Reactor (DNRR) in the late 1980s but the result was limited. Therefore, the testing of NTD-Si at the DNRR are necessary to have a better understanding in order to apply the NTD-Si in a new research reactor of the Research Centre for Nuclear Science and Technology (RCNEST), which has planned to be built in Viet Nam. This report presents the results of design and testing NTD-Si at the DNRR using screen and inversion methods. Calculation using MCNP5 computer code and experiment were carried out to confirm the thermal flux uniformity is less than 5% in both radial and axial directions of the irradiation rigs. After irradiation and annealing processes, however, the resistivity of Silicon ingots in both methods have axial uniformity about 20%, which is much larger than 5% of the target and market requirement. The resistivity of irradiated Silicon ingots has been affected by low ratio of thermal/fast neutron flux at irradiation rigs.

Keywords: *NTD-Si, MCNP5, Dalat Nuclear Research Reactor (DNRR), screen method, inversion method, foil activation, irradiation rig.*

1. INTRODUCTION

One of the most important requirements of NTD-Si is to maintain the uniformity of radial and axial thermal neutron flux in irradiation channels. At present, the uniformity of irradiation from ± 5 ~ 6% would meet commercial request depending on ingot dimension [1]. In research reactors, normally, the axial and radial distributions of thermal neutron in irradiation channels are not uniformed. In order to meet customer's requirements, a change in configuration of irradiation channels is needed to uniform thermal neutron flux distribution and maximize usage of the irradiation channel. Three major methods could be applied to axially uniform thermal neutron flux distribution are inversion, reciprocating motion and flux screen [1]. Depending on the design characteristics and core configuration of the reactors, the method applied for neutron flux uniformity should be chosen. In the late 1980s, the inversion method was tested at the DNRR but the results were limited [2]. Therefore, the design and testing of irradiation rigs using flux screen and inversion method for NTD-Si at the DNRR are necessary to have a better understanding and experience in NTD-Si application. The results would provide good experiences in the application of NTD-Si on the new research reactor, which has planned to be built in Vietnam.

2. CALCULATION MODEL AND EXPERIMENTAL METHOD

2.1. Dalat reactor and its parameters

The DNRR, 500-kW pool-typed, light water cooled and moderated, was reconstructed and upgraded from the USA 250 kW TRIGA MARK II reactor. The reactor has been officially put into operation for the purposes of radioisotope production, neutron activation analysis, fundamental and applied research, and manpower training. The summary description of the DNRR is shown in **Table 1** and **Figure 1** [3].

Table 1: Summary description of the DNRR [3]

Parameter	Description
Nominal power	500 kW
Neutron flux (thermal, max)	2×10^{13} n/cm^2.s
Fuel	VVR-M2, mixed UO_2-Al, 19,75% enrichment
Moderator and coolant	Light water
Reflector	Graphite, beryllium and light water
Core cooling	Natural convection
Heat rejection	Two-loop cooling system
Control rods	2 safety, 4 shim (B_4C) and 1 regulating (stainless steel)

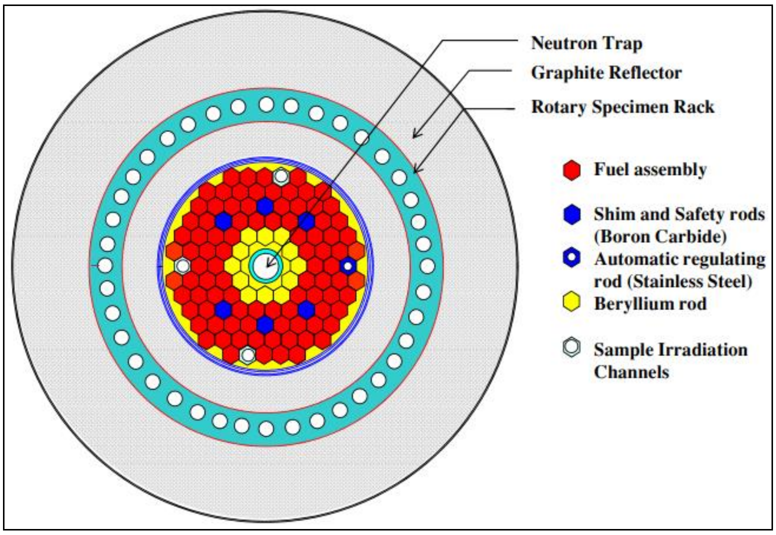

Figure 1: Present working configuration of DNRR.

Since thermal neutrons are mainly used in NTD-Si, higher thermal neutron flux would result in a shorter irradiation time. The neutron trap, which has maximum thermal neutron flux in the core of DNRR, is dedicated for NTD-Si testing. Neutron trap is a water cylinder surrounded by Beryllium blocks located in center of the core. The neutron trap has 6.5 cm in diameter and about 2050 cm^3 in volume [3]. An aluminum tube installed in the neutron trap to load irradiation samples which have maximum of 4.2 cm in diameter as shown in **Figure 1**.

2.2. Determination of neutron spectrum and flux distribution

Determination of neutron spectrum and flux distribution at the neutron trap was obtained by using foil activation method. Bare gold foils and Cadmium covered gold foils were irradiated to obtain absolute neutron flux [4]. The following equation can be used to obtain thermal neutron flux:

$$\Phi_{th} = \frac{2.Ae^{-\lambda\tau}}{\sqrt{\pi}N_A\alpha\sigma_{0,act}G_{th}(1-e^{-\lambda T})}\sqrt{\frac{T_n}{T_0}}\left[\frac{A_b(T,\tau)}{m_b}-\frac{A_{Cd}(T,\tau)}{m_{Cd}}\right] \tag{1}$$

Where, m_b - mass of bare gold foil (g); m_{Cd} - mass of Cadmium covered gold foils (g); T - Irradiation duration (s); τ - cooling duration after irradiation (s); t_m - measurement in real time (s); $t_{m,eff}$ - effective time measurement (s); λ - decay constant of nuclide compound (s^{-1}); η - counting efficiency of detector; γ - gamma abundance factor; m - mass of foil (g); α - isotope enrichment; G_{th} - thermal neutron self-shielding factor; N_A - Avogadro constant; A - Atomic number of isotope; G – ratio of isotope in foil; T_n neutron temperature (K); T_0 room temperature (293 K).

To determine the thermal neutron flux distribution at the neutron trap, Lu-176 foils which have large thermal neutron absorption cross-section were used. Thermal neutron flux distribution was scaled relatively. The relative thermal neutron distribution was obtained by comparing of ratios of corresponding Lu-176 activities at various positions in the neutron trap.

The method used for neutron spectrum measurement is based on activation of a set of foils and determination of reaction rates. SANDBP program is used to obtain the neutron energy spectra after irradiation of the foils. The SANDBP program is designed to obtain a ’best fit’ neutron flux spectrum for a given input set of infinitely dilute foil activities [4].

MCNP5 computer code was also used for calculation of neutron flux distribution and neutron spectrum. This computer code is developed at the Los Alamos National Laboratory, USA

[5]. The MCNP5 has been being officially used for core management of DNRR with ENDF/B7.0 library [6]. The calculation model for DNRR using MCNP5 computer code is shown in **Figure 2**.

Neutron spectrum divided into 3 energy groups calculated using MCNP5 computer code and neutron spectrum obtained from experiments at the neutron trap are shown in **Table 2**. The reliability of calculation by MCNP5 computer code was confirmed through the good agreement of experimental and calculational results. The discrepancies are about 2% in thermal neutron flux and more than 4% in epithermal neutron flux in comparison between the experimental and calculational results.

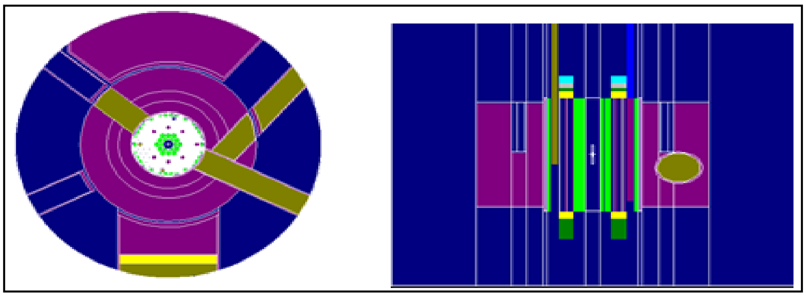

Figure 2: Calculation model of DNRR using MCNP5 computer code

Table 2: Comparison of neutron flux of the neutron trap between calculation and experiment

Flux (n/cm^2.s)	Calculation	Experiment (error ±5-6%)
Thermal	2.24 x 10^{13}	2.29 x 10^{13}
epithermal	6.52 x 10^{12}	6.22 x 10^{12}
Fast	2.56 x 10^{12}	2.64 x 10^{12}

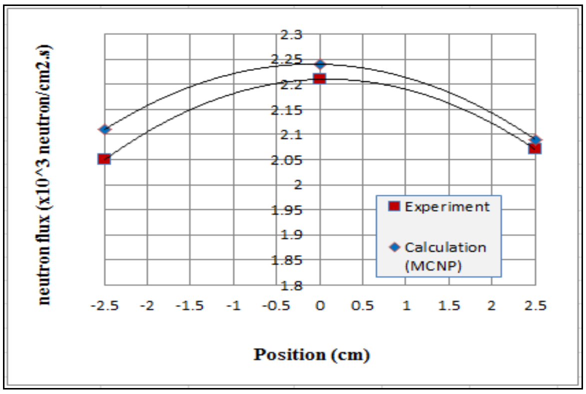

Figure 3: Thermal neutron distribution in radial direction at the neutron trap (zero position is the neutron trap center)

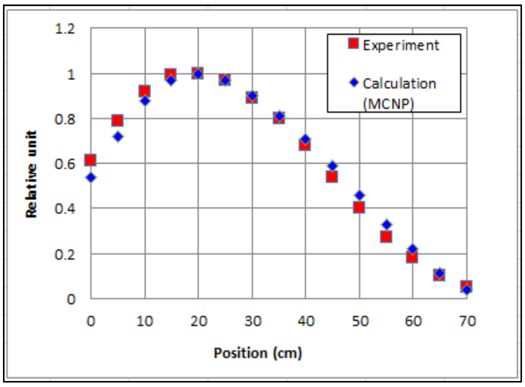

Figure 4: Thermal neutron distribution in axial direction at the neutron trap

The experimental and calculational results in **Figure 3** and **Figure 4** show that the deviation of thermal neutron flux distribution in the radial direction at the neutron trap ranges within 5-7%. The experimental result is consistent with the calculational result for thermal neutron flux distribution in the axial direction. The maximum thermal neutron flux value is located at 20 cm away from the core bottom. The shift of maximum flux to the bottom of the neutron trap is mainly affected by control rod positions. With a large discrepancy of the thermal neutron distribution in both radial and axial directions, the current neutron trap needs to be redesigned to meet the requirements of NTD-Si test.

3. DESIGN CHARACTERISTICS OF IRRADIATION RIGS FOR NTD-SI TESTING IN DNRR

3.1 Characteristic of irradiation rig using flux screen.

The principle of flux screen method is to use screens from different materials to absorb neutron or change the appropriate thickness of neutron absorbers to flatten the neutron flux distribution [1]. The screens are made of strong neutron absorbers in high neutron flux region (stainless steel) and weak absorbers in low flux region (aluminum).

Dimensions of the irradiation rig and screen materials used to flatten flux distribution has been calculated and modified by comparing calculational results using MCNP computer code and experimental results. **Figure 5** shows the details of the design and materials of irradiation rig.

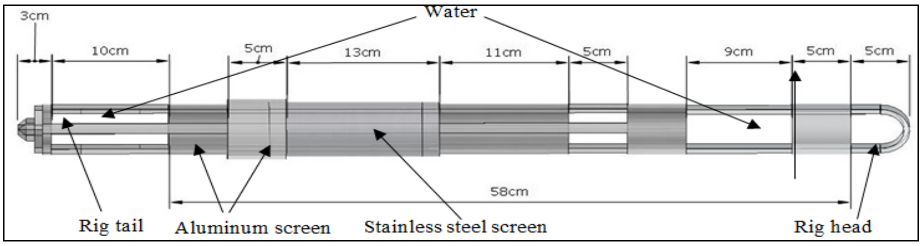

Figure 5: The design of the irradiation rig for NTD-Si testing in DNRR using flux screen

Figure 6: Silicon ingot (left hand side) and aluminum ingot (right hand side)

Figure 7: Aluminum ingots with Lu foils

The important parameters related to nuclear safety and radiation safety issues such as reactivity and radiation dose rate have been calculated before installing the irradiation rigs into the neutron trap [7]. The experiments using aluminum 6061, which have similar neutronic characteristics and dimension of testing silicon ingots were also performed as shown in **Figure 6**. Each ingot has a diameter of 4 cm and 2 cm in length. Lu-176 foils were attached on aluminum ingots and irradiated for determination of thermal neutron flux distribution in the irradiation rigs as shown in **Figure 7.**

Experimental and calculational results presented in **Table 3** show that the deviation of thermal flux in axial direction at the irradiation region ranges within 5%. The distribution of thermal neutron flux in experiment is consistent with the calculation results. The thermal neutron flux peaks at 10cm away from the bottom of the irradiation rig in the experiment and about 12cm in the calculation. The flux distribution in the top half of the irradiation rig tends to increase but still below the desired value of 5% in both calculation and experiment. These results show that the irradiation region from 10cm to 36cm in axial direction of the irradiation rig is suitable for NTD-Si test.

Table 3: The relative distribution of thermal neutron flux in axial direction at the irradiation rig using flux screen method

Position (cm)	**Experiment** (error ±5-6%)	**Calculation**
10	1.000	0.991
12	0.992	1.000
14	0.999	0.995
16	0.991	0.987
18	0.960	0.972
20	0.980	0.974
22	0.967	0.969
24	0.968	0.955
26	0.979	0.962
28	0.961	0.951
30	0.958	0.953
32	0.955	0.968
34	0.960	0.971

Table 4 presents the deviation of thermal neutron flux in radial direction, which is less than 3% in experiment and 1% in the calculation in the rig. The maximum thermal neutron flux value drops to 1.31×10^{13} n/cm^2.s in the irradiation rig due to combination of the absorption effects from the screen layers and the replacement of moderator by aluminum ingots in the irradiation rig.

Table 4: Calculational result of thermal neutron flux distribution in radial direction at the irradiation rig using screen method

Flux x10^{13} n/cm^2.s			
Position (cm)	*Left side (-1.9 cm)*	*Center (0 cm)*	*Right side (+1.9 cm)*
10	1.30	1.30	1.31
20	1.26	1.28	1.27
30	1.25	1.26	1.25

The irradiation configuration for Silicon ingots from 10cm to 43cm away from bottom of the rig using screen method was calculated using MCNP5 computer code. For calculation, neutron energy regions were divided into thermal region <0.625eV, epi-thermal region ~0.82 MeV and fast region >1.0MeV. The calculational result shows that the ratio of thermal/fast neutron is about 4.42 in irradiation region of the rig using screen method.

3.2 Characteristics of inversion irradiation rig for NTD-Si testing in DNRR

The inversion method is carried out by putting Silicon ingots into linear flux distribution area of the rig. These silicon ingots should be irradiated with a duration equivalent to a half of the expected irradiation time. Then, the silicon ingots are inversed for the remaining half of irradiation time [1]. At a particular power level, the same irradiation time before and after inversion will provide the uniformity of irradiation thermal neutron flux. **Figure 8** shows the design of a linear inversion rig for the NTD-Si testing on DNRR.

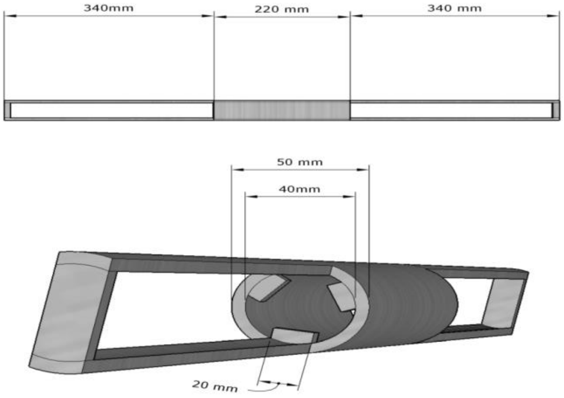

Figure 8: The inversion rig for NTD-Si testing on DNRR.

Table 5 shows the calculational results from the MCNP computer code and experiment for neutron flux distribution in radial direction of irradiation rig using inversion method. The value of thermal neutron flux decreases from 1.7x10^{13} to 1.42x10^{13} neutron/cm^2.sec in the irradiation region (30cm to 50cm from the bottom of the rig) mainly due to the replacement of water by the silicon ingots. The deviation in radial direction of thermal neutron flux of the rig is less than 1% in calculation.

Table 5: Distribution of thermal neutron flux in radial direction of the inversion rig.

Flux x10^{13} n/cm^2.s			
Position (cm)	*Left side (-1.9 cm)*	*Center (0 cm)*	*Right side (+1.9 cm)*
10	1.70	1.71	1.70
20	1.51	1.51	1.51
30	1.42	1.42	1.43

The calculational results using MCNP computer code show that the ratio of thermal/ fast neutron flux is 5.42 in the rig using inversion method. These calculations were carried out for irradiation rig loaded with Sillicon ingots from 30 cm to 48 cm from the rig bottom.

4. THE ANNEALING PROCESSE OF IRRADIATED SILLICON INGOTS

The DNRR was operated in 16-hours to provide an integral irradiation flux about 7.40 x 10^{17}neutron/cm^2 for NDT-Si testing of screen method. In case of inversion method, the irradiation time was 14 hours to provide an integral irradiation flux about 7.56 x 10^{17}neutron/cm^2.

In NTD-Si, Silicon crystal ingots are not only irradiated by thermal neutron but also by fast neutron. Since the most important issue in the NTD-Si is the effect of fast neutron (> 1MeV) causing defects in the silicon lattice [1],[8]. These defects would significantly affect the resistivity of silicon ingots compared to the initial resistivity value [7]. A good experience in designing of irradiation channels for NTD-Si in many research reactors is to ensure a high ratio of thermal/fast neutron flux (at least 7/1) to avoid defects in Silicon lattice after irradiation [1].

The defects in the Silicon lattice after irradiation would be partly mitigated by annealling process with a suitable annealing condition [8]. Normally, the annealing process and measurement of the irradiated silicon ingots will be carried out by the companies, which are interesting in NTD-Si. The facilities, which have research reactors, only ensure irradiation conditions to meet the requirements of the NTD-Si companies. Since the DNRR has no specialized equipment to measure Silicon ingot resistivity, the annealling process and the resistivity measurement of the irradiated silicon ingots were carried out in the laboratories of Faculty of Advanced Materials, VNUHCM-University of Science.

Table 5 shows the resistivity of the irradiated silicons ingot as a function of the annealing temperature. The irradiated silicon ingots were annealed in argon atmosphere during 1 hour in different temperature to find the most satisfactory annealing condition. The resistivity value of the Silicon samples decreased rapidly from 600°C to 800°C, however, stable in annealing temperature from 800°C to 850°C. The resistivity of Silicon ingots tends to increase in the annealling temperature from 850°C to 900°C.

Table 5: Resistivities of Silicon sample as a function of temperature.

Temperature (°C)	**Inversion 1** (Ohm.cm)	**Inversion 2** (Ohm.cm)	**Screen 1** (Ohm.cm)	**Screen 2** (Ohm.cm)
20	4.65E+05	4.69E+05	4.70E+05	4.71E+05
600	1.79E+03	1.59E+03	1.89E+03	3.04E+03
700	7.78E+02	8.11E+02	8.92E+02	8.92E+02
800	4.30E+01	4.45E+01	5.64E+01	5.59E+01
850	4.19E+01	4.26E+01	5.60E+01	5.64E+01
900	4.81E+01	4.66E+01	6.40E+01	6.52E+01

Thus, the most suitable annealling condition for the irradiated silicon ingots is 1 hour in 850°C (temperature gradient <1°C). In addition, the rate of increasing and decreasing temperature during annealling process should be lower than 2 °C/min to avoid thermal shock causing cracks in silicon ingots.

5. DETERMININATION OF SILICON RESISIVITY AFTER IRRADIATION

The Ecopia Hall HMS-3000 system of the Material Science Laboratory, HCM University of Technology is used to determine the resistivity of irradiated silicon ingots from the DNRR. This is a complete system for measuring resistivity, charge and mobility density of different semiconductor materials. Measurements include four ohmic contact points on the sample. All conductor wires are made from the same material to minimize thermal effect [8,9]. **Table 6** and **Table 7** show the measurement results of the axial and radial resistivity determination of the irradiated silicon ingots, respectively. The position of the samples is numbered from 1 to 11 corresponding to the position of each silicon ingot from the irradiation rig bottom.

Table 6: Measurement results of axial resistivity of Silicon samples

Silicon sample	**Inversion** (ohm.cm)	**Screen** (ohm.cm)
1	3.72E+01	5.86E+01
2	3.73E+01	5.72E+01
3	3.77E+01	6.20E+01
4	4.05E+01	6.43E+01
5	4.20E+01	6.84E+01
6	4.45E+01	6.56E+01
7	4.49E+01	6.13E+01
8	4.40E+01	5.99E+01
9	3.94E+01	5.95E+01
10	3.83E+01	5.96E+01
11	3.74E+01	5.71E+01

Table 7: Measurement results of radial resistivity of Silicon samples

Cutting position	**Screen 1** (Ohm.cm)	**Screen 2** (Ohm.cm)	**Inversion 1** (Ohm.cm)	**Inversion 2** (Ohm.cm)
Left side	5.81E+01	6.20E+01	3.78E+01	4.26E+01
Center	5.86E+01	6.43E+01	3.72E+01	4.20E+01
Right side	5.99E+01	6.40E+01	3.71E+01	4.27E+01

The resistivity measurements of the irradiated silicon ingots from the two methods show that the radial uniformity is less than 4%. However, the axial uniformity of the irradiated silicon ingots is quite high, about 20%, much larger than the target value of 5%. The resistivity value tends to be high in the middle region compared to the two ends of the irradiation rigs in both methods. The resistivity uniformity of the silicon ingots at the center of the rigs has been affected by fast neutron flux. At two ends of the irradiation rigs using screen and inversion method, a water layers are still acting as a moderator and reflector. Therefore, neutron flux tends to be higher thermalized at two ends of the irradiation rigs compared to that at the center. The resistivity of silicon ingots using inversion method is lower than that by screen method mainly due to the higher integral irradiation flux and thermal/fast neutron ratio.

6. CONCLUSION

The irradiation methods using flux screen and inversion were chosen for NTD-Si testing on the DNRR. Based on the calculational and experimental results on neutronic characteristic of the current neutron trap of the DNRR, the irradiation rigs of the two mentioned methods have been calculated, designed and installed in the core of the DNRR for NTD-Si testing requirements. The study of the neutronic characteristics of the irradiation rigs before NTD-Si testing was also carried out. The calculational and experimental results show that the irradiation rigs were designed with uniformity of thermal neutron flux lower than 5% in both radial and axial directions. The low ratio of thermal and fast neutron flux in irradiation rigs, however, significantly influences on the resistivity of the irradiated silicon ingots. The uniformity of resistivity for both methods is about 20%, much larger than the target value and requirement of the market (5%). The knowledge and experience gained during NTD-Si testing on the DNRR is very important in effectively applying NTD-Si on the new research reactor, which has been planned to be built in Vietnam in future.

REFERENCE

[1] International Atomic Energy Agency - TECDOC-1681, “Neutron Transmutation Doping of Silicon at Research Reactors”, IAEA, Vienna, (2012).

[2] Phan An, “‘Research on using neutron of the Dalat Nuclear Research Reactor for doping single silicon crystals used in semiconductor components”, Report in Vietnamese, Z181, (1989).

[3] Dalat Nuclear Research Institute, “Safety Analysis Report”, (2012).

[4] International Atomic Energy Agency, “Regional Training Course on calculation and measurement of neutron flux spectrum for research reactors”, Serpong, Indonesia, (1993).

[5] X-5 Monte Carlo Team, “MCNP, A General Monte Carlo N-Particle Transport Code, Version 5", Los Alamos National Laboratory report LA-UR-03-1987 (April 2003).

[6] M. B. Chadwick et al., “ENDF/B-VII.0: Next Generation Evaluated Nuclear Data Library for Nuclear Science and Technology," Nuclear DataSheets, 107, (2006).

[7] Dalat Nuclear Research Institute, “Lookup table of excess reactivity of the Dalat Nuclear Research Reactor”, Internal Report in Vietnamese, (2018).

[8] Tej Singh et al., “Neutron transmutation doping technology of Silicon and overview of trial irradiation at Cirus reactor”, BARC/2007/E/023, (2007).

[9] Look, David C., Electrical Characterization of GaAs Materials and Devices, John Wiley & Sons, Chichester (1989).

[10] http://www.fourpointprobes.com/hms3000_brochure.pdf [Accessed 22 March 2019].

STUDY OF SOURCE TERM FOR FANGCHENGGANG NUCLEAR POWER PLANT DURING LOCA ALONG WITH SBO

Pham Ngoc Dong[1], Doan Manh Long[1], Le Dai Dien[1] and Bui Thi Hoa[2]

[1.] *Nuclear Training Centre, 140 Nguyen Tuan, Thanh Xuan, Hanoi*
[2.] *Nuclear Power Centre – Institute for Nuclear Science and Technology,*
179 Hoang Quoc Viet, Hanoi, Email: hoa.hnk52@gmail.com

Project information:

- **Code:** CS/18/10-1
- **Managerial Level:** Institute
- **Allocated Fund:** 80,000,000 VND
- **Implementation time:** 12 months (Jan 2018- Dec 2018)
- **Contact email:** dongpn@vinatom.gov.vn
- **Paper published in related to the project:**

Bui Thi Hoa*, Le Đai Dien, Pham Ngoc Dong, Doan Manh Long, 2018. Source term analysis and evaluation for PWR900 during LOCA along with SBO. 11p., *The 5th Conference on Nuclear Science and Technology for Young Scientist*, Hanoi, Vietnam, 3-4 October 2018, (in Vietnamese).

Abstract: This project has been done as the first phase of capability building for nuclear safety analysis, specially in source term study (ex-vessel phase) at Viet Nam Atomic Energy Institute (VINATOM). The research work of the project focussed on 2 major issues: 1) General study on source term problem including methods of source term evaluation and manner of source term release during design basic accident (DBA) and beyond design basic accident (BDBA); 2) Analysis on PWR900 reactor technology in order to relevance for Fangchenggang nuclear power plant and evaluation on source term for PWR900 by using MELCOR under Loss of Coolant Accident (LOCA) plus loss of offsite power (LOOP). The outcomes of the project are: 1) General report of methods of source term evaluation in case of core melt accident; 2) Report of analysis on source term evaluation for PWR900 reactor during LOCA plus LOOP. The outcomes also are showed that members basically understood and grasped at source term problem and how to use MELCOR code for source term evaluation.

Keywords*: Source term, severe accident, MELCOR, CPR1000.*

1. INTRODUCTION

A source term can be defined as description of the radioactivity releases from nuclear power plant (NPP), including relevant parameters such as core inventory, containment failure mode, effective release high, energy contain of the release, delay between the beginning of the accident and the time that radioactivity release begins, and the duration of the release. Radioactivity release is usually defined for severe accident source terms as fractional release of the core inventory.

Source term study and analysis for NPP in Viet Nam have been stared from 2014 and carried out by research group of VINATOM under frame work of National R&D Project No. KC-05.04/11-15 [1-4]. In that study, it was focusing on the radioactivity release, dispersion and consequences of accident but it was not focusing on the in-vessel phase includes subsequent core melting, relocation, and reactor vessel failure or ex-vessel phase including pressurized melt ejection, interaction of core debris with concrete in the reactor cavity, and ex-vessel steam explosions. Therefore, the project “SOURCE TERM ANALYSIS AND EVALUATION FOR FANGCHENGGANG NPP DURING LOCA ALONG WITH SBO”, code CS/18/10-1 was approved by VINATOM for implementation during year 2018.

The objective of this project is to maintain and develop the capacity of a team of specialist to study nuclear safety, in particular in source term analysis group. Source term analysis and evaluation of NPP’s accidents will be essesstial to support environmental radiation warning and morntoring network in case of nuclear power failure occurs near by the Chinese’s border such as Fangchenggang NPP.

Thus, this study only focus on source term analysis and evaluation for French PWR900 - which was imported to China and improved to have a net power output of 1000 MWe, known as CPR1000 technology built in Fangchenggang NPP during LOCA along with SBO by using MELCOR code.

2. SOURCE TERM EVALUATION METHODS

As mentioned above, the source term could be defined as the magnitudes, forms, modes of release, physical and chemical forms of release from In-Vessel and Out-vessel sources, which in term depend upon the fissile content, operation time and schedule, operation power and accident's consequences, etc [5]. The source term is categorized in two ways one for the licensing of nuclear power plant and second for the probabilistic risk assessment (PRA) as described in TID-14844 [6], NUREG-1465 [7] and WASH-1400 [8].

In case of core melt accident, the source term release process could be divided into five consequence phases as defined in NUREG-1465:

- *Coolant Activity Release*: is start with a postulated pipe rupture and end when first fuel cladding fails;
- *Gap Activity Release*: starts when fuel cladding failure commences, and ends when fuel pellet bulk temperature sufficiently high such that fuel cannot retain fission products;
- *Early in-vessel release*: Begins at the end of the gap release phase (fuel cannot retain fission products), ends when the reactor vessel lower head fails;
- *Ex-vessel Release*: Begins when molten core debris exits the reactor vessel, ends when debris cooled sufficiently such that significant fission products releases stop;
- *Late in-vessel release*: Begins when the reactor vessel lower head fails, No definition provided – infer that definition is analogous to end of ex-vessel release phase.

In order to evaluate the source term, we can use these following methods:

1) *Reduction mechanism method* proposed in NUREG-112, following below equation:

$$Source\ term_i = FPI_i \times Power\ level\ (MW) \times CRE_i \times \left(\pi_{j=1}^{n} RDF_{(i,j)}\right) \times EF_i \quad (1)$$

Where:

+ FPI_i is total mass of radioisotope *i* in coolant per in reactor core;

+ CFR_i is total released mass of radioisotope i from core per total inventory of radioisotope i in reactor core;

+ RDF_i is radioisotope *i* released when using reduction mechanism per radioisotope i released without using reduction mechanism;

\+ EF_i is radioisotope *i* released to environment per total released mass of radioisotope *i* from reactor core.

2) Based on postulated initial conditions through these steps as present in WASH-1400:

- Step 1: Estimation of total inventory of fission products in reactor core;
- Step 2: Estimation of total mass of fission product released from reactor core;
- Step 3: Estimation of total mass of fission product released to containment environment;
- Step 4: Estimation of total mass of fission product in containment;
- Step 5: Estimation of speed of release from containment to outside environment

3) Based on a five-element equation:

$$ST = MAR \times DR \times ARF \times RF \times LPF \tag{2}$$

Where:

\+ *ST* is source term;

\+ *MAR*: material at risk to produce radioactivity material;

\+ *DR*: damage ratio;

\+ *ARF*: airborne release fraction;

\+ *RF*: respirable fraction;

\+ *LPF*: leak path factor.

3. ANALYSIS ON SOURCE TERM EVALUATION FOR PWR900 REACTOR DURING LOCA PLUS LOOP BY USING MELCOR CODE

3.1. MELCOR code and source term problem

MELCOR code [9], is an integral severe accident code, has been developed by Sandia Laboratory, USA. It is intended as a tool for PRA then its capability could account for source term problem through a package named RadioNuclide (RN) package.

The RN package in MELCOR calculates the release and transport behavior of fission product vapors and aerosols during an accident. Rather than tracking all fission product isotopes, the masses of all the isotopes of an element are modeled as a sum in RN package; that is, the total element mass, not its individual isotopes, is modeled. Fifteen material classes are typically used, thirteen containing fission products, plus water, and concrete oxides. Combination of classes to form new classes upon release, such as Cs + I to CsI, is permitted. More detail about model and calculation in RN package could be found in [9].

3.2. PWR900 reactor as reference for CPR1000 reactor

Chinese CPR1000 is a Generation II+ pressurized water reactor, based on the French 900 MWe three cooling loop design imported in the 1990s, improved to have a net power output of 1000 MWe. The information about NPP with CPR1000 technology are limited, that why PWR900 MW is chosen one for this study in case of CPR1000.

French PWR900 pressurized water reactor consists of three cooling loops include of a hot leg, a vertical steam generator, a cold leg and reactor coolant pump (RCP). Pressurizer (PZR) is connected with primary loop by surge line. Reactor core contains 157 fuel rods and 48 control rods with Ag-In-Cd absorption material. Thermal gross power is 2700 MW with primary pressure about 15.5 MPa, thermal surface of Steam Generator (SG) is around 5000 m 2 and PZR volume is 40 m^3.

Safety Relief Valve (SRV) and Pressure Operated Relief Valve (PORV) are mounted inside PZR and connected with Pressurized Tank. SRVs are also mounted on the lines of SG.

3.3. Nodalization scheme of PWR900 for MELCOR code

Nodalization scheme of PWR900 reactor is demonstrated in Fig.1. Thermal hydraulic volumes were modeled as control volumes with their names assigned as numbers. Three primary loops were modeled into two loops which loop 3 and loop 1 were merged into one single loop, and loop 2 was modeled as individual loop containing pressurizer. The volumes of reactor vessel were nodalized into 6 control volumes with their corresponding assigned numbers, such as lower reactor vessel (106), downcomer area (105), bypass area (102), reactor core (101), upper reactor vessel (103) and reactor vessel head (104).

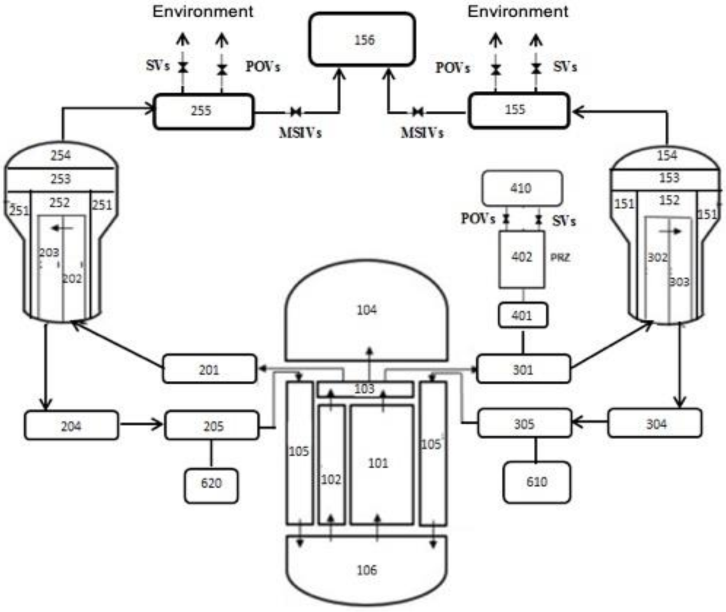

Figure 1: Primary system node graph of PWR900

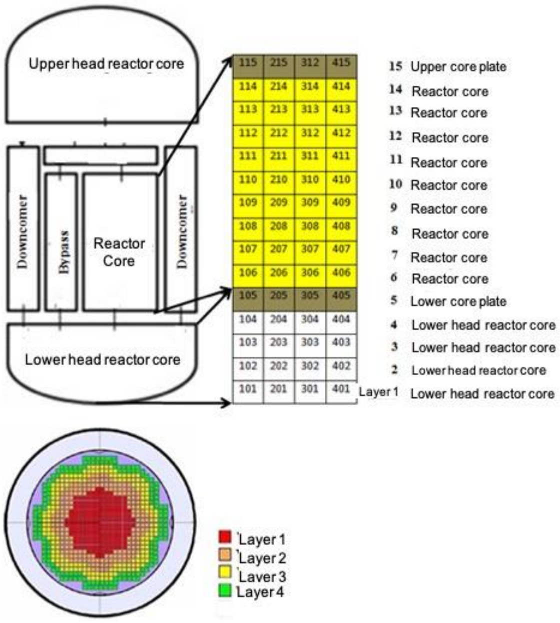

115	215	312	415	15 Upper core plate
114	214	314	414	14 Reactor core
113	213	313	413	13 Reactor core
112	212	312	412	12 Reactor core
111	211	311	411	11 Reactor core
110	210	310	410	10 Reactor core
109	209	309	409	9 Reactor core
108	208	308	408	8 Reactor core
107	207	307	407	7 Reactor core
106	206	306	406	6 Reactor core
105	205	305	405	5 Lower core plate
104	204	304	404	4 Lower head reactor core
103	203	303	403	3 Lower head reactor core
102	202	302	402	2 Lower head reactor core
101	201	301	401	1 Lower head reactor core

Figure 2: Reactor core and lower head node graphs

The reactor core and lower plenum were nodalized into four radically concentric rings and fifteen axial levels as demonstrated in Fig.2.

The ppressurizer system includes nozzle for volume-compensation, pressurizer and pressurizer relief tank which are modeled as control volumes with their numerical names as 401, 402 and 403 respectively (Fig.1). PZR is connected with pressurizer relief tank by two pipelines and two SV and PORV which are modeled in the input file.

Passive safe water injection system includes three tanks with high pressure at 4.48 MPa and their models are numbered and named as 610 for the primary connection and 620 for secondary connection, flow lines together with safe valves are modeled in the input file (see in Fig.1).

3.4 Initial conditions and definition of accident scenario

The scenario choosing for this study is LBLOCA, heat transfer material released along with SBO. Scenario event with following assumptions:

- Heat transfer material released because of large break of cold leg (in the part of PZR circular) with the area of 0.2 m^2;
- SBO lead to broken down of all active safety system, diesel generator, backup batteries except for PZR’s safety relief valve and SG’s safety;
- Emergency water injection of SG not working;
- Not included the water released at the position of primary loop pump;
- SG pressure are maintained by safety valve system below 6.7 MPa;
- Not taking into account the role of safety valves of PZR in this scenario.
- Pressure set point of Hydro-accumulators was at 4.48 MPa;
- Time duration of accident in 24 hours.

4. RESULTS AND DISCUSSION

4.1 Analysis on consequence of accident

Due to the large break, the reactor pressure rapidly decreased equal to the presssure of the cavity (Fig.3) and water inventory in reactor vessel quickly reduced as well (Fig.4). The main events of accident consequence are listed in Table 1.

Table 1: The main events of accident consequence

Events	Time
Starting time	0.0 s
Stopping Reactor	2.0 s
Stopping RCP	7.0 s
Initiated ACC	10.0 s
ACC dry out	32.0 s
Starting oxidation of fuel cladding	240 s

Radionuclides released out of nuclear fuel Pellet	670 s
Core dry out	0.56 h
Relocation molten matterials and moving to lower core head	0.64 h
Total mass of H2 products	200 kg

Due to loss of offsite power, all active safety injection systems were eliminated, only four passive hydro-accumulators (HAs) were available in order to implement emergency core cooling fuction. ACCs were initiated at 10s since initiation of accident, and injection process lasted only 22s then all HAs were run out of water. There was only of the water supplied from the HAs, so that the amount of additional water could not maintain the core cooling flooding due to insufficient core cooling process, the core temperature increased. Under high temperature conditions and direct contact with water vapor, oxidation reactions started to occur at 240 seconds, and total mass of H_2 generated in reactor core is about 200 kg. The oxidation reactions were exothermic reactions which contributed to heat up core structure, fuel cladding started to failed at 670 s at center of reactor core, the trend of temperature down to zero means failure of cladding. After 2318 seconds, the corium started to relocate to the lower pleum.

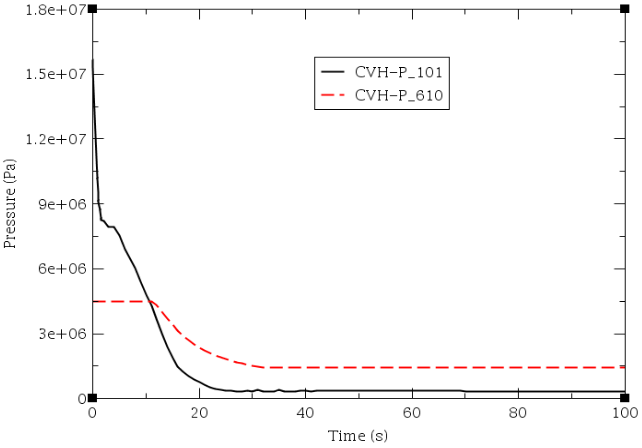

Figure 3: Pressure in Primary (black) and secondary (red) loop

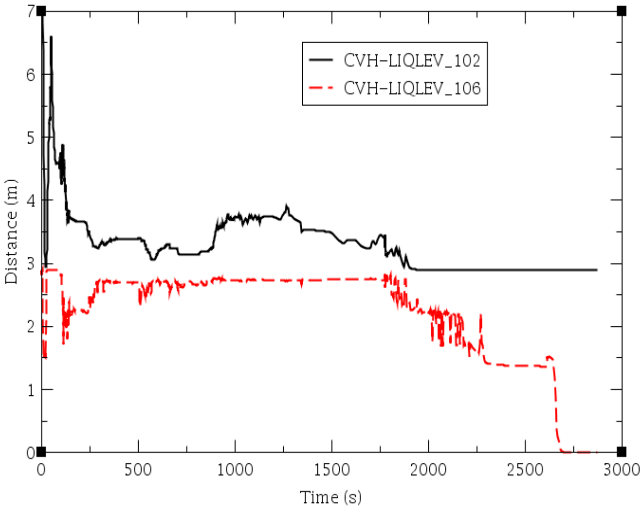

Figure 4: Water level in reactor core and in the lower head

4.2 Evaluation on source term released into primary loop and containment

At the early stage of the accident, the reactor core began to lose water, temperature of the fuel pellet increased, leading to the bulging phenomena of cladding as results of gas fission products released inside the reactor vessel and after that go in to the containment building because of cladding broken through out the breaks. The simulation results show that the radioactive gas begins to release into the reactor vessel space at 0.64 hours since begin of the incident. After 0.8, the calculation results predict the total mass of radioactive aerosols released inside the reactor vessel and inner containment. The radioactive material depositing on structure about 263.42 kg and mass of radioative gas in the water and in the air of the containment building is about of 90.6 kg respectively. However, the mass of radioative gas did not take into account the amount of aerosols and radioactive gases on the surface of thermal structures such as the surface of primary system structures and containment's wall.

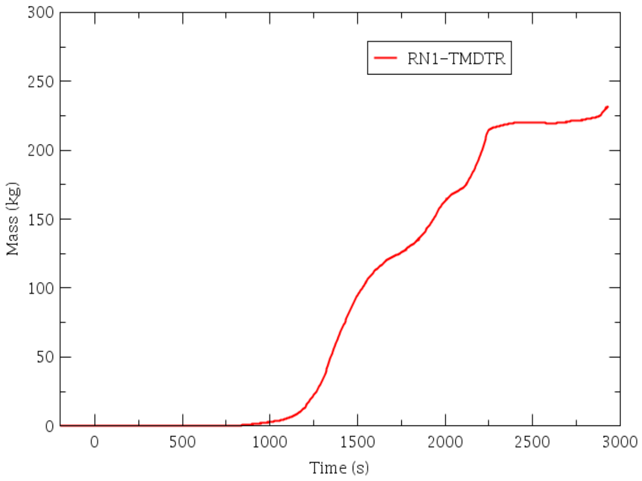

Figure 5: Total radioactive mass of I in primary system and containment buiding

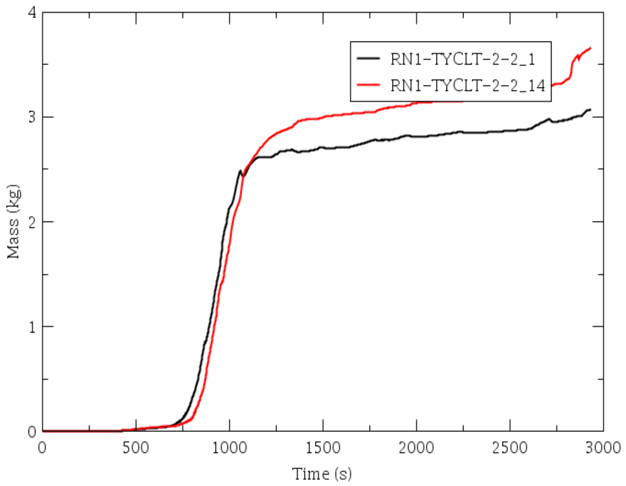

Figure 6: Total radioactive mass of CsOH in primary system and containment buiding

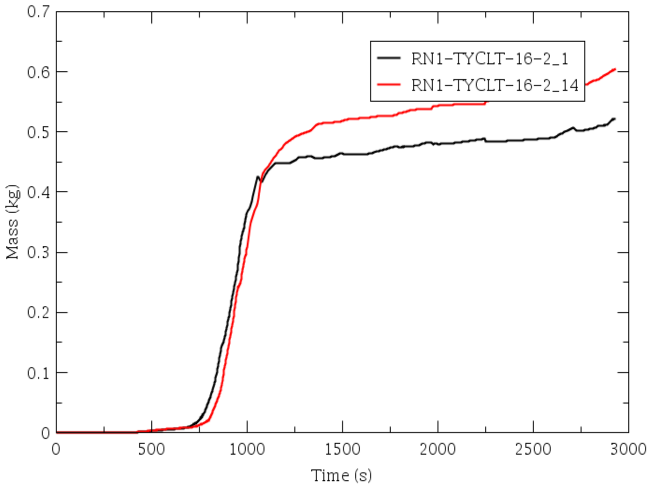

Figure 7: Total radioactive mass of CsI in primary system and containment

Because all most of the radioactive isotopes of Cs and I are released during severe accident, so that the analysis and evaluation of these radionuclides are very important for the source terms. So, we only care about two isotopes as Cs and I under single form and compound forms. From Fig.5 to Fig.7 presents total mas of I, CsOH, CsI respectively, whereas total mass of I is about 3.91 x 10^{-6} kg, total mass of CsOH is about 3.66 kg, and total mass of CsI is about 0.61 kg.

5. CONCLUSION

Transient analysis of accident events and evaluation of source terms is one of the first steps in the study of the source terms released inside the containment building of nuclear power plant in order to support the assessment of source term dispersion to the invironment in the accident conditions and to support to environmental radiation warning in case of accident happended.

This study provides important parameters related to the process of degradation of reactor core and radioactive materials released in case of LBLOCA along with SBO of PWR900 as reference for CPR1000. The results show that after 240 seconds, the fuel oxidation reactions began to occur and the fission products also began to release into containment building. The total amount of radioacitve aerosols and vapor fission products are released in 24 hours after the accident about

17 kg in which about 13 kg of rare element gases and the rest are volatile fission products and CsOH, CsI compounds.

The results presented in this report only show the simulation ability of MELCOR for source term analysis in case of severe accident conditions, but not yet able to produce the main prediction results to determine the processes or behavior of the source term in real scenario conditions. In practice, the caculated results mostly depend on input data of design paramenters of the nuclear power plant. We do not have those data because of limited information about CPR1000 technology and barier of chinese language.

With the first preliminary results, we hope that we will have a full proven input data to validate not only the PWR900 results and also the CPR1000 supporting the assessment of radiation dispertion of NPPs located near by the northern boder of Viet Nam.

REFERENCE

[1] Nguyen Hao Quang et al., Assessment of radiation dose caused by radioactive gaseous effluent released from nuclear power plant Ninh Thuan 1 under scenario of normal operation, Nuclear Science and Technology, Vol. 4, No. 4 (2014), pp. 09-16.

[2] Nguyen Tuan Khai et al., Assessment of radioactive gaseous effluent released from Ninh Thuan 1 nuclear power plant under scenario of Ines-level 5 Nuclear Accident, Communication in Physics, Vol.25, No.2 (2015), pp. 165-172.

[3] Nguyen Tuan Khai et al., Assessment of radioactive gaseous effluent released from Ninh Thuan 1 nuclear power plant under scenario of Ines-level 6 Nuclear Accident, Nuclear Science and Technology, Vol. 5, No. 1 (2015), pp. 01-07.

[4] Nguyen Tuan Khai and Le Dinh Cuong, Assessment of radioactive gaseous effluent released from Ninh Thuan 1 nuclear power plant under scenario of Ines-level 7 Nuclear Accident, Communication in Physics, Vol.25, No.5 (2015), pp. 375-382.

[5] Khurram Mehboob et al., “US NRC progress in source term evaluation,” DOI: 10.1109/APPEEC.2012.6401509, January 2012.

[6] J. J. DiNunno et al, “Calculation of Distance Factors for Power and Test Reactor Sites,” Technical Information Document (TID)-14844, U.S. Atomic Energy Commission, 1962.

[7] L. Soffer, S.B. Burson, C.M. Ferrell, R.Y. Lee, and J.N. Ridgely, “Accident Source Terms for Light-Water Nuclear Power Plants,” NUREG-1465, U.S. Nuclear Regulatory Commission, Washington, DC, February 1995.

[8] U.S. Nuclear Regulatory Commission; “Reactor Safety Study: An Assessment of Accident Risks in U.S. Commercial Nuclear Power Plants,” WASH-1400 (NUREG-75/014), December 1975.

[9] L.L. Humphries. MELCOR Computer Code Manuals, Vol. 2: Reference Manual Version 2.2.9541 2017 Sandia National Laboratories Albuquerque, SAND2017-0876.

1.3- Instrumentation, Nuclear Electronics

STUDY ON DESIGN AND CONSTRUCTION OF ELECTRONIC PERSONAL DOSIMETER

Nguyen Duc Tuan, Mai Van Dien, Bui Duc Ky,
Chu Vu Long, Vu Van Tien and Nguyen Thi Thuy Mai

Institute for Nuclear Science and Technology,179 Hoang Quoc Viet, Ha Noi

Project information:

- **Code:** DTCB-01/17/VKHKTHN
- **Managerial Level:** Ministry
- **Allocated Fund:** 880,000,000 VND
- **Implementation time:** 24 months (Jan 2017- Dec 2018)
- **Contact email:** ngdtuan108@gmail.com
- **Paper published in related to the project:**

Nguyen Duc Tuan, Mai Van Dien, Bui Duc Ky, Chu Vu Long, Vu Van Tien, Nguyen Thi Thuy Mai, 2017. Development of measurement methods and dose evaluating algorithmsfor electronic personal dosimeter. *Nuclear Science and Technology*, Vol.7, No. 3 (2017), pp. 25-33.

Abstract : For personal radiation dose monitoring, electronic personal dosimeters (EPD), also known as active personal dosimeter (APD), using silicon diode detector has the advantage capability of measuring and displaying directly the exposure results of gamma, beta, neutron radiation in real time. They are mainly considered as good complement to passive dosimeters to satisfy ALARA principle in the radiation protection. The measurement method and algorithm for evaluating personal dose equivalents such as Hp(10) and Hp(0.07) from air kerma are studied and developed in the way of matching the shape of a detector’s energy response curve to the kerma-to-personal dose equivalent conversion function, providing an approximate means of determining the dose equivalent without the need to resolve the actual incident energies. The algorithm has also been experimentally verified at Secondary Standards Dosimetry Laboratory (SSDL) of INST by the beam of radiation defined in ISO 4037-1. Based on these method and algorithm, in the framework of the project, we have successfully researched and manufactured the electronic personal dosimeter complying with IEC-61256 standard.

Keywords: *Personal dose equivalent, Silicon diode detector, EPD.*

1. INTRODUCTION

Radiation monitors fall into the categories of environmental radiation monitoring, personal dose monitoring, surface contamination monitoring, radioactive material monitoring and area process monitoring. For personal dose monitoring, electronic personal dosimeter was carried in a worker’s pocket measures and displays in real time the amount of radiation received while the worker performs their task. This dosimeter is also equipped with a function that issues an alarm in cases where the exposure dosage exceeds a preset value. The development of electronic personal dosimeters has made progress in recent years, and an IEC standard (IEC 61526) has been established for electronic personal dosimeters.

The silicon PIN photodiode detector with its advantage in sensitivity, volume, power consumption, low cost, etc. is one of the key components of the EPD for radiation detection and measurement. However, because the atomic coefficient of the detector is higher than that of the tissue material and the sensitive layer is thin, the photon energy response of the Si-PIN detector is not consistent in the energy range from 20 keV to 1.25 MeV, especially in the low-energy region (less than 100 keV), where the photon energy response is high. This characteristic of detector seriously affects the measurement accuracy of the instrument.

The aim of the present study is to develop the measurement methods and algorithms to calculate the dose in terms of two dose quantities Hp(10) and Hp(0.07) (respectively, the personal dose equivalent at 10 and 0.07 mm depth) applicable for photon energies in the range of 20–1250 keV to archive an appropriate photon dosimetry response used for electronic personal dosimeter. In the framework of the project, we have also successfully researched and manufactured the electronic personal dosimeter based on the method and algorithm developed.

2. METHOD AND ALGORITHM

Secondary or operational quantities are used for occupational monitoring. The ICRU-39 (1985) has defined the operational quantities for individual monitoring is personal dose equivalent Hp(d). For photons, the reference primary physical quantity is kerma, free in air, or "air kerma", K_a. Like the ambient dose equivalent $H^*(d)$, the personal dose equivalent Hp(d) is not directly measurable and therefore also derived from air-kerma using appropriate conversion coefficient. Energy dependent dose conversion coefficients are used to establish the relationship between the primary physical quantities and the operational quantities Hp(d). Therefore, for the case of mono-energetic photon at energy E, the personal dose equivalent Hp(d) can be determined by

$$\mathbf{Hp(d) = C_p(E).K_a(E)} \tag{1}$$

where $K_a(E)$[Gy] isair-kermaandC$_p$(E)[Sv/Gy]is air-kerma to dose equivalent conversion coefficient (Figure 1). The conversion coefficients from air kerma K_a to the quantities Hp(10) and Hp(0.07) for individual monitoring for workplace monitoring depend on photon energy as shown in Figure 1 (ICRP74 or ICRU51).

In actual field conditions, the energy of the photons is not known. The aim of this method described here is to discuss how the difficulty encountered can be overcome in a different approach, which is called the fitted-shape method. In the effect of the radiation field, that is, to the count readings N, of the detectors worn by the exposed individual, and air-kerma, Ka, have the following relation analogous to following equation

$$\mathbf{N = R(E).\,K_a(E)} \tag{2}$$

where R(E) is energy dependent detector response function in units of counts per unit air-kerma.

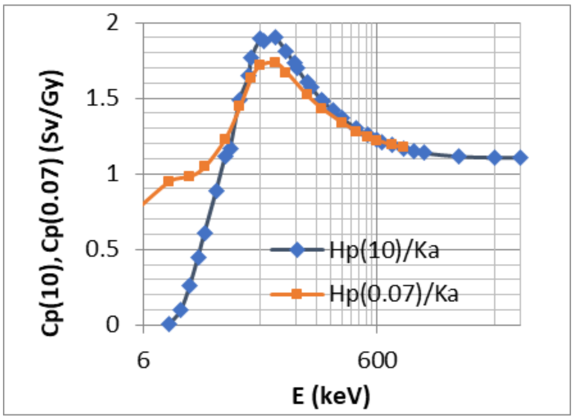

Figure 1: Conversion coefficients from air kerma Ka to Hp(10) and Hp(0.07)

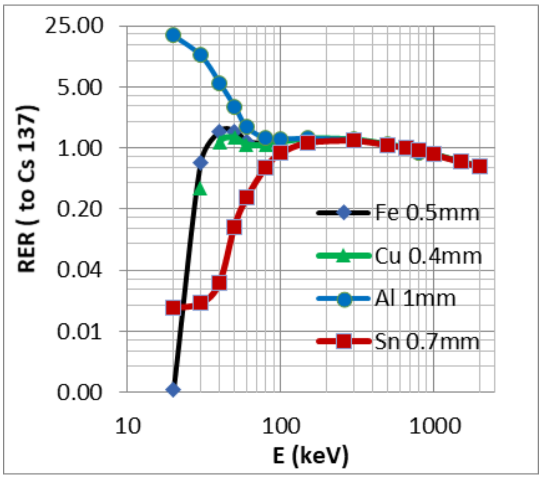

Figure 2: Filtered detector’s response

Equation(2) implies that N, is proportional to air kerma in the case of monodirectional monoenergetic radiation fields. Most detectors for photons have this property. Note the similarity in form between Equations (1) and (2). Assuming that the photon fields are identical, it **is shown** that matching the shape of a detector’s energy response curve to the kerma-to-personal dose equivalent conversion function provides an approximate means of determining the dose equivalent without the need to resolve the actual incident energies. As long as R(E) has a similar energy response to that of $C_p(E)$, the dosimeter measurement can be said to be accurate. Based on this design philosophy, the ratio is determined by:

$$\frac{\mathbf{Hp(d)}}{\mathbf{N}} = \frac{\mathbf{C_p(E)}}{\mathbf{R(E)}} = \mathbf{k} \tag{3}$$

K is termed dose calibration constant [Sv/Cnt], which defines the traditional energy response of the dosimeter in terms of dose equivalent per unit count. This is a quantitative formulation of a design criterion for detectors. Assuming such a fitted dosimeter system, one immediately obtains

$$\mathbf{Hp(d) = k.N} \tag{4}$$

This is the relationship being sought between H and N. It is significant for arbitrary movements of the individual within radiation fields with variable energy spectra. The detector response function, R(E), can be determined in monoenergetic, monodirectional radiation fields. In order to measure Hp(d) according to equation (4) the dose calibration constant k must be determined from equation (3). In order to satisfy equation (3), the following “fitting procedure” is carried through. The algorithm of these determination and fitting procedure are implemented as shown in Figure 3.

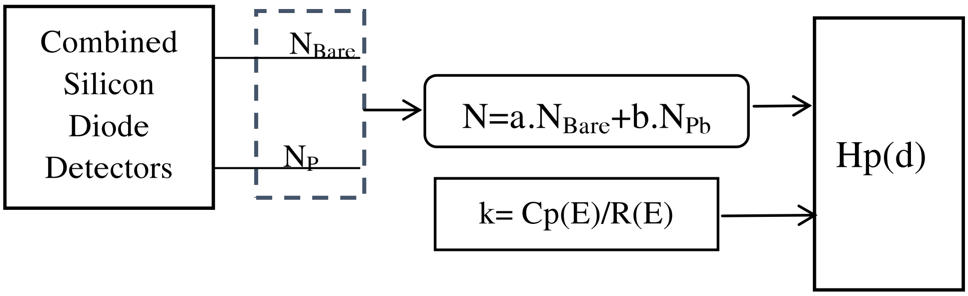

Figure 3: Hp(d) Evaluating Algorithm of Fitting-shape Method

Based on the evaluation results of the metal filtered silicon (PIN) diode detector relative energy response (RER) as shown in Figure 2 by Monte Carlo radiation transport methods and the known shape of the kerma to personal dose equivalent conversion function curve, this dose calculation algorithm is implemented mathematically by combining the signals of the two silicon diode detectors, the bare and lead filtered (1.5 mm Pb) ones, expressed by N_{Bare} and N_{Pb} counters. The linear combination of counts and the corresponding responses are determined by:

$$N = a.N_{Bare} + b.N_{Pb} \tag{5}$$

and

$$R(E) = a.R_{Bare}(E) + b.R_{Pb}(E) \tag{6}$$

From Equations (3) and (6), this method involves solving the following equations

$$C_p(E) = k.\,(\,a.R_{Bare}(E) + b.R_{Pb}(E)) \tag{7}$$

for the desired energy range. The constants a,b and k in equation (7) are obtained by using the 3D least square fit method of the curve fitting z=ax+by wherez = $C_p(E)$, x = $R_{Bare}(E)$ và y = $R_{Pb}(E)$.The practical values and formulation of Hp(d) for application will be calculated in detail in the experimental part.

3. EXPERIMENTAL

In the experimental part, we considered and carried out in detailed the algorithm of fitted-shape method by its advantages for evaluating the Hp(d) quantities.

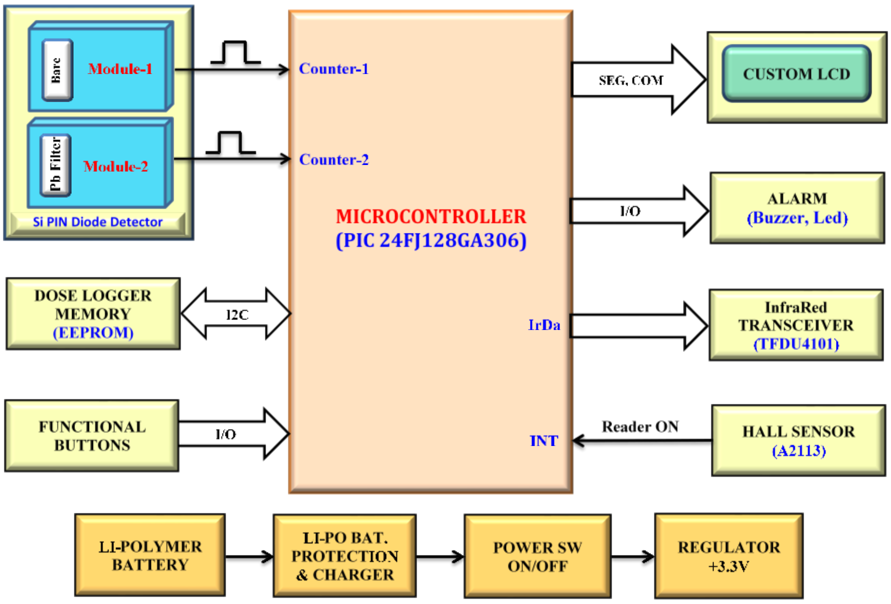

Figure 4: Block diagram of electronic personal dosimeter

The EPD has been designed and manufactured and its block diagram is shown in Figure 4, which consists of a number of functional electronic parts as follows.

1. ***Module-1, module-2***: consist of combined bare and lead filter silicon PIN diode detectors;the front-end electronic parts functioned as charge pre-amplifier, shaping amplifier and discriminator.

2. ***Dose Logger Memory***: Non-volatile memory EEPROM for information accumulation and storage;

3. ***Functional Buttons***: Buttons for selecting the dosimeter's indication and setting mode;

4. ***Microcontroller***: The microprocessor controls the dosimeter's operating modes, alarm device, infrared communication channel, custom LCD, non-volatile memory. It also operates the control buttons and performs all necessary calculations and communication.

5. ***Custom LCD***: Custom LCD design with 4-digits and radiation unit symbols.

6. ***Alarm***: Audible (buzzer) and light (LED) alarm signals;

7. ***Infrared ENC/DEC and Transceiver:***The IR-communication channel enables the exchange of information with a PC.

8. ***Proximity Hall Sensor:***signals the interface between EPD and the dosimeter reader.

9. ***Battery Power Supply***: consist of ***Li-polymer battery, Li-polymer battery protection and charger***, ***Power SW On/Off, LDO 3,3V Regulator***.

The silicon PIN diode detector generates the pulse charge output by the incident photon. The charge is converted to voltage by the charge pre-amplifier. The long-width signal is converted to a practical pulse signal by using a shaping amplifier, and then to logic pulse for digital counting by discriminator. Microcontroller counts the pulses from two independent channels of silicon diode detectors for calculation.

Firmware for this dosimeter device was developed under C language that designed for PIC micro-controller from CCS Company.The C source code written for this application was designed to control the hardware such as the counter, timer, LCD panel, Real Time Clock circuit and Buzzer. This program also processes the count accumulated in measuring time to calculate the personal dose equivalents and display on LCD.

Figure 5: The complete electronic personal dosimeter VinaDOSE-01

The complete electronic personal dosimeterVinaDOSE-01 was shown in Figure 5 with the following specifications in Table 1.

Table 1. Specifications of VinaDOSE-01

Detector	**Silicon PIN diodes**	**Angular Response**	**0º to 60º: ≤ ±20% for Cs-137**
Energy Range	20 keV-3MeV for X andgamma radiation	**Display**	Custom LCD 4 digits and symbols

Dose Range	0.1µSv to 10Sv	**Operating Environment**	Temperature: -10°C to 50° C Humidity: 0% to 90%
Dose Rate Range	0.1µSv/h to 100 mSv/h	**Power**	Li-polymer Battery 2500 mAh Operating Hours 1250 hours of continuous use
Dose Accuracy	<±30%	**Dimensions**	90 x 67 x21 mm
Dose Alarm Settings	Continuously adjustable 1 mSv tới 9999 mSv	**Weight**	130g
Dose Rate Alarm Settings	Continuously adjustable 1 µSv/h tới 9999 uSv/h	**IP Rating**	IP65
Dose Storage	2330 records	**Radiation performance requirements**	According to IEC 61526

To investigate the dosimetry characteristics of the method on the device manufactured, experiments were performed for an actual photon radiation field. The EPD was located in the front of the ISO PMMA Phantom (30x30x15 cm) and the Si detector was coincident with the center of the reference radiation fields at the Secondary Standard Dosimetry Laboratory (SSDL) of Institute for Nuclear Science and Technology (INST). The experimental data has been obtained by performing irradiation according to the following characteristics of reference radiation field. A low-energy reference radiation is based on the narrow-spectrum series of the ISO Standard 4037-1 produced by an X-ray machine. The narrow-spectrum series used in the research described in this paper mainly include N-30 (24 keV), N-40 (33 keV), N-60 (48 keV), N-80 (65 keV), and N-100 (83 keV) and a high-energy reference radiation is based on 137-Cs (662 keV) and 60-Co (1.25 MeV) isotope radiation sources.

4. RESULTS AND DISCUSSION

Response determination and calibrations

Measurement results of the bare and Pb filtered detector’s energy responses on air-kerma rate are shown in Table 2 and illustrated on Figure 6 and 7. From these data, the fitting procedures by least square fit were carried out in case of Cp(10) and Cp(0.07) according to equation (11) and the linear combination response R10 and R07 of two practical responses were obtained. The calculated ratios k in Table 2 show good matching or similarity of combined response and conversion function. The formulation of Hp(10) and Hp(0.07) quantities are given in Equations (14) and (15).

$$Hp(10)= 0.0176(0.09805\ N_{Bare} + 0.18341\ N_{Pb}) \quad (8)$$

$$Hp(0.07)=0.0182(0.09574N_{Bare}+ 0.17481\ N_{Pb}) \quad (9)$$

where N_{Bare}, N_{Pb}: count values [Cnts]. It is can be seen from the obtained Equations (8)and (9) that the personal dose equivalents Hp(d) have a simple one-to-one relationship with the counting numbers of pulses acquired from two detectors.

Table 2. VinaDOSE-01 energy response function

STT	Energy (keV)	R_{Bare} (Cnts/μGy)	R_{Pb} (Cnts/μGy)	Cp(10) (μSv/μGy)	$R_{10}(E)$ (Cnts/μGy)	$k(10)=C_p(10)/R_{10}(E)$ (μSv/Cnts)	Error (%)
1	20	9.66	0.00	0.61	0.95	0.0107	38.77
2	33	7.43	0.03	1.17	0.73	0.0268	52.38
3	48	15.06	1.31	1.65	1.52	0.0180	2.77
4	65	14.77	2.48	1.88	1.57	0.0199	13.42
5	83	19.66	3.98	1.90	2.13	0.0148	15.47
6	100	16.55	2.59	1.81	1.85	0.0163	7.30
7	200	11.38	4.06	1.49	1.48	0.0168	4.22
8	300	9.31	6.05	1.37	1.45	0.0157	10.63
9	400	8.59	6.75	1.30	1.45	0.0150	14.66
10	500	7.76	6.61	1.26	1.35	0.0155	11.83
11	662	4.97	4.97	1.21	1.30	0.0155	11.50
12	800	6.21	6.21	1.19	1.16	0.0170	2.97
13	1000	5.48	5.48	1.17	1.03	0.0189	7.73
14	1250	2.75	2.75	1.15	0.77	0.0248	41.05

- Average ratio k(10)=0.0176
- Constants a=0.09805, b=0.18341

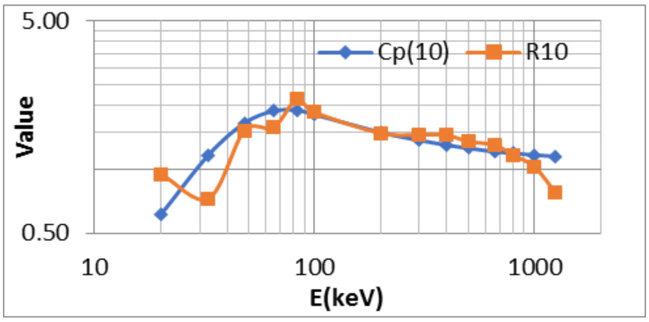

Figure 6: Similarity of response R10 and conversion Cp(10)

STT	Energy (keV)	R_{Bare} (Cnts/μGy)	R_{Pb} (Cnts/μGy)	Cp(0.07) (μSv/μGy)	$R_{0.07}$(E) (Cnts/μGy)	$k(0.07)=C_p(0.07)/R_{0.07}(E)$ (μSv/Cnts)	Error (%)
1	20	9.66	0.00	1.045	0.93	0.0188	3.41
2	33	7.43	0.03	1.300	0.71	0.0304	67.18
3	48	15.06	1.31	1.600	1.49	0.0179	1.52
4	65	14.77	2.48	1.720	1.53	0.0187	2.66
5	83	19.66	3.98	1.700	2.08	0.0136	25.15
6	100	16.55	2.59	1.669	1.81	0.0154	15.39
7	200	11.38	4.06	1.432	1.44	0.0166	8.70
8	300	9.31	6.05	1.336	1.41	0.0158	13.11
9	400	8.59	6.75	1.280	1.40	0.0153	16.19
10	500	7.76	6.61	1.244	1.31	0.0159	12.86
11	662	4.97	4.97	1.200	1.25	0.0160	12.02
12	800	6.21	6.21	1.189	1.12	0.0176	3.16
13	1000	5.48	5.48	1.173	0.99	0.0197	8.15
14	1250	2.75	2.75	1.030	0.74	0.0231	26.72

- Average ratio k(0,07)=0.0182
- Constants: a=0.09574, b=0.17481

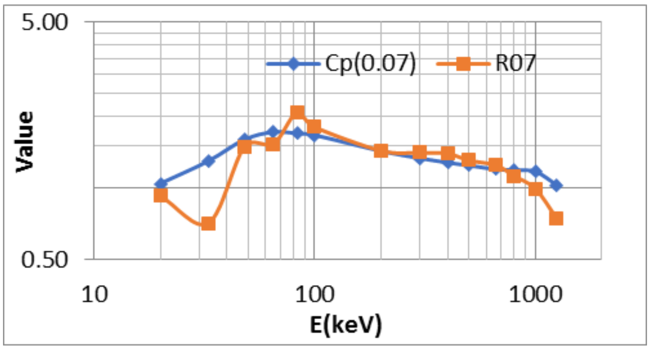

Figure 7: Similarity of response R07 and conversion Cp(0.07)

The VinaDOSE-01 was calibrated in terms of personal dose equivalent, Hp (d). The calibration method was carried out as follows:

- Selection of a suitable reference radiation field and a point of test.
- Determination of the value of the appropriate basic physical quantity (air-kerma) in the point of test and calculation of the value of the delivered dose.

- Position of the dosimeter and a phantom with its reference point at the point

of test, irradiating the dosimeter and reading the indicated value.

- Calculation of the calibration factors, CF(10) and CF(0.07) of the dosimeter defined as the ratio of the delivered dose value to the measured dose value according to formulas above.

- The responses, Res(10) and Res(0.07), of dosimeter is determined as the quotient of the measured dose value and the delivered dose value.

The calibration results for VinaDOSE-01 are presented in Table 3.

Table 3: The calibration of VinaDOSE-01 dosimeter results

References	**Delivered Dose (uSv)**		**Measured Dose (uSv)**		**Calibration Factors**		**Response**	
Mean Energy (keV)	Hp(10)	Hp(0.07)	Hp(10)	Hp(0.07)	CF(10)	CF(0.07)	Res(10)	Res(0.07)
20	930.0	1593.2	1296.7	1309.4	0.72	1.22	1.39	0.82
33	1595.5	1772.7	1014.3	1024.1	1.57	1.73	0.64	0.58
48	4116.8	3992.0	3699.0	3734.7	1.11	1.07	0.90	0.94
65	3241.1	2965.3	2201.3	2221.5	1.47	1.33	0.68	0.75
83	828.4	741.2	841.1	847.8	0.98	0.87	1.02	1.14
662	2420.0	2400.0	2437.0	2423.7	0.99	0.99	1.01	1.01
Mean:					1.14	1.20	0.94	0.87

Linearity test

To perform the linearity of dosimeter test, the dosimeter is irradiated at the same dose rates for different durations (1, 2, 3, 4, 5, 6 and 7 minutes). Deviation was calculated from the standard reading as follows:

$$\text{Deviation} = \frac{(\text{Calculated Dose} - \text{Measured Dose})}{\text{Calculated Dose}} \times 100\%$$

The results of linearity tests for VinaDOSE-01 are presented in Table 4.

The dosimeter under study showed a good response in all energies except, the response at quality N-40 (33 keV) which was rather high. The linearity of the dosimeters was within ±30 %.This is in exception to the qualitiesN-25, N-40, where these limits were exceeded.

Table 4: VinaDOSE-01 linearity test

Quality /Energy (keV)	**Elapsed Time (min)**	**Hp(10) Measured (uSv)**	**Hp(0.07) Measured (uSv)**	**Hp(10) Calculated (uSv)**	**Hp(10) Deviation (%)**	**Hp(0.07) Calculated (uSv)**	**Hp(0.07) Deviation (%)**
N-25/	1	21.59	21.8	15.50	-39.3	26.55	17.9

20	2	43.06	43.48	31.00	-38.9	53.1	18.1
	3	65.06	65.7	46.50	-39.9	79.65	17.5
	4	86.66	87.51	62.00	-39.8	106.2	17.6
	5	108.17	109.23	77.50	-39.6	132.75	17.7
	6	130.02	131.29	93.00	-39.8	159.3	17.6
	7	151.28	152.76	108.50	-39.4	185.85	17.8
N-40/ 33	1	16.89	17.06	26.59	36.5	29.55	42.3
	2	33.74	34.07	53.18	36.6	59.1	42.4
	3	50.57	51.07	79.77	36.6	88.65	42.4
	4	67.67	68.33	106.36	36.4	118.2	42.2
	5	84.6	85.42	132.95	36.4	147.75	42.2
	6	101.46	102.44	159.54	36.4	177.3	42.2
	7	118.34	119.48	186.13	36.4	206.85	42.2
N-60/ 48	1	53.31	53.82	68.61	22.3	66.53	19.1
	2	116.79	117.91	137.22	14.9	133.06	11.4
	3	180.04	181.77	205.83	12.5	199.59	8.9
	4	243.56	245.91	274.44	11.3	266.12	7.6
	5	306.7	309.66	343.05	10.6	332.65	6.9
	6	369.9	373.47	411.66	10.1	399.18	6.4
N-80/ 65	1	36.77	37.11	54.02	31.9	49.42	24.9
	2	73.82	74.5	108.04	31.7	98.84	24.6
	3	110.83	111.84	162.06	31.6	148.26	24.6
	4	147.48	148.83	216.08	31.7	197.68	24.7
	5	184.03	185.72	270.1	31.9	247.1	24.8
	6	221.07	223.09	324.12	31.8	296.52	24.8
	7	256.82	259.17	378.14	32.1	345.94	25.1
N-100/ 83	1	13.46	13.57	13.81	2.5	12.35	-9.8
	2	27.32	27.54	27.62	1.1	24.7	-11.5

	3	41.57	41.9	41.43	-0.3	37.05	-13.1
	4	55.56	56	55.24	-0.6	49.4	-13.4
	5	69.54	70.1	69.05	-0.7	61.75	-13.5
	6	83.96	84.63	82.86	-1.3	74.1	-14.2
	7	98.13	98.91	96.67	-1.5	86.45	-14.4
Cs-137/ 661	1	40.33	40.11	40.33	0.0	40	-0.3
	2	80.72	80.27	80.66	-0.1	80	-0.3
	3	121.28	120.61	120.99	-0.2	120	-0.5
	4	162.01	161.12	161.32	-0.4	160	-0.7
	5	203.17	202.06	201.65	-0.8	200	-1.0
	6	243.44	242.1	241.98	-0.6	240	-0.9
	7	284.32	282.76	282.31	-0.7	280	-1.0

Angle dependence

The angle dependence of the personal dosimeter was investigated for the following angles: 0^{o}, $\pm25^{o}$, $\pm35^{o}$, $\pm45^{o}$, $\pm60^{o}$using Cs-137 radiation quality for the test performance.The results are presented in Table5 and Figure 8. The angle dependence of the relative response is not higher than15%.

Table 5: The angle dependence of the relative response of VinaDOSE-01

Angle (Degree)	**Hp(10) Measured (uSv)**	**Relative Response Hp(10) (%)**	**Hp(0.07) Measured (uSv)**	**Relative Response Hp(0.07) (%)**
0	34.07	100.0	33.85	100.0
25	33.47	98.2	33.25	98.2
35	32.92	96.6	32.71	96.6
45	32.08	94.2	31.89	94.2
60	30.19	88.6	30.02	88.7
-25	33.54	98.4	33.31	98.4
-35	33.07	97.1	32.86	97.1
-45	31.85	93.5	31.65	93.5
-60	30.29	88.9	30.13	89.0

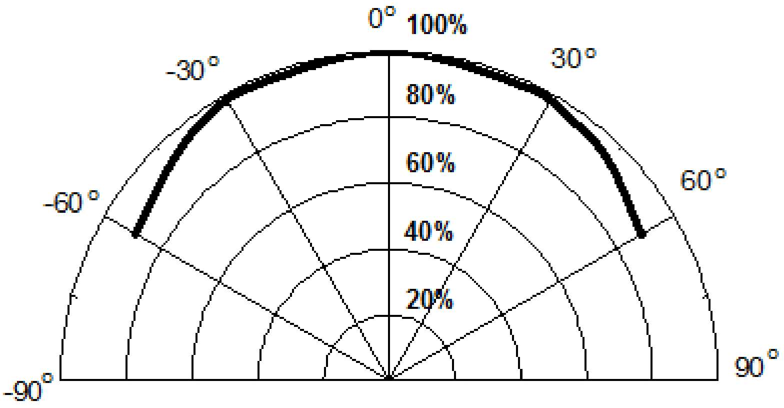

Figure 8: VinaDOSE-01 Angular Response

5. CONCLUSIONS

The electronic personal dosimeter VinaDOSE-01 was completely designed and constructed. The measurement methods and dose evaluating algorithms for electronic personal dosimeter were described in detail. The testing of the algorithm for EPD exposed by the beam of radiation defined in ISO 4037-1 at SSDL of INST shows good results of personal dose equivalents are partially met the EPD design requirements according to the IEC 61526 Standard and proving the suitability of the algorithm for evaluating personal dose equivalents.

REFERENCE

[1] Dang Thanh Luong, PhD thesis, "Some results of research on methods of measurement of ionizing radiation dose by the thermoluminescent dosimeter".

[2] F. Sinclair, A. Clapp, G. Entine, R.M.D., 4 4 Hunt St., Watertown, MA 02172 and S. Kronenberg ..."Energy Compensated Solid State Gamma Dosimeter".

[3] H. Stadtmann, C. Hranitzky, "Comparison of different dose algorithms used to evaluate a two element LiF:Mg,Ti TL personal dosimeter", Radiation MeasurementsVolume 43 Issues 2-6H, , pp 571-575 (2008).

[4] International Organization for Standardization. X and Gamma Reference Radiation for Calibrating Dosimeters and Doserate Meters and for Determining their Response as a Function of Photon Energy. ISO 4037-1 (Geneva: ISO) (1996).

[5] International Electrotechnical Commission. Radiation protection instrumentation. Measurement of personal dose equivalent Hp(10) and Hp(0.07) for X, gamma, neutron and beta radiation: direct reading personal dose equivalent and monitors. IEC 61526 (Geneva: IEC) (2005).

DESIGN, MANUFACTURE, INSTALLATION AND TEST OF A HEAT RECOVERY DEVICE OF A REGENERATIVE FURNACE FOR THE ZINC OXIDATION AT THE CENTER FOR TECHNOLOGY DEVELOPMENT – INSTITUTE FOR TECHNOLOGY OF RADIOACTIVE AND RARE ELEMENTS

Luong Manh Hung, Tran Ngoc Vuong and Nguyen Dinh Dang

Institute for Technology of Radioactive and Rare Elements,
48 Lang Ha, Dong Da, Hanoi

Project information:

- **Code:** CS/17/03-02
- **Managerial Level:** Institute
- **Allocated Fund:** 70,000,000 VND
- **Implementation time:** 12 months (Jan 2017- Dec 2017)
- **Contact email:** luonghung2505@gmail.com
- **Paper published in related to the project:**

Luong Manh Hung, Tran Ngoc Vuong, Nguyen Dinh Dang, Nguyen Thi Hong Anh, 2018. Study of a heat recovery device of a regenerative furnace for the zinc oxidation at the center for technology development – institute for technology of radioactive and rare elements. *Scientific and Technological Review*, Viet Tri University of Industry (ISSN 0866 – 7772), 55-58, 2018 (in Vietnamese).

Abstract: This paper presents the theoretical calculations, installation results and test of a heat recovery device of a regenerative furnace for the oxidation of zinc at Center for Technology Development – Institute for Technology of Radioactive and Rare Elements. Based on the requirements of reality, the heat recovery device is designed as a system of heat exchanging including heat exchanger with a diameter of 110 mm and distribution pipes with a diameter of 210 mm. The air at ambient temperature is blown by the blower through the heat recovery unit, where the air is exchanged with hot gas flow. After the heat exchange, the air is used for the combustion process and can enhance the combustion process, thereby reduce the coal consumption. It is shown that after performing with the heat recovery device the temperature of the air increases from 40^0C to over 300^0C.

Keywords: Heat exchanger, oxidation recovery process, zinc.

I. INTRODUCTION

Nowadays, energy is becoming increasingly exhausted leading to many serious environmental problems. The main limitation of using energy from fossil fuels is that it causes environmental pollution due to the emissions of SO_2, CO_x, NO_x.

At factories, the heat is lost by waste gas, sewage or cooling machine ... escaping into the surrounded environment, contributing to the global warming. If we can fully use the heat generated by combustion processes and make less the amount of CO_2, SO_2 and the toxic gases discharged by industrial production, the fuel and raw material consumption can be significantly reduced. By using modern heat recovery devices, it is possible to utilize most of the waste heat to bring it back to the production. Therefore, the recovery of heat from waste gas and wastewater to reuse can result in the increasing of the thermal efficiency of industrial systems to more than 90%.

The Center for Technology Development (CTD) has been producing zinc products, especially zinc oxide by oxidation recovery technology for more than twenty years. In recent years, the CTD has produced thousands of tons of zinc oxide per year, which require a large amount of coal as a fuel material (about 1500 tons/year). Therefore, it is necessary to have fuel saving methods to optimize and improve the efficiency of the production process. The aims of this work are calculation, design and manufacture of heat recovery units to address two issues: i) Reducing the temperature of airflow and dust before they enter the canal, the product hierarchy and the product compartment systems. This can increase the life of the fabric bag and reduce the cost of the production. ii) Increasing the temperature of the clean air flow into the furnace that may lead to the reducing of the coal consumption and increasing the price competitiveness in the market.

II. EXPERIMENTALS

The purpose of the project has been reached by performing the following steps:

1. Calculating, designing, manufacturing and installing heat recovery device of a regenerative furnace for the zinc oxidation at the Center for Technology Development – Institute for Technology of Radioactive and Rare Elements.

2. Operating the heat recovery tests, estimating the efficiency and proposing solutions of thermal utilization to the technology deployment center in the near future.

2.1. Calculate and design of heat recovery equipment [1, 2, 3, 4]

Experimental parameters were chosen as follows:

The heat exchanger was ϕ 110 mm and the distribution tube was ϕ 210 mm.

The fan flow was 1200 m^3/h.

The temperature of the air passing through the heat exchanger was 320^{0}C.

The temperature of the environment was 40^{0}C.

The amount of heat the air is calculated according to the formula:

$$Q = G_2.C_{P_2}.(t_2 - t_1)$$

The average temperature of the air in the tube is defined as follows:

$$t_{tb} = \frac{t_1 + t_2}{2} = \frac{320 + 40}{2} = 180^0 C$$

According to the average temperature of the air:

$$P_2 = 0{,}779 \ (Kg/m^3);$$

$$C_{P_2} = 1{,}022 \ (kJ/Kg.\ grad);$$

$$\lambda_2 = 3{,}87.10^{-2} \ (W/m.K);$$

$$\alpha_2 = 47{,}5.10^{-6} \ (m^2/s);$$

$$P_{r_2} = 0{,}681.$$

The Flow of air: $G_2 = 1200\ m^3/h = 0{,}43\ (kg/s)$.

As a result: Q = 0,43. 1,022. (320-40) = 123 (kW).

a) Consideration with the smoke of the furnace

Temperature before the heat transfer was 1025^0C, because the experiment distance was short and experiment cross section was large, the temperature difference of the oxidation smoke before and after the heat transfer was considered 25^0C. Therefore, the temperature of the dust after the process was 1000^0C.

The average temperature of oxidized fume was as follows:

$$t_{tb1} = \frac{1000 + 1025}{2} = 1012{,}5\ (\ ^oC)$$

With the following parameters:

$$P_1 = 0{,}282\ (Kg/m^3);$$

$$\lambda_1 = 8{,}12.10^{-2}\ (W/m.K);$$

$$v_1 = 1{,}306.10^{-6}\ (m^2/s);$$

$$P_{r_1} = 0{,}720.$$

The cross section of the oxidation chamber was 2.5x2.7

=> The area of the cross section was $6{,}75m^2$;

The Flow of gas: $12000\ m^3/h$.

=>The speed of the gas $\omega_1 = (12000/6.75*3600) = 0{,}494\ (m/s)$.

The speed of the oxidized gas is ω_1: 0,494 (m/s).

Therefore: $$Re_1 = \frac{\omega_1.d_1}{v_1} = \frac{0.494.11.10^{-3}}{1{,}306.10^{-5}} = 415{,}95.$$

Tube beams were arranged in parallel, with $Re_1 < 10^3$, thus:

$$Nu_1 = 0{,}4.Re_1^{0{,}6}.Pr_1^{0{,}35} = 0{,}4.(415{,}95)^{0{,}6}.(0{,}01)^{0{,}36} = 13{,}2$$

$$\alpha_1 = \frac{Nu_1.\lambda_1}{d_1} = \frac{13{,}2.8.12.10^{-2}}{1{,}1.10^{-2}} = 97{,}79\ (W/m^2.K).$$

b) Consideration with the air

Applying the parameters defined above, Re_2 is determined as such:

$$Re_2 = \frac{\omega_2.d_2}{v_2} = \frac{8{,}7.1{,}1.10^{-3}}{3{,}95.10^{-6}} = 2269{,}62$$

$Re_2 > 10^3$, therefore:

$$Nu_2 = 0{,}4.Re_2^{0{,}6}.Pr_2^{0{,}36} = 0{,}4.(2269{,}62)^{0{,}6}.(0{,}681)^{0{,}36} = 35{,}94.$$

$$\alpha_2 = \frac{Nu_2.\lambda_2}{d_2} = \frac{35{,}94.3{,}75.10^{-2}}{1{,}1.10^{-2}} = 123{,}5\ (W/m^2.K)$$

c) Calculation of the heat transfer coefficient K

The coefficient of heat transfer through the tube wall was:

$$K = \frac{1}{\frac{1}{\alpha_1}+\frac{\delta}{\lambda}+\frac{1}{\alpha_2}} = \frac{1}{\frac{1}{97{,}79}+\frac{0{,}002}{22}+\frac{1}{123{,}5}} = 54{,}31\ (W/m^2.K)$$

Where: λ – The thermal conductivity of steel (W/m.K)

δ- The thickness of tube (m).

d) Calculation of heat transfer area

The average temperature difference was:

$$\overline{\Delta_t} = \frac{960-705}{ln\frac{960}{705}} = 826{,}04\ (^{0}C)$$

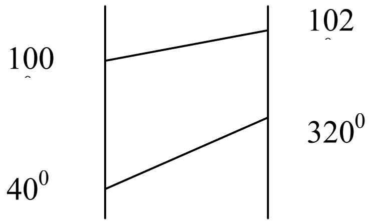

Δ_{tmin}= 1000^0- Δ_{tmax}= 1025^0-

The heat transfer area of the equipment F:

$$F = \frac{Q}{K.\overline{\Delta_t}} = \frac{123.10^3}{54{,}31.826{,}04} = 2{,}74\ (m^2)$$

Based on the actual furnace parameters, a horizontal pipe length was selected 1,5 m (φ 110 mm) and the length of the distribution pipe was selected 1.1 m (φ 210 mm).

The heat transfer area for distribution pipe: $S_1 = 2.\ \Pi.\ d_2.\ 1{,}1 = 2.\ 3{,}14.\ 0.105.\ 1{,}1 = 0{,}8\ m^2$.

The horizontal heat transfer area: $S_2 = F - S_1 = 1{,}92\ (m^2)$.

The number of tubes required for equipment is:

$$n = \frac{1{,}92}{(\Pi.d_1).1{,}5} = 3{,}71 \text{ (tubes)}$$

The above result is approximately 4 tubes.

1.2. Results and Discussion [5]

This work investigated and measured the temperature of some areas in the reactor, which have been shown in Figure 1.

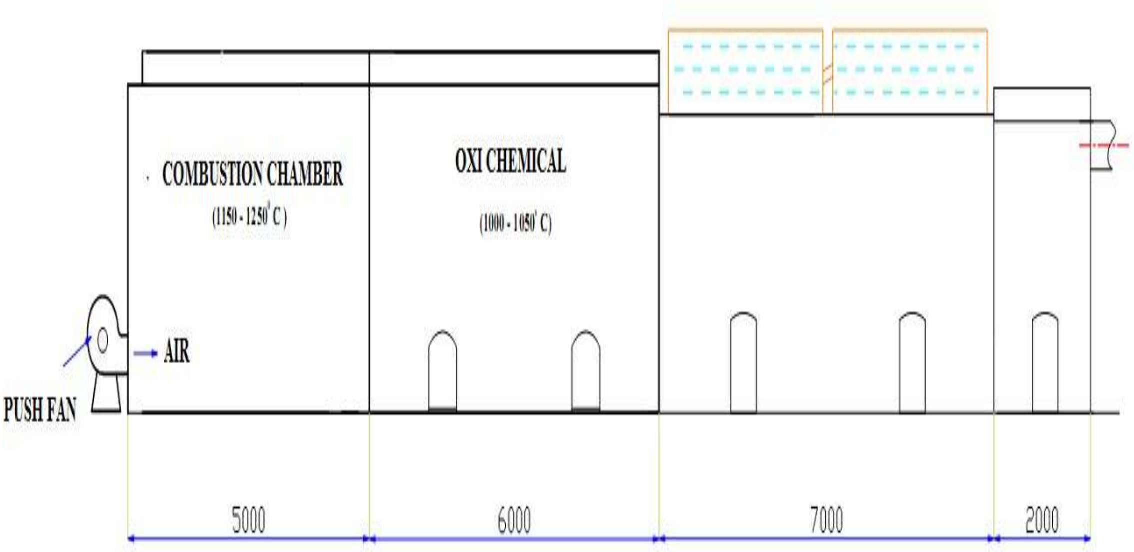

Figure 1: Temperature in some areas of the reactor 3A

Figure 2 showed that the temperature of the reaction chamber was 1000 - 1050^{0}C. In this research, the heat recovery system was installed in this chamber. The scheme of the heat recovery device is shown in Figure 2.

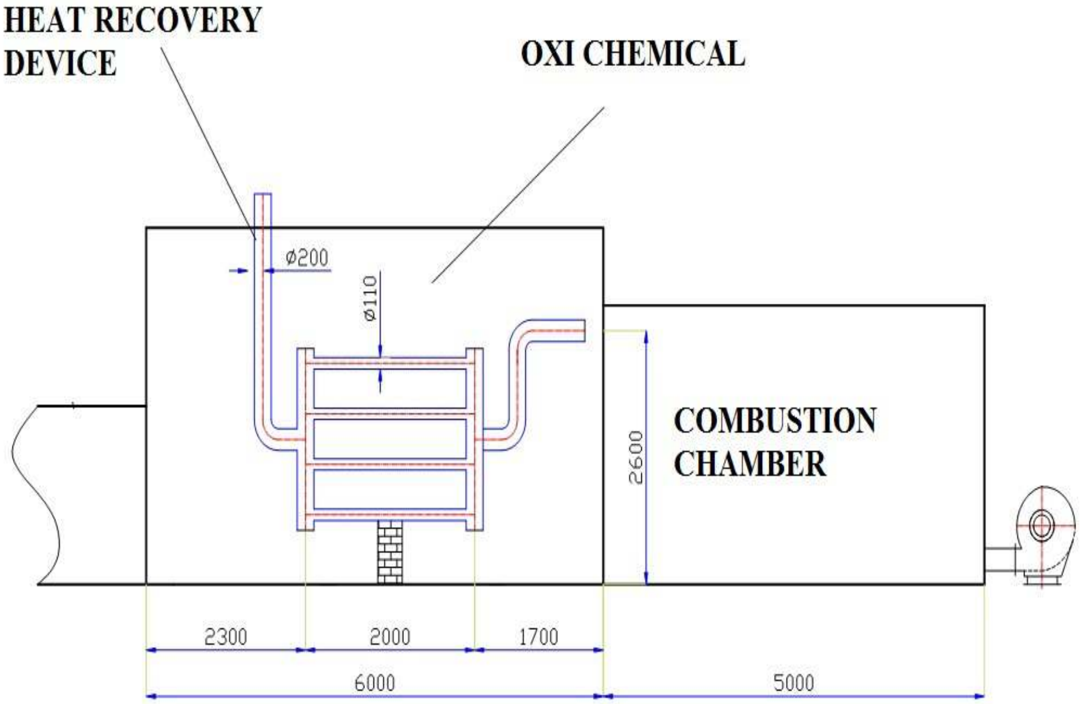

Figure 2: The installation drawing of the heat recovery unit in the oxidation boiler

After completing the installation of the heat recovery, the technical parameters were studied on several production days.

On the first day of production, the temperature of the external environment was 40^{0}C. The dependence of the outlet temperature on the flow of air is shown in Table 1 and Figure 3.

Table 1: Effect of air temperature on the incoming air flow
at the first day of production

Flow of incoming gas, m^3/h	50	00	50	00	50	00	050	200
Temp., ^{0}C	10	05	00	995	90	90	90	90

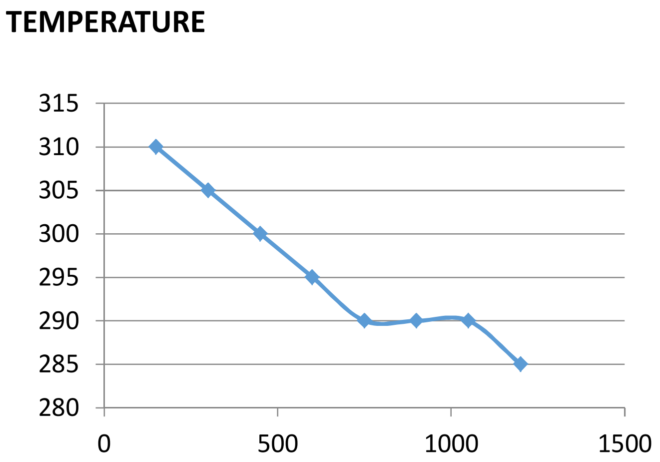

Figure 3: Effect of the air temperature on the incoming air flow on the first day of production

From the second day of production onwards, the system temperature was quite stable; the environment temperature was 40^{0}C. The effect of the flow of incoming air on the final temperature of the system is shown in Table 2 and Figure 4.

Table 2: Influence of the temperature of the outing air on the flow of gas
for the second day of production

Flow of incoming gas, m^3/h	50	00	50	00	50	00	050	200
Flow of outing gas, m^3/h	67	140	485	752	875	034	103	204
Temp, ^{0}C	80	74	68	60	40	22	19	16

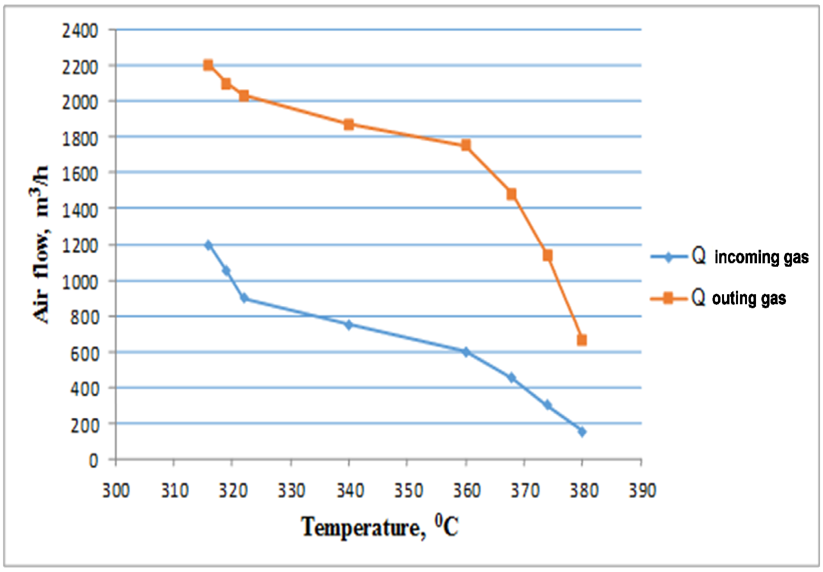

Figure 4: Effect of air temperature on the provided air flow provided for the second day of production

From Table 2 and Figure 4, it could be seen that the heat exchanger worked well. Depending on the air flow, the output air temperature is from 316 to 380^{0}C.

The gas temperature after the heat exchanger at fixed gas flows at various production dates was also investigated. The results are shown in Table 3.

Table 3: Effect of temperature on different airflows at production dates

Flow of incoming gas, m^3/h		150	300	450	600	750	900	1050	1200
Temp, ^{0}C	The first day of production	310	305	300	295	290	290	290	290
	The 2^{sd} day of production	380	374	368	360	340	322	319	316
	The 5th day of production	382	373	369	359	341	321	320	318
	The 8th day of production	381	374	369	360	341	321	319	318
	The 11th day of production	380	375	370	361	342	323	321	319

In table 3, it was shown that the heat recovery unit worked quite stable, with different incoming gas flow, the temperature does not significantly change during the production days. On the first production day, the temperature of the kiln system is unstable. From the second day of production, the temperature of the furnace is stable; the temperature of the gas passing through the heat recovery is regular.

The theoretical results are in a good agreement with the experimental data. After exchanging heat, the temperature of the gas reached over 300^{0}C.

III. CONCLUSION

Based on the results of the study on the heat exchanging process using the 3A oxidation furnace, the important results were obtained as follows:

1. A heat recovery device was calculated, designed and built. The obtained results have shown that the heat recovery device is highly reliable. The calculation data shows that the temperature of the gas and dust in the oxidation chamber in front of the heat exchanger unit was 1025^0C. After installing the heat recovery device at one side of the furnace wall, the temperature of the gas and dust was reduced by 20^0C and was determined to be 1000^0C.

2. The heat exchanger has a quite high efficiency. It could increase the temperature of the air flow from ambient temperature (40^0C) to over 300^0C. With a gas flow of 1200 m^3/h, the temperature of the air after heat exchange was about 316 ^{0}C.

In conclusion, it can be said that the heat recovery not only has the effect on heat exchange to provide hot air for the combustion chamber, but also reduces the temperature of the dust, increases the durability of filter bags at the product collection chamber.

3. When connecting the heat recovery unit to the system of the furnace of oxidized regeneration, as a result of theoretical calculations, it is shown that the amount of coal used is reduced by about 4% compared to when not using a heat exchanger.

On the other hand, a theoretical study has shown that increasing the temperature of the air to burn anthracite coal can reduce the amount of heat needed to reach the ignition state. This will increase the efficiency of the combustion process and reduce coal consumption. This proves that the amount of coal used for burning can be further reduced, reaching 5% in accordance with the grant requirement. However, there was no verification in real production, therefore, it was not proven that the efficiency of coal burning increases and coal consumption decreases by 5%.

REFERENCE

[1] Bui Hai, Duong Đuc Hong, Ha Manh Thu, Thiet bi trao đoi nhiet, publishing company Khoa hoc và ky thuat, 2001.

[2] Bui Hai, Tran Van Vang, Tinh toan thiet ke thiet bi trao đoi nhiet, NXB Khoa hoc và ky thuat, 2002

[3] Hoang Đinh Tin, Truyen nhiet & Tinh toan thiet bi trao đoi nhiet, NXB Khoa hoc và ky thuat, 2001.

[4] Pham Minh Tuan, “Hoan thien cong nghe va xay dung day chuyen cong nghe san xuat thu nghiem san pham kem oxit chat luong cao (99.5%) cong suat 150 tan/nam theo phuong phap khu nhiet – oxi hoa” HĐDA.06/10/NLNT.

[5] Pham Van Que, “Nghien cuu, thiet ke, che tao bo say khong khi cua he thong trao doi nhiet nham tan dung nhiet cua khi thai, tang hieu suat lo hoi trong to hop thiet bi nhiet dien cong suat den 300MW” 151-07.RD/HĐ-KHCN.

RESEARCH AND MANUFACTURING ON EDDY CURRENT SENSORS BASED ON GIANT MAGNETO RESISTANCE EFFECT AND ITS APPLICATIONS IN NDE

Nguyen Duc Huyen, Luong Van Su, Dang Thanh Dung and Vu Tien Ha

Center for Non-Destructive Evaluation, 140 Nguyen Tuan, Thanh Xuan, Hanoi

Project information:

- **Code:** CS/18/09-01
- **Managerial Level:** Institute
- **Allocated Fund:** 80,000,000 VND
- **Implementation time:** 12 months (Jan 2018- Dec 2018)
- **Contact email:** huyennguyenduc2401.com
- **Paper published in related to the project:**

Nguyen Duc Huyen et al., 2018. Research and manufacturing on Eddy current sensors based on giant magneto resistance effect and its applications in NDE. *The 5th Conference on Nuclear Science and Technology for Young Researchers*. Hanoi, Vietnam. October 2018, 4 p. (In Vietnamese).

Abstract: Non-destructive testing methods (NDT) are widely applied in mechanical manufacturing, energy, construction and maintenance of industrial projects. These methods are used in product development, or in the production and testing of final products. Especially, Eddy current (EC) technology is used effectively and widely to control and evaluate the lifespan of components in order to provide repair or replacement solutions. Manufacturing of the EC based GMR sensor sample, which is capable of detecting some types of discontinuities in the sample (faults and pores in the material), was investigated and analyzed in this work. An AC magnetic field emitted by exciting coils then an eddy currents will be generated in the sample material. The GMR sensor is alignmented inside the exciting coil. The faults are made into narrow spaces with different thicknesses to verify the capabilities of the EC sensor. The results obtained by the EC sensor allowed a preliminary assessment of the location of the faults on the surface of the sample. Further works should be the development of the EC sensor system and manufacture of the handheld EC device combined with a set of data collection and processing by computers realtime.

Keywords: *Eddy current, EC, GMR, NDT*

1. INTRODUCTION

Non-destructive evaluation (NDT) plays an extremely important role in the industry for evaluating product quality and identifying defects in the finished product structure. In general, NDT is considered as a method of the evaluation on the most types of samples without destroying or interfering the sample structure [1]. There are many evaluation methods used in NDT, such as Magnetic Particle Testing, Ultrasonic Testing and Digital Radiographic Testing [2]. However, the use of EC is one of the widespread methods of the electromagnetic method in the evaluation of metallic materials [3].

The EC sensor is based on the magnetic flux variation of the magnetic field produced by the exciting coil which is located on the surface of the sample. This magnetic field generates a secondary magnetic field due to Eddy current and it can be detected by sensors using choke coil or other magnetic field sensors [4]. When there are discontinuous faults on the surface of the sample, the Eddy current fluctuates, caused by the secondary magnetic field variation. So the magnetic sensor records this variation to give the fault information. Nowadays, there are many EC sensor manufacturing technologies [4-8]. However, the use of GMR sensors to replace the conventional choke coil is intended to reduce the size of the sensor, increase the resolution and sensitivity of the EC [9]. For example, a high-density EC sensor on a printed circuit has been fabricated and its ability to detect faults with a width of 70 μm and a thickness of 9 μm on the printed circuit [10].

The operation of NDT in Vietnam has been put into practice very early (1960-70 of the previous century). However, until 2000s the roles of NDT with the industry in Vietnam was widely recognized and increasingly developed (up to now, there are over 60 NDT companies in Vietnam). Most industries (petrochemical refining, power plants, shipbuilding, construction, etc.) have been using NDT services to ensure and control the quality of products and works. The demand for evaluating the duration of the life or the composition of components in industrial projects (thermoelectricity, petrochemical refining, etc.) are required increasingly (even in Vietnam - Mong Duong Thermal Power Plant, Formosa Ha Tinh, Dung Quat Oil Refinery, etc.) [11].

However, the problem is that most of the equipment and even accessories for NDT activities in Vietnam being imported from abroad. This has greatly affected the effectiveness of NDT activities, especially the cost of services. Moreover, if this situation persists, Vietnam will not have the technology in the field of manufacturing NDT equipment. In this research, the EC based on the GMR generation, operates according to the principle of the giant magnetoresistive effect. Magnetoresistive technology has overcome most of the disadvantages of the coil generation and has the following advantages: easy power, work with very low frequencies (<1Hz), small size (due to thin film manufacturing technology using the sputtering technique) and especially fully compatible with modern CMOS technology.

2. DESIGN AND MANUFACTURING

A. EC Control Circuit

Figure 1 shows the control circuit for the EC sensor consisting of two parts: Part 1 is the excitation signal and the second part is the signal measuring circuit. Circuits are designed on Eagle software and implemented on a single layer circuit. A 2 MHz quartz is used to measure the EC response. Because the frequency of the quartz is quite large and the EC requires only dozens of kHz so that the frequency of the quartz is subdivided by two IC4024 ICs. To generate a sinusoidal signal from a square pulse, an LC sweep filter circuit is used. To maximize the sensitivity of the EC, the phase of the reference signal and the excitation signal are adjusted by OP37G phase shift circuit. A 0.1 uF capacitor is inserted to remove the DC component in the reference signal. Then the sine wave is amplified through a DC additive circuit for two purposes; One is to generate an excitation signal with sufficient current and a DC signal to adjust the GMR work point. The DC signal is tuned via a 2 kΩ resistor on the circuit. The AC component is about 20 mA and the DC is about 10 mA. The excitation signal must be controlled because if we generate a small excitation signal, the GMR response is similar to that in the absence of excited field, ie the harmonic signal of GMR is not enhanced. On the other hand, if the excitation signal is too large, this leads to GMR saturation, GMR will not respond to any change in magnetic field. Besides, large current leads to the energy consumption. There is only one point gives the maximum harmonic function response. In practice, the excitation current is adjusted to the GMR response changes from an unsaturated point to a near-saturated point. Therefore, with any slight change of magnetic field, the GMR work point moves, where the second harmonic function of the output is the highest response. The output response of GMR is amplified with AD620 circuit with amplification can be switched in 10, 50, 100, 200, 500 and 1000 times. The phase-sensitive circuit uses an IC which doubles the signal is AD633. The reference signal for AD633 is a square pulse from CD4024 with the frequency determined when designing the circuit. The conversion function of AD633 is shown below:

$$W = \frac{(X_1 - X_2)\cdot(Y_1 - Y_2)}{10} + Z \tag{1}$$

Where W is the modulated signal, X is the GMR response signal, Y is the reference signal, Z is the complementary DC signal used as a way to adjust the off-set output W. Finally, the modulated output is filtered through a low pass filter with a 10 Hz cutoff frequency to extract the DC signal, which is proportional to the EC magnetic field.

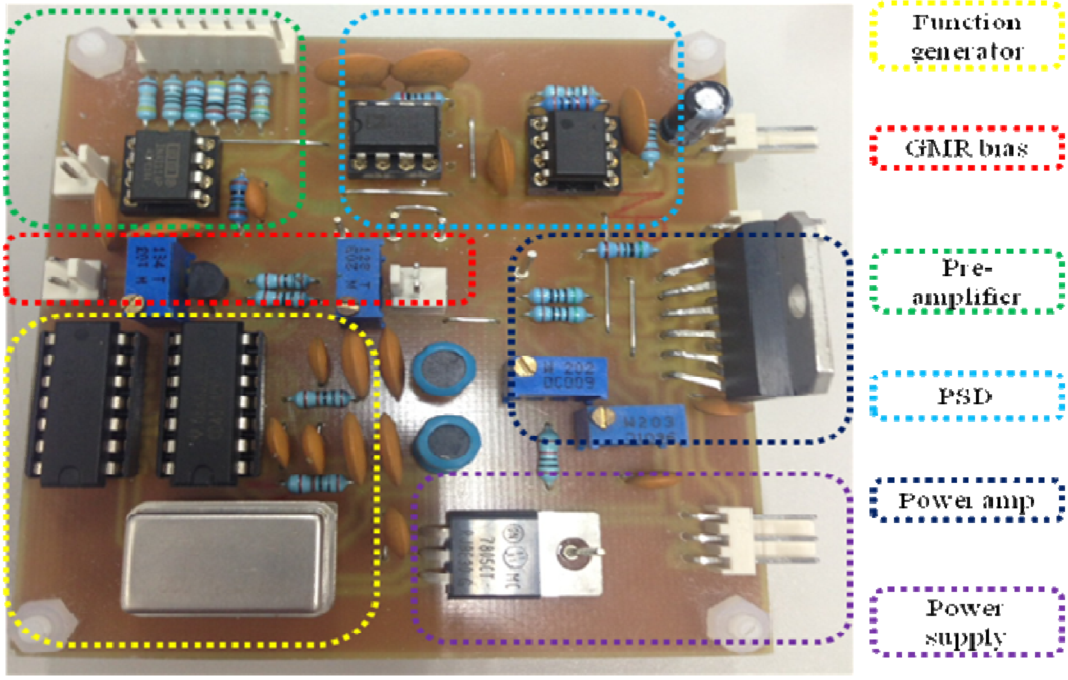

Figure 1: The EC control circuit

B. Excitation Coil Design

The excitation coil is designed to produce a primary magnetic field with a maximum output power of magnetic field *B*, of 0.5 mT. We can apply the law of *Biot-Savart* to calculate the magnetic field of the coil as follows:

$$B = \frac{\mu_0.N.I}{2.\sqrt{l^2 + r^2}} \tag{2}$$

where μ_0 is the magnetic permeability of the vacuum, N is the number of loops of the excitation coil, l is the coil length and r is the radius of the coil. For example, $l = 3$ mm, $r = 2$ mm and $N = 100$. Current will be calculated using formula (2).

C. Testing Sample Design

To show the relationship between the electrical signal response and the testing sample system, a steel sample (CT38) was fabricated by wire cutting method with different widths and depths as shown in Figure 2. Figure 3 shows a photograph of the sample after handling.

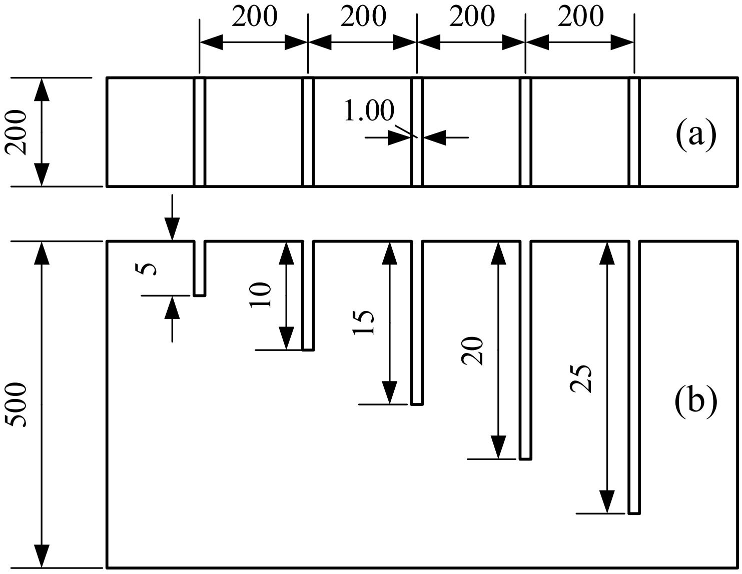

Figure 2: Front and cross-sectional views of the sample

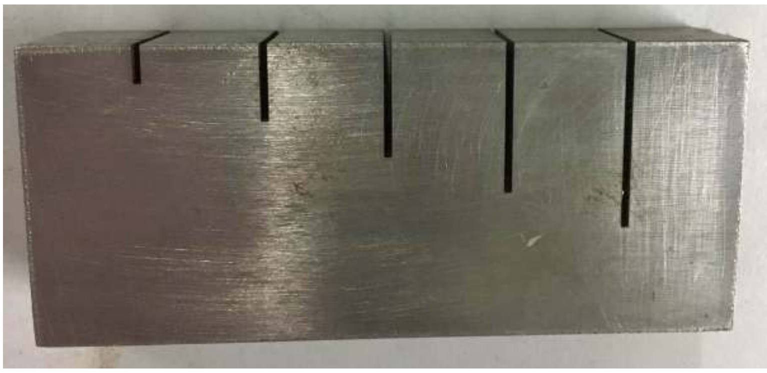

Figure 3: Photograph of the sample

D. Setting up the experiment system

To ensure the accuracy of the EC test measurement with the fractured standard sample after handling in the previous section. The EC sensor and testing sample were mounted on a 3-axis CNC machine. The *X*-axis moves with a fixed step and the EC sensor was mounted on the *Z*-axis with the distance to the sample being constant (0.1 mm). The EC sensor probe is controlled by a computer along to the *X*-axis with a step of 0.5 mm, while the *Y*-axis will remain constant to ensure that the measured data is uniform on a straight line and scanned overall standard cut on the testing sample. The output response of the EC sensor was recorded by a DAQ (Arduino Nano) and displays the obtained data via an oscilloscope.

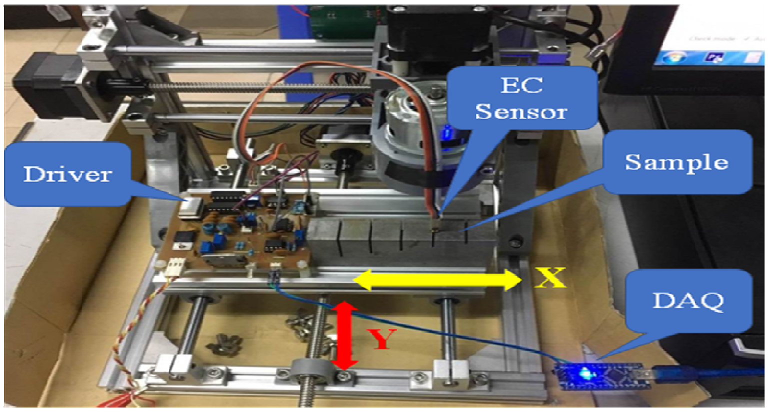

Figure 4: Measurement setup of the EC

3. RESULTS AND DISCUSSION

A. The EC Probe

The EC-based GMR sensors were manufactured as single-element units with a size of 2 µm × 200 µm. The 4-probe method was applied through ultrasonic vibration bonding technology in the device packaging technology. Two of the four connectors were used for the polarized current. The other two connectors were taken to an amplifier circuit to obtain the output signal of the GMR element. The polarization circuit for the GMR element was fabricated using the current source principle incorporating with the control circuit of the EC sensor system. Figure 5 shows a photograph of an EC sensor with a size of 3 mm × 20 mm.

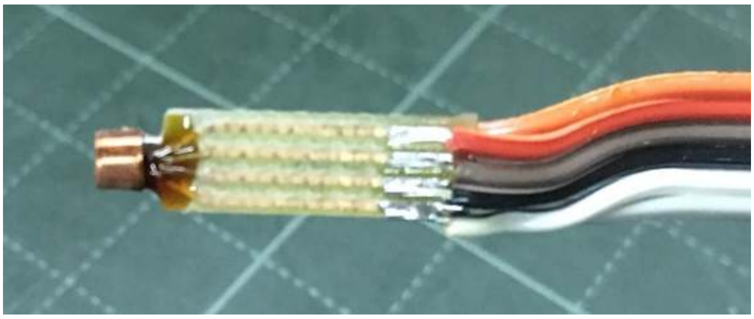

Figure 5: A photography of the EC measuring head

B. Measuring results

To apply GMR to NDT, the GMR sensor is integrated with additional components: sinewave generator, the magnetic field generating coil, and the feedback circuit. The functional generator induces a sinewave generating a magnetic field with a frequency of approximately 1 kHz. When the sample was taken near to this magnetic field, an Eddy current appeared on the surface of the sample. Especially at the defect position, where the Eddy current fluctuates. The waveform generated from the control circuit is shown in Figure 6. Besides, the square wave was also generated on the circuit with a frequency equal to 2 times the sinewave frequency owing to the GMR sensor responds best to the second harmonic mode. The squarewave was supplied to the reference pin of the AD633 phase-sensitive circuit.

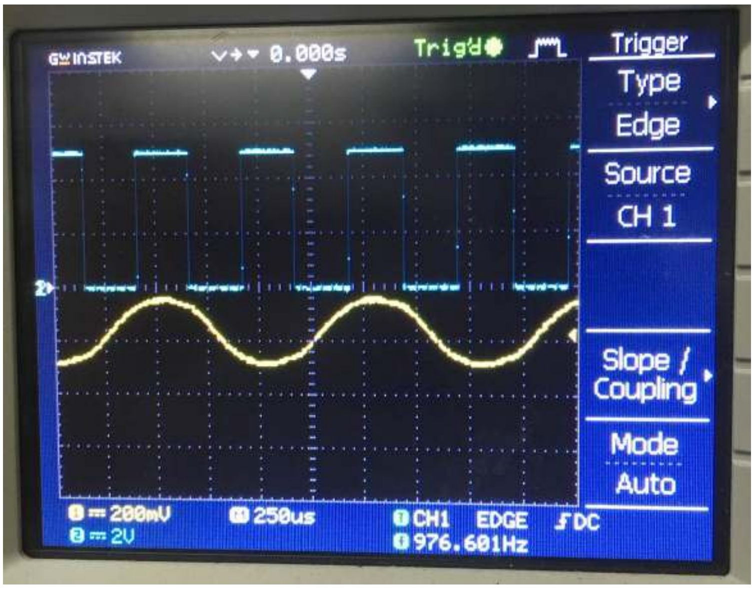

Figure 6: The waveform supplying for the excitation coil and obtained from the control circuit

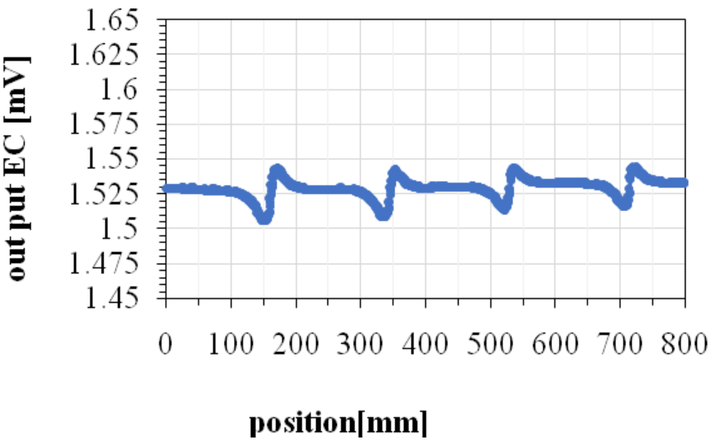

Figure 7: The EC response of the testing sample

Figure 7 shows the measuring results of the EC sensor fabricated with the standard sample. The best response frequency of the sensor is determined at 0.976 kHz (~ 1kHz). By the working area limitation of the X-axis on the CNC machine of the research group, the test-measuring distance was only scanned through four fractured channels, which were represented by the signal fluctuation points in Figure 7. The signal amplitude was low due to the sensors were fabricated in a single-element GMR. However, this can be overcome by applying the N-element in series circuit GMR method then the sensitivity will be increased by N times. The signal amplitude was quite similar and unable to distinguish clearly the width and depth of fractures. Furthermore, the initial expectation of this work is to produce an EC sensor which is able to detect fractured locations. More detailed information about fractures such as width and depth will be further developed in the future, and more advanced technologies and algorithms will be incorporated.

4. CONCLUSIONS

This research focused on the manufacturing of an Eddy current sensor based on the magnetic sensor GMR for non-destructive evaluation in Vietnam. Manufactured sensors with good signal response to the location of fractures were introduced. To test the ability of the sensor, the output signal of the sensor was compared to the shape of fractured locations on the surface of the standard sample. The distance between the signal output fluctuated points of the sensor showed respectively the location of the fracture on the testing sample. In addition, information about the amplitude or signal strength of the sensor will be further exploited to providing more detailed information on the fractures; such as width and depth. The observed results in this work are initial for further proposals, carrying out further study to step by step improve the method and technology as well as towards the successful manufacture of EC equipment and contributing to the practical needs of NDE testing in Vietnam.

REFERENCES

[1] C. Hellier and M. Shakinovsky, *Handbook of nondestructive evaluation* vol. 10: Mcgraw-hill New York, 2001.

[2] L. Janousek, K. Capova, N. Yusa, and K. Miya, "Multiprobe Inspection for Enhancing Sizing Ability in Eddy Current Nondestructive Testing," *IEEE Transactions on Magnetics,* vol. 44, pp. 1618-1621, 2008.

[3] D. C. Jiles, "Review of magnetic methods for nondestructive evaluation (Part 2)," *NDT International,* vol. 23, pp. 83-92, 1990.

[4] T. Dogaru and S. T. Smith, "Giant magnetoresistance-based eddy-current sensor," *IEEE Transactions on Magnetics,* vol. 37, pp. 3831-3838, 2001.

[5] A. E. Mahdi, L. Panina, and D. Mapps, "Some new horizons in magnetic sensing: high-Tc SQUIDs, GMR and GMI materials," *Sensors and Actuators A: Physical,* vol. 105, pp. 271-285, 2003.

[6] A. Jander, C. Smith, and R. Schneider, "Magnetoresistive sensors for nondestructive evaluation," in *Nondestructive Evaluation for Health Monitoring and Diagnostics*, 2005, p. 13.

[7] A. L. Ribeiro and H. G. Ramos, "Inductive Probe for Flaw Detection in non-Magnetic Metallic Plates Using Eddy Currents," in *2008 IEEE Instrumentation and Measurement Technology Conference*, 2008, pp. 1447-1451.

[8] G. Betta, L. Ferrigno, and M. Laracca, "GMR-Based ECT Instrument for Detection and Characterization of Crack on a Planar Specimen: A Hand-Held Solution," *IEEE Transactions on Instrumentation and Measurement,* vol. 61, pp. 505-512, 2012.

[9] O. Postolache, A. L. Ribeiro, and H. G. Ramos, "Induction defectoscope based on uniform eddy current probe with GMRs," in *2010 IEEE Instrumentation & Measurement Technology Conference Proceedings*, 2010, pp. 1278-1283.

[10] K. Chomsuwan, T. Somsak, C. P. Gooneratne, and S. Yamada, "High-Spatial Resolution Giant Magnetoresistive Sensors - Part I: Application in Non-Destructive Evaluation," in *Giant Magnetoresistance (GMR) Sensors: From Basis to State-of-the-Art Applications*, C. Reig, S. Cardoso, and S. C. Mukhopadhyay, Eds., ed Berlin, Heidelberg: Springer Berlin Heidelberg, 2013, pp. 211-241.

[11] Tài liệu đào tạo, "*Kiểm tra chụp ảnh phóng xạ*", Trung tâm đánh giá không phá hủy, Viện năng lượng nguyên tử Việt Nam, 2014, Lưu hành nội bộ.

STUDY ON PRODUCTION OF PORTABLE NUCLEAR DEVICE BASED ON LATTEPANDA

Nguyen Thanh Hung, Nguyen Van Sy, Nguyen Xuan Vinh and Dang Quang Bao

Hanoi Iradiation Center Km 12, Route 32, Minh Khai, Bac Tu Liem, Hanoi

Project information:

- **Code:** CS/18/D8-01
- **Managerial Level:** Institute
- **Allocated Fund:** 75,000,000 VND
- **Implementation time:** 12 months (Jan 2018- Dec 2018)
- **Contact email:** hungxom933@gmail.com
- **Paper published in related to the project:**

Nguyen Thanh Hung, 2018. Study on production of portable nuclear device based on Lattepanda. *The 5th Conference on Nuclear Science and Technology for Young Researchers*. Hanoi, Vietnam. October 2018 (In Vietnamese).

Abstract: LattePanda is the first single-board computer equipped two microprocessors: Intel x86 64bit X5-Z8300 and AtMega32u4 8bit (Arduino Leonardo). The use of Intel microprocessors allows LattePanda to run on multiple operating system platforms (Windows, Linux, Android, …), supported all programming languages (C/C++, C#, Python, LabVIEW, MatLAB, …) and equipped with high-speed communication ports (USB, LAN, GPIO, …), so it's easy to put LattePanda into control systems. In this study, LattePanda goal is portable nuclear devices that integrate spectrum processing programs with the same functions as on personal control computers. To confirm the advantages of LattePanda, the team completed the construction of a test device that coupled the MCA with LattePanda, displaying the processing results on a 7-inch LCD touch screen. The device has the ability to connect and process spectrum directly from a Scintillation Radiation Detectors through a high-voltage block and pre-amplifier power source with low noise. In addition, the device is equipped with a backup power block to ensure that the test equipment can operate continuously for about 6 hours.

Keywords: LattePanda, MCA, Portable, Single-Board Computer.

1. INTRODUCTION

LattePanda is a single-board computer running Windows 10 operating system, designed based on Intel x86 Z8300 / Z8350 and AtMega32u4 processors with modern processing techniques, supporting multiple operating systems, integrated built-in high speed interface and up to 64GB of storage.

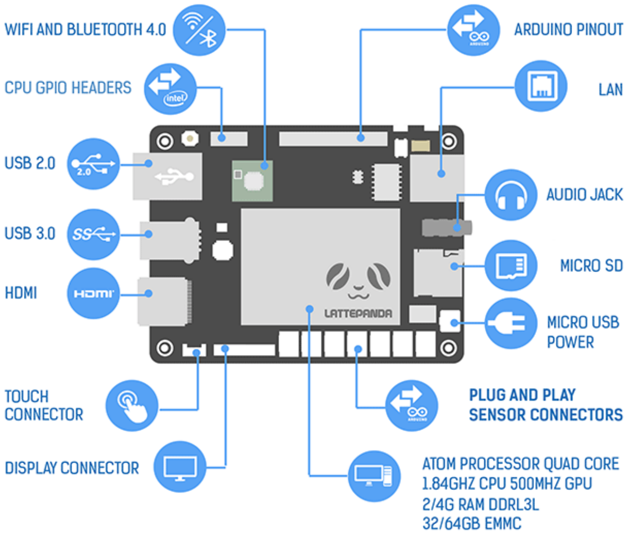

Figure 1: Block diagram of LattePanda

Currently, portable nuclear devices continue to be researched and developed to improve quality, integrate many processing functions and direct signal processing capabilities. Basically, portable nuclear devices come in two forms:

- The device has built-in Windows or Linux operating system to bring all processing functions on the PC to the device;
- The device only analyzes some of the necessary parameters and requires a PC to accompany it to process data fully.

The goal of LattePanda is to make portable devices of type 1. With x86 structure and multi-platform support, this is the appropriate and quality choice for making portable nuclear devices. In this study, the team confirmed the applicability of LattePanda by creating the test device that connects LattePanda to MCA and displays the spectrum processing program on the LCD 7-inch touchscreen.

2. RESEARCH CONTENTS

2.1. Research topics and methodology

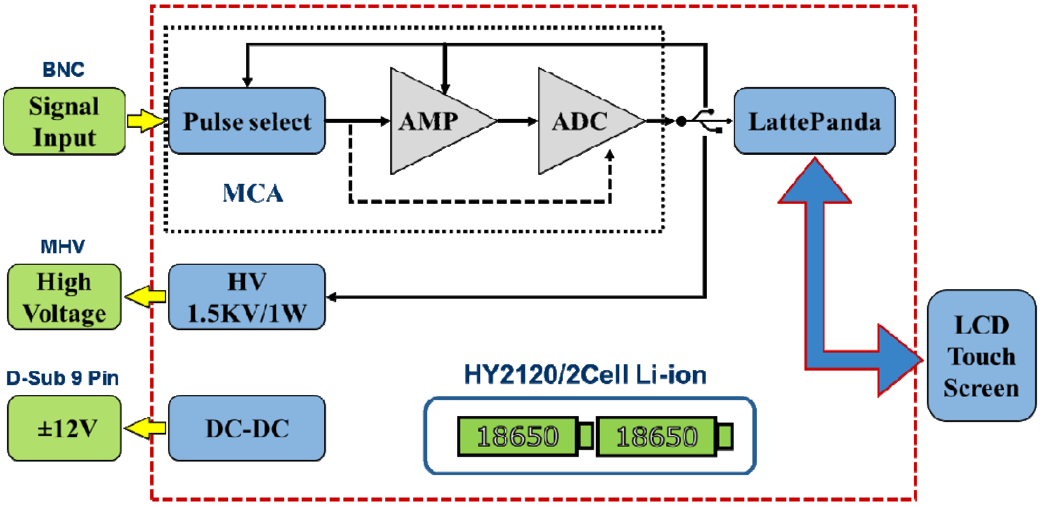

Figure 2: Block diagram of the test equipment

For the purpose above, the block diagram of the test device includes:

- Pulse selection block: Select the pulse source, pulse from the preamplifier or external spectrum amplifier;
- Spectrum amplifier block: The amplifier controls pulse amplitude, the output is Gaussian pulse;
- Multichannel analyzer block: Responsible for recording the multichannel spectrum from detector, data transfer via USB interface;
- Process and Display block: Spectrum processing has been built on the LattePanda circuit and displayed on a 7-inch touch screen;
- Power supply block: Including high voltage 1.5kV and pre-amplifier power supply with low noise.

Programming for LattePanda:

MCA installation program: This program allows users to set the operation parameters for MCA such as pulse source settings, pulse polarization, spectrum amplification coefficient and high voltage for detector. The program has been built as a dialog box on the LabVIEW software.

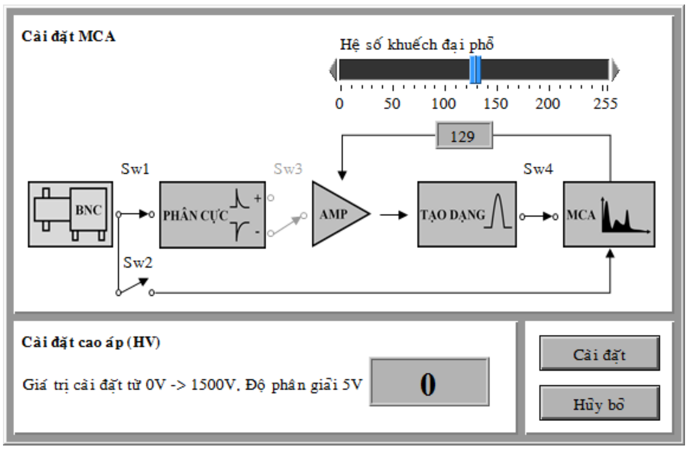

Hệ số khuếch đại phổ: 129

Giá trị cài đặt từ 0V -> 1500V. Độ phân giải 5V: 0

Figure 3: MCA installation program

The program reads and displays the spectrum from the MCA: The MCA has a resolution of 4000 channels, the width of each channel is 4 bytes, the total capacity is 16000bytes. To ensure smooth data transfer, 20 bytes were added for use as an MCA identifier. Therefore, a packet from the MCA is 16020 bytes and uses a USB interface.

Spectrum smoothing program: Due to the statistical nature of the nuclear decay process and the identification process, at a channel in the spectrum, it is a random variable that fluctuates around the real value. To limit fluctuation, the spectrum is smoothed before analysis. The program has been integrated with two smoothing programs with optional smoothing points of three or five points.

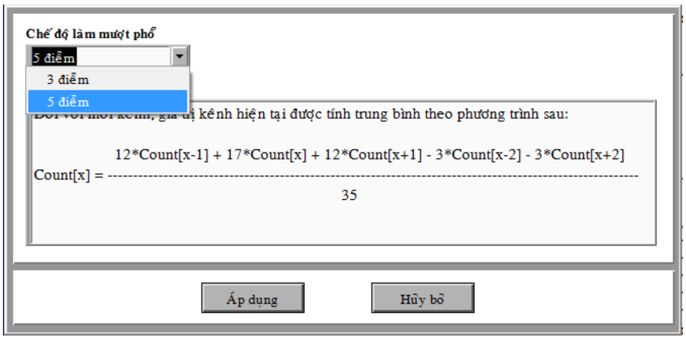

Chế độ làm mượt phổ: 5 điểm

```
kênh hiện tại được tính trung bình theo phương trình sau:

              12*Count[x-1] + 17*Count[x] + 12*Count[x+1] - 3*Count[x-2] - 3*Count[x+2]
Count[x] = -----------------------------------------------------------------------------
                                          35
```

Figure 4: Spectrum smoothing program

Energy calibration program: The program has been built as a dialog box with visualization that allows for linear observation between E and the position of the vertex.

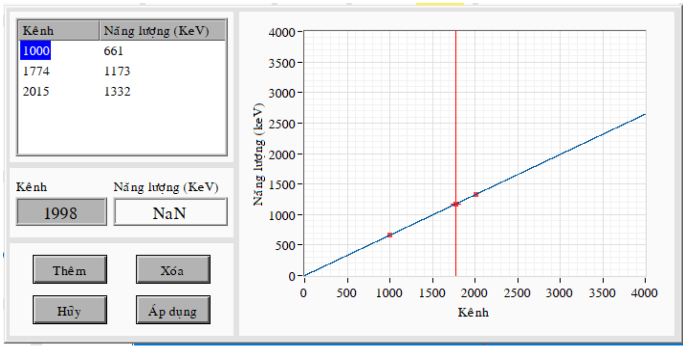

Kênh	Năng lượng (KeV)
1000	661
1774	1173
2015	1332

Kênh: 1998

Năng lượng (KeV): NaN

Figure 5: Energy calibration program

Net area calculation program, FWHM and isotope recognition: The peak is described by the Gaussian function:

$$f(X) = Ae^{\left(-\frac{(X-\mu)^2}{2\sigma^2}\right)} + C(X) \qquad (1)$$

Where:

- A is amplitude;
- μ is center;
- σ is standard deviation,
- $C(X) = aX + b$ is background.

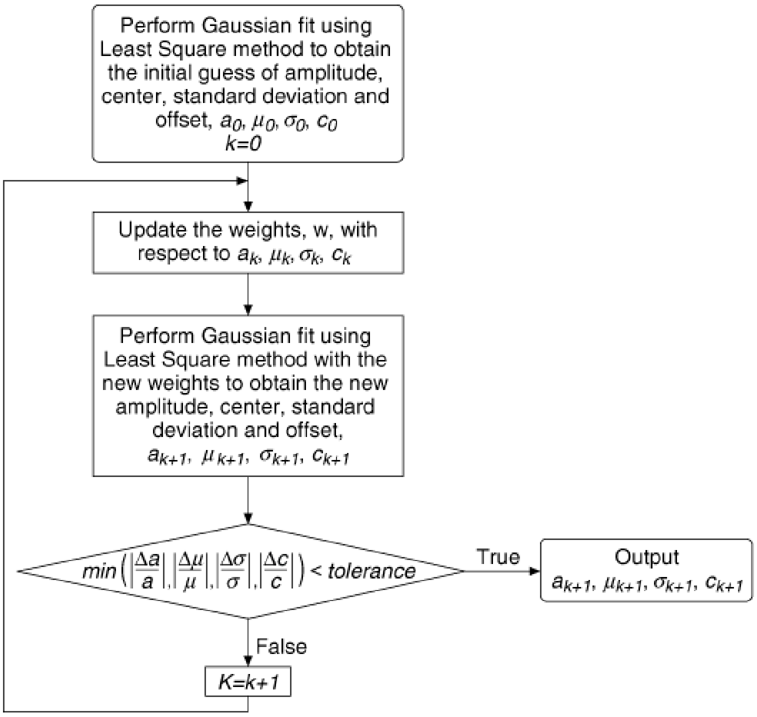

Figure 6: Gaussian Peak Fit

FWHM is defined as follows

$$FWHM = 2\sqrt{2\ln 2}\,\sigma \approx 2.355\sigma \qquad (2)$$

As a result, it is easy to calculate the position of the peak, net area, background, isotope information and radioactivity:

$$H = \frac{A}{\varepsilon_E . I_\gamma . t} \ (Bq) \tag{3}$$

Where:

- H is radioactivity;
- S is peak area;
- ε_E is absolute efficiency;
- I_γ is the number of gammas per disintegration of this nuclide for a transition at energy E;

2.2. Results and discussion

The team completed the construction of the test device that coupled the MCA with LattePanda. Parameters of the test device:

- Power Supply:
  - DC input: 9V/2A - DC 5mm;
  - HV output: 1.5KV 1mA - MHV;
  - DC output for Pre-AMP: ±12V D-Sub 9 pin;
  - Battery backup: 6h.
- Signal input (BNC): Positive/Negative pulse or Gauss pulse;
- Hardware:
  - Spectrum amplifier block;
  - MCA block:
    - Resolution: 4000 channels;
    - Count per channel: 4.294.967.295;
    - Convertion time: 7µs;
    - Integral nonlinearity: 0.022%;
    - Differential nonlinearity: 1.44%;
- Software:
  - Select pulse source: from preamplifier or external Gaussian pulse;
  - Select the polarity of the pulse: positive or negative pulse;
  - Adjust the spectrum gain;
  - On/Off HV for detector;
  - Spectrum processing:
    - Spectrum smoothing;
    - Energy calibration program;
    - Net area calculation program, FWHM and isotope recognition.

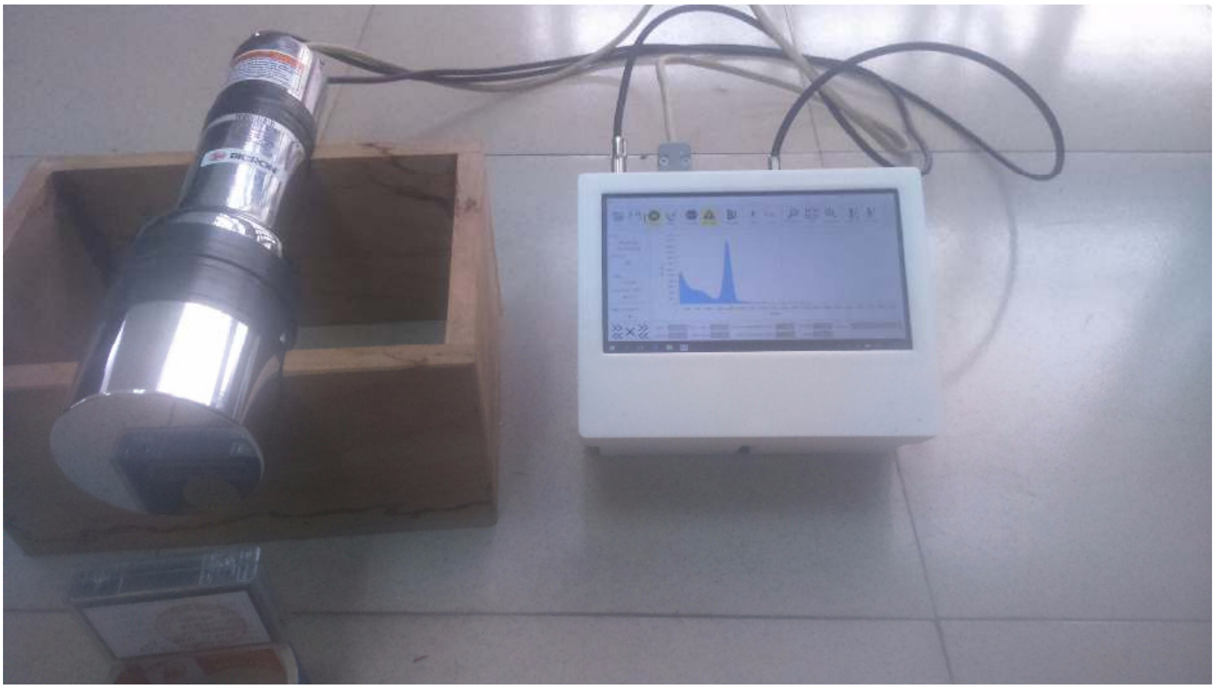

Figure 7: The test device

Start:
12:21:05
20/12/2018
Real (s):
54

Count:
388097
Count Rate (CPS):
7187

High Voltage (V):
0

Roi_L 3949
Gross Area 0
Gross Count Rate (CPS) 0,00
FWHM NaN
Library
Roi_R 3949
Net Area 0
Net Count Rate (CPS) 0,00
Peak 0

Figure 8: Spectrum processing interface on LattePanda

To evaluate the accuracy of the spectral processing program, the results were compared with the gamma-vision 6.0 software:

Table 1: Compare spectral processing results on LattePanda and GammaVisison

Nuclide	Time (s)	Energy (KeV)	LattePanda		Gamma Vision 6.0		$\frac{G_L}{G_G}$	$\frac{N_L}{N_G}$
			Gross (CPS)	Net (CPS)	Gross (CPS)	Net (CPS)		
Co-60 + Cs-137	889	661	4.30	2.29	4.20	2.74	0.9756	1.1943
		1173	38.08	37.02	38.55	37.04	1.0123	1.0005
		1332	32.49	31.51	33.39	32.77	1.0275	1.0398
Co-57	105	122	80.60	78.00	80.32	78.82	0.9965	1.0104
		136	10.42	9.66	10.02	9.47	0.9616	0.9798
Cd-109	183	88	16.50	18.19	16.01	15.10	0.9700	0.8301
Cs-137	90	661	312.49	307.48	339.76	334.88	1.0873	1.0891
Mn-54	200	834	24.66	24.31	24.62	24.345	0.9984	1.0014

The results of the LattePanda spectral processing program showed a slight deviation from the results obtained on Gamma Vision 6.0 software. Area ratio between the results showed that the program ran stably.

3. CONCLUSION

Lattepanda is single-board computer compatible to Windows operating system, supports multiple high-speed communication ports (USB, LAN, GPIO, ...) and can use many programming languages to develop software (C/C++, C#, JAVA, …). As a result, the product launch time is shortened. In this study, the research team produced the testing equipment conjunction LattePanda with MCA circuit while the spectrum processing program was displayed and controlled on the LCD touch screen.

REFERENCES

[1] Datasheet, LattePanda: http://lattepanda.com/docs/#Troubleshooting

[2] LabVIEW software: http://ni.com

[3] Nguyễn Trung Tính, "Giáo trình xử lý phổ hạt nhân tự động"

[4] Đặng Quang Thiệu, "Nghiên cứu chế tạo thiết bị quan trắc cảnh báo phóng xạ"

[5] Gamma Vision 6.0 software

DESIGN AND COMPLETE THE MASS THICKNESS DETECTOR FOR DOSE-ESTIMATED INSIDE PRODUCT IRRADIATED BY 10 MEV ELECTRON BEAM ON UELR-10-15S2 ACCELERATOR

Cao Van Chung*, Đoan Binh, Nguyen Đuc Hoa,
Phan Phuoc Thang and Le Quang Thanh

Research and Development Center for Radiation Technology, Vietnam Atomic Energy Institute,
202A, 11 Street, Linh Xuan Ward, Thu duc District, Ho Chi Minh City

Project information:

- **Code:** CS/18/07-03
- **Managerial Level:** Institute
- **Allocated Fund:** 80,000,000 VND
- **Implementation time:** 12 months (Jan 2018- Dec 2018)
- **Contact email:** chungvingamma@gmail.com
- **Paper published in related to the project:**

Cao Van Chung, Nguyen Duc Hoa, Phan Phuoc Thang, Le Quang Thanh, 2018. Design the mass thickness detector for dose-estimated inside product irradiated by 10 MeV electron beam on UELR-10-15S2 accelerator. *The 5th Conference on Nuclear Science and Technology for Young Researchers*. Hanoi, Vietnam. October 2018 (In Vietnamese).

Abstract: The counter by sodium iodide (NaI) scintillation counters from gamma source were used in estimate the density distribution on product. The dose distribution in-side product irradiated by 10 MeV on UELR-10-15S2 was also estimated. The moving system and controller were designed. The quick density detector had been compare with dose mapping by dosimeter . There was a good agreement between the results of both methods. The mass thickness detector has a meaning in QA/QC electron irradiation processing at VINAGAMMA.

Keyworks: *UELR-10-15S2, dose distribution, density detector…*

1. OBJECTIVES

- The 10 MeV electron has short penetration in product (at 5.6 cm water, the 10 MeV electron are almost absorbed), that mean the product irradiated on 10 MeV have a limited with the areal density [1,2]. In other hand, with the random arraged of product, it's too difficult to estimated exactly density of the product for calculate the dose distribution inside the product after irradiated on UELR-10-15S2 at Research and Development Center for Radiation Technology.
- Design and complete the mass thickness detector for dose-estimated inside product irradiated by 10 MeV electron beam on UELR-10-15S2 accelerator.

2. APPROACH

- To measure surface density distribution of product (carton box), we use one of probability of interaction of gamma, attenuation. The intensity of radiation decreases exponentially with the thickness of the product, with the ratio of number of gamma before and after passes through a portion of product, the density (thickness of product) can be find-out.

- Measurement schematic had been carry out, the mass thickness detector has been finished, the calibration and testing had been verify for the accuracy.

3. RESULTS

3.1 Measurement schematic

The mass thickness detector (MTD) based on gamma attenuation probability. The intensity of radiation decreases exponentially with the thickness of the product. From the counter number record by NaI scintillation detector, the thickness of product can be calculated via thickness – counter curve (1). Measurement schema is showed as in Fig.1.

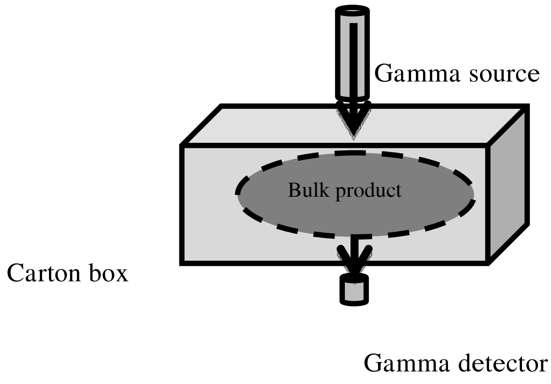

Figure 1: Measurement schematic

3.2 Mass thickness detector design

From the schematic showed in 3.1, the mass thickness detector had designed, consist:

- Gamma source – Cs137 (activity of 1 mCi) with the conformity shielding;
- Mechanic system (Fig.3a);
- Controller system, radioactive record and power supplement (Fig.3b);
- Interface display, record input and show output.

A complete mass thickness detector is showed in Fig.5. The parameter of device are showed in Table 1.

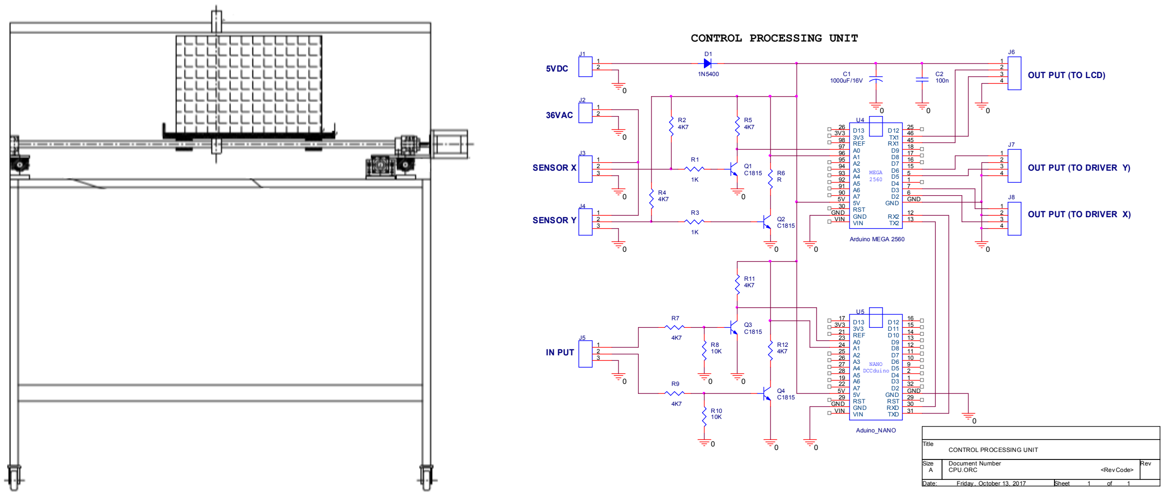

Figure 3: Mechanic system and controller system design

Figure 4: The completed mass thickness detector

Table 1: Mass thickness detector's parameter

Carton box size (cm)	50 x 50 x 30
Time duration for each point	1 second
Number of point	1, 25, 400
Operate mode	High Accuracy Mode, Quick Mode, Certificate Mode
Time duration for complete measurement	600 second for High Accuracy Mode, 60 second for Quick Mode.

3.3 Calibration

The MTD had calibrated by using MDF plates from density 0.0 g/cm^2 to 11.19 g/cm^2. The MDF plate using in calibration are show in Fig. 5, for each plate has density of 1.12 g/cm^2. To increase density (thickness) we increase the number of plates. The relationship between density and the counter record via NaI scintillation are showed in Table 2. The density can be calculated via the function (1).

$$\rho\ [g/cm^2] = -19.081 * \ln(N) + 189.29 \qquad (1)$$

With N is the number of gamma, recorded by NaI detector.

Table 2: The relationship between the number recorded by NaI detector and density

No. of MDF plate	Counted by NaI (N)	Ln(N)	Density (g/cm^2)
0	20,097	9.90	0.00
1	18,979	9.85	1.12
2	18,067	9.80	2.24
3	17,250	9.75	3.36
4	16,159	9.69	4.48
5	15,313	9.63	5.60

6	14,337	9.57	6.71
7	13,634	9.52	7.83
8	12,667	9.44	8.95
9	12,017	9.39	10.07
10	11,135	9.31	11.19

3.4 Testing on product at EB Dept. - VINAGAMMA

MTD after calibrated were tested on real product at EB Dept., VINAGAMMA. Tested product were chosen variety from frozen food, dried fish, garlic powder, chew-pet… (Fig. 5) and variety on packaging.

(a) (b) (c) (d) (e)

Figure 5: Tested product: frozen tuna (a), garlic (b), yellow dried fish (c), pet chew (d,e).

The accuracy of system had checked by compare between dose mapping in product and dose calculated via the density determined by MTD. With the different no more than 8% showed in Table 3 from a pet chew product, the MTD show that it's a good practice in routine at EB Dept. VINAGAMMA.

Table 3: Compare dose mapping with dose calculate via density determined by MTD on pet chew product carton

Carton size (cm)	28 x 36 x24				
Gross weight (g)	7.200				
Ave. density (g/cm^2)	7,14				
Density determined by MTD (g/cm^2)	8,2	7,6	5,0	6,2	5,6
Dose mapping (kGy)	6,8	9,4	10,5	12	12,0

Calculated dose (kGy)	7,2	8,7	9,9	11,3	11,0
Diffirent (%)	5,5	8,0	6,0	6,0	8,6

3.5 Dose distribution inside carton box calculated by the "Calculate irradiation parameter for UELR-10-15S2" Software

The software calculate dose distribution inside product read the density distribution measured by MTD system via USB/RS232 gate. The software had been modified for reading information from MTD and calculate more than one point. The modified software than calculate depth dose distribution inside product at the points as number of points had determined by MTD system. Fig.6 showed a tested product carton calculated by the modified software.

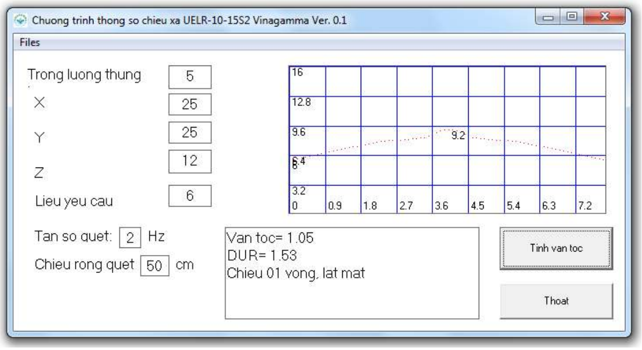

Chuong trinh thong so chieu xa UELR-10-15S2 Vinagamma Ver. 0.1

Trong luong thung: 5

X: 25

Y: 25

Z: 12

Lieu yeu cau: 6

Tan so quet: 2 Hz

Chieu rong quet: 50 cm

Van toc= 1.05
DUR= 1.53
Chieu 01 vong, lat mat

Figure 6: Modified software calculate dose distribution in product combined with MTD

4. CONCLUSION

Appling gamma attenuation probability, the MTD can estimate the density distribution of carton box than combined with modified "Calculate irradiation parameter for UELR-10-15S2" Software to calculate the dose distribution inside the carton box irradiated on UELR-10-15S2 at Research and Development Center for Radiation Technology.

The different result calculate from system are low than 8% with the dose mapping in practice on a pet chew carton box (higher than expected but in accepted). The limited of this system is number of point and use matrix point on working, to increase more accuracy, we need to improve the MTD system by continuous measurement and upgrade the software for more function.

REFERENCES

[1] R.B. Miller, Electronic Irradiation of Foods, An Introduction to the Technology, Springer, 2005.

[2] Trần Văn Hùng, "*Tính toán phân bố liều trong thùng hàng chiếu xạ trên máy gia tốc điện tử 10 MeV*", đề tài cơ sở, Trung tâm Nghiên cứu và Triển khai Công nghệ Bức xạ, 2010.

[3] MCNP4C, Monte Carlo N-Particle Transport Code System, Radiation Safety Information Computation Center, 2000.

[4] Cao Văn Chung, "*Xây dựng chương trình tính các thông số vận hành máy chiếu xạ chùm tia điện tử UELR-10-15S2 dựa trên các số liệu đo thực nghiệm*", đề tài cơ sở, Trung tâm Nghiên cứu và Triển khai Công nghệ Bức xạ, 2013.

1.4- Industrial Applications

STUDY ON MULTIPOINT TRACING MODEL IN OILFIELD USING NATURAL PARTITIONING INTERWELL TRACERS

Le Van Son, Huynh Thi Thu Huong, Le Thanh Tai, Nguyen Huu Quang, Bui Trong Duy and Tran Tri Hai.

Centre for Applications of Nuclear Technique in Industry (CANTI),
01 DT 723, ward 12, Dalat city, Lam Dong province

Project information:

- **Code:** 10/CS/HĐ/ĐT(NV)
- **Managerial Level:** Institute
- **Allocated Fund:** 80,000,000 VND
- **Implementation time:** 12 months (Jan 2017- Dec 2017)
- **Contact email:** sonlv@canti.vn
- **Paper published in related to the project:**

Huynh Thi Thu Hương, Le Thanh Tai, Nguyen Huu Quang, Le Van Son, 2019. Determination of contribution proportion of injection wells in oil production by interwell tracer method using partitioning organic compounds from crude oil. Accepted for publication in Petrovietnam Journal in 2019.

Abstract: In this study, the method using partitioning organic compounds in crude oil as Natural Partitioning Interwell Tracers (NPITs) was used for calculation of oil saturation and flow rate proportion of injection wells in the case of many injection wells contributing to the oil recovery process of a production well in homogeneous single-layered reservoir. The principle of method is based on the transport of NPITs from oil phase to water phase during waterflooding. The method was tested on the numerical models using UTCHEM software and on the physical model. The simulation results showed that the calculated values of flow rate proportion are different from modelling values between 1 to 2%. Oil saturation calculated from the proposed method gives the errors of less than 20% at the stage of up to 2 PV. Experimental result showed that the calculated value of oil saturation gives smaller deviation with the swept area has slower flow rate.

***Keywords**: Natural Partitioning Interwell Tracers, NPITs, flow rate proportion, oil saturation.*

I. INTRODUCTION

The previous studies have shown the existence of alkylphenols (APs) and aliphatic acids (AAs) in the crude oil is from a few ppm to thousands of ppm, depending on the geological characteristics of the reservoir [1]. Due to the partition ability between oil/water phase, alkylphenol and aliphatic acid can diffuse from oil phase to water phase during waterflooding. Based on the correlation between *concentration distribution* in production water and partition coefficient, alkylphenols and aliphatic acids can be used as Natural Partitioning Interwell Tracers (NPITs) for calculation of oil saturation and swept pore volume [2, 3]. The Research Project coded DTCB 06/14/TTUDKTHN-CN 2014-2015 has proposed the Linear method for determining oil saturation based on the *decrease rate* of NPITs concentration in production water. The method has been tested on the numerical models using UTCHEM software and on the physical model in the case of *one injection well - one production well* [4]. In this project, the method of determining the oil saturation proposed in the previous project is investigated on the numerical models using UTCHEM software in the case of multipoint model (Five-Spot, Direct-Line) and on the physical model. By determining the NPITs concentration curve characteristic for each swept area, it is possible to determine the oil saturation of respective swept areas. The flow rate proportion of injection wells is also evaluated.

II. THEORY

II.1. Method of determining oil saturation

Linear method for calculation of oil saturation has been proposed based on the decrease rate of NPITs concentration in production water [4]. At the end of waterflooding, the decrease rate of NPITs concentration *i* is related to the partition coefficient K_{di} according to the expression:

$$\frac{1}{a_i} = a_2.K_{di}^2 + a_1.K_{di} + a_0 \tag{1}$$

in which, a_2, a_1, a_0 are model parameters that depend on oil saturation, water velocity and dispersion coefficient. Establishing the ratios a_2/a_1 and a_0/a_2, oil saturation S_{or} is the solution of equation:

$$\frac{a_2}{a_1} = \frac{S_{or}}{(1-S_{or}).\left(1+\frac{a_0}{a_2}.\frac{S_{or}^2}{(1-S_{or})^2}\right)} \tag{2}$$

In case of many injection wells having flow rate Q_i influence on the transport of NPITs in homogeneous single-layered reservoir, the concentration of NPITs in water phase at production well is the total concentration of NPITs contributed by component swept areas. The faster the injection flow rate, the faster the decrease rate of NPITs concentration. The decrease rate of the total NPITs concentration depends strongly on the swept area which has slower flow rate.

Besides *Linear method*, *Moment* method proposed by Sinha and Asakawa was used as reference method in this project. The method is based on the chromatography retardation principle of a pair of NPITs [2, 3].

$$S_o = \frac{\bar{t}_2 - \bar{t}_1}{(K_{d2}-1)\bar{t}_1 - (K_{d1}-1)\bar{t}_2} \tag{3}$$

By determining the NPITs concentration curve characteristic for each swept area, it is possible to calculate the oil saturation of respective swept areas. Compared with the *Moment method* proposed by Sinha and Asakawa, the *Linear method* allows determining oil saturation based only on a part of the concentration curve of NPITs. This provides the basis for practical application of the method of using NPITs for calculation the oil saturation of reservoir.

II.2. Method of determining flow rate proportion

Let $C_{kA} = C_{kwI} + (f_w + K_{dko}.f_o).(C_{kw} - C_{kwI})$ be the apparent concentration of NPITs compound *k*. The differential distribution of apparent concentration $C'_{kA} = \partial C_{kA}/\partial t$ has the form of chromatographic peak as illustrated in Figure 1, in which, its mean residence time is proven to be equal to the mean residence time of apparent distribution.

In case the oil recovery process of a production well is contributed by many injection wells, the concentration of NPITs in production water is the total concentration of NPITs contributed by component swept areas. The differential apparent concentration distribution of each swept area can be determined to calculate the mean residence time of NPITs in each swept area, therefore the contribution proportion of respective injection wells F_i is determined.

$$F_i = \frac{1}{1 + \bar{t}_{ki} \sum_{j \neq i} \frac{1}{\bar{t}_{kj}}} \tag{4}$$

The Eq. (4) is based on assumptions such as reservoir is homogeneous single-layered and the distance between the injection wells and production well are the same.

In particular, the appropriate algorithm and distribution function are applied to deconvolute the total differential apparent concentration curve with the condition that the component swept areas have sufficiently differentiated flow rate, $Q_2/Q_1 \geq 1.5$.

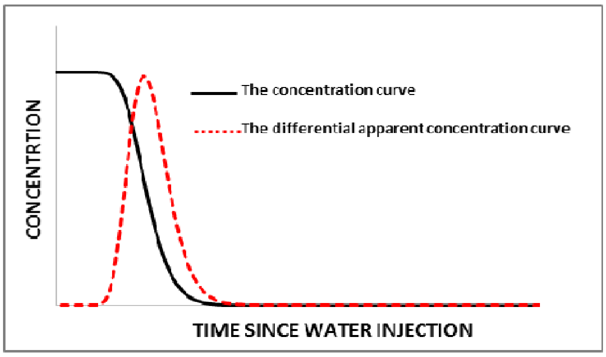

Figure 1: Illustration of the apparent concentration curve of NPIT compound and its differential curve. The differential distribution of apparent concentration is in the form of a chromatogram.

III. SIMULATION RESULTS

UTCHEM (The University of Texas's Chemical Simulator) is the software for simulating reservoir model with multiphase, multicomponent developed by Texas University [5, 6]. UTCHEM was used to run 3D reservoir model with two water injection patterns: Five-spot pattern– common pattern in stratified sediment reservoir and Direct line pattern – typical pattern in edge water injection or gravity injection.

The models have initial oil saturation of 0.65 and initial water saturation of 0.35.

Five-Spot model includes 4 injection wells and 1 production well has the size of 132 m x 132 m x 15 m divided into 33 x 33 x 4 grid cells. Total flow rate is 261.36 m^3/d with contribution proportion of injection wells equal to 10:20:30:40 (%).

Direct-Line model includes 2 injection wells and 1 production well has the size of 102 m x 204 b m x 8 m divided into 25 x 51 x 4 grid cells in corresponding ratio of length to width d/a = 2. Total flow rate is 200 m^3/d with contribution proportion of injection wells equal to 30:70 (%).

The general parameters of the models are:

- Porosity ϕ = 0.2, water viscosity μ_w = 0.7 cp, oil viscosity μ_o = 4 cp;

- Longitudinal and transversal dispersivity are α_{DL} = 0.03 m, α_{DT} = 0.003 m;

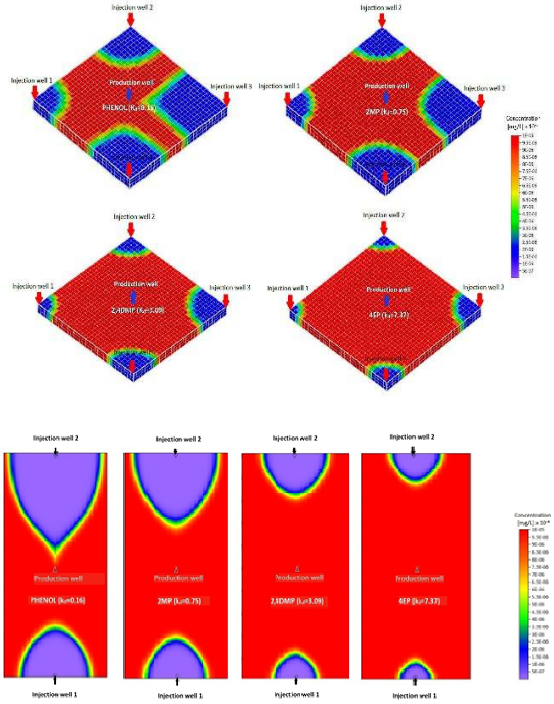

Figure 2: Concentration distribution in space of Phenol, 2-Methylphenol, 2,4-Dimethylphenol, 4-Ethylphenol at 0.3 PV in Five-spot model and Direct line model.

- Relative permeability curve is described by Corey model with critical water saturation S_{cwr} = 0.3, residual oil saturation S_{or} = 0.35 (Five-Spot model) and S_{or} = 0.4 (Direct-Line model), water endpoint: 0.15, oil endpoint 0.85, water exponent: 1.5, oil exponent: 2, endpoint mobility ratio: 1.

The NPITs initial concentration in water phase was 10 mg/L and its partition coefficient between phases determined in the experimental data of Tracer Lab of CANTI was listed in Table 1. All compounds were supposed to have same density, ankane number and chemical properties but different partition coefficient. The waterflooding lasted 10 PV of the model to obtain the whole concentration curves of the NPITs at the production well. The concentration of NPITs between phases is instantaneously achieved equilibrium while oil/water in contact. Figure 2 illustrates NPITs concentration distribution of the models at 0.3 PV.

Table 1: The partition coefficient K_d of NPITs used in the models

NPITs	Partition coefficient $K_d = C_o/C_w$
Phenol	0.16
4-Methylphenol	0.58
2-Methylphenol	0.75
4-Propylphenol	1.34
3,4-Dimethylphenol	1.61
2,4-Dimethylphenol	3.09
4-Ethylphenol	7.37

Figure 3a and Figure 4a show NPITs concentration curves at production well decreasing over time, in which the greater K_d the slower reduction of concentration. The Levenberg-Marquart (LM) algorithm and Exponential Modified Gauss (EMG) function were applied to determine the differential apparent concentration curve of each swept area. Figure 3b and Figure 4b show the results of applying LM algorithm to separate the overlapping chromatographic peaks of Phenol (K_d = 0.16). The mean residence time of NPITs in each swept area can be determined by using corresponding chromatographic peak.

The results of calculating the contribution proportion of injection wells of Five-spot model and Direct-line model are presented in Table 2.

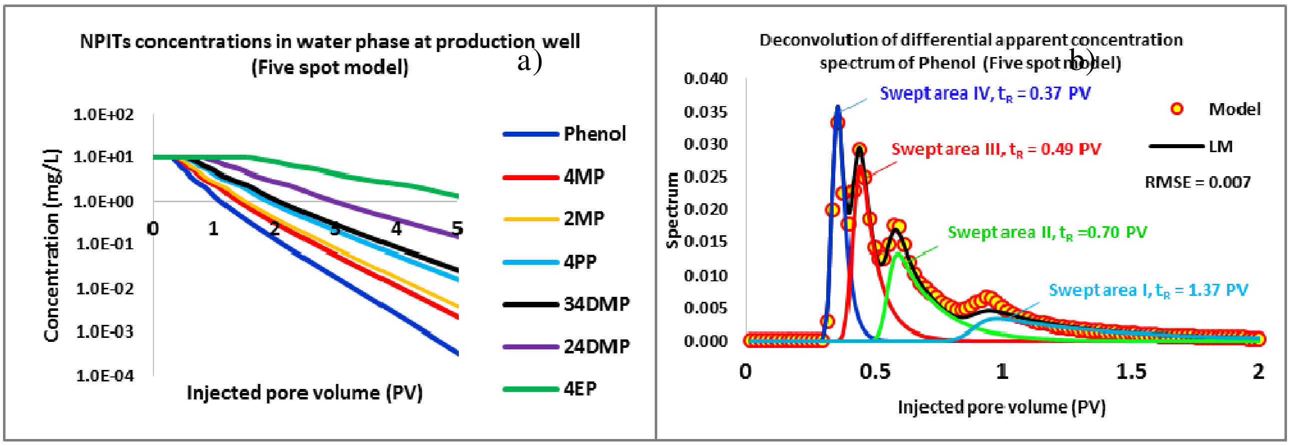

Figure 3: NPITs concentration curves in water phase at production well of Five-spot model (a) and differential apparent concentration of Phenol (K_d = 0.16) of Five-spot model was obtained after using LM algorithm (b). The mean residence time t_R of NPITs in each swept area was determined by using corresponding chromatographic peak.

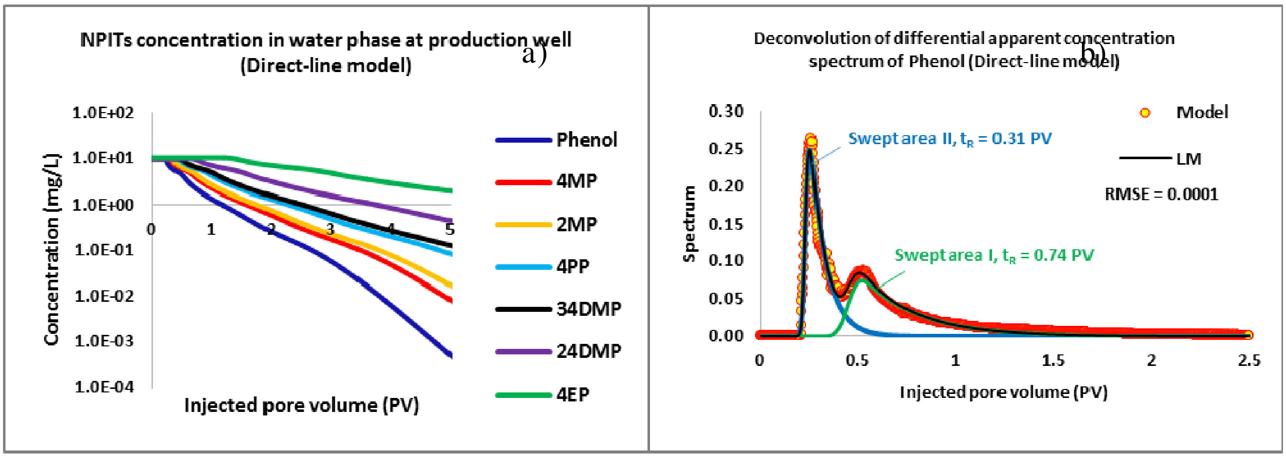

Figure 4: NPITs concentration curves in water phase at production well of Direct line model (a) and differential apparent concentration of Phenol (K_d = 0.16) of Direct line model was obtained after using LM algorithm. The mean residence time t_R of NPITs in each swept area was determined by using corresponding chromatographic peak.

Table 2: The results of calculating the flow rate proportion of injection wells of Five-spot model and Direct-line model

Model	**Five-Spot model**				**Direct-Line model**	
Swept area	**I**	**II**	**III**	**IV**	**I**	**II**
Contribution ratio of swept areas of models	**10.0%**	**20.0%**	**30.0%**	**40.0%**	**30%**	**70%**
Phenol (K_d = 0.16) F (%)	10.6%	20.6%	29.8%	39.0%	29.7%	70.3%
4MP (K_d = 0.58) F (%)	10.9%	20.4%	29.7%	39.0%	30.2%	69.8%
2MP (K_d = 0.75) F (%)	10.9%	20.3%	29.7%	39.0%	29.7%	70.2%
4PP (K_d = 1.34) F (%)	11.0%	20.3%	29.6%	39.1%	30.3%	69.7%
34DMP (K_d = 1.61) F (%)	11.0%	20.2%	29.6%	39.2%	29.6%	70.4%
24DMP (K_d = 3.09) F (%)	11.0%	20.1%	29.6%	39.3%	29.9%	70.1%
4EP (K_d = 7.37) F (%)	12.1%	19.8%	29.2%	38.9%	30.9%	69.1%

The calculated flow rate proportion values are different from the model values in range of 1 to 2% for all NPITs in both models.

Based on the mean residence time of a pair of NPITs in each swept area, the oil saturation of respective swept area can be determined by using *Moment method*. The average calculation value of oil saturation using compounds having K_d smaller than 3 are given in Table 3.

Table 3: The results of calculating the oil saturation of swept area using *Moment method*

Model	**Five-Spot model**				**Direct-Line model**	
Swept area	I	II	III	IV	I	II
Contribution ratio of swept areas of models	10%	20%	30%	40%	30%	70%
Residual oil saturation of models	0.35				0.4	
Average calculation value	0.357	0.386	0.377	0.370	0.450	0.470
Standard deviation	0.008	0.005	0.014	0.016	0.082	0.071
Relative error	2.1%	10.0%	7.7%	5.7%	12.6%	17.0%

The oil saturation of the whole model is calculated by both *Moment* and *Linear* method. The results calculated from *Moment method* give the relative errors of less than 2% for all pairs of NPITs. The oil saturation calculated from *Linear method* are presented in Table 4. The results show that the compounds having partition coefficient less than 1 such as Phenol (K_d = 0.16), 4MP (K_d = 0.58), 2MP (K_d = 0.75) give the lowest relative error.

Table 4: The results of calculating the oil saturation of the whole model using Linear method and relative errors (%)

Model	**Five-Spot model**			**Direct-Line model**		
Injection pore volume (PV)	**0.5-2PV**	**2-6PV**	**6-10PV**	**0.5-1PV**	**1-4PV**	**4-10PV**
Oil saturation of model	**0.442**	**0.415**	**0.407**	**0.391**	**0.366**	**0.356**
Phenol - 4MP - 2MP (K_d = 0.16, 0.58 và 0.75)	0.433 **2.04%**	0.444 **7.12%**	0.355 **12.70%**	0.383 **2.12%**	0.380 **3.86%**	0.367 **3.24%**
Phenol - 4MP - 2MP - 4PP (K_d = 0.16, 0.58, 0.75 và 1.34)	0.412 **6.96%**	0.564 **35.98%**	N/A	N/A	0.360 **1.52%**	0.381 **7.20%**
Phenol - 4MP - 2MP - 4PP - 34DMP (K_d = 0.16, 0.58, 0.75, 1.34 và 1.61)	0.381 **13.91%**	0.612 **47.61%**	N/A	N/A	0.357 **2.55%**	0.384 **7.93%**
Phenol - 4MP - 2MP - 4PP - 34DMP - 24DMP (K_d = 0.16, 0.58, 0.75, 1.34, 1.61 và 3.09)	N/A	0.731 **76.29%**	N/A	N/A	0.314 **14.11%**	0.394 **10.72%**

Phenol - 4MP - 2MP - 4PP - 34DMP - 24DMP -4EP (K_d = 0.16, 0.58, 0.75, 1.34, 1.61, 3.09 và 7.37)	N/A	0.639 **54.20%**	0.624 **53.24%**	N/A	N/A	0.416 **16.95%**

IV. EXPERIMENTAL RESULTS

Alkylphenol compounds (APs) such as Phenol (P), 2 – methylphenol (2MP), 4 – methylphenol (4MP), 3,4 – dimethylphenol (34DMP) were chosen as experimental investigation subjects in this study. The physical model was designed to describe the transport of APs from oil phase to water phase during waterflooding in the case of two injection wells using Su Tu Nau crude oil and distilled water at 40°C. Two experiments simulating the transport of APs in two component swept area were separately carried out with different flow rates (Q_1 and Q_2). The total concentration of APs was then determined by the sum of APs concentration of component swept areas $C=(Q_1/Q)C_1+(Q_2/Q)C_2$, in which, the total flow rate is $Q = Q_1+Q_2$.

The experiments of oil displacement by waterflooding through the packed column were conducted with each swept area. At the same time, water samples were collected over time until the residual oil saturation state was approximately reached. The concentrations of the APs in the water samples were analyzed on HPLC Dionex Ultimate 3000, detector DAD, C18 column. The detection limit is about 10^{-7}. The partition coefficients of APs between two phases were determined in experimental condition by the Flow Injection Analysis (FIA) method.

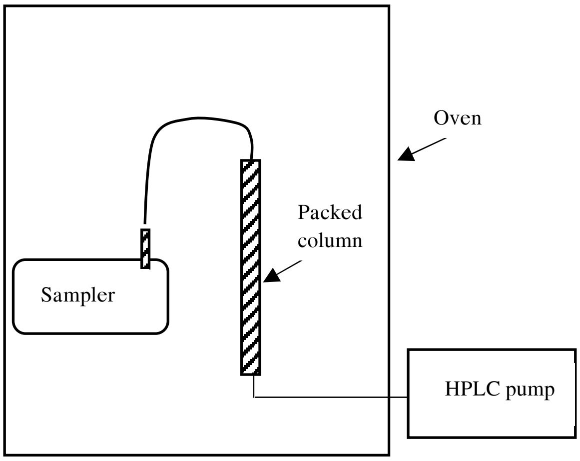

Figure 5: Arrangement of the waterflooding experiments

Table 5: Experimental parameters

Content	Swept area I	Swept area II
Stainless steel column (SS316L)	Length: 30,5 (cm) Inner diameter: 1,6 (cm)	
Glass bead	Average diameter: 100 - 150 µm Density: 2,7 g/cm^3	
Pore volume of packed column (PV)	24,0 cm^3 (porosity 41%)	
Su Tu Nau crude oil	Density at 40^{0}C: 0,82 g/cm^3	
Distilled water	Density at 40^{0}C: 0,992 g/cm^3	
APs compounds (Merck):	Initial concentration of	Initial concentration of

Phenol ($K_d = 2$) 2MP ($K_d = 3$) 4MP ($K_d = 4$) 34DMP ($K_d = 6$)	APs in crude oil: Phenol: 56,21 mg/L 2MP: 103,23 mg/L 4MP: 98,10 mg/L 34DMP: 268,25 mg/L	APs in crude oil: Phenol: 134 mg/L 4MP: 128 mg/L 2MP: 137 mg/L 34DMP: 194 mg/L
Flow rate (HPLC pump)	0,4 mL/min	0,3 mL/min
Residual oil saturation	65,06% pore volume (PV)	63,46% pore volume (PV)

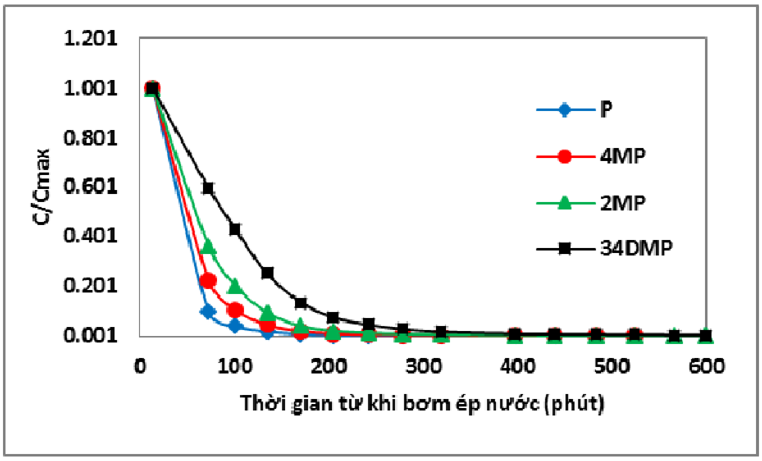

Figure 6: The concentration of APs in water phase over time of Swept area I

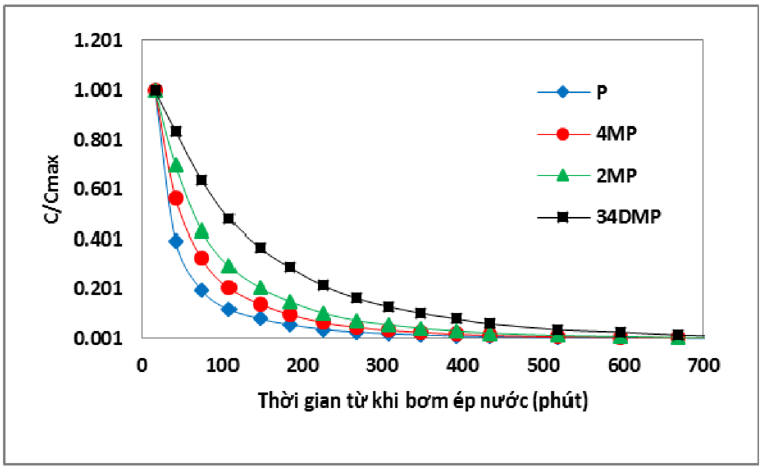

Figure 7: The concentration of APs in water phase over time of Swept area II

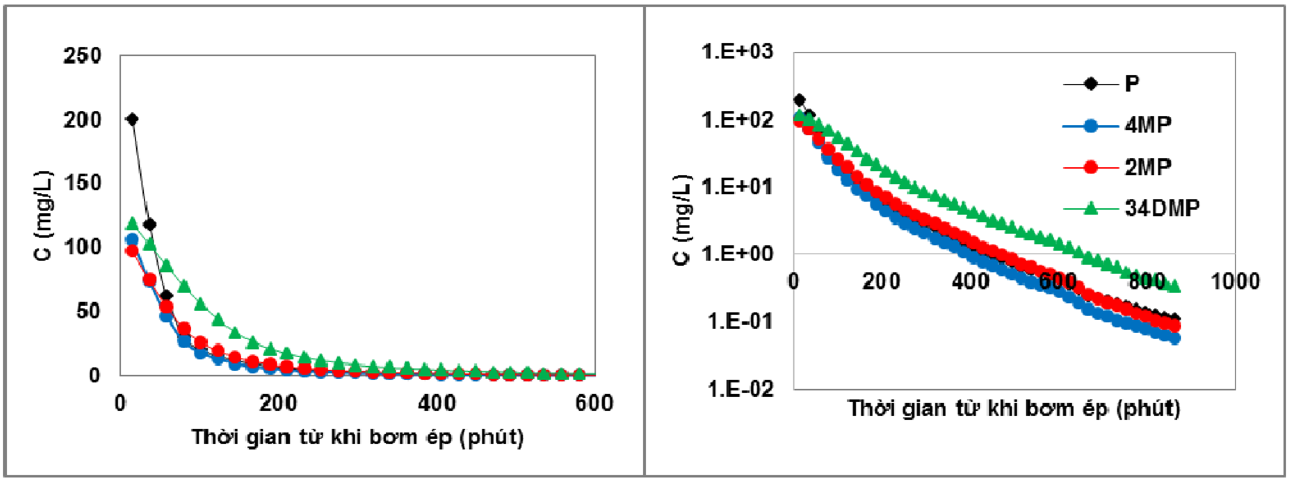

Figure 8: The concentration of APs in water phase over time of the whole swept area

Linear method was applied to determine the residual oil saturation of the whole model in the range of 50 - 300 minutes (1-4 PV). The procedure for determining residual oil saturation is as follows:

1. Representing LnC +0,5Lnt relation over time with all compounds
2. Determining the slope (a) of the straight line that represents the above relationship
3. Determining the fitting parameters (a_2, a_1, a_0) represent the relation between 1/slope and K_d in Eq. (1)
4. Calculating the oil saturation of the model based on obtained parameters using Eq. (2)

As a result, the residual oil saturation of the whole model is equal to 63.92%. The deviation of the calculated value from the residual oil saturation of Swept area I and Swept area II are equal to 1.8% and 0.7%, respectively.

In case the oil recovery process of a production well is contributed by many injection wells, the decrease rate of the total NPITs concentration depends strongly on the swept area has slower flow rate. APs concentration decreases more rapidly in the case of faster injection flow rate. Experiments showed that the oil saturation calculated from the *Linear method* in this case represents the swept area has slower flow rate. The difference of the deviations is not large due to the injection flow rate of two experiments are relatively close together.

IV. CONCLUSIONS

The method using partitioning organic compounds in crude oil as Natural Partitioning Interwell Tracers (NPITs) for calculation of oil saturation and flow rate proportion of injection wells in homogeneous single-layered reservoir has been verified on the numerical models using UTCHEM software and on the physical model. The simulation results showed that the calculated values of flow rate proportion are different from modelling values between 1 to 2%. The compounds having K_d smaller than 3 allow for the calculation at the stage of up to 3 PV whereas those having Kd more than 3 need greater observation time period. Oil saturation calculated from the proposed method with compounds having K_d smaller than 1 gives the errors of less than 20% at the stage of up to 2 PV. Experimental result showed that the calculated value of oil saturation gives smaller deviation with the swept area has slower flow rate.

REFERENCES

[1] Green J.B., Thomas J.S., et al, "*Separation and analysis of hydroxyaromatic species in liquid fuel*", National Institute for Petroleum and Energy Research, Bartlesville, OK, unpublished Topical Report, pp. 1-34.

[2] Sinha, R., Asakawa, K., Pope, G., "*Simulation of natural and partitioning interwell tracers to calculate saturation and swept volumes in oil reservoirs*", SPE 89458, SPE/DOE 14th Symposium on Improved Oil Recovery, Tulsa, Oklahoma, USA, 17-21 April, 2004.

[3] Huseby, O., et al., "*Transport of organic components from immobile and bypassed oil in porous media*", AICHE Journal, May, 2003.

[4] Phan N.H, Quang N.H, Cuong T.B, Huong H.T.T, Phát triển mô hình mô phỏng quá trình vận động của các chất chỉ thị tự nhiên (NPITs) để đánh giá trữ lượng dầu trong khai thác", BCTK đề tài NCKH cấp Bộ 06/14/TTUDKTHNCN, 2015.

[5] Technical Documentation for UTCHEM 9.0, Center for Petroleum and Geosystems Engineering, The University of Texas at Austin, July 2000.

[6] User's Guide for UTCHEM 9.0, Center for Petroleum and Geosystems Engineering, The University of Texas at Austin, July 2000.

CONSTRUCTION AND ANALYSIS OF STABLE ISOTOPE RATIOS δD AND δ^{18}O IN WATER SAMPLES ON IWA-35EP DEVICE COMBINED WITH CHEMICAL COMPOSITION ANALYSIS TO INVESTIGATE SEEPAGE WATER THROUGH THE DON DUONG DAM

Huynh Thi Thu Huong, Le Van Son, Phan Thi Luan, Le Thanh Tai, Duong Thi Bich Chi, Lai Viet Hai and Tran Trong Hieu

Centre for Applications of Nuclear Technique in Industry (CANTI),
01 DT 723, ward 12, Dalat city, Lam Dong province

Project information:

- **Code:** CS/18/06-01
- **Managerial Level:** Institute
- **Allocated Fund:** 80,000,000 VND
- **Implementation time:** 18 months (Jan 2018- Jun 2019)
- **Contact email:** office@canti.vn
- **Paper published in related to the project:**

Huynh Thi Thu Huong, Le Van Son, Le Thanh Tai, Phan Thi Luan. Assessment on typical characteristics of seepage water through dam based on hydration method and stable isotope. *Journal of Water Resources and Environmental Engineering.* No. 65. June 2019 (In Vietnamese).

Abstract: This study presents the method of analyzing stable isotope in the water on IWA-35EP device. The repeatability of the measurement method is 0.9% for δD and 0.8% for δ^{18}O. The method is then used to analyze the reservoir water, dam body water, dam foundation water, and water from two leak points at the downstream of Don Duong dam (Lam Dong). The stable isotope composition combined with the concentration of water-soluble ions and physical indicators is interpreted to give the most basic visualization of the permeability regime. The results show that water from the lake seeps through the dam body is dominated by the dissolution and ion exchange process. The dam foundation water is recharged by reservoir water and local CO_2 - rich groundwater. Besides, the dam foundation water significantly contributes to the origin of water from two leak points in the downstream of the dam.

The achieved results will be the basis for further studies related to the application of stable isotope methods combined with chemical composition analysis in the water for the survey of dam leakage, groundwater recharge, and hydrology.

Keywords: *Stable isotope, chemical composition, seepage, earth dam*

I. INTRODUCTION

The stable isotopes of water, Deuterium and Oxygen-18, are strongly governed by isotopic fractionation occurs alternately between evaporation and condensation process, in which water molecules with light isotopes are more volatile while the molecules contain heavy isotopes are easier to condense. Based on the properties of typical for each basin depending on geological conditions, water origin, climate as well as other local processes, Deuterium and Oxygen-18 are used as a natural indicators to provide information on the hydrogeological characteristics of aquifers, the relation between groundwater, surface water and atmosphere [1], assess groundwater pollution [2], and study the source of water seepage through hydroelectric dams [3, 4]. On the other hand, the chemical compositions of water are adjusted along to the water movement by the enrichment due to the evaporation, or by the dilution due to the rainfall and the interaction between water and rock such as mineral dissolution, cation exchange, oxidation-reduction process, allowing consolidation of information on the mixing of water sources and chemical processes take place in the basin.

The objective of the project is to approach the stable isotope method combined with chemical composition analysis in water to investigate leakage water through a dam. The method of analyzing stable isotope ratios built on IWA-35EP device is used to analyze and test on the samples of reservoir water, dam body water, dam foundation water, and water from two leak points at the downstream of the Don Duong dam (Lam Dong). The result of the stable isotope ratio combined with the chemical composition of the water is interpreted to evaluate the characteristics of the permeability flow through the dam, as a basis for future studies.

II. METHOD FOR ANALYZING STABLE ISOTOPE RATIO ON IWA-35EP DEVICE

Water samples from the environment with the salinity of less than 4% are filtered through quantitative filter paper and 0.22 um syringe filter before being analyzed. The pipette is used to draw 1 mL of the measurement samples and calibrators into 2 mL vials and tighten the cap. Samples are pumped into the measuring chamber via the PAL CTC autosampler integrated with the device. The autosampler is set up using a Hamilton syringe 1.2 µL to draw 1 uL of sample to pump into an injector block, in which the sample is completely vaporized at 85^0C and taken into the measuring chamber for analyzing stable isotope directly through vapor based on the principle of optical absorption. Hamilton Syringe 1.2 µL are always cleaned before each run with distilled water and 1- Methyl-2-pyrrolidinone solution to reduce volume fluctuations during the sample run. Five standard samples provided by Los Gatos Research are used to calibrate analytical values. The sample analysis program was established with six measurements per sample. The first two measurements are ignored to reduce the "remember effect" of the device. After finishing all of the sample measurements, the raw results are transferred from the device to the USB (Los Gatos Research) and processed on LWIA Post Analysis (Los Gatos Research) software to give the measurement results [5, 6].

III. EXPERIMENTAL RESULTS

The method of analyzing stable isotope ratios built on IWA-35EP device is then used to analyze and test on the samples of reservoir water (NH), dam body water (collected from the body piezometer-ĐDA), dam foundation water (collected from the foundation piezometer-ĐD and collected from the pressure relief wells-W), and water from two leak points in the downstream of the Don Duong homogeneous earth dam (Lam Dong). Results of control parameters of the method show the correlation coefficient of the calibration curve > 0.999, the deviation of the reference point ≤ 5%, the repeatability error in range of 0.6-0.7% and the uncertainty in the range of 0.8-0.9%.

The dam site map is illustrated in Fig. 1. The leak without fine sand (RNT) appeared from many years and has a stable flow of 120 L/min even when the lowest water level elevation of 1023 m. The leak with fine sand (RCC) was discovered recently when the reservoir water level reached the maximum elevation of 1040 - 1042 m, the average flow of 6 L/min.

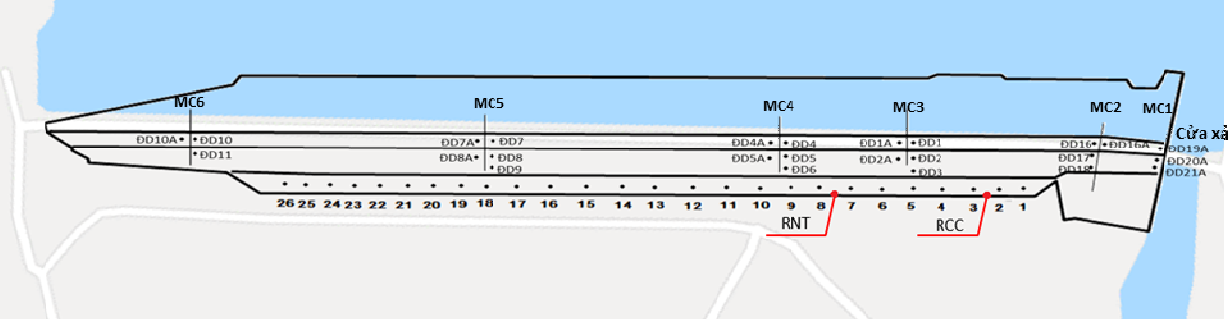

Figure 1: Map of the dam site with the position of each section (MC)

A total of 321 water samples were collected for the analysis of stable isotopic composition and water chemistry in this study. The concentration of the main ions (Na^+, K^+, Ca^{2+}, Mg^{2+}, Cl^-, SO_4^{2-}, NO_3^-, PO_4^{3-}) was analyzed by ion chromatography techniques with the repeatability error for anion and cation in range of 3 - 6% and 3 - 4%, respectively. The concentration of HCO_3^- is measured by titration technique with the repeatability error of 1%. Conductivity and pH were measured on the Laboratory's equipment with the repeatability error below 0.5%.

Results of chemical composition analysis

The results of the pH distribution of water samples show slightly acidic to slightly alkaline conditions. TDS range of less than 250 mg/L with all samples. Conductivity distribution (EC) of the samples in order: reservoir water < dam body/foundation water < water from two leak points. The conductivity of RNT is greater than that of RCC about 1.5 times. The Piper diagram shows the dam body water (except for the piezometer ĐD2A) belongs to the Na-HCO3 water type, while the dam foundation water (except for the piezometer ĐD5) is Ca-HCO3 water type (Fig. 2). At MC3 and MC4 cross sections (Fig. 1), ĐD2A represents ionic components as dam foundation water and ĐD5 expresses ionic components as dam body water, implying that there may be a hydraulic connection between the dam body and dam foundation in the area. In addition, RNT and RCC belong to the water classification similar to the dam foundation water.

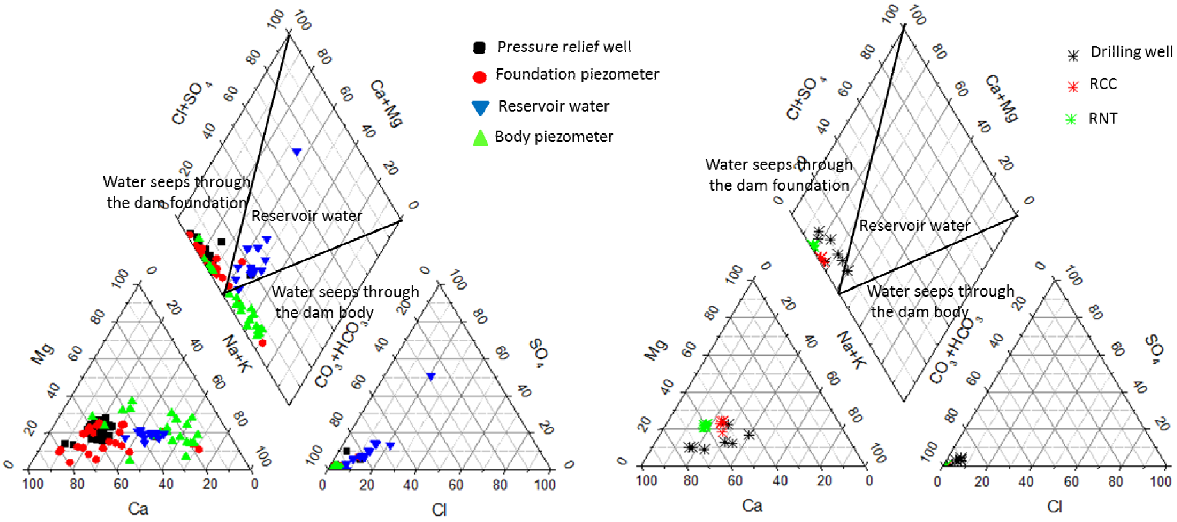

Figure 2: Piper diagram of water samples

The relationship between TDS and $Na^+/(Na^+ + Ca^{2+})$ shows that water-rock interaction is the main process affecting the chemical composition of water samples (Fig. 3) [7]. The ratio $Na^+/(Na^+ + Ca^{2+})$ of RNT and RCC is quite similar to that of dam foundation water.

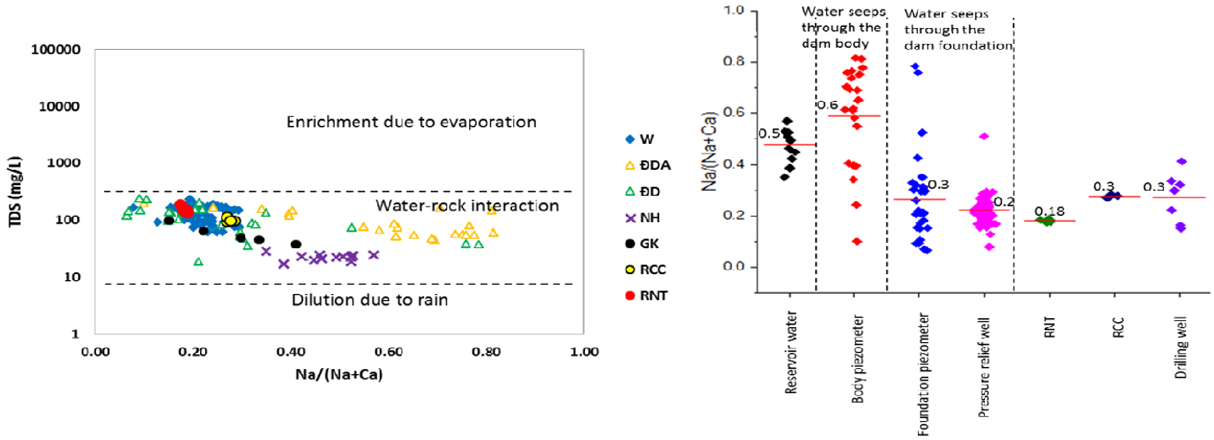

Figure 3: Relationship between TDS and $Na^+/(Na^++Ca^{2+})$ of water samples

Figure 4a illustrates the Na^+/Cl^- ratio > 1 with all samples, showing that Na^+ can be generated from silicate weathering. The $(Ca^{2+}+Mg^{2+})/HCO_3^-$ < 0.5 is shown as Figure 4b, showing the ion exchange process between Ca and/or Mg in water with Na and/or K in rock can be responsible for the decrease of Ca^{2+} and Mg^{2+} [7]. The ratios of RNT and RCC are in the range of dam foundation water.

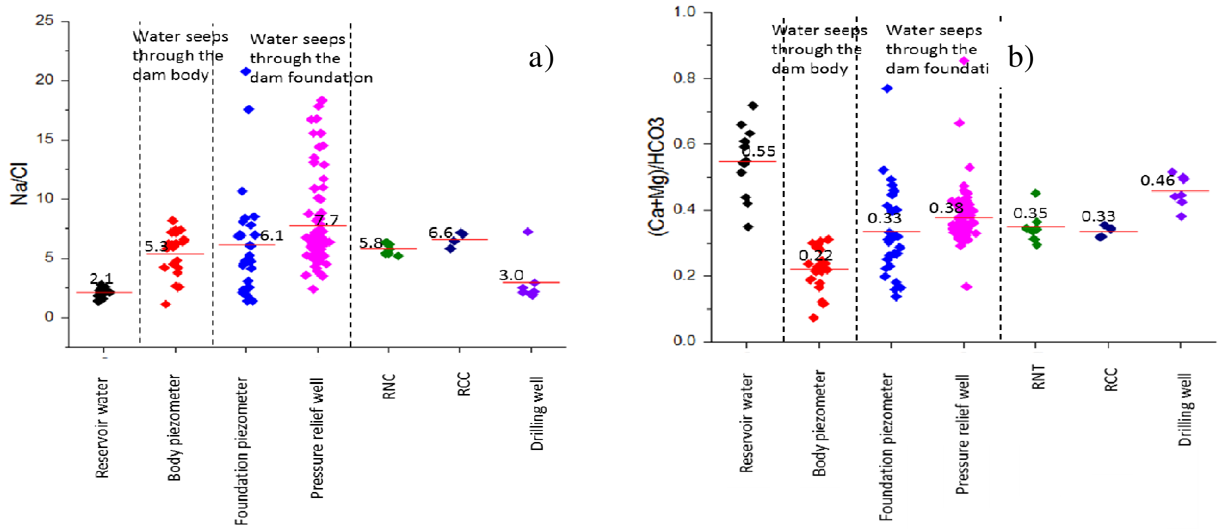

Figure 4. Na^+/Cl^- ratio and $(Ca^{2+}+Mg^{2+})/HCO_3^-$ ratio of water samples

Results of stable isotope analysis

The δD - $\delta^{18}O$ plot of the samples with the rainwater line (RL) and the Global Meteoric Water Line (GMWL) are shown in Figure 5. The relationship between δD and $\delta^{18}O$ of RL is shown by the equation: $\delta D = 7.66\delta^{18}O + 10.82$ (‰). The slope of RL is smaller than the slope of GMWL (7.66 < 8) and its intercept of about 10% indicates that rainwater has undergone evaporation under conditions of less than 85% humidity [8]. The samples of dam body/foundation water and reservoir water locate along RL and GMWL show that their origin mainly from meteorological water less affected by evaporation [9]. The samples of pressure relief wells and water from two leak points are on the left side of GMWL may be a result of an ^{18}O balance between dissolved CO_2 and water at low temperatures often observed in CO_2-rich aquifers with long water-rock-CO_2 interaction time [10].

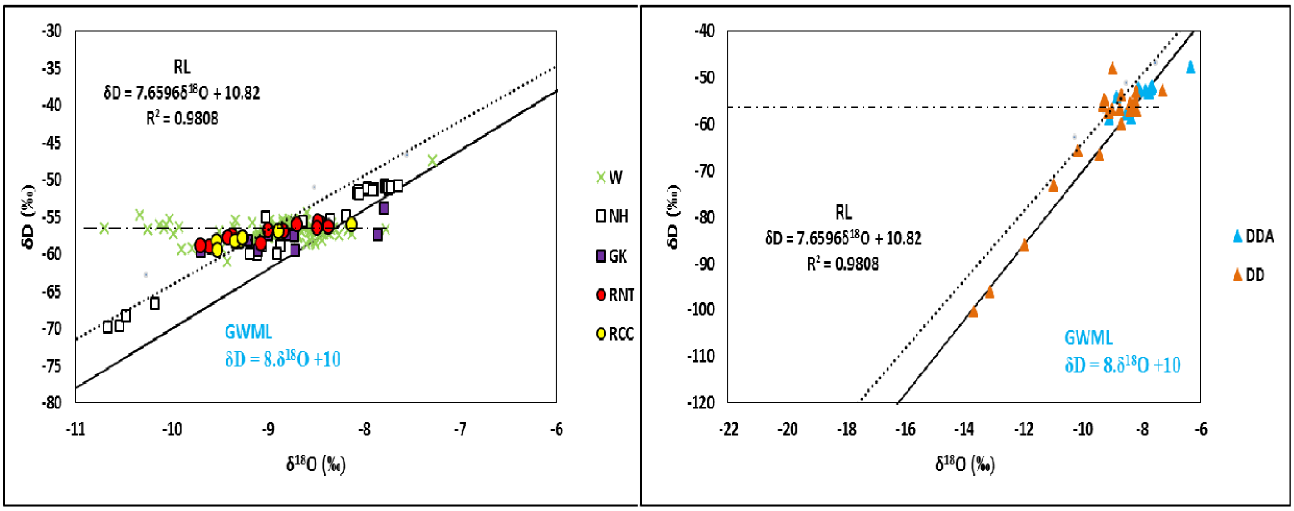

Figure 5: δD - δ^{18}O plot of the samples

The correlations between δ^{18}O and conductivity, HCO_3^- of the water samples are shown in Figure 7. Conductivity and HCO_3^- concentration increase gradually in the order of reservoir water (NH)> Dam body water and RCC > RNT > pressure relief well water but not much change in δ^{18}O, indicating that the mineralization process gradually increases from reservoir water to water collected from pressure relief well [11]. The mineralization of RCC is close to the dam body water, while the mineralization of RNT is close to the dam foundation water.

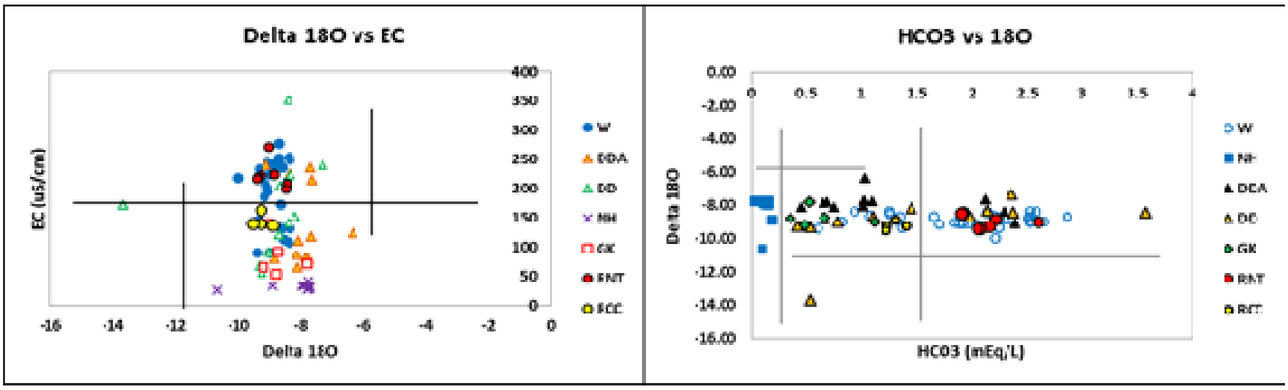

Figure 6: Correlations between δ^{18}O and conductivity, HCO_3^-

Discussion

The ionic components and stable isotopes of water samples provide the most basic visualization of the permeability regime of a dam. Reservoir water is recharged by rainwater in conditions of humidity below 85%, less affected by evaporation. Based on the hydraulic pressure difference, the reservoir water seeps through the dam body, dissolving the mineral components and occurring ion exchange process between Ca and/or Mg in water with Na and/or K in rock. Dam foundation water is recharged by reservoir water, local groundwater with mineral dissolution processes dominate. The results of stable isotope analysis show that the water from pressure relief wells is characteristic of CO_2-rich groundwater with long of water-rock-CO_2 interaction time. On the other hand, at section MC3 and section MC4, represents ionic components as dam foundation water and ĐD5 expresses ionic components as dam body water, implying that there may be a hydraulic connection between the dam body and dam foundation in the area. The results of ion analysis and stable isotope combined with hydraulic monitoring show that the origin of RNT can be from dam foundation water influenced by the local groundwater. Besides, the ion ratio, water type and isotopic composition of RCC is very similar to that of dam foundation water, however, the mineralization is closer to the dam body water, implying its source of water may come from dam body water influenced by dam foundation water.

IV. CONCLUSIONS

This study presents the method of analyzing stable isotope ratios built on IWA-35EP device. Results of method control parameters show the correlation coefficient of the calibration curve > 0.999, the deviation of the reference point ≤ 5%, the repeatability error in range of 0.6-0.7% and the uncertainty in the range of 0.8-0.9%. The method is then used to analyze and test on the samples of reservoir water, dam body/foundation water, and two concentrated seepage points in the downstream of the Don Duong homogeneous earth dam (Lam Dong). The stable isotope composition combined with the concentration of water-soluble ions and physical indicators such as EC, pH, and TDS are interpreted to evaluate the characteristics of the permeability flow through the dam. The results showed that water from the lake seeps through the dam body is dominated by the dissolution and ion exchange process. The dam foundation water is recharged by reservoir water and local CO_2 - rich groundwater. In addition, the results show that the dam foundation water significantly contributes to the origin of the water from two leak points at the downstream of the dam.

REFERENCES

[1] Mook W.G., "*Environmental isotopes in the hydrological cycle, principles and applications*", International Atomic Energy Agency (IAEA) and United Nations Educational, Scientifc and Cultural Organization (UNESCO), 2001.

[2] Gomaah M., Meixner T., Korany E.A., Garamoon H., Gomaa M.A., "*Identifying the sources and geochemical evolution of groundwater using stable isotopes and hydrogeochemistry in the Quaternary aquifer in the area between Ismailia and el Kassara canals, Northeastern Egypt*", Arab J Geosci, 9(6), pp. 437, 2016.

[3] Lynn J.T., et al, "*Physical and Hydrochemical Evidence of Lake Leakage near Jim Woodruff Lock and Dam and of Ground-Water Inflow to Lake Seminole, and an Assessment of Karst Features in and near the Lake, Southwestern Georgia and Northwestern Florida*", Scientific Investigations Report 2005–5084 (USGS), 2005.

[4] Kumar C. P., "*Hydrological Studies Using Isotopes*", International Journal of Innovative Research & Development, 2(13), pp.8-15, 2013.

[5] LGR, *Liquid Water Isotope Analyzer (LWIA) - User Manual*, Model 912-0008.

[6] Hussin N. H., Yusoff I., "*Multivariate statistical analysis for identifying water quality and hydrogeochemical evolution of shallow groundwater in Quaternary deposits in the Lower Kelantan River Basin, Malaysian Peninsula*", Springer, 75(14), pp.1081, 2016.

[7] Hussin N. H., Yusoff I., "*Multivariate statistical analysis for identifying water quality and hydrogeochemical evolution of shallow groundwater in Quaternary deposits in the Lower Kelantan River Basin, Malaysian Peninsula*", Springer, 75(14), pp.1081, 2016.

[8] István F., "*Processes behind the isotopic water line: water cycle and climate*", Studia universitatis bases-bolyai, Physica, 2005.

[9] Lesleigh A., Max B. et al., "*Lake oxygen isotopes as recorders of North American Rocky Mountain hydroclimate: Holocene patterns and variability at multi-decadal to millennial time scales*", Global and Planetary Change, 137, pp.131–148, 2016.

[10] Pauline H., Julie L. et al., "*CO2 intrusion in freshwater aquifers: Review of geochemical tracers and monitoring tools, classical uses and innovative approaches*", Applied Geochemistry, 46, pp.95 – 108, 2014.

[11] Obed F.F., Sandow M.Y. et al., "*Evaluating groundwater recharge processes using stable isotope signatures—the Nabogo catchment of the White Volta, Ghana*", Arab J Geosci, 9(4), pp.1 – 15, 2016.

STUDY ON THE DECOLORATION OF TEXTILE WASTEWATER BY ELECTRON BEAM IRRADIATION METHOD

Nguyen Ngoc Duy, Dang Van Phu, Nguyen Thi Kim Lan, Nguyen Thanh Duoc,
Pham Thi Thu Hong, Truong Thi Hanh and Nguyen Quoc Hien

Research and Development Center for Radiation Technology, Vietnam Atomic Energy Institute,
202A, 11 Street, Linh Xuan Ward, Thu duc District, Ho Chi Minh City

A. Project information:

- **Code:** CS/18/07-02
- **Managerial Level:** Institute
- **Allocated Fund:** 80,000,000 VND
- **Implementation time:** 12 months (Jan 2018- Dec 2018)
- **Contact email:** ngocduy158@yahoo.com
- **Paper published in related to the project:** None

Abstract: Decoloration of textile wastewater using electron beam irradiation method was studied. The effect of initial dye concentration, absorbed dose and the present of hydrogen peroxide (H_2O_2) concentration were investigated. The results indicated that dye concentration, chemical oxygen demand, biological oxygen demand and pH decreased with increasing absorbed dose. A sufficient amount of H_2O_2 in radiation method could accelerate decoloration process. The suitable H_2O_2 concentration was achieved at 5 mM and absorbed dose of 5 kGy or 10 mM and absorbed dose of 3 kGy with initial dye concentration from 267 to 330 (Pt-Co), respectively. For the initial dye concentration of 450 (Pt-Co), the suitable H_2O_2 concentration was achieved at 10 mM and absorbed dose of 5 kGy. In the same condition, a decoloration efficiency of ~90% was obtained with EB/H_2O_2, in contrast with decoloration efficiency by using EB alone (~71%). These results highlighted the potential of EB radiation technology for dye removal from textile wastewater.

Keywords: *dye; textile wastewater; electron beam; hydrogen peroxide.*

I. INTRODUCTION

Reactive dye-containing textile wastewater is one of the most difficult wastewater to treat, because most of reactive dye has complex chemical structure with high water–solubility [1]. Moreover, the dye structures are commonly highly resistant to biodegradation process [2]. One of the greatest concerns in wastewater treatment of a textile effluent is the color removal. Previous researches showed that conventional water treatment process cannot achieve efficient the extent of decreased color in reactive dyeing wastewater. Coagulation and adsorption sometimes could eliminate color from reactive dye compound, but the process required large of chemicals (acid, coagulant or adsorbent) that produce a huge toxic sludge which increases the cost of construction and running [3, 4]. Biological treatment using biofiltration [5], could effectively alleviate color in textile wastewater. However, this method requires a long period of time due to acclimation and great dependence on the types of organism presence. Some oxidation processes such as ozonation, sonolysis, photo degradation, etc. were reported to be not completely effective [6-8]. Hence, the approach for the rapid and effective removal of color in reactive dyeing wastewater is necessary to be further developed. Recently, ionizing radiation method using gamma Co-60 radiation and electron beam, a kind of oxidation method which could induce oxidizing species ($^{\bullet}OH$, H_2O_2,

$HO_2^•$...) and reducing species (e_{aq} and $H^•$) through water radiolysis [9], received great attention for the effective treatment of toxic organic pollutants in wastewater.

The electron beam radiation has been used successfully to treat textile wastewater [10-14]. However, the radiation process normally required high absorbed dose to degrade the complex organic compounds. In this way, there is a need of an additional alternative to combine with the radiation process to effectively enhance the decomposition. Hydrogen peroxide (H_2O_2) could be the key to the problem. Some researchers indicated that adding small amounts of hydrogen peroxide could improve the radiation capacity for eliminating pollutants in wastewater through increasing the formation of $^•OH$ radicals as follows [15, 16]:

$$e_{aq} + H_2O_2 \rightarrow •OH + OH^- \quad (1)$$

$$H^• + H_2O_2 \rightarrow {}^•OH + H_2O \quad (2)$$

The aim of this study was to investigate the color removal of synthetic textile wastewater by electron beam radiation combined with H_2O_2. Several factors such as initial dye concentration, absorbed dose and concentration of H_2O_2 were examined to determine suitable operating condition.

II. EXPERIMENTAL

1. Chemicals

Textile wastewater used in this research was obtained from Thu Duc textile factory, Ho Chi Minh City. The textile wastewater was a mixture of Reactive Black 5 + Reactive Red 10 + Reactive Orange 13 (sample 1); Reactive Red 10 + Yellow GR (sample 2) and Yellow GR + Reactive Black 5 + Turquoise Blue HF–G (sample 3). The textile wastewater (1000 ml) was put in plastic box so that the thickness of the solution is 2.5 cm. After that, the radiation experiments were carried out at an electron accelerator UERL – 10 – 15S2 in VINAGAMMA center. The absorbed doses were measured using dichromate dosimetry (ASTM International, 2004) [19]. Hydrogen peroxide solution 30% (w/w) was purchased from Merck, Germany.

2. Method

2.1. Effect of absorbed dose

The textile wastewater put in plastics box was irradiated with various absorbed doses from 5 to 20 kGy to investigate the effect of absorbed dose on characteristics of textile wastewater such as pH, COD, BOD and dye concentration.

2.2 Effect of H_2O_2 concentration at absorbed dose of 5 kGy

The textile wastewater was added H_2O_2 to reach the desired concentration particularly 5, 10, 15, and 20 mM. After that, the samples were irradiated at absorbed doses of 5 kGy.

2.3 Effect of absorbed dose at the concentration of 10 mM H_2O_2

The textile wastewater was added H_2O_2 to reach 10mM. The samples then were irradiated with various absorbed doses from 3 to 12 kGy.

2.4. Analysis method

The values of COD, BOD_5 pH and dye concentration were measured according to standard method TCVN 6491:1999 (ISO 6060:1989), TCVN 6001–2:2008 (ISO 5815–2:2003), TCVN 6492:2011 (ISO 10523:2008) and TCVN 6185:2008 (ISO 7887:1994), respectively.

III. RESULTS AND DISCUSSION

3.1. Effect of absorbed dose

Table I: The Influence of absorbed dose on the pH, COD, BOD and dye concentration of textile wastewater

Standard column B according to QCVN 13–MT:2015/BTNMT		**Absorbed dose (kGy)**	0	5	10	15	20
pH	**5.5 – 9**	**Sample 1**	8.93 ±0.30	7.56±0.20	7.26±0.15	8.10±0.20	7.34±0.15
		Sample 2	9.46±0.25	8.75±0.30	8.46±0.25	8.3±0.15	8.1±0.20
		Sample 3	9.38±0.20	9.26±0.30	9.19±0.15	8.98±0.25	8.90±0.30
COD (mg/l)	**200**	**Sample 1**	100±2.0	77±1.0	46±2.0	41±1.5	25±1.0
		Sample 2	150±2.0	84±1.5	61±0.5	49±1.5	35±0.5
		Sample 3	260±2.0	174±2.0	136±1.5	101±1.5	82±1.3
BOD (mg/l)	**50**	**Sample 1**	67±1.5	40±1.0	35±1.5	27±1.0	23±1.5
		Sample 2	77±1.5	46±1.0	40±0.5	35±0.5	26±1.0
		Sample 3	90±1.5	68±1.0	57±1.5	45±1.0	38±0.5
[dye] (Pt–Co)	**200**	**Sample 1**	267±2.5	67±1.0	32±0.5	21±1.0	18±0.5
		Sample 2	330±2.0	61±1.5	16±1.0	10±1.0	8±0.5
		Sample 3	451±2.5	288±2.0	215±1.5	138±2.0	98±1.5

To elucidate the effect of absorbed dose on the pH, COD, BOD and dye concentration of textile wastewater, the samples were irradiated with the absorbed dose from 5 to 20 kGy. The results in the table I showed that pH, COD, BOD and dye concentration decreased with increasing absorbed dose for all three samples. The degree of decolorization of sample 1, 2 and 3 increased with increasing absorbed dose. When the absorbed dose was 20 kGy, the degree of decolorization of sample 1, 2 and 3 increased to 93%, 98% and 78%, respectively. A similar result was also obtained by Kim et al. when they applied electron beam raiation technology to enhance the biodegradability of textile wastewater for an activated sludge process [12].

3.2. Effect of H_2O_2 concentration at absorbed dose of 5 kGy

Table II: The Influence of H_2O_2 concentration at absorbed dose of 5 kGy on the pH, COD, BOD and dye concentration of textile wastewater

[H_2O_2] mM		0	5	10	15	20
pH	**Sample 1**	7.56±0.30	6.62±0.25	6.63±0.2	6.68±0.15	6.67±0.10
	Sample 2	8.75±0.20	8.20±0.30	8.00±0.15	7.90±0.30	7.60±0.20
	Sample 3	9.26±0.15	9.00±0.25	8.89±0.30	8.82±0.10	8.75±0.15
COD (mg/l)	**Sample 1**	77±1.5	38±0.10	84±1.6	134±2.0	179±1.5
	Sample 2	84±1.5	55±1.0	61±1.0	76±1.5	114±2.0
	Sample 3	174±2.0	131±1.5	121±1.0	115±1.5	98±1.0
BOD (mg/l)	**Sample 1**	40±1.0	38±1.0	36±1.0	28±1.5	20±1.0
	Sample 2	46±0.6	40±1.0	37±1.5	30±1.0	25±1.5
	Sample 3	68±1.0	61±1.0	58±1.0	52±1.0	49±1.5
[Dye] (Pt–Co)	**Sample 1**	67±1.0	10±1.0	6±1.0	5±1.5	3±1.0
	Sample 2	95±1.0	29±1.0	33±0.5	34±0.6	30±0.5
	Sample 3	288±1.0	212±1.5	210±2.0	200±2.5	196±1.0

Previous studies reported that the presence of H_2O_2 in the solution could lead the formation of hydroxyl radical which contributed the removal efficiency of COD, BOD and dye concentration in wastewater [16, 18]. In order to investigate of the effect of different H_2O_2 concentration from 5 to 20 mM on the characteristics of wastewater was carried out. The results in table II showed that adding small amounts of hydrogen peroxide could improve the radiation capacity for eliminating pollutants in wastewater. The pH, COD, BOD and dye concentration of textile wastewater decreased fast at 5 mM H_2O_2 concentration and absorbed dose of 5 kGy. The degree of decolorization of sample 1, 2 and 3 increased to 96%, 91% and 53%, respectively. The results also indicated that the optimal H_2O_2 concentration was achieved at 5 mM for the sample 1, 2 and 10 mM for the sample 3 at absorbed dose of 5 kGy to achieve standard column B according to QCVN 13–MT:2015/BTNMT for textile wastewater.

3.3. Effect of absorbed dose at the concentration of 10 mM H_2O_2

Table III: The Influence of absorbed dose at the concentration of 10 mM H_2O_2 on the pH, COD, BOD and dye concentration of textile wastewater

Absorbed dose (kGy)		3	6	9	12
pH	**Sample 1**	7.74±0.3	7.09±0.25	6.80±0.15	6.21±0.20
	Sample 2	8.35±0.15	8.00±0.20	7.80±0.25	7.50±0.3
	Sample 3	9.05±0.25	8.95±0.3	8.83±0.15	8.76±0.10

COD (mg/l)	**Sample 1**	106±2.0	66±1.0	44±1.5	30±1.5
	Sample 2	64±1.0	35±1.0	21±0.5	12±0.5
	Sample 3	145±2.0	118±1.5	102±1.5	79±1.0
BOD (mg/l)	**Sample 1**	33±1.0	21±1.5	14±0.5	6±0.5
	Sample 2	41±1.0	29±1.5	20±1.0	14±0.5
	Sample 3	68±1.5	47±1.5	40±1.0	36±1.0
[Dye] (Pt–Co)	**Sample 1**	5±0.5	5±0.5	4±0.5	3±0.5
	Sample 2	45±1.0	31±1.5	18±1.0	6±0.5
	Sample 3	245±2.5	175±2.0	154±2.0	90±1.5

Hydrogen peroxide reacts rapidly with hydrated electron formed in the radiolysis of water, leading to the formation of $^{\bullet}$OH radical. Therefore, the increase in the degree of decoloration, COD and BOD removal percentage by the addition of hydrogen peroxide would be mainly attributed to increase the $^{\bullet}$OH radical. The influence of absorbed dose at the 10 mM H_2O_2 Concentration on the pH, COD, BOD and dye concentration of textile wastewater was carried out and showed in the table III. The results indicated that pH, COD, BOD and dye concentration of textile wastewater decreased with increasing absorbed dose from 3 to 12 kGy at 10 mM H_2O_2 concentration. The optimal absorbed dose achieved at 3 kGy for the sample 1, 2 and 6 kGy for the sample 3 at 10 mM H_2O_2 concentration to achieve standard column B according to QCVN 13–MT:2015/BTNMT for textile wastewater. The same tendency was also obtained by Vahdat et al. when they studied the decoloration of reactive dyes by electron beam irradiation method [10].

IV. CONCLUSIONS

The results presented infer that electron beam treatment is quite efficient for both decoloration and removal of COD and BOD. To achieve standard column B according to QCVN 13–MT:2015/BTNMT the suitable H_2O_2 concentration was achieved at 5 mM and absorbed dose of 5 kGy or 10 mM and absorbed dose of 3 kGy with initial dye concentration from 267 to 330 (Pt-Co), respectively. For the initial dye concentration of 450 (Pt-Co), the suitable H_2O_2 concentration was achieved at 10 mM and absorbed dose of 5 kGy. These results showed that the electron beam radiation technology could be potential and promising method for dye removal from textile wastewater.

ACKNOWLEDGEMENTS:

This research work was supported by the Ministry of Science and Technology, Vietnam under Project No. CS/ The authors are thankful to VINATOM and VINAGAMMA Center for providing necessary conditions during implementation of this project.

REFERENCES

[1] Perng, Y.S., Bui, H.M., “The feasibility of cassia fistula gum with polyaluminium chloride for decolorization of reactive dyeing wastewater”, *J. Serb. Chem. Soc.* 80, 115 –125, 2015.

[2] Kim, H.L., Cho, J.B., Park, Y.J., Cho, I.H., “Treatment and to xicity reduction of textile dyeing wastewater using the electrocoagulation -electroflotation process”, *J. Environ. Sci. Health.* A 51, 661–668, 2016.

[3] Salleh, M.A.M., Mahmoud, D.K., Karim, W.A.W.A., Idris, A., "Cationic and anionic dye adsorption by agricultural solid wast es: A comprehensive review", *Desalination* 280, 1–13, 2011.

[4] Teh, C.Y., Budiman, P.M., Shak, K.P.Y., Wu, T.Y., "Recent Advancem ent of Coagulation–Flocculation and Its Application in Wastewater Treatment", *Ind. Eng. Chem. Res.* 55, 4363–4389, 2016.

[5] Pocedič, J., Hasal, P., Novotný, Č., "Decolorization of organic dyes by I rpex lacteus in a laboratory trickle -bed biofilter using various mycelium supports", *J. Chem. Technol. Biotechnol.* 84, 1031–1042, 2009.

[6] Alinsafi, A., Khemis, M., Pons, M.N., Leclerc, J.P., Yaacoubi, A., Benhammou, A., Nejmeddine, A., "Electro-coagulation of reactive textile dyes and textile wastewater", *Chem. Eng. Process.* 44, 461–470, 2005.

[7] Kim, T.H., Park, C., Kim, S., "Water recycling from desalination and purification process of reactive dye manufacturing industry by combined membrane filtration", *J. Clean. Prod.* 13, 779–786.

[8] Lee, J.W., Choi, S.P., Thiruvenkatachari, R., Shim, W.G., Moon, H., "Submerged microfiltration membrane coupled with alum coagulation/powdered activated carbon adsorption for complete decolorization of reactive dyes", *Water Res.* 40, 435 –444, 2006.

[9] LaVerne, J.A., "OH radicals and oxidizing products in the gamma radiolysis of water", *Radiat. Res.* 153, 196–200, 2000.

[10] Vahdat, A.,Bahrami, S.H., Arami, M., Bahjat, J., Tabakh, F., Khairkhah, M., "Decoloration and mineralization of reactive dyes using electron beamirradiation, Part I: Effect of the dye structure, concentration and absorbed dose (single, binary and ternary systems)", *Radiat. Phys. Chem.* 81, 851-856, 2012.

[11] Zhang, S.J., Yu, H.Q.,Li, Q.R., "Radiolytic degradation of Acid Orange 7: A mechanistic study", *Chemosphere*, 61, 1003-1011, 2005.

[12] Kim, T, H., Lee, J.K., Lee, M.J., "Biodegradability enhancement of textile wastewater by electron beam irradiation", *Radiat. Phys. Chem.* 76, 1037-1041, 2007.

[13] Paul, J., Rawat, K.P., Sarma, K.S.S., Sabharwal S., "Decoloration and degradation of Reactive Red-120 dye by electron beam irradiation in aqueous solution", *Appl. Radiat. Isotopes.* 69, 982-987, 2011.

[14] He, S., Sun, W., Wang, J.L., Chen, L., Zhang, Y., Yu, J., "Enhancement of biodegradability of real textile and dyeing wastewater by electron beam irradiation", *Radiat. Phys. Chem.* 124, 203-207, 2016.

[15] Sánchez-Polo, M., López-Peñalver, J., Prados-Joya, G., Ferro-García, M.A., RiveraUtrilla, J., "Gamma irradiation of pharmaceutical compounds, nitroimidazoles, as a new alternative for water treatment", *Water Res.* 43, 4028 –4036, 2009.

[16] Yulin, X., Weijiang, Z., Hao, Z., "Synergetic decolorization and deodorization of sludge protein foaming solution by ^{60}Co γ-ray irradiation/H_2O_2 oxidation", *Process Saf. Environ. Prot.* 88, 285–291, 2010.

[17] Getoff, N., "Factors influencing the efficiency of radiation -induced degradation of water pollutants", *Radiat. Phys. Chem.* 65, 437–446, 2002.

[18] Jung, J., Yoon, J.-H., Chung, H.-H., Lee, M.-J., "Comparative study of H_2O_2 and O_3 effects on radiation treatment of TCE and PCE", *Chemosphere* 51, 881 –885, 2003.

[19] ASTM International, "Standard practice for use of a dichromate dosimetry system. ISO/ASTM 51401: 2003(E)", Standards on dosimetry for radiation processing, pp. 69 –75, 2004.

1.5- Applications in Ecology, Environment and Geology

USING NATURAL RADIUM ISOTOPES TO DETERMINE DIFFUSION COEFFICIENT AND RESIDENCE TIME OF COASTAL WATER AT LOCATION FOR THE NINH THUAN I NPP

Nguyen Van Phuc, Phan Son Hai, Nguyen Thi Huong Lan, Vo Thi Mong Tham,
Phan Quang Trung, Nguyen Minh Dao and Le Xuan Thang

Dalat Nuclear Research Institute
01 Nguyen Tu Luc Street, Dalat, Lam Dong province

Project information:

- **Code:** DTCB.06/17/VNCHN
- **Managerial Level:** Ministry
- **Allocated Fund:** 850,000,000 VND
- **Implementation time:** 24 months (Jan 2017- Dec 2018)
- **Contact email:** plnn08@yahoo.com
- **Paper published in related to the project:**

- Vo Thi Mong Tham, Phan Son Hai, Nguyen Van Phuc, Nguyen Minh Dao, Phan Quang Trung, Le Xuan Thang, Nguyen Thi HuongLan, 2017. Using a delayed coincidence counting system to determine ^{223}Ra and ^{224}Ra in seawater samples, *Nuclear Science and Technology (Accepted).*
- Vo Thi Mong Tham, Phan Son Hai, Nguyen Van Phuc, Nguyen Minh Dao, Phan Quang Trung, Le Xuan Thang, Nguyen Thi Huong Lan. Efficiency calibration of radium delayed coincidence counter for ^{223}Ra and ^{224}Ra analysis in seawater samples, *The Twelfth National Conference on Nuclear Science and Technology*, Nha Trang, 2–4 August, 2017 (in Vietnamese).

Abstract: For the purpose of using radium isotopes as tracers for estimating diffusion coefficient and residence time of coastal water in Vietnam, after two years (2015-2016) of implementing the Project entitled:"Research on the use of natural radium radionuclides as tracers for determination of diffusion coefficient and residence time of coastal water" *(Phan Son Hai, et al., 2016)* the research team has manufactured a delayed coincidence alpha counting system for ^{223}Ra and ^{224}Ra radioactivity concentrations determination. This system has a counting efficiency of (26±2)% and operates stably and reliably. Also during this time, *acrylic fibers impregnated* with manganese *dioxide* used to extract radium from sea water have been made with a maximum adsoption capacity of …Bq Ra/g. A procedure for in-situ separation of radium from seawater using manganese fiber were also established. A procedure of measuring short lived radium isotopes was established for the delayed coincidence alpha counting system. The detection limit of the counting system was estimated as low as 0.002 Bq for ^{223}Ra and 0.01 Bq for ^{224}Ra. The accuracy of the procedure was not exceeded ±..% compared with the certified value and its repeatability was within ±...% of the mean value. This technique is quite applicable for the quantification of ^{223}Ra and ^{224}Ra activity in sea water samples at low concentration.

With the facility made and procedures established the research team has determined diffusion coefficient and residence time of coastal water in the area of the Ninh Thuan I PPN. In the rainy season, the diffusion coefficient is in a range of 222 - 287 m^2/s and the residence time is 19 - 23 days within a distance of 30 km from the coast. In the dry season, the diffusion coefficient is 233 - 361 m^2/s and the residence time is 14 - 22 days.

The results of this study opened up the possibility of using radium isotopes to assess diffusion coefficient and residence time of wastes entering the marine environment. This is very essential for assessing the environmental impact of industrial facilities along the marine coast of Vietnam.

Keywords: *Diffusion coefficient, residence time, coastal waters.*

I. INTRODUCTION

Coastal water receives many forms of materials from the mainland through rivers, groundwater, and industrial facilities. After entering the coastal water body, the materials are mixed, and then diluted with offshore waters.They exist in coastal water for a certain period of time which is called residence time. Exchange of material between the continental margin and ocean interior plays a major role in global biogeochemical cycles. Material fluxes through the coastal ocean are difficult to quantify because these systems are exceedingly complex due to small-scale temporal and spatial variability. Chemical tracers offer promise but a few techniques respond requirement for this complex region. To quantify fluxes of dissolved components across the continental shelf, new methods based on four Ra isotopes are used *(Willard S.Moore, 2000).*Radium isotopes have been applied to study residence time of coastal water, the mixing factors of coastal water with ocean *(Bourquin, M. et al., 2008; Beek P. van et al., 2008; Moore W.S. et al., 2008; Rapaglia J. et al., 2010; Souza T.A. et al., 2010; HequanGu et al., 2012)*. The information about the exchange rate between coastal waters and offshore waters and the residence time of coastal seawater are really significant for many research files related to the marine environment.

Industrial facilities discharge liquid waste directly into the marine environment, the information on the residence time, the diffusion coefficient of the coastal waters at waste receiving area should be known to calculate maximum allowable waste. Currently, along the marine coast of our country, many industrial facilities have been built. The assessment of diffusion coefficient and residence time of coastal waters is necessary as a basis to assess the environmental impact of industrial facilities on the marine environment.

The goal of this study was to determine the diffusion coefficient and residence time of coastal water in the area of the Ninh Thuan I NPP based on the results of the Project implemented during the 2017-2018 period.

II. METHODS OF STUDY

2.1. Determination of diffusion coefficient (K_h) and residence time of coastal waters using natural Ra isotopes

2.1.1. Determination of diffusion coefficient (K_h)

Moore (2000a) used the distribution of the short-lived Ra isotopes to estimate exchange rates in the coastal ocean. The change in concentration or activity (A) with time (t) as a function of distance offshore (x) for a radioactive tracer with the decay constant (λ) may be expressed as a balance of diffusion, advection, and decay, as follows:

$$\frac{dA}{dt} = K_h \frac{\partial^2 A}{\partial x^2} - \omega \frac{\partial A}{\partial x} - \lambda A \qquad (1)$$

Where A: radium activity concentration (dpm/L); x: distance offshore (m); λ: radioactive decay constant (1/s); K_h: eddy diffusion coefficient (m^2/s); ω: advection velocity (m/s).

If net advection can be neglected (i.e *ω =0)*, this reduces to

$$\frac{dA}{dt} = K_h \frac{\partial^2 A}{\partial x^2} - \lambda A \qquad (2)$$

The criterion for setting $\omega = 0$ is based on the offshore distribution of conservative tracers such as ^{226}Ra (half-life =1,600 yr) and ^{228}Ra (half-life = 5.7 yr). These long-lived isotopes decay little during the residence time of coastal water A constant offshore concentration gradient of these tracers provides evidence that diffusion dominates offshore or onshore advection (Moore, 2000a,b). In the case where $\omega = 0$, the boundary conditions of Eq. (2) are as follows:

$A = A_0$ at $x = 0$; $A \to 0$ as $x \to \infty$; If K_h is constant and the system is in steady state the the solution of (2) is:

$$A_x = A_0 exp\left[-x * \sqrt{\frac{\lambda}{K_h}}\right] \tag{3}$$

Where A_x is activity at distance x from the coast, A_0 is activity at distance 0 from the coast and λ *is* decay constant.

A plot of ln (^{223}Ra) or ln (^{224}Ra) as the function of distance from the coast may be used to estimate K_h if the exchange is dominated by eddy diffusion rather than advection and if the system is at steady state:

$$lnA_x = lnA_0 - x * \sqrt{\frac{\lambda}{K_h}} \tag{4}$$

In this case the slope $m = -\sqrt{\frac{\lambda}{K_h}}$

This model requires that the system is at steady state over the time scale of the short-lived isotopes and that there are no additions of these isotopes beyond the near shore zone.

2.1.2. Determination of residence time of the coastal waters.

Using the equation in studies of molecular diffusion to large-scale dispersion in the ocean, we can estimate the residence time of the coastal water *(Chris Garrett, 2006; Philip J. W. Roberts and Donald R. Webster, year of publication?)* from ^{224}Ra or ^{223}Ra as follows:

$$x = \sqrt{2K_h t} \tag{5}$$

Where x is the distance from the coast (m); K_h is the diffusion coefficient (m^2/s)

t is the residence time of the coastal waters (day).

An alternate way to use the short-lived Ra isotopes is to utilize the ^{224}Ra/^{223}Ra activity ratio (AR) to estimate the residence time of the coastal waters (Moore, 2000b). This method is based on the assumptions that the ^{224}Ra/^{223}Ra AR is initialized to a constant value near shore and only changes by decay as the water is isolated from the radium source. The ^{224}Ra/^{223}Ra AR decreases with an apparent half-life of 5.4 days, as follows:

$$\left(\frac{^{224}Ra}{^{223}Ra}\right)_{obs} = \left(\frac{^{224}Ra}{^{223}Ra}\right)_i \frac{e^{-\lambda_{224} t}}{e^{-\lambda_{223} t}} \tag{6}$$

where: $(^{224}Ra/^{223}Ra)_i$ is activity ratio near shore; $(^{224}Ra/^{223}Ra)_{obs}$ is the activity ratio at the distance x; λ_{223} and λ_{224} are decay constants of ^{223}Ra and ^{224}Ra, respectively.

2.2. Determination of activity concentration of natural Ra isotopes (^{223}Ra, ^{224}Ra, ^{226}Ra, ^{228}Ra) in seawater samples

2.2.1. Calibration of alpha delayed coincidence counting system for analyzing ^{223}Ra and ^{224}Ra

a) Alpha delayed coincidence counting (RaDeCC) system

A cylinder chamber was made of plexiglass with a volume of 1.6 L. The inner surface was covered with a 250µm thick ZnS(Ag) scintillator (EJ-440, ELJEN TECHNOLOGY). The photomultiplier tube is the R877-01 type of Hamamatsu. The chamber was connected to a counter consisting of 3 counting channels, one of which is for counting total activity and the two other are delayed coincidence channels for analysis of ^{223}Ra and ^{224}Ra. A radon pumping system includes an Air Cadet pump linked to a flow rate meter, the cartridge filled with Mn-fiber and the chamber. The pump can maintain closed circulation with the flow rate of 0,5 - 10 L/min inside the system.

- *Background:* Background count rates for ^{223}Rn and ^{224}Rn channels were (0.01 ± 0.001) cpm and (0.13 ± 0.05) cpm, respectively.

- *Efficiency:* Mean counting efficiencies (%) at ^{223}Rn and ^{224}Rn channels were (26.6 ± 2.0) and (26.0 ± 2.3), respectively.

b) Assessing the efficiency of the RaDeCC system

The efficiency of the RaDeCC system was determined by using ^{223}Ra and ^{224}Ra standard sources. The ^{223}Ra standard source was prepared from a ^{227}Ac standard solution (14.241 Bq/L) supplied by Eckert & Ziegler Analytics and ^{224}Ra was prepared by digesting standard Thorium ore No. AMD/Phy/Std-7/76 with the ThO_2 content of (0.360 ± 0.003)%.

2.2.2. Analytical method for ^{223}Ra and ^{224}Ra in seawater samples determination on the RaDeCC system

- *Sample preparation:* 300 L of seawater was pumped through a cartridge filled with 35 g of Mn-fiber at a flow-rate of 2 ÷ 3 L/min. Then 10 L of deionized water was continuously pumped through this cartridge at the same flow-rate to remove salt. The fiber in the cartridge was dried by air flow until the ratio of moisture to dry weight of Mn-fiber was about 50 ÷ 80%. Two valves of the cartridge were closed tightly for Radon to grow inside the cartridge and attain radioactive equilibrium with Ra.

- *Measurement:* The sample was counted twice in 4 hours each. The first measurement and the second one were conducted, respectively, within 1-3 days and 7-17 days since the radon confinement,.

- *Calculation of activity:* ^{223}Ra and ^{224}Ra activities were calculated based on ^{219}Rn and ^{220}Rn net count rates of samples and those of standard that were corrected for chance coincidence events as well as reciprocal interferences between ^{219}Rn and ^{220}Rn channels.

- *Limit of detection:* Based on background count rates and standard sample count rates, limit of detection were estimated to be 0.002 Bq for ^{223}Ra and 0.01 Bq for ^{224}Ra.

- *Accuracy of the method:* Analyzing standard samples showed that analytical values and certified values agreed to each other in a maximum deviation of 3.5%.

- *Repeatability of the method:* Repeated analysis of standard samples showed that all analytical values were within 95% confidence level of certified value.

2.2.3. Analytical method for ^{226}Ra and ^{228}Ra in seawater samples determination on HPGe3019 gamma spectrometer

- *Standard preparation:* ^{226}Ra standards were prepared from ^{226}Ra standard solution with a specific activity of 785 mBq/g. ^{228}Ra standards were prepared from the standard thorium ore No. AMD/Phy/Std-7/76 with the ThO_2 content of (0.360 ± 0.003)%.

- *Sample preparation:* After measurements on RaDeCC, the sample was ash at 500^0C for 8 hours. The ash was pressed in disk geometry of 70 mm i.d. and 5 mm thick, closely covered with an aluminum foil and sealed by silicone gel.

- *Measurement:* Standards and samples were stored at least 21 days and then counted on low background gamma spectrometers for 48 hours. - *Calculation of activity:*The ^{226}Ra activity was determined by weighted averaging over individual activities which were derived from peaks 295 keV, 352 keV, and 609 keV. Similarly, the ^{228}Ra activity was calculated through ^{228}Ac by weighted averaging over single values which were inferred from the intensity of 338 keV, 911 keV, and 969 keV peaks.

- *Limit of detection:* Based on background count rates, limit of detection was estimated to be 0.05 Bq for ^{226}Ra, and 0.1 Bq for ^{228}Ra.

- *The accuracy of the method:* Analysis of standard samples showed that measured values agreed with the certified value with a deviation within ±...%.

- *Repeatability of the method:* Repeated analysis of standard samples showed that all analytical values were within 95% confidence level of the certified value.

2.2.4. Producing manganese oxide impregnated acrylic fiber

50 g of acrylic fiber was soaked in 1L of 0.3 M $KMnO_4$ solution for 12 hours at 50-80^{o}C. After the fiber had turned black, it was removed and rinsed well with deionized water to remove excess $KMnO_4$ as well as MnO_2 that did not attach firmly to the fiber. The fiber then was dried completely in an oven at 50^0C for 48 hours.

2.2.5. Determination of the radium recovery yield of Mn-fiber

^{133}Ba tracer is used to study the adsorption capacity of Mn-fiber at laboratory conditions. An amount of tracer ^{133}Ba with the specific activity of 44.879 Bq/gram was blent with sea water. This solution was passed through 2 grams of the Mn-fiber and each volume of 0.5 L solution was collected over time and then counted on gamma spectrometers to determine the ^{133}Ba activity in the solution. Based on these data, the amount of ^{133}Ba adsorbed on the Mn-fiber was determined.

Data obtained from the experiments using ^{133}Ba tracer showed that 2 grams of Mn-fiber completely adsorbed radium in 16 lites of seawater.

2.2.6. Seawater sampling for assessing diffusion coefficient and residence time of coastal water in the Phuoc Dinh (Ninh Thuan) site

The study area selected for this research was a sea area of Phuoc Dinh commune, Ninh Thuan province (NinhThuan I). The selected site has an area of about 750 km^2. Seawater samples were collected on five shore-perpendicular transects from the coastline towards offshore. Each transect was about 30 km long. The transects were 5 km apart from each other and each sample on each transect was1.5 ÷ 6 km apart from each other (Fig.2.1). The depth of sea level at the study site was also surveyed along the transects by echo-sounding technique. Total 105 seawater samples were collected in May 2017, September 2017 and May 2018. The samples were pumped from 2-3 m below the surface. The temperature, pH, and salinity of seawater were measured. Radium in seawater was concentrated by pumping 300 L of seawater through a cartridge filled with 35 g of the Mn-fiber at a flow rate of 2 ÷ 3 L/min. After that, 5 ÷ 10 L of deionized water were passed through the cartridge at the same flow rate to remove salt on the fiber. The cartridge was then dried by air flow until the ratio of moisture to dry weight fiber reaching 50 ÷ 80%. Short-lived ^{223}Ra and ^{224}Ra nuclides were measured using the RaDeCC. Long-lived nuclides ^{226}Ra and ^{228}Ra were analyzed by gamma spectrometer.

Figure 2.1: Sampling points on five shore-perpendicular transects

III. RESULTS AND DISCUSSION

3.1. Temporal and spatial distribution of ^{223}Ra, ^{224}Ra, ^{226}Ra, ^{228}Ra isotopes

Profiles distance - Ra activities (dpm/L) in surface waters on five transects are presented in Table 3.1.

Table 3.1: Profiles distance - Ra activities in surface waters

Sample	Distance (km)	^{223}Ra		^{224}Ra		^{226}Ra		^{228}Ra	
		Activity (dpm/L)	Unc.	Activity (dpm/L))	Unc.	Activity (dpm/L))	Unc.	Activity (dpm/L)	Unc.
The transect No.1 (5/2017)									
PDC1	1,4	0,0254	0,0018	0,0374	0,0019	0,080	0,009	0,244	0,043
PDC2	4,4	0,0097	0,0006	0,0177	0,0010	0,087	0,009	0,229	0,030
PDC3	7,4	0,0115	0,0010	0,0246	0,0017	0,076	0,008	0,187	0,026
PDC4	10,4	0,0100	0,0008	0,0346	0,0030	0,078	0,012	0,227	0,033
PDC5	13,4	0,0220	0,0009	0,0209	0,0014	0,051	0,007	0,212	0,026
PDC6	16,4	0,0177	0,0008	0,0202	0,0012	0,031	0,005	0,213	0,027
PDC7	19,4	0,0117	0,0004	0,0188	0,0012	0,038	0,006	0,210	0,026
PDC8	22,4	0,0111	0,0009	0,0081	0,0005	0,068	0,007	0,213	0,029
PDC9	25,4	0,0121	0,0013	0,0112	0,0005	0,017	0,003	0,171	0,031
PDC10	28,4	0,0067	0,0005	0,0152	0,0007	0,074	0,008	0,204	0,031

The transect No.2 (5/2017)									
PDB1	1,4	0,0169	0,0013	0,0491	0,0018	0,091	0,014	0,227	0,030
PDB2	4,4	0,0105	0,0007	0,0255	0,0014	0,073	0,010	0,189	0,033
PDB3	7,4	0,0130	0,0011	0,0111	0,0007	0,079	0,007	0,192	0,026
PDB4	10,4	0,0080	0,0006	0,0156	0,0017	0,086	0,011	0,197	0,024
PDB5	13,4	0,0083	0,0008	0,0178	0,0007	0,076	0,010	0,195	0,027
PDB6	16,4	0,0247	0,0008	0,0147	0,0007	0,093	0,008	0,191	0,026
PDB7	19,4	0,0175	0,0006	0,0138	0,0014	0,079	0,007	0,188	0,024
PDB8	22,4	0,0162	0,0011	0,0207	0,0013	0,066	0,009	0,171	0,029
PDB9	25,4	0,0180	0,0007	0,0114	0,0012	0,087	0,013	0,189	0,037
PDB10	28,4	0,0478	0,0050	0,0109	0,0004	0,109	0,011	0,174	0,034
The transect No.3 (5/2017)									
PDB11	1,4	0,0154	0,0015	0,0421	0,0034	0,068	0,009	0,191	0,041
PDB12	4,4	0,0139	0,0006	0,0349	0,0014	0,054	0,006	0,192	0,034
PDB13	5,9	0,0076	0,0008	0,0252	0,0021	0,066	0,012	0,181	0,034
PDB14	7,4	0,0096	0,0005	0,0224	0,0007	0,066	0,009	0,192	0,026
PDB15	8,9	0,0127	0,0005	0,0173	0,0007	0,116	0,023	0,208	0,028
PDB16	10,4	0,0114	0,0011	0,0131	0,0017	0,081	0,011	0,205	0,029
PDB17	11,9	0,0077	0,0003	0,0124	0,0007	0,100	0,011	0,211	0,034
PDB18	16,4	0,0146	0,0013	0,0111	0,0005	0,074	0,008	0,186	0,029
PDB19	19,4	0,0112	0,0014	0,0168	0,0006	0,069	0,011	0,186	0,030
PDB20	22,4	0,0152	0,0009	0,0196	0,0009	0,072	0,007	0,182	0,023
The transect No.4 (5/2017)									
PDC21	1,4	0,0125	0,0006	0,0575	0,0028	0,045	0,005	0,208	0,034
PDC22	4,4	0,0106	0,0008	0,0436	0,0013	0,031	0,005	0,210	0,037
PDC23	7,4	0,0087	0,0006	0,0205	0,0010	0,125	0,015	0,179	0,024

PDC27	10,4	0,0076	0,0004	0,0213	0,0013	0,127	0,011	0,179	0,029
PDC25	13,4	0,0160	0,0011	0,0161	0,0007	0,157	0,021	0,179	0,034
PDC28	16,4	0,0199	0,0008	0,0248	0,0009	0,195	0,012	0,187	0,021
PDC24	19,4	0,0116	0,0005	0,0141	0,0008	0,145	0,011	0,182	0,028
PDC26	22,4	0,0180	0,0007	0,0233	0,0018	0,101	0,013	0,172	0,016
PDC29	25,4	0,0181	0,0005	0,0237	0,0009	0,150	0,017	0,154	0,024
PDC30	28,4	0,0194	0,0008	0,0310	0,0014	0,106	0,007	0,173	0,030
The transect No.5 (5/2017)									
PDC11	1,4	0,0103	0,0007	0,0493	0,0041	0,071	0,009	0,195	0,026
PDC12	4,4	0,0081	0,0007	0,0289	0,0019	0,042	0,007	0,165	0,028
PDC13	7,4	0,0069	0,0007	0,0172	0,0006	0,041	0,005	0,174	0,028
PDC14	10,4	0,0129	0,0005	0,0229	0,0009	0,063	0,006	0,164	0,028
PDC15	13,4	0,0184	0,0013	0,0147	0,0006	0,043	0,005	0,161	0,027
PDC16	16,4	0,0161	0,0015	0,0194	0,0008	0,220	0,019	0,183	0,036
PDC17	19,4	0,0074	0,0008	0,0183	0,0006	0,045	0,007	0,177	0,026
PDC18	22,4	0,0111	0,0007	0,0277	0,0012	0,065	0,009	0,175	0,027
PDC19	25,4	0,0204	0,0003	0,0271	0,0009	0,166	0,021	0,168	0,022
PDC20	28,4	0,0138	0,0004	0,0226	0,0006	0,118	0,010	0,163	0,033
The transect No.1 (9/2017)									
PDC42	1,4	0,0284	0,0009	0,0666	0,0046	0,298	0,032	0,215	0,029
PDC43	4,4	0,0189	0,0005	0,0496	0,0023	0,261	0,023	0,190	0,027
PDC44	10,4	0,0295	0,0013	0,0466	0,0025	0,439	0,048	0,170	0,029
PDC45	16,4	0,0118	0,0012	0,0366	0,0023	0,331	0,026	0,188	0,019
PDC46	22,4	0,0074	0,0002	0,0225	0,0024	0,274	0,029	0,171	0,019
PDC47	28,4	0,0103	0,0018	0,0210	0,0014	0,207	0,028	0,187	0,035

The transect No.2 (9/2017)									
PDC41	1,4	0,0135	0,0007	0,0685	0,0060	0,262	0,035	0,178	0,027
PDC40	7,4	0,0128	0,0022	0,0413	0,0019	0,380	0,034	0,182	0,019
PDC39	13,4	0,0058	0,0002	0,0345	0,0014	0,078	0,007	0,182	0,023
PDC38	19,4	0,0092	0,0004	0,0124	0,0010	0,055	0,007	0,192	0,032
PDC37	25,4	0,0131	0,0007	0,0116	0,0008	0,189	0,030	0,193	0,031
The transect No.3 (9/2017)									
PDC31	1,4	0,0488	0,0024	0,0617	0,0034	0,144	0,015	0,155	0,024
PDC32	4,4	0,0367	0,0024	0,0238	0,0018	0,156	0,022	0,157	0,024
PDC33	10,4	0,0230	0,0003	0,0510	0,0024	0,058	0,006	0,153	0,019
PDC34	16,4	0,0245	0,0011	0,0216	0,0017	0,062	0,006	0,147	0,022
PDC35	22,4	0,0234	0,0005	0,0133	0,0008	0,121	0,013	0,171	0,018
PDC36	28,4	0,0105	0,0007	0,0108	0,0007	0,095	0,011	0,144	0,023
The transect No.4 (9/2017)									
PDC48	1,4	0,0102	0,0023	0,0558	0,0024	0,239	0,021	0,175	0,030
PDC57	7,4	0,0126	0,0013	0,0844	0,0056	0,152	0,018	0,215	0,036
PDC56	13,4	0,0135	0,0008	0,0886	0,0042	0,183	0,025	0,252	0,039
PDC55	19,4	0,0139	0,0047	0,1087	0,0056	0,234	0,030	0,321	0,038
PDC54	25,4	0,0141	0,0007	0,0684	0,0042	0,217	0,023	0,383	0,041
The transect No.5 (9/2017)									
PDC49	4,4	0,0288	0,0022	0,1562	0,0086	0,194	0,022	0,288	0,034
PDC50	10,4	0,0262	0,0038	0,1282	0,0057	0,153	0,013	0,346	0,036
PDC51	16,4	0,0180	0,0015	0,1031	0,0056	0,194	0,019	0,365	0,061
PDC52	22,4	0,0197	0,0020	0,0329	0,0029	0,245	0,035	0,319	0,035
PDC53	28,4	0,0059	0,0009	0,0205	0,0016	0,199	0,027	0,363	0,051

The transect No.1 (5/2018)									
PD9	1,4	0,0129	0,0017	0,0333	0,0014	-	-	-	-
PD8	4,4	0,0203	0,0005	0,0400	0,0016	-	-	-	-
PD7	10,4	0,0138	0,0004	0,0115	0,0007	-	-	-	-
PD6	16,4	0,0053	0,0005	0,0116	0,0010	-	-	-	-
PD5	22,4	0,0183	0,0015	0,0090	0,0004	-	-	-	-
The transect No.2 (5/2018)									
PD34	0,3	0,0232	0,0025	0,0486	0,0026	-	-	-	-
PD10	1,4	0,0189	0,0008	0,0463	0,0020	-	-	-	-
PD1	7,4	0,0137	0,0008	0,0190	0,0009	-	-	-	-
PD2	13,4	0,0127	0,0006	0,0160	0,0007	-	-	-	-
PD3	19,4	0,0157	0,0006	0,0203	0,0009	-	-	-	-
PD4	25,4	0,0126	0,0004	0,0153	0,0006	-	-	-	-
The transect No.3 (5/2018)									
PD18	0,2	0,0157	0,0008	0,0719	0,0062	-	-	-	-
PD17	4,4	0,0120	0,0012	0,0655	0,0028	-	-	-	-
PD14	10,4	0,0144	0,0012	0,0284	0,0018	-	-	-	-
PD13	16,4	0,0115	0,0019	0,0136	0,0007	-	-	-	-
PD12	22,4	0,0044	0,0014	0,0131	0,0006	-	-	-	-
PD11	28,4	0,0093	0,0006	0,0118	0,0006	-	-	-	-
The transect No.4 (5/2018)									
PD33	0,2	0,0017	0,0006	0,0478	0,0042	-	-	-	-
PD19	1,4	0,0131	0,0011	0,0212	0,0013	-	-	-	-
PD27	7,4	0,0136	0,0020	0,0155	0,0015	-	-	-	-
PD26	13,4	0,0037	0,0005	0,0084	0,0006	-	-	-	-
PD25	19,4	0,0136	0,0014	0,0066	0,0005	-	-	-	-

PD24	25,4	0,0191	0,0016	0,0023	0,0002	-	-	-	-
The transect No.5 (5/2018)									
PD20	4,4	0,0156	0,0016	0,0482	0,0024	-	-	-	-
PD21	10,4	0,0109	0,0011	0,0063	0,0007	-	-	-	-
PD22	16,4	0,0086	0,0007	0,0198	0,0016	-	-	-	-
PD23	22,4	0,0038	0,0006	0,0101	0,0010	-	-	-	-

The activity concentrations of ^{226}Ra, ^{228}Ra, ^{224}Ra and ^{223}Ra in the dry (May) and rainy (Sep) seasons as functions of distance offshore for each transect are shown in Figs.3.1 to 3.10..

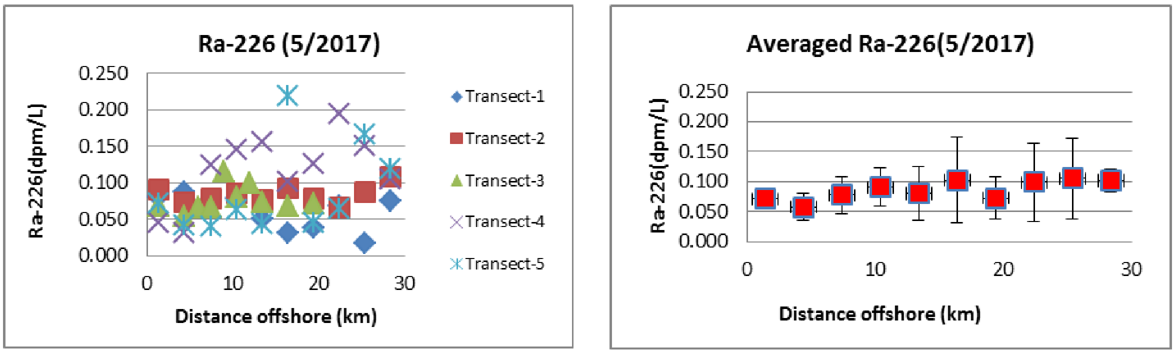

a b

Figure 3.1: The activity concentration (AC) of ^{226}Ra as a function of distance offshore for each transect (a) and average AC of ^{226}Ra for all transects (b) (in dry season, May 2017)

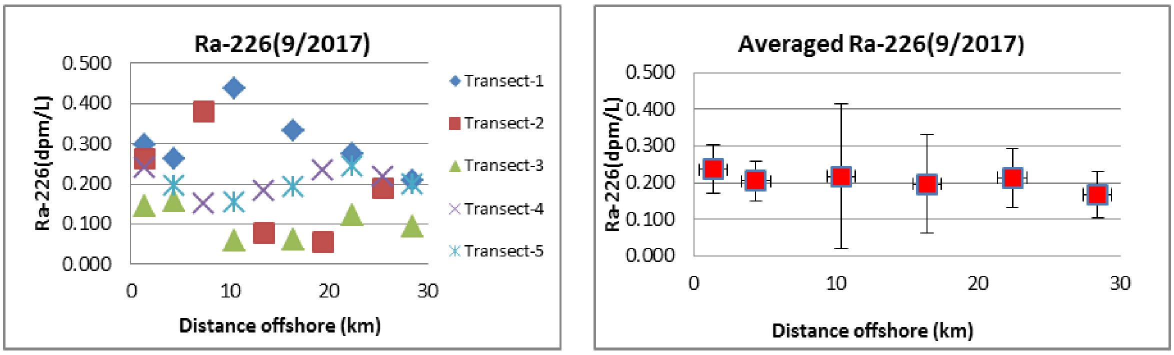

Figure 3.2: The activity of ^{226}Ra as a function of distance offshore for each transect (in rainy season, September 2017)

As seen from Fig. 3.1 and 3.2 the averaged ^{226}Ra activities were almost constant for all the transects. However, the ^{226}Ra activity varies significantly at various distances from 15 km to 25 km offshore in the dry season (Fig.3.1) and from 10 km to 20 km offshore in the rainy season (Fig. 3.2).

The activity of ^{228}Ra as a function of distance offshore for each transect (in May 2017) is shown Fig.3.3. Averaged ^{228}Ra activities reach a relatively constant value.

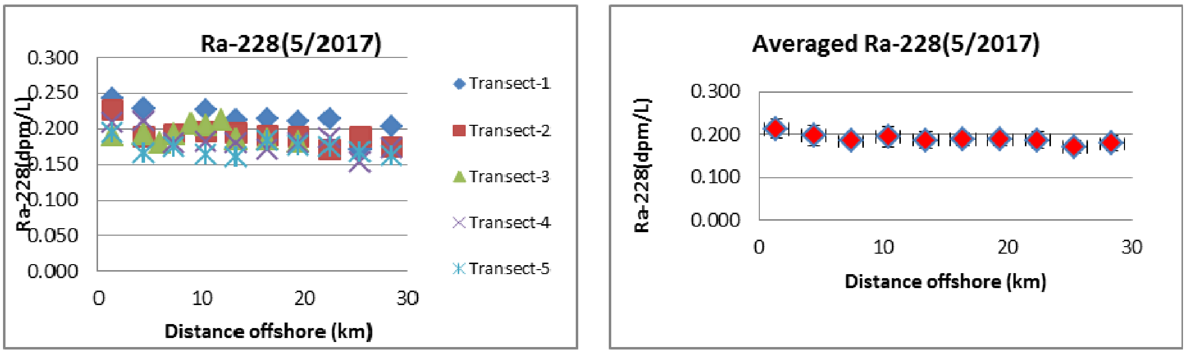

Figure 3.3: The activity of ^{228}Ra as a function of distance offshore for each transect (in May 2017)

The activity of ^{228}Ra as a function of distance offshore for each transect (in September 2017) is shown Fig.3.4. Averaged ^{228}Ra activities reach a relatively constant value. However, ^{228}Ra varies significantly at various distances from 10 km to 30 km offshore.

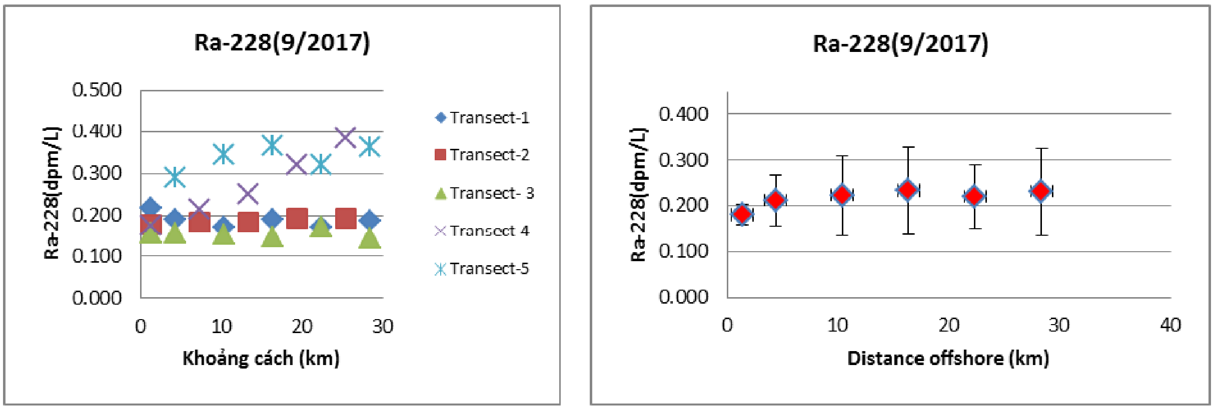

Figure 3.4: The activity of ^{228}Ra as a function of distance offshore for each transect (in September 2017)

As seen from Fig. 3.3 and 3.4 the averaged ^{228}Ra AC were almost constant for all the transects. However, the ^{228}Ra activity concentration varies significantly at various distances from 10 km to 30 km offshore in both dry and rainy season (Fig.3.3, 3.4).

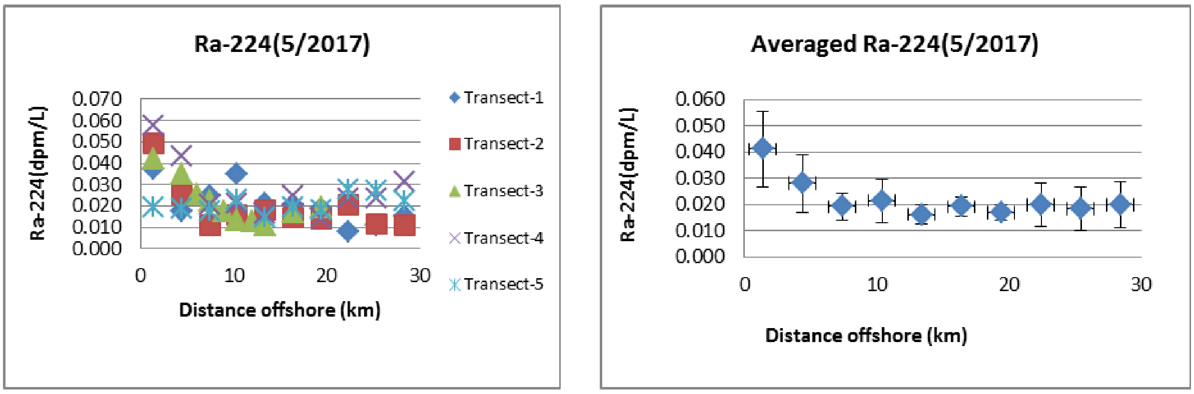

Figure 3.5: The activity of ^{224}Ra as a function of distance offshore for each transect (in May 2017)

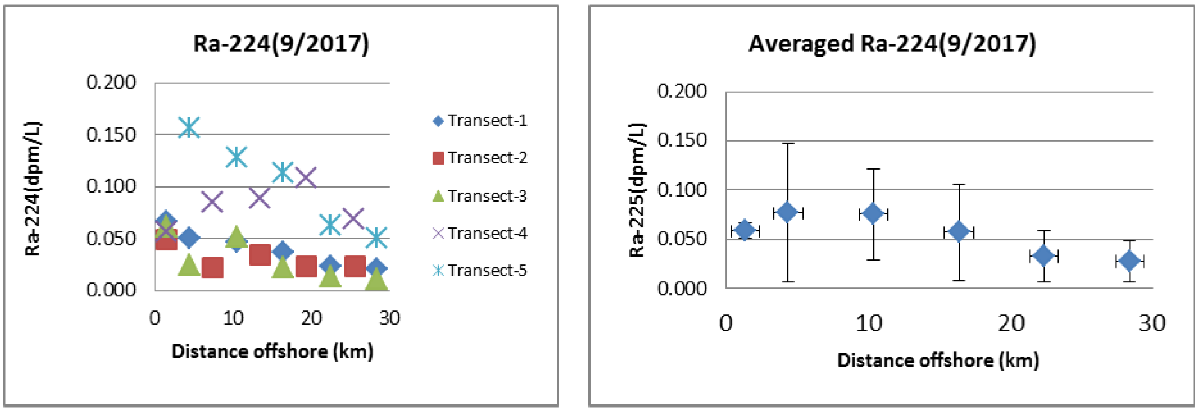

Figure 3.6: The activity of ^{224}Ra as a function of distance offshore for each transect (in September 2017)

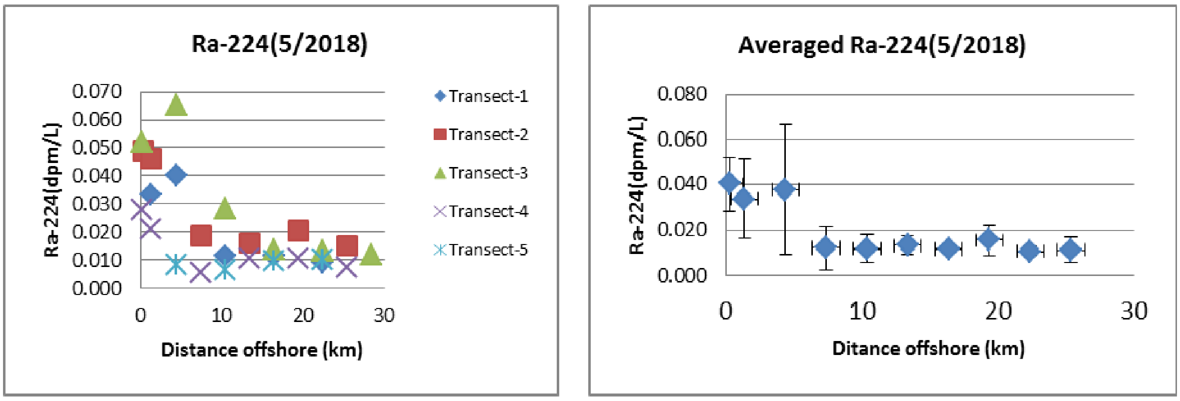

Figure 3.7: The activity of ^{224}Ra as a function of distance offshore for each transect (in May 2018)

As seen from Fig 3.5, 3.6 and 3.7 the averaged ^{224}Ra activity concentration decreases with increasing distance from the coast in both the dry and rainy seasons..

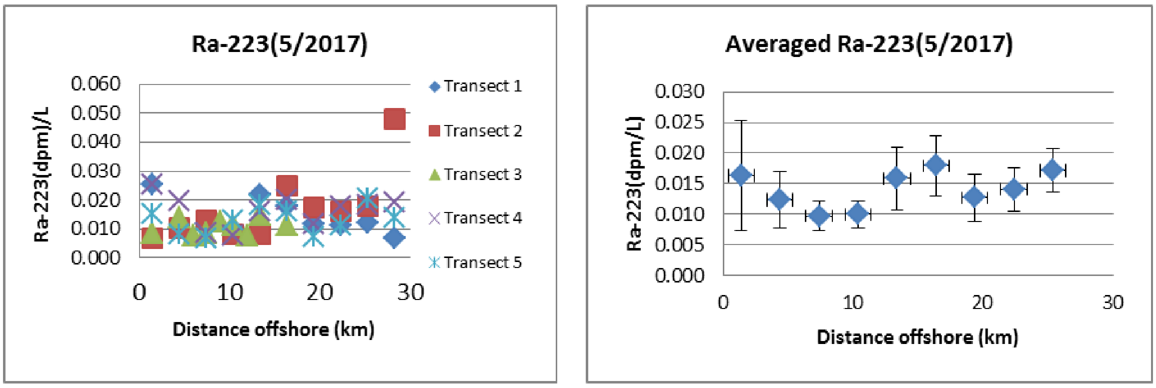

Figure 3.8: The activity of ^{223}Ra as a function of distance offshore for each transect (in May 2017)

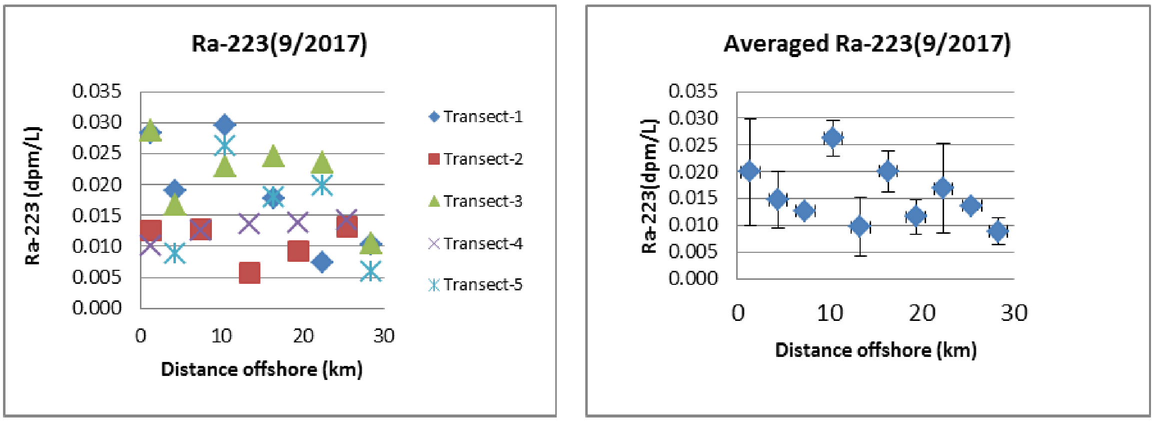

Figure 3.9: The activity of ^{223}Ra as a function of distance offshore for each transect (in September 2017)

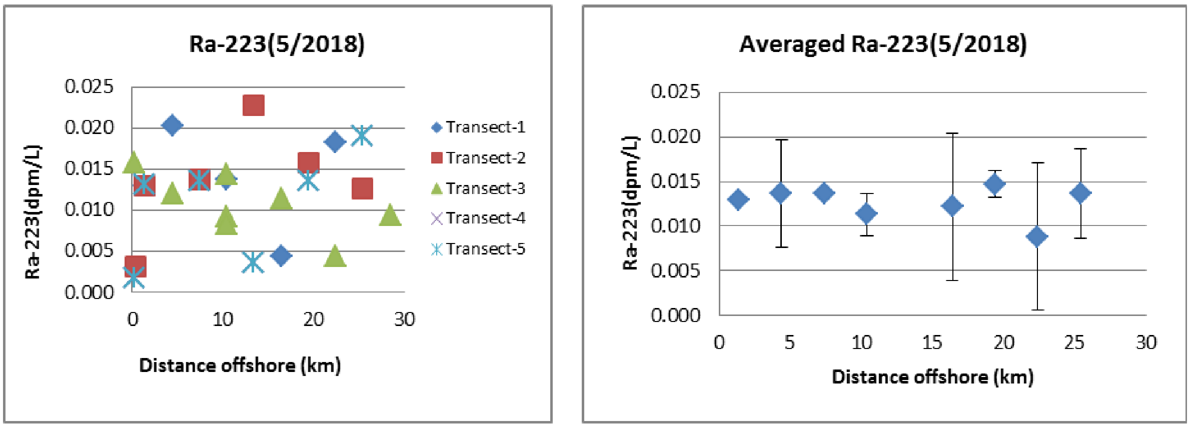

Figure 3.10: The activity of ^{223}Ra as a function of distance offshore for each transect (in May 2018)

It was seen from Fig 3.8 through 3.10 that in both dry and rainy seasons the averaged ^{223}Ra activity concentration decreases with increasing distance to 15 km from the coast. However, there was no consistent trend of decreasing activity with increasing distance from 15 km to 30 km offshore.

3.2. Determination of diffusion coefficient (K_h)

Based on the experimental results, the diffusion coefficient (K_h) is determined by the equation (4). The diffusion coefficients (K_h) of the coastal waters of study site in May 2017, September 2017 and May 2018 are sumarized in Table 3.2; 3.3; 34

Table 3.2: The diffusion coefficients (K_h) of the coastal waters of study site in May 2017

Transect	**K_h (m^2/s)**			
	Based on ^{224}Ra	R^2	Based on ^{223}Ra	R^2
Transect - 1 (5/2017)	390	0.864	363	0.787
Transect - 2 (5/2017)	423	0.813	260	0.712
Transect - 3 (5/2017)	150	0.975	209	0.832

Transect - 4 (5/2017)	188	0.891	224	0.996
Transect - 5 (5/2017)	283	0.778	162	0.987
Minium value	150		162	
Maxium value	423		363	
Mean	**287**		**244**	
Standard deviation	120		76	

Table 3.3: The diffusion coefficients (K_h) of the coastal waters of study site in September 2017

Transect	**K_h (m^2/s)**			
	Based on ^{224}Ra	R^2	Based on ^{223}Ra	R^2
Transect - 1 (9/2017)	400	0.906	217	0.963
Transect - 2 (9/2017)	351	0.931	144	0.796
Transect - 3 (9/2017)	423	0.993	347	0.837
Transect - 4 (9/2017)	-	-	-	-
Transect - 5 (9/2017)	271	0.909	224	0.730
Minium value	271		144	
Maxium value	400		347	
Mean	**361**		**233**	
Standard deviation	67		85	

Table 3.4: The diffusion coefficients (K_h) of the coastal waters of study site in May 2018

Transect	**K_h (m^2/s)**			
	Based on ^{224}Ra	R^2	Based on ^{223}Ra	R^2
Transect - 1 (5/2018)	290	0.836	162	0.615
Transect - 2 (5/2018)	265	0.911	381	0.865
Transect - 3 (5/2018)	188	0.961	217	0.996

Transect - 4 (5/2018)	219	0.933	-	-
Transect - 5 (5/2018)	326	0.978	128	0.932
Minium value	188		128	
Maxium value	326		381	
Mean	**257**		**222**	
Standard deviation	55		112	

^{226}Ra and ^{228}Ra are used to assess the relative roles of advection and eddy diffusion. For ^{226}Ra the data within 30 km from the coast fit with a line having correlation coefficient of R^2=0.590 (May 2017) and R^2=0. 573 (September 2017) ; For ^{228} Ra the data within 30 km from the coast fit with a line having correlation coefficient R^2=0.676 (May 2017) and R^2=0.563 (September 2017). These linear correlations are evidence for a fact that the distributions within 30 km from the coast is controlled by eddy diffusion.

The values of K_h derived from ^{224}Ra and ^{223}Ra are relatively similar to each other. The diffusion cofficient of the coastal water at the study area in May 2017 is 244 – 287 (m^2/s) in May 2017, in September 2017 is 233 – 361 (m^2/s), and in May 2018 is 222 – 257 (m^2/s).

3.3. Determination of residence time of the coatals waters.

Based on the K_h value obtained residence time of coastal water can be determined by the equation (5). The residence time of coastal water at study site is shown in Table 3.5.

Table 3.5: Residence time of coastal water at various distances offshore in the study site

Period	**K_h (m^2/s)**	**Residence time (day) of seawater at distance offshore**					
		5 km	10 km	15 km	20 km	25 km	30 km
May 2017	244	0,6	2,4	5,3	9,5	14,8	21,3
	287	0,5	2,0	4,5	8,1	12,6	18,1
September 2017	233	0,6	2,5	5,6	9,9	15,5	22,4
	361	0,4	1,6	3,6	6,4	10,0	14,4
May 2018	222	0,7	2,6	5,9	10,4	16,3	23,5
	257	0,6	2,3	5,1	9,0	14,1	20,3

From Table 3.5 one can see that in May (the rainy? Or dry? season), residence time of coastal water within 30 km from the coast was 19 - 23 days whereas in September (the dry? rainy season), the residence time was 14 - 22 days.

IV. CONCLUSION

From the results presented above some conclusions could be drawn as follows.

- The counting efficiency of the home-made delayed coincidence alpha counting system (DeCC) for analysing of ^{223}Ra and ^{224}Ra was calibrated and it was (26±2)%.

- Verification of A procedure for quantification of the short-lived ^{223}Ra and ^{224}Ra on the DECCwas established. The limit of detection of analytical method for the radionuclides was found to be ...Bq , the accuracy of the mothod was not exceeded ±...% of the certified value, the repeatability of the method was within ±5% of the mean value. The methof was quite applicable for analyzing ^{223}Ra and ^{224}Ra in large volume of sea water.

- Verification of the procedures by using gamma spectrometer. An analytical procedure for analyzing of long-lived ^{226}Ra and^{228}Ra radionuclides was established and verified. The procedure has high sensitivity, accuracy and repeatability that quite applicable for analyzing ^{226}Ra and^{228}Ra in large volume of sea water.

- Verification of A procedure for making *acrylic fibers impregnated* with manganese *dioxide* to extract radium from sea water was established. The fiber has maximum adsorption capacity of …Bq/g.

- Collection of 105 seawater samples from the study area were collected in the two seasons to determine the ^{223}Ra, ^{224}Ra, ^{226}Ra and ^{228}Ra activity concentrations for assessing the temporal and spatial distributions of those isotopes in the study area.

- Diffusion coefficient (K_h) of coastal water in the study area in the two seasons was estimated based on the ^{223}Ra and ^{224}Ra activity concentrations distibution along the distance from the coastlines. It was found that the diffusion coefficient of coastal water in the rainy season was 244-287 (m^2/s) whilst in the dry season it was 233-361 (m^2/s).

- Residence time of coastal water in the study site in two seasons was estimated based on the diffusion coefficient. The results show that the residence time of coastal water within 30 km from the coastline was 19-23 days in the rainny season and 14-22 days in the dry season.

REFERENCES

[1] Beek, P. van et al., (2008). Radium isotopes to investigate the water mass pathways on the Kerguelen Plateau (Southern Ocean), *Deep-Sea Research II, 55, pp. 622-637.*

[2] Bourquin, M. et al., (2008). Comparison of techniques for pre-concentrating radium from seawater, *Marine Chemistry 109, pp. 226-237.*

[3] Breier, J.A. and H.N. Edmonds, (2007). High ^{226}Ra and ^{228}Ra activities in Nueces Bay, Texas indicate large submarine saline discharges, *Marine Chemistry, 103, 131–145.*

[4] Chubarenko, I and N. Demchenko, (2010). On contribution of horizontal and intra-layer convection to the formation of the Baltic Sea cold intermediate layer, *Ocean Science, 6, 285–299.*

[5] Chris Garrett (2006). Turbulent dispersion in the ocean, *Progress in Oceanography 70, 113–125.*

[6] Dimova, N. et al., (2007). Automated measurement of ^{224}Ra and ^{226}Ra in water, *Applied Radiation and Isotopes* 65, 428–434.

[7] Li, Y.-H., Mathieu, G., Biscaye, P., Simpson, H.J., (1977). The flux of ^{226}Ra from estuarine and continental shelf sediments*, Earth and Planetary Science Letters 37, 237–241.*

[8] GuogangJia, Jing Jia, (2012). Determination of radium isotopes in environmental samples by gamma spectrometry, liquid scintillation counting and alpha spectrometry: a review of analytical methodology*, Journal of Environmental Radioactivity 106, pp. 98-119.*

[9] Gu, H. et al., (2012). Using radium isotopes to estimate the residence time and the contribution of submarine groundwater discharge (SGD) in the Changjiang effluent plume, East China Sea, *Continental Shelf Research 35, pp. 95-107.*

[10] Kim, G., et al., (2001). Measurement of ^{224}Ra and ^{226}Ra Activities in Natural Waters Using a Radon-in-Air Monitor*, Environ. Sci. Technol., 35, 4680-4683.*

[11] Krishnaswami et al., (1972), Silicon, radium, thorium and lead in seawater: in-situ extraction by synthetic fiber*, Earth Planet. Sci. Lett. 16, 84-90.*

[12] Moore, W.S. (1969). Oceanic concentration of ^{228}Ra, *Earth Planet. Sci. Letter.* ***6****, pp. 437-446.*

[13] Moore, W.S., Reid, D.F. (1973), Extraction of radium from natural waters using manganese-impregnated acrylic fibers, *J. Geophys. Res.* ***78*** *(36), 8880-888.*

[14] Moore, W.S. et al., (1985), Techniques for precise mapping of ^{226}Ra and ^{228}Ra in the Ocean, *J. Geophys. Res.* ***90*** *(C4), 6983-6994.*

[15] Moore, W.S., (2000a). Determining coastal mixing rates using radium isotopes, *Continental Shelf Research 20, 1995- 2007.*

[16] Moore, W.S., (2000b). Ages of continental shelf waters determined from ^{223}Ra and ^{224}Ra, *Journal of Geophysical Research VOL 105, 22,117- 22,122.*

[17] Moore, W.S. (2008). Fifteen years experience in measuring ^{224}Ra and ^{223}Ra- by delayed-coincidence counting, *Marine Chemistry, 109, 188 – 197.*

[18] Moore, W.S. and Joselene de Oliveira, (2008). Determination of residence time and mixing processes of the Ubatuba, Brazil, inner shelf waters using natural Ra isotopes, *Estuarine, Coastal and Science 76, pp. 512-521.*

[19] Philip J. W. Roberts and Donald R. Webster. Turbulent diffusion, *School of Civil and Environmental Engineering, Georgia Institute of Technology, Atlanta, Georgia 30332-0355, E-mail proberts@ce.gatech.edu*

[20] Purkl, S. et al., (2003). A rapid method for a-spectrometric analysis of radium isotopes in natural waters using ion-selective membrane technology, *Applied Radiation and Isotopes 59, 245–25.*

[21] Phan Sơn Hải (2016). Báo cáo tổng kết đề tài cấp Bộ 2015-2016: “Nghiên cứu sử dụng các đồng vị radi để xác định hệ số khuếch tán và thời gian lưu của nước biển ven bờ - Pha 1 Xây dựng phương pháp xác định hệ số khuếch tán và thời gian lưu của nước biển ven bờ”,*Bộ Khoa học và Công nghệ.*

[22] Rapaglia, J. et al., (2010). Investigation of residence time and groundwater flux in Venice Logoon: Comparing radium isotope and hydrodynamical models*, Journal of Environmental Radioactivity 101, pp. 571-581.*

[23] Souza, T.A. et al., (2010). Use of multitracers for the study of water mixing in the Paraiba do Sul River estuary, *Journal of Environmental Radioactivity 101, pp. 564-570.*

[24] Veeh H.H. et al., (1995). The behaviour of uranium and radium in an inverse estuary, *Continental Shelf Research, Vol. 15, No. 13, pp. 1569-1583.*

1.6- Applications in Biology, Agriculture and Medicine

ESTABLISHMENT OF PREPARATION PROCESS OF NANO-PRODUCT GENERATED FROM CURCUMIN AND CHITOSAN USING A COMBINING METHOD OF RADIATION AND CHEMISTRY FOR WOUND HEALING AND SCAR TREATMENT

Nguyen Minh Hiep[1], Tran Thi Thuy[1], Bui Chi Bao[2], Le Huu Tu[1], Nguyen Trong Hoanh Phong[1], Nguyen Duy Hang[1], Le Xuan Cuong[1], Nguyen Tuong Ly Lan[1], Pham Thi Sam[1], Tran Thi Tam[1], Pham Ngoc Duy[3], Nguyen Tan Man[1], Vu Ngoc Bich Dao[1] and Le Van Toan[1]

[1]Radiation Technology Center, Nuclear Research Institute, Dalat city, Vietnam
[2]Center for Molecular Biomedicine, University of Medicine and Pharmacy at Ho Chi Minh City, Vietnam.
[3]Center for Biotechnology, Nuclear Research Institute, Dalat city, Vietnam

Project information:

- **Code:** DTCB.07/17/VNCHN
- **Managerial Level:** Ministry
- **Allocated Fund:** 880,000,000 VND
- **Implementation time:** 24 months (Jan 2017- Dec 2018)
- **Contact email:** jackminhhiep@yahoo.com
- **Paper published in related to the project:**

1. **M.H Nguyen**, S.E. Lee, T.T. Tran, C.B. Bui, T.H.N. Nguyen, N.B.D. Vu, T.T. Tran, T.H.P. Nguyen, T.T. Nguyen, K. Hadinoto. A simple strategy to enhance the in vivo wound-healing activity of curcumin in the form of seft-assembled nanoparticle complex of curcumin and oligochitosan. Mater. Sci. Eng. C (2019) doi.org/10.1016/j.msec.2018.12.091.
2. **M.H. Nguyen**, P.N. Duy, B. Dong, T.H.N Nguyen, C.B. Bui, K. Hadinoto. Radioprotective activity of curcumin-encapsulated liposomes against genotoxicity caused by gamma Cobalt-60 irradiation in human blood cells. Int. J. Radiat. Biol. 93 (2017) 1267–1273.
3. **Nguyen Minh Hiep**, Tran Thi Thuy, Vu Ngoc Bich Dao, Nguyen Thi Huynh Nga, Nguyen Trong Hoanh Phong, Le Huu Tu, Nguyen Tan Man, Le Xuan Cuong, Pham Thi Sam, Tran Thi Tam, Nguyen Tuong Ly Lan, Le Van Toan, Nguyen Duy Hang, Nguyen Ngoc Phuong. Khao sat anh huong cua khoi luong phan tu chitosan den su hinh thanh phuc hop nano voi Curcumin. *Journal of Science,* No.15 (2018) 130–138 (In Vietnamese)

Abstract: With the purpose to generate a novel commercial product with a high effectiveness for wound healing and scar treatment, this research was carried out with 2 phases. In the phase 1 (2017 – 2018), with the aim to develop a most suitable nanocarrier system for curcumin (CUR) as well as a most suitable physical state for the commercial formulation, firstly, oligochitosan (OCH) was prepared using gamma irradiation method in the presence of H_2O_2 5% (v/v), and its complexation with CUR was also prepared using the drug – polysaccharide complexation method. In addition, CUR encapsulated nanoliposome (Lip-CUR) was also prepared using a combining method of hydration and sonication (for reducing particle size). After that, OCH was coated onto the surface of Lip-CUR using the drop-wise method to form OCH-Lip-CUR. The cytotoxicity and the effect of CUR-OCH nanoplex and OCH-Lip-CUR on the growth of 3T3 cells (mouse fibroblast) were studied using MTT assay. The *in vivo* effectiveness with respect to wound healing and scar treatment of CUR-OCH nanoplex and OCH-Lip-CUR was evaluated using white mice *Musculus var. albino*. Moreover, the *in vivo* effectiveness of a cream form, a hydrogel film form containing a higher effectiveness nano-CUR system (CUR-OCH nanoplex or OCH-Lip-CUR) was also investigated. The results indicate that both of CUR-OCH nanoplex and OCH-Lip-CUR were at nanosize (140 nm for CUR-OCH nanoplex and 238,9 nm for OCH-Lip-CUR); zeta potential of 2 these nanosystems was above 20 mV; complexation efficiency of CUR-OCH nanoplex and encapsulation efficiency of OCH-Lip-CUR were above 90%; payload of CUR-OCH nanoplex and OCH-Lip-CUR was above 85% and 8%, respectively (suitable for *in vivo* experiments). The MTT results demonstrate that CUR-OCH nanoplex and OCH-Lip-CUR at low CUR concentration of 0.05 mg/mL and 0.01 mg/mL, respectively, exhibited a negligible toxicity to 3T3 cells. The *in vivo* results of wound healing and scar treatment on white mice indicate OCH-Lip-CUR at the optimal CUR concentration (0.01 mg/mL) exhibited higher effectiveness compared to that of CUR-OCH nanoplex at optimal CUR concentration (0.05 mg/mL). The *in vivo* experiment also indicated the higher wound healing and scar treatment effect was achieved when OCH-Lip-CUR-contained hydrogel film was used at CUR concentration of 0.05 mg/mL compared to that of the cream form at optimal CUR concentration. On the other hand, the *in vivo* results imply that CUR-OCH nanoplex and OCH-Lip-CUR had a significantly higher wound healing and scar treatment effect compared to those of other nano-CUR systems containing in some commercial products on the market.

Keywords: Curcumin, CUR-OCH nanoplex, oligochitosan, wound healing, nanoliposome, scar

1. INTRODUCTION

The long healing time of wounds causes itching and increases the possibility of inflammation [1]. It might also negatively affect the lives and health of patients [1].

Curcumin (CUR), a natural polyphenolic compound isolated from turmeric, possesses wound healing and scar-treatment effects [2, 3]. However, CUR shows poor aqueous solubility (only 0.6 mg/L), rapid degradation at alkaline pH, and low penetration, which are responsible for its poor clinical applications [4]. To overcome these drawbacks, CUR was recently encapsulated into nanocarrier systems [5]. However, most of them are nano-emulsions or polymeric nanoparticles that exhibit low biocompatibility with the human body, occasionally resulting in allergy, toxicity, and low payload (less than 15 %) [5]. In addition, the nano-crystalline form of CUR did not significantly improve its bioavailability [6]. Therefore, novel nanosystems of CUR to overcome the above problems as well as increase suitability for wound healing and scar treatment are required.

Nanoplexes, a novel nanosystem, have been recently developed with outstanding advantages compared to other nano-carriers, including no use of surfactants, a very high payload (4–5 times higher than that of the other nano-systems), no or negligible toxicity to human health, use of inexpensive biological polymers such as chitosan (CHI), alginate, dextran sulfate etc. and simple preparation process [6]. On the other hand, OCH can promote the division of fibroblasts and regulate the development of keratinocytes [7]. Therefore, formation of nanoplexes between CUR and OCH could combine the advantages of these two substances as well as the prominent advantages of nanoplexes in wound healing and scar treatment. However, the *in vivo* effectiveness of CUR-OCH nanoplexes for wound healing and scar treatment has not been determined so far.

On the other hand, liposomes have been recognized as the most safe and suitable nanosystem for application in humans because of their highest compatibility resulting from the usage of phosphatidylcholine and cholesterol (also the components of cells) as the main components of their structure [8]. Liposomes could also enhance the solubility and penetration of both hydrophobic and hydrophilic active ingredients leading to an increase in their bioavailability [8, 9]. There are many studies about the encapsulation of CUR into liposomes (Lip-CUR), but most of them only concentrate on the treatment of cancers and gastrointestinal diseases and there are few studies on the application of Lip-CUR in wound healing and scar treatment [8, 9]. Moreover, the coating OCH on the surface of Lip-CUR might enhance its wound healing and scar treatment effect [7, 8].

In addition, determination of physical state (cream form or gel form) for the commercialized product of nano-CUR is also necessary. This is because it directly relates to the effectiveness of the nano-CUR product.

Therefore, with the aim to develop the most effective nano-CUR formulation for wound healing and scar treatment, the project entitled "Establishment of preparation process of nanoproduct generated from curcumin and chitosan using a combining method of radiation and chemistry for wound healing and scar treatment" (Phase I (2017 – 2018): Establishment of preparation process of a new trial product; *in vivo* experiment on animal for evaluation of wound healing and scar treatment effect) was carried out.

2. EXPERIMENTS

2.1. Equipments

Rotary evaporator IKA RV 06 (IKA GmbH, Germany), UV-Vis spectrophotometer UVmini-1240 (Shimadzu, Japan), Crytotome Tissue-Tek Cryo3 B115 Microtome (Sakura Finetek, U.S.), ELISA absorbance microplate reader (IRE 96, France), Zetasizer Nano ZS90 (Malvern Instruments Ltd., U.K.), Transmission electron microscopy (TEM) JEM-1400 (JEOL Ltd., Japan), Field emission scanning electron microscopy (FE-SEM) S-4800 (Hitachi, Japan), Technical ruler (Hoffmann, Germany), Pipetman (Corning, U.S.).

2.2. Reagents

Crude chitosan (CH0) (Vietnam), CUR (Alfa Aesar, U.S.), Phospholipon 90 (phospholipid) (Lipoid GmbH, Germany), Sodium alginate (Sigma Aldrich, U.S.), Xanthan gum (Sigma Aldrich, U.S.), Chloroform (J. T. Baker, U.S.), Methanol (J. T. Baker, U.S.), MTT (Methylthiazolyldiphenyl-tetrazolium bromide) (Sigma Aldrich, U.S.), DMSO (Dimethyl sulfoxide) (Sigma Aldrich, U.S.), DMEM (Dulbecco's Modified Eagle Medium) (Thermo Fisher Scientific, U.S.)

2.3. *Subjects*

CUR-OCH nanoplex, OCH-Lip-CUR, 3T3 cell line (mouse fibroblast) for cytotoxicity experiment, white mice Mus musculus var. albino for in vivo evaluation of wound healing and scar treatment of the novel developed products.

2.4. Experiment designs

2.4.1. Preparation of OCH by gamma irradiation method

OCH was prepared by gamma irradiation method. Briefly, after being irradiated at condition of 5% H_2O_2 (v/v), dose of 30 kGy and dose rate of 2.4 kGy/h, OCH in the resulting irradiated solution was obtained by precipitation method using ethanol, acetone and NH_4OH 2,5% (v/v). After that, the precipitation was washed 3 times by ethanol, dried at 60 ^oC and ground into powder.

The molecular weight of OCH was determined by Gel Permeation Chromatography using LC-20AD Liquid Chromatograph (Shimadzu, Japan), RID-20A detector and Shodex Ohpak SB-803 HQ column.

2.4.2. Preparation of CUR-OCH nanoplex

CUR-OCH nanoplex was prepared using drug-polysaccharide complexation method [6]. Briefly, CUR was dissolved into 0.1 M KOH to form an negative charged $CUR^{(-3)}$ solution 5 mg/mL. OCH was dissolved in acetic acid aqueous solution 0.8% (v/v) to form a positively charged biopolymer solution 9.05 mg/mL. The resulting mixture of OCH solution and CUR solution (1:1, v/v) was vortexed for 10 seconds to form nanoplexes. The resulting nanoplex suspensions were washed with 2 cycles of centrifugation at 13000 rpm for 25 min using SORVALL ST 16R centrifuge (Thermo Fisher Scientific, NH, USA) and re-suspended in deionized water.

Complexation efficiency was determined based on equation (1) and equation (2):

$$\text{Complexation efficiency (\%)} = \frac{\text{Amount of CUR that formed nanoplex}}{\text{Initial amount of CUR}} \times 100 \quad (1)$$

$$\text{Payload (\%)} = \frac{\text{Amount of CUR containing in nanoplex}}{\text{Amount of nanoplex}} \times 100 \quad (2)$$

2.4.3. Preparation of OCH-Lip-CUR

Lip-CUR was prepared using a combination of lipid-film hydration and sonication [10]. Briefly, Phospholipon 90 G and curcumin (ratio 10:1, w/w) were fully dissolved in a mixture of chloroform and methanol (2:1, v/v) and added to a round-bottom flask. A thin and homogenous lipid film was formed when the solvents were evaporated using a Rotary Evaporator (IKA RV6, Germany) for 6 hours at 55 °C. After that, the thin lipid-film was hydrated with distilled water for 2 hours at 55 °C to form “crude” Lip-CUR. The resulting dispersion of Lip-CUR was subjected to particle size reduction using a probe sonicator (Vibra-Cell Ultrasonic Liquid Processor VC 750, Sonics & Materials, Inc., USA) for 30 min (3 cycles, pulse on: 7 min and pulse off: 3 min). The resulting Lip-CUR dispersion was filtered using a cellulose ester membrane with a 3 μm pore size to remove the unencapsulated CUR precipitated in the solution.

OCH was coated onto the surface of Lip-CUR in a drop-wise manner [9]. Briefly, OCH was added to aqueous acetic acid solution 0.5 % (v/v) and stirred for 24 hours to form OCH solution 0.3% (w/v). The OCH solution was added drop-wise to the Lip-CUR dispersion at a ratio of 1:20 (v/v) with stirring for 3 hours to form OCH-Lip-CUR.

Encapsulation efficiency and payload of OCH-Lip-CUR was calculated using equation (3) and equation (4):

$$\text{Encapsulation efficiency (\%)} = \frac{\text{Amount of CUR containing in liposome}}{\text{Initial amount of CUR}} \times 100 \quad (3)$$

$$\text{Payload (\%)} = \frac{\text{Amount of CUR containing in liposome}}{\text{Amount of liposome}} \times 100 \quad (4)$$

2.4.4. Characterization of CUR-OCH nanoplex and OCH-Lip-CUR

The mean particle size, polydispersity index (PDI), and zeta potential were determined using the Zeta Sizer Nano ZS90 (Malvern Instruments Ltd., UK) at 25°C and a measurement angle of 90^o.

2.4.5. Morphology of CUR-OCH nanoplex and OCH-Lip-CUR

The morphology of CUR-OCH nanoplexes was examined with a Field Emission Scanning Electron Microscope (FE-SEM) S – 4800 (Hitachi Ltd., Japan) using freeze-dried powder of the CUR-OCH nanoplexes sputter coated with platinum.

The success of OCH-coating onto the surface of Lip-CUR and the morphology of OCH-Lip-CUR was also determined using negative staining transmission electron microscopy (TEM) using a transmission electron microscope (TEM) JEM – 1400 (JEOL Ltd., Japan) and 2% (w/v) sodium phosphostungstate.

2.4.6. Cytotoxicity of OCH-CUR nanoplexes and OCH-Lip-CUR

The cytotoxicity of OCH-CUR nanoplexes and OCH-Lip-OCH was evaluated in 3T3 cells (mouse fibroblasts) using the MTT assay [11]. The experimental design was as follows: Control sample, OCH (0.004, 0.0088 and 0.00176 mg/mL), Native CUR (0.25, 0.05 and 0.01 mg/mL), CUR-OCH nanoplex (0.25, 0.05, 0.01 mg/mL) and OCH-Lip-CUR (0.25, 0.05 and 0.01 mg/mL).

2.4.7. Wound healing and scar treatment effect of OCH-CUR nanoplex, OCH-Lip-CUR, OCH-Lip-CUR contained cream-form, OCH-Lip-CUR contained gel-form, and some commercial nano-CUR products.

Briefly, 18–22 g male mice *Mus musculus var. Albino*. were anesthetized with ketamine solution (dose of 2 mg/kg). Back hair of mice was shaved and wounds of approximately 8 cm-diameter were created using a surgical clamp and scissors. The mice were divided into groups non-treated group (negative control), treated with CUR native (postitive control), treated with CUR-OCH nanoplex, OCH-Lip-CUR, OCH-Lip-CUR contained cream-form, OCH-Lip-CUR contained gel-form, and some commercial nano-CUR products. Wound healing rate was evaluated based on the reduction in wound size after treatment for 3, 5, 7, 9, 12, and 14 days.

Scar formation was evaluated at day 22 when the structure of the scars was relatively stable [12]. Scar evaluation was carried out based on the scar-size and appearance (dim or sharp) of the scar. In addition, images of collagen staining were also used to evaluate the scar structure.

3. DATA ANALYSIS

Values are expressed as mean ± standard deviation (at least n = 6). Mean and standard deviation of the results from at least three independent experiments were calculated using Microsoft Excel software. In all results related to *in vivo* effectiveness of wound healing and scar treatment, the significance of each mean property value was determined using one-way ANOVA with a post hoc Duncan's test in SPSS software ($P < 0.05$).

4. RESULTS AND DISCUSSION

4.1. Preparation of OCH by gamma irradiation method

The FTIR result shown in Figure 1A indicates that deacetylation degree of crude CH was more than 80%. In addition, the result of GPC analysis has indicated that OCH prepared by irradiation method in the presence of 5% H_2O_2 with dose of 30 kGy and dose rate of 2.4 kGy/h has an average molecular weight of approximately 3.7 kDa.

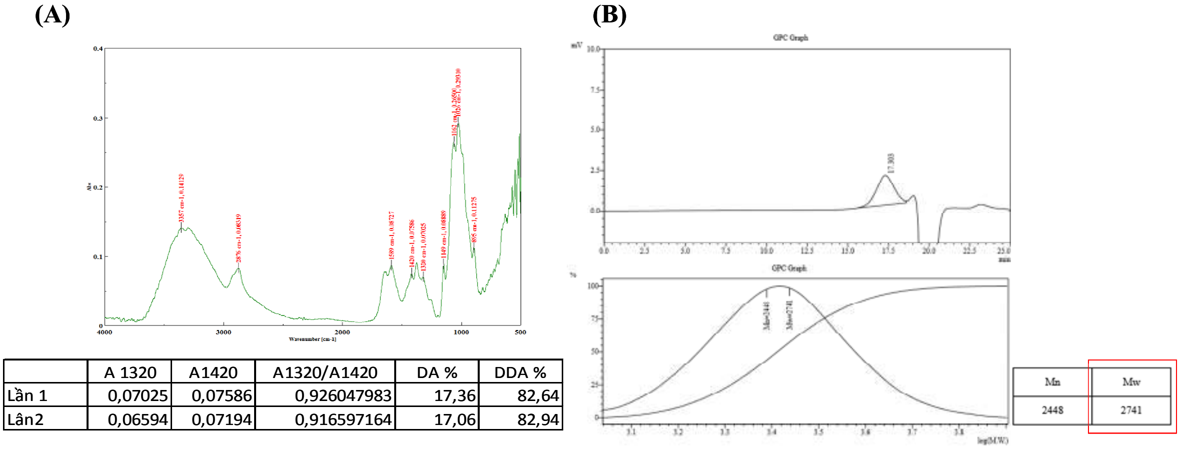

	A 1320	A1420	A1320/A1420	DA %	DDA %
Lần 1	0,07025	0,07586	0,926047983	17,36	82,64
Lân2	0,06594	0,07194	0,916597164	17,06	82,94

Mn	Mw
2448	2741

Figure 1: (A) FTIR spectrum of crude CH; (B) GPC result of OCH.

4.2. Preparation of CUR-OCH nanoplex and OCH-Lip-CUR

As shown in Table 1, the CUR-OCH nanoplexes were formed with a very small size (139.8 nm), a high zeta potential (+22.1 mV), a moderate PDI (0.294), a high complexation efficiency (95.5%), and a very high payload (85.8%). In addition, the FE-SEM images (Figure 2A) also indicated that native CUR had a crystalline structure, whereas the morphology of CUR-OCH nanoplexes was spherical. All these results indicate the successful preparation of CUR-OCH nanoplexes.

As also shown in Table 1, Lip-CUR was prepared by a combination of lipid-film hydration and sonication resulting in 237.4 nm particle size, 0.235 PDI, -26.9 mV zeta potential, 93.3% encapsulation efficiency, and 8.4% payload. Coating of OCH (0.3 %, w/v) onto the surface of Lip-CUR resulted in a slight increase in particle size, a negligible decrease in encapsulation efficiency and payload (from 93.3% to 91.7% and from 8.4% to 8.3%, respectively), and altered zeta potential from negative (-26.9 mV) to positive (+23.7 mV). The formation of Lip-CUR and OCH-Lip-CUR was also affirmed by negative staining TEM (Figure 2B), which showed that the morphology of Lip-CUR was spherical with a multilamellar model, and the existence of OCH surrounding Lip-CUR was observed as a dark area layer on the surface of each OCH-Lip-CUR.

Table 1: Characteristics of CUR-OCH nanoplex, Lip-CUR and OCH-Lip-CUR.

	Mean particles size (nm)	**Polydispersity index (PDI)**	**Zeta potential (mV)**	**Complexation efficiency or encapsulation efficiency (%)**	**Payload (%)**
CUR-OCH nanoplex	139.8 ± 7.1	0.294 ± 0.052	22.1 ± 0.9	95.5 ± 0.8	85.8 ± 1.5
Lip-CUR	237.4 ± 11.5	0.235 ± 0.004	-26.9 ± 0.3	93.3 ± 0.5	8.4 ± 0.1
OCH-Lip-CUR	238.9 ± 8.6	0.258 ± 0.006	23.7 ± 0.5	91.7 ± 0.6	8.3 ± 0.1

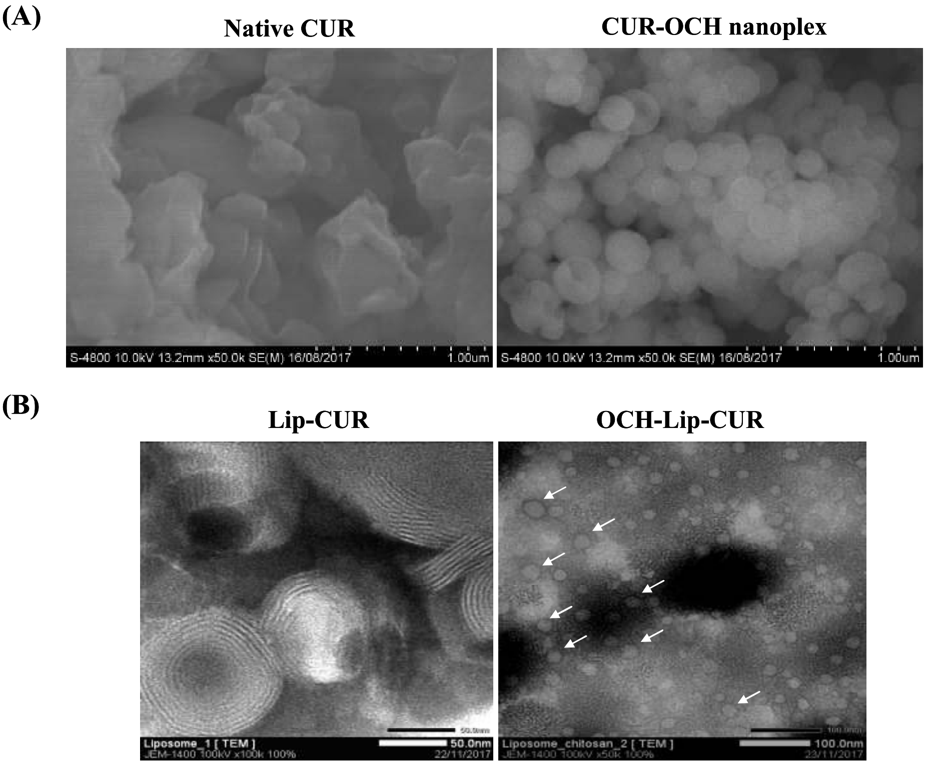

Figure 2: (A) FE-SEM images of native CUR and CUR-OCH nanoplex; (B) Negative-staining TEM images of Lip-CUR and OCH-Lip-CUR.

4.3. Cytotoxicity of CUR-OCH nanoplex and OCH-Lip-CUR

Cytotoxicity of OCH, native CUR, CUR-OCH nanoplexes, and OCH-Lip-CUR in 3T3 cells (mouse fibroblasts) was studied using the MTT assay [11]. Notably, the concentration of CUR (native CUR or CUR amount containing in nanoplex and liposome) and the concentration of OCH used in this experiment were similar to those used in the *in vivo* study on wound healing and scar treatment in white mice.

As shown in Figure 3, OCH exhibited minimal *in vitro* cytotoxicity to 3T3 cells. Particularly, cell survival was 96.03% and 98.60% when the cells were treated with high concentration (0.044 mg/mL) and low concentration (0.00176 mg/mL) of OCH, respectively. This implies that OCH did not have any toxic effect on mouse fibroblasts.

Treatment with native CUR (dissolved in DMSO) at high concentration (more than 0.01 mg/mL) exhibited high toxicity to the cells (Figure 3). This is because the solvent used for dissolving CUR (DMSO) at the high concentration caused toxicity to the cells and reduced their growth as well [13]. In addition, there are many studies mentioning that the treatment with CUR at low concentrations could stimulate cell growth, whereas treatment at high concentration could inhibit the growth or even kill the cells [14].

However, treatment with the CUR-OCH nanoplexes and OCH-Lip-CUR resulted in a higher percentage of cell survival compared to that with native CUR at the corresponding concentrations (Figure 3). Moreover, at low CUR concentration (0.01 mg/mL), both CUR-OCH nanoplexes and OCH-Lip-CUR exhibited negligible toxicity to 3T3 cells.

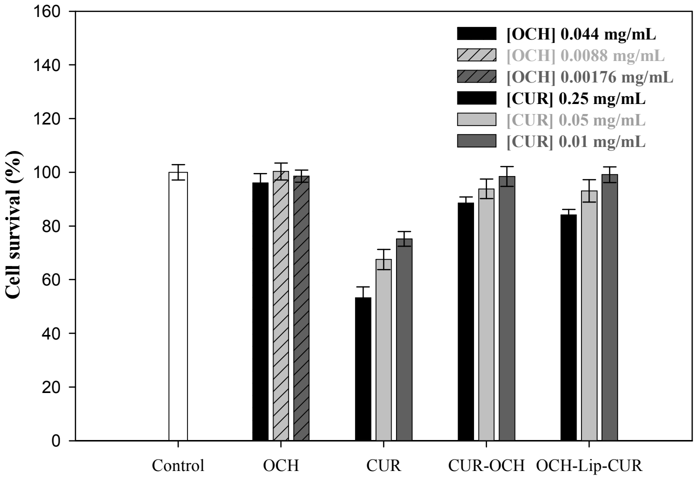

Figure 3: In vitro cytotoxicity of OCH, native CUR, CUR-OCH nanoplex and OCH-Lip-CUR on 3T3 cells. Data are plotted as the mean ± standard deviation (n=3).

4.4. Wound healing and scar treatment effect of CUR-OCH nanoplexes, OCH-Lip-CUR, OCH-Lip-CUR contained cream-form, OCH-Lip-CUR contained gel-form, and some commercial nano-CUR products.

As shown in Table 2A and Table 2B, after 9 days of being treated with OCH-Lip-CUR at optimal CUR concentration (0.01 mg/mL) and CUR-OCH at optimal concentration (0.05 mg/mL), the remaining size of the wound was 3,05% and 2,41%, repectively. In addition, the scar length and width in the OCH-Lip-CUR group were 3.2 mm and 1.45 mm, respectively, compared to 3.19 mm and 1.63 mm with CUR-OCH nanoplexes. Combined with the results of Figure 4, it is clear to see that the *in vivo* wound healing and scar treatment effect of OCH-Lip-CUR was higher than that of CUR-OCH nanoplex. Therefore, OCH-Lip-CUR was chosen for commercialization.

Moreover, as shown in Table 2 and Figure 4, the wound treated with the OCH-Lip-CUR contained cream-form exhibited a lower wound healing and scar treatment effect compared to the hydrogel-form. Particularly, after 9 days, the remaining size of the wound treated with OCH-Lip-CUR contained hydrogel-form at the optimal CUR concentration was 12,69% compared to that of 14,5% of OCH-Lip-CUR contained cream-form. In addition, the scar length and width in the hydrogel-form group were 2.75 mm and 1.38 mm, respectively, compared to 3.14 mm and 1.45 mm with the cream-form. The collagen staining images (Figure 5) also showed that, the tissue structure at the scar area was fully recovered to normal when the wound was treated with OCH-Lip-CUR contained hydrogel at CUR concentration of 0.05 mg/mL.

On the other hand, although containing some active ingredients in the formulation such as vitamin E, Aloe Vera extract, etc., some nano-CUR commercial products such as Curmagold gel and Curmagold capsule also exhibited the lower *in vivo* wound healing and scar treatment compared to both of OCH-Lip-CUR and CUR-OCH nanoplex (Table 2, Figure 4 and Figure 5).

Table 2: In vivo (A) wound healing and (B) scar treatment effect of native CUR, CUR-OCH nanoplexes, OCH-Lip-CUR, OCH-Lip-CUR contained cream-form, OCH-Lip-CUR contained gel-form, and some commercial nano-CUR products

(A)

Days	Control (-)	Control (+)	Cumargold capsule 0,05 mg/mL	Cumargold capsule 0,01 mg/mL	Cumargold gel	CUR-OCH 0,05 mg/mL	OCH-Lip-CUR 0,01 mg/mL	Cream	Cream+ OCH-Lip-CUR 0,05 mg/mL	Cream + OCH-Lip-CUR 0,01 mg/mL	Cream + OCH-Lip-CUR 0,005 mg/mL	Gel-Film	Gel-Film + OCH-Lip-CUR 0,05 mg/mL	Gel-Film + OCH-Lip-CUR 0,01 mg/mL	Gel-Film + OCH-Lip-CUR 0,005 mg/mL
0	100	100	100	100	100	100	100	100	100	100	100	100	100	100	100
3	73,38 ± 4,6^{a}	69,70 ± 3,36^{b}	66,25 ± 3,87^{bcd}	64,26 ± 4,60^{cde}	62,53 ± 4,96^{def}	58,72 ± 4,66^{fgh}	56,34 ± 3,08^{h}	64,60 ± 4,27^{cde}	67,71 ± 4,17^{bc}	63,99 ± 2,35^{cde}	67,76 ± 4,58^{bc}	62,26 ± 2,96^{defg}	58,28 ± 2,14^{gh}	60,45 ± 1,97^{efg}	61,88 ± 2,46^{efg}
5	58,41 ± 3,89^{a}	53,84 ± 4,07^{b}	50,15 ± 3,58^{bc}	46,99 ± 4,76^{cdef}	48,51 ± 4,31^{cde}	44,47 ± 5,11^{efg}	40,90 ± 3,03^{gh}	49,04 ± 2,75^{cd}	47,73 ± 4,15^{cdef}	43,50 ± 4,17^{fg}	48,11 ± 3,58^{cde}	48,18 ± 1,20^{cde}	38,67 ± 2,89^{h}	43,56 ± 2,35^{fg}	45,69 ± 4,27^{def}
7	48,49 ± 5,41^{a}	40,55 ± 3,39^{b}	37,50 ± 3,00^{bc}	36,50 ± 3,76^{bcd}	36,85 ± 4,59^{bcd}	31,09 ± 4,69^{e}	29,09 ± 2,65^{ef}	36,89 ± 2,71^{bcd}	31,12 ± 3,66^{e}	28,78 ± 2,27^{ef}	30,11 ± 3,09^{ef}	35,77 ± 1,46^{cd}	26,69 ± 3,39^{f}	29,91 ± 2,96^{ef}	32,96 ± 5,06^{de}
9	34,25 ± 4,21^{a}	30,04 ± 3,51^{b}	26,95 ± 2,79^{bc}	22,38 ± 3,85^{de}	23,05 ± 2,55^{cd}	17,72 ± 5,02^{fg}	12,50 ± 2,21^{h}	24,61 ± 3,40^{cd}	18,47 ± 3,51^{efg}	14,50 ± 3,91^{gh}	18,11 ± 3,08^{efg}	23,07 ± 2,34^{cd}	12,69 ± 4,45^{h}	16,89 ± 3,90^{fgh}	20,19 ± 7,77^{def}
12	16,46 ± 2,91^{a}	11,70 ± 3,59^{bc}	11,91 ± 1,79^{b}	8,56 ± 4,40^{cd}	7,41 ± 2,52^{de}	3,05 ± 2,85^{fg}	2,41 ± 1,01^{fg}	9,05 ± 5,14^{bcd}	4,56 ± 4,20^{efg}	2,05 ± 2,04^{fg}	3,59 ± 2,46^{fg}	6,89 ± 1,83^{de}	1,31 ± 1,58^{g}	3,31 ± 2,75^{fg}	4,95 ± 4,33^{ef}
14	1,37 ± 1,78^{a}	0^{b}	0,62 ± 1,52^{b}	0^{b}	0^{b}	0^{b}	0^{b}	0^{b}	0^{b}	0^{b}	0^{b}	0^{b}	0^{b}	0^{b}	0^{b}

(B)

Scar size (mm)	Control (-)	Control (+)	Cumargold capsule 0,05 mg/mL	Cumargold capsule 0,01 mg/mL	Cumargold gel	CUR-OCH 0,05 mg/mL	OCH-Lip-CUR 0,01 mg/mL	Cream	Cream + OCH-Lip-CUR 0,05 mg/mL	Cream + OCH-Lip-CUR 0,01 mg/mL	Cream + OCH-Lip-CUR 0,005 mg/mL	Gel-Film	Gel-Film + OCH-Lip-CUR 0,05 mg/mL	Gel-Film + OCH-Lip-CUR 0,01 mg/mL	Gel-Film + OCH-Lip-CUR 0,005 mg/mL
Length	4,48 ± 0,42^{a}	4,70 ± 0,77^{a}	4,64 ± 0,46^{a}	4,41 ± 0,44^{ab}	4,01 ± 0,29^{bc}	3,19 ± 0,49^{ef}	3,20 ± 0,31^{ef}	4,45 ± 0,39^{ab}	3,49 ± 0,43^{de}	3,14 ± 0,25^{ef}	3,76 ± 0,38^{cd}	3,88 ± 0,39^{cd}	2,75 ± 0,43^{f}	3,48 ± 0,33^{de}	3,50 ± 0,38^{de}
Width	2,02 ± 0,30^{a}	1,65 ± 0,29^{bcde}	1,95 ± 0,48^{a}	1,78 ± 0,22^{abc}	1,67 ± 0,17^{bcd}	1,63 ± 0,23^{bcde}	1,45 ± 0,19^{de}	1,93 ± 0,21^{a}	1,61 ± 0,23^{bcde}	1,46 ± 0,15^{de}	1,58 ± 0,16^{cde}	1,86 ± 0,24^{ab}	1,38 ± 0,20^{e}	1,54 ± 0,19^{cde}	1,57 ± 0,21^{cde}

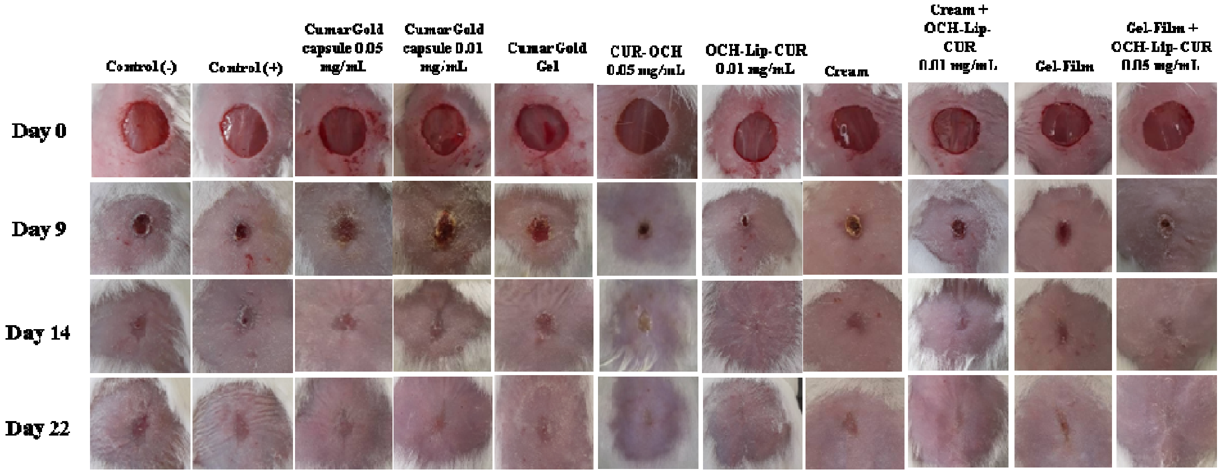

Figure 4: Images of the wounds treated with native CUR, CUR-OCH nanoplexes, OCH-Lip-CUR, OCH-Lip-CUR contained cream-form, OCH-Lip-CUR contained gel-form, and some commercial nano-CUR products at 9th, 14th and 22nd day.

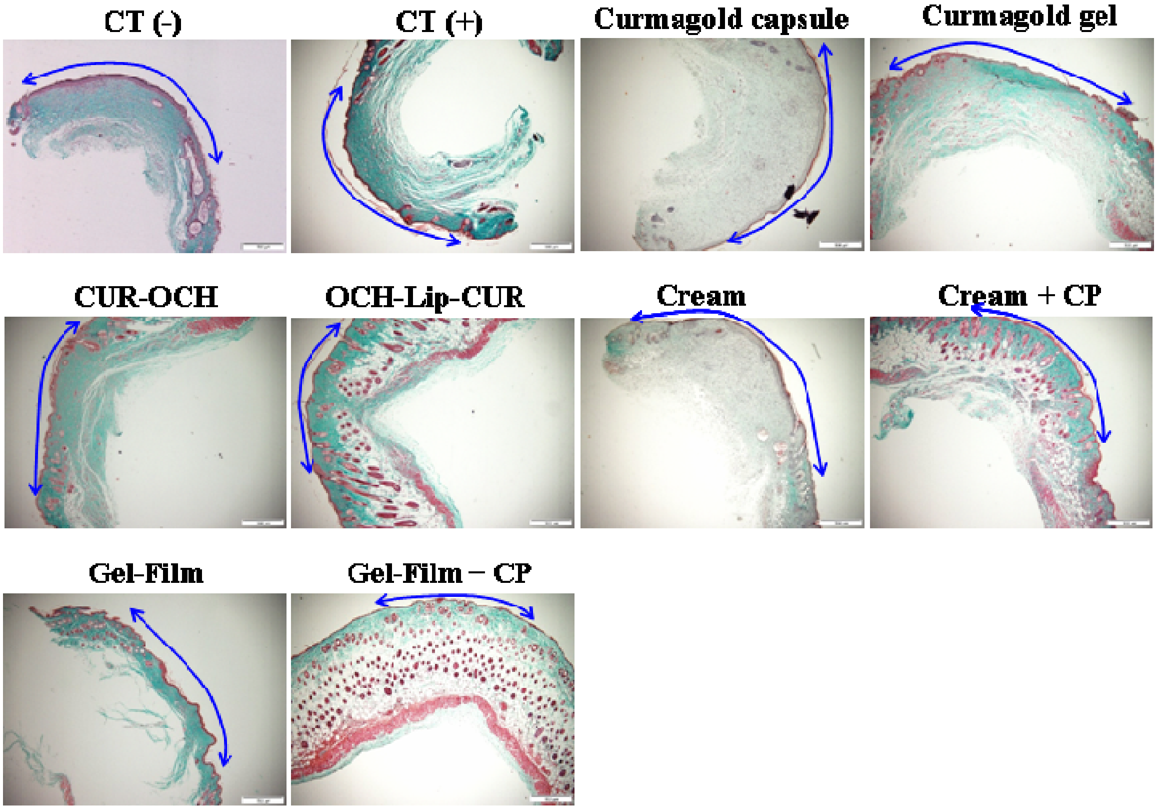

Figure 5: Histological images of the injury areas (A) without treatment (negative control) and with treatment by (B) native CUR, CUR-OCH nanoplexes, OCH-Lip-CUR, OCH-Lip-CUR contained cream-form, OCH-Lip-CUR contained gel-form. The length of blue arrows indicates the width of the scars.

5. CONCLUSIONS

In conclusion, OCH (Mw 3.7 kDa) was successfully prepared by gamma irradiation method in the presence of 5% H_2O_2. CUR-OCH nanoplexes and OCH-Lip-CUR was synthesized with a very small size, a high zeta potential, a moderate PDI, a high complexation efficiency or complexation efficiency. Both of CUR-OCH nanoplexes and OCH-Lip-CUR exhibited neglibible cytotoicity to 3T3 cells. At optimal CUR concentration, OCH-Lip-CUR showed higher *in vivo* wound healing and scar treatment effect compared to CUR-OCH nanoplex. The results of *in vivo* experiment also indicated the hydrogel form containing OCH-Lip-CUR at CUR concentraiton of 0.05 mg/mL exhibited the highest effectiveness. Moreover, the results imply that *in vivo* effectiveness of OCH-Lip-CUR and CUR-OCH nanoplexes was higher than that of the nano-CUR contained in Curmagold capsule and Curmagold gel.

REFERENCES

[1] Cameron, I.L., Greulich, R.C., 1963. Evidence for an essentially constant duration of DNA synthesis in renewing epithelia of the adult mouse. *J. Cell Biol.* 18, 31–40.

[2] Powers, P.S., Sarkar, S., Goldgof, D.B., Cruse, C.W., Tsap, L.V., 1999. Scar assessment: current problems and future solutions. *J. Burn Care Rehabil.* 20, 54– 60.

[3] Aggarwal, B.B., Sundaram, C., Malani, N., Ichikawa, H., 2007. CUR: the Indian solid gold. *Adv. Exp. Med. Biol.* 595, 1–75.

[4] Shoba, G., Joy, D., Joseph, T., Majeed, M., Rajendran, R., Srivivas, P., 1998. Influence of piperine on the pharmacokinetics of curcumin in animals and human volunteers. *Planta Med.*, 64, 353–356.

[5] Sun, M., Su, X., Ding, B.Y., He, X.L., Liu, X.Y., Yu, A.H., Lou, H.X., Zhai, G.X., 2012. Advances in nanotechnolohy-based delivery systems for curcumin. *Nanomedicine* 7, 1085–1100.

[6] Nguyen, H.M., Yu, H., Kiew, T.Y., Hadinoto, K., 2015. Cost effective alternative to nanoencapsulation: amorphous curcumin-chitosan nanoparticle complex exhibiting high payload and supersaturation generation. *Eur. J. Pharm. Biopharm.* 96, 1–10.

[7] Dai, T., Tanaka, M., Huang, Y.Y., Hamblin, M.R., 2011. Chitosan preparations for wound and burns: antimicrobial and wound-healing effects. *Expert Rev. Anti-Infect. Ther.* 9, 857–879.

[8] Mufamadi, M.S., Pillay, V., Choonara, Y.E., Toit, L.C.D., Modi, G., Naidoo, D., Ndesendo, V.M.K., 2011. A review on composite liposomal technologies for specialized drug delivery. *J. Drug Delivery* doi: 10.1155/2011/939851.

[9] Liu, N., Park, H.J., 2010. Factors effect on the loading efficiency of vitamin C loaded chitosan-coated nanoliposomes. *Colloids Surf., B* 76, 1–19.

[10] Nguyen, M.H., Duy, P.N., Dong, B., Nguyen, T.H.N., Bui, C.B., Hadinoto, K., 2017. Radioprotective activity of curcumin-encapsulated liposomes against genotoxicity caused by gamma Cobalt-60 irradiation in human blood cells. *Int. J. Radiat. Biol.* 93, 1267–1273.

[11] Denizot, F., Lang, R., 1986. Rapid colorimetric assay for cell growth and survival. Modifications to the tetrazolium dye procedure giving improved sensitivity and reliability. J. *Immunol. Methods* 89, 271–277.

[12] Guo, S., DiPietro, L.A., 2010. Factors Affecting Wound Healing. *J. Dent. Res.* 89, 219–229.

[13] Costa, L.D.A., Ottoni, M.H.F., Santos, M.G.D., Meireles, A.B., Almeida, V.G.D., Pereira, W.D.F., Avelar-Freitas, B.A.D., Brito-Melo, G.E.A., 2017. Dimethyl Sulfoxide (DMSO) decrease cell proliferation and TNF-α, IFN-γ, and IL-2 cytokines production in cultures of peripheral blood lymphocytes. *Molecules* 22, E1789.

[14] O'Sullivan-Coyne, G., O'Sullivan, G.C., O'Donovan, T.R., Piwocka, K., McKenna, S.L., 2009. Curcumin induces apoptosis-independent death in oesophageal cancer cells. *Br. J. Cancer* 101, 1585–1595.

PRELIMINARY RAPD DATA OF STATICE VARIETIES FOR THEIR MUTATION BREEDINGS

Le Van Thuc, Le Duc Hung, Le Thi Thuy Linh, Han Huynh Dien,
Le Thi Bich Thy and Tran Que

Dalat Nuclear Research Institute, 01 Nguyen Tu Luc, Dalat, Lam Dong province

Project information:

- **Code:** CS/18/01-01
- **Managerial Level:** Institute
- **Allocated Fund:** 100,000,000 VND
- **Implementation time:** 12 months (Jan 2018- Dec 2018)
- **Contact email:** thucbiovhn@gmail.com
- **Paper published in related to the project:**

Le Van Thuc, Le Duc Hung, Le Thi Thuy Linh, Han Huynh Dien, Le Thi Bich Thy, Tran Que, Hoang Thanh Tung and Duong Tan Nhut. "Analysis of genetic diversity of Statice (*Limoniumsinuatum* L.) in Lam Dong using RAPD-PCR technique towards conservation and plant mutation breeding", *Journal of Biotechnology* (*in Vietnamese*). (*Submission*).

Abstract: In this study, 12 statice varieties (*Limonium sinuatum* L.) were collected from famous flower growing areas (Van Thanh, Thai Phien, Da Thien, Ha Dong and Trai Mat) in Lam Dong. Young foliage of flowering cultivars after 45 days of planting at the experimental site was collected for DNA extraction and genetic correlation analysis using RAPD with 13 random primers. The results showed that out of 145 RAPD bands, there were 133 polymorphic bands (91.72%) and 12 monomorphic bands (8.28%). In particular, the OPB-03 primer has the highest number of amplifiers, which is 17 bands (with 16 polymorphic bands). The genetic difference coefficients ranged from 0.30 to 0.90, mean 0.55. The results of the genetic sequence analysis using NTSYSpc 2.1 showed that 12 statice varieties were divided into 4 groups: group I consisting of 3 varieties (rose pink, dark pink and pure magenta); Group II including 2 varieties (blue violet and new violet); Group III including 6 varieties (light pink, old violet, new white, old white, light yellow and light violet); Group IV consisting of only 1 variety (cadimi yellow).The results of *in vitro* propagation showed that 7 to 10-day-old flower buds (5 - 7 cm respectively) were efficiently surface sterilized by dipping in 0.1% fresh aqueous mercuric chloride ($HgCl_2$) solution for 6 minutes. MS medium supplemented with 0.5 mg/l BA, 2-3 mg/l KIN, 0.1 mg/l NAA, 30 g/l sucrose, 8 g/l agar gave the best shoot regeneration (10.87shoots).Modified MS medium (reducing NH_4^+ to 75% and replacing $CaCl_2$ with $Ca(NO_3)_2$) was found to be suitable for the shoot growth and development. Root formation was successfully obtained when these shoots were transferred to MS medium supplemented with 0.5 mg/l NAA, 1.0 mg/l BA, 25 g/l sucrose, 9 g/l agar. *The well rooted plantlets* survived (*100*%) after *acclimatization*to the greenhouse. This result is an important database in the conservation of statice genetic resources, as well as provides the necessary information to select mutant breeding of this species in the coming time.

Keywords: *Genetic diversity, in vitro propagation, Limoniumsinuatum L., molecular marker, primer, RAPD-PCR.*

1. INTRODUCTION

Statice (*Limoniumsinuatum* L.) originates from the Mediterranean coastal areas. Before 1975, statice was found in Lam Dong province. This flower is cultivated all year round in Dalat city, which is used for both fresh cut flower and dried flower production. In recent years, the scientists have done a lot of resear n [5]. However, there have not been any reports mentioning genetic identification among the statice varieties in Lam Dong based on DNA molecular markers. Establishing a genetic database and *in vitro* propagation procedures will be important documents for conservation, which is the premise for the research orientation of mutant breeding by ionizing radiation.ch on this species, including hybridization [8], *in vitro* culture [4, 7], optimum density and nutritio

In addition, statice is also one of the flowers labeled Da Lat - Lam Dong flower brand. Therefore, it is essential to build genetic data as a basis for conserving and developing statice varieties. In recent years, the RAPD technology was used to investigate the genetic diversity within and between populations and has been applied to many of plant species. Typically: tomato, raspberry, apple, apricot, orange, grapefruit, barley, peanut (Bogani *et al.,* 1994; Davis *et al.,* 1995; Dubouzet *et al.,* 1997; Mariniello *et al .,* 2002; Dehesdtani *et al.,* 2007; Yong *et al.,* 2006) (*Quoted by Mariniello et al., 2004*) [6]. In this study, we used random amplified DNA polymorphism (RAPD) based on polymerase chain reaction (PCR) to analyze the genetic correlation between salem varieties in Lam Dong. On this basis, this data will complement genetic researchers and breeders. In particular, this result will also be a premise for the research team in selecting the preferred varieties to cause mutation by ionizing radiation in the near future.

2. EXPERIMENTS

2.1. Materials

The Varieties used in the present study are listed in Table 1.The collected leaf samples were separately placed in air lock packs and stored at -80°C for DNA extraction. In addition, young flower buds are used for *in vitro* culture.

Table 1: The selected statice cultivars used in the present study along with region of origin

Ordinal number	Varieties	Cultivar	Symbol
1	Rose Pink	Trai Mat	RP
2	Dark Pink	Van Thanh	DP
3	Light Pink	Thai Phien	LP
4	Pure Magenta	Thai Phien	PM
5	Blue Violet	Da Thien	BV
6	New Violet	Van Thanh	NV
7	Old Violet	HaDong	OV
8	Light Violet	Da Thien	LV
9	New White	Thai Phien	NW
10	Old White	Van Thanh	OW
11	Light Yellow	HaĐong	LY
12	Cadimi Yellow	Trai Mat	CY

2.2. Reagents

DNA extraction: CTAB (2% w/v), 1.4 M NaCl, 100 mMTris (pH 8.0), 20 mM EDTA, chloroform, isopropanol, phenol, isoamylalchohol, SDS 1% (w/v) (Bio Basic Canada Inc.).

RAPD assay: Master mix 2X, primer, DEPC, agarose, GelRed DNA loading buffer, TBE 0.5X, 1kb DNA Ladder, 100bp DNA Ladder (Bioline -UK).

In vitro propagation: salt macro, salt micro, vitamins, hormones used in all experiments powder were purchased from Merck (Germany); agar and sucrose were purchased from the Company and Ha Long Canned Food Joint Stock Company Bien Hoa Sugar, respectively.

2.3. Methods

Total DNA extraction was performed according to Doyle and Doyle (1990) [2] and modified according to Clarke (2009) [1].

A total of 13 RAPD primers were used in the study provided by Operon (Table 2). PCR was performed on ProFlex ™ 3 x 32-well PCR - Applied Biosystems (USA).

Table 2: Nucleotide sequences of random amplified polymorphic DNA (RAPD) markers

Ordinal number	Primer Name	Sequence (5’-3’)
1	OPA-07	5’ – GAAACGGGTG – 3’
2	OPA-08	5’ – GTGACGTAGG – 3’
3	OPA-10	5’ – GTGATCGCAG – 3’
4	OPA-12	5’ – TCGGCGATAG – 3’
5	OPA-15	5’ – TTCCGAACCC – 3’
6	OPA-19	5’ – CAAACGTCGG – 3’
7	OPA-20	5’ – GTTGCGATCC – 3’
8	OPB-03	5’ – CATCCCCCTG – 3’
9	OPB-04	5’ – GGACTGGAGT – 3’
10	OPB-12	5’ – CCTTGACGCA – 3’
11	OPB-19	5’ – ACCCCCGAAG – 3’
12	OPE-14	5’ – TGCGGCTGAG – 3’
13	OPE-18	5’ – GGACTGCAGA – 3’

In vitro propagation:study the effect of flower bud age, surface disinfection time, culture medium, plant growth regulator on shoot multiplication and root formation.

3. RESULTS AND DISCUSSION

3.1. *Random amplified polymorphic DNA* (RAPD)analysis of Limoniumsinuatum L.

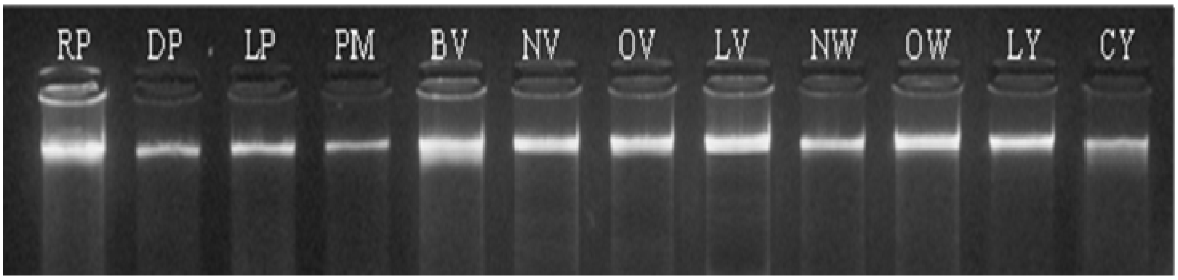

Figure 1: DNA electrophoresis of 12 samples total.

Table 3: Genetic similarity coefficient among 12 statice cultivars obtained from RAPD markers

Genotypes	RP	DP	LP	PM	BV	NV	OV	LV	NW	OW	LY	CY
RP	0											
DP	**0,30**	0										
LP	0,50	0,62	0									
PM	0,52	0,39	0,57	0								
BV	0,66	0,62	0,47	0,44	0							
NV	0,65	0,67	0,63	0,52	0,43	0						
OV	0,51	0,47	0,55	0,47	0,57	0,59	0					
LV	0,64	0,58	0,59	0,48	0,64	0,75	0,54	0				
NW	0,59	0,56	0,51	0,50	0,61	0,66	0,36	0,42	0			
OW	0,72	0,62	0,45	0,57	0,72	0,78	0,51	0,40	0,32	0		
LY	0,82	0,70	0,57	0,77	0,68	**0,90**	0,54	0,52	0,45	0,32	0	
CY	0,59	0,76	0,54	0,70	0,71	0,75	0,68	0,57	0,50	0,54	0,55	0
Mean	**0,59**	**0,60**	**0,54**	**0,55**	**0,62**	**0,74**	**0,53**	**0,48**	**0,42**	**0,43**	**0,55**	**0,55**

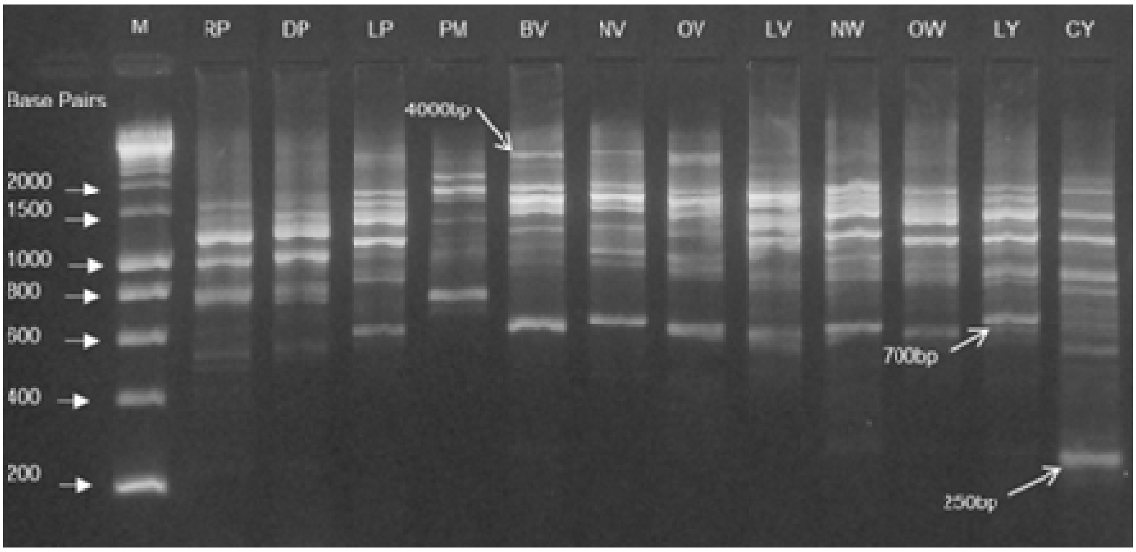

Figure 2: PCR amplification of DNA from 12 statice genotypes with RAPD OPB-03 primer.The polymorphic bands are shown by an arrow symbol.

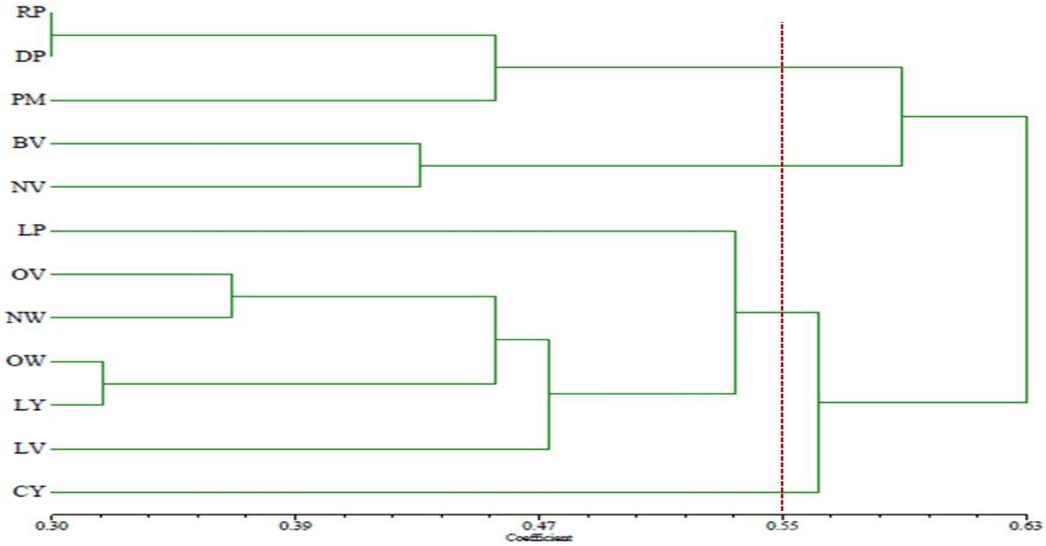

Figure 3: Genetic diversity among the survey sample.

The results of the genetic sequence analysis using NTSYSpc 2.1 showed that 12 varieties of statice were divided into 4 groups: group I consisting of 3 varieties (Rose Pink, Dark Pink and Pure Magenta); Group II including 2 varieties (Blue Violet and New Violet); Group III including 6 varieties (Light Pink, Old Violet, New White, Old White, Light Yellow and Light Violet); Group IV consisting of only 1 variety (Cadimi Yellow).

3.2. In vitro propagation

3.2.1. Effect of surface sterilization and young flower buds on in vitro survival of explants of statice

The effect of mercuric chloride concentration (0.1%) with various exposure periods (3, 4, 5, 6, 7 and 8 minutes) on the survival of explants, the results showed that the highest survival of 76.16% was observed in treatment with 0.1% mercuric chloride for 6 minutes.7 to 10-day-old flower buds (5 - 7 cm respectively) were suitable for the process *in vitro* samples.

3.2.2. Effect of growth regulator and mineral nutrition on in vitro shoot multiplication

** Effect of growth regulator (NAA, KIN and BAP):*

Table 4: Effect of NAA, KIN and BAP on *in vitro* shoot multiplication after 35 days culture

Cytokinin			***Old White***		***Rose Pink***		***Blue Violet***		***Light Yellow***		***Cadimi Yellow***	
BA (mg/l)	KIN (mg/l)	NAA (mg/l)	Shoot percentage (%)	No. of shoots	Shoot percentage(%)	No. of shoots	Shoot percentage (%)	No. of shoots	Shoot percentage (%)	No. of shoots	Shoot percentage (%)	No. of shoots
0.5	2	0.0	100.00^{a*}	5.93^{c}	93.33^{ab}	4.93^{c}	93.33^{ab}	5.33^{c}	100.00^{a}	6.27^{c}	86.67^{bc}	5.00^{d}
0.5	**2**	**0.1**	**100.00^{a}**	**10.87^{a}**	**100.00^{a}**	**7.27^{a}**	**100.00^{a}**	**6.33^{b}**	**100.00^{a}**	**11.00^{a}**	**93.33^{ab}**	**8.20^{ab}**
0.5	**2**	**0.2**	**100.00^{a}**	**10.20^{a}**	**100.00^{a}**	**7.00^{a}**	**100.00^{a}**	**7.20^{a}**	**100.00^{a}**	**10.47^{a}**	**100.00^{a}**	**8.60^{a}**
0.5	2	0.3	100.00^{a}	9.20^{b}	93.33^{ab}	6.60^{b}	93.33^{ab}	5.27^{c}	100.00^{a}	7.27^{b}	86.67^{bc}	6.60^{c}
0.5	2	0.5	80.00^{c}	5.20^{c}	66.67^{c}	5.00^{c}	60.00^{cd}	4.81^{cd}	73.33^{b}	4.40^{d}	60.00^{d}	1.93^{e}
0.5	2	0.7	53.33^{d}	2.27^{e}	40.00^{e}	1.80^{e}	46.67^{e}	1.93^{f}	53.33^{c}	2.33^{f}	46.67^{e}	2.00^{e}
0.5	3	0.0	100.00^{a}	5.93^{c}	93.33^{ab}	5.13	93.33^{ab}	5.20^{c}	100.00^{a}	7.00^{b}	100.00^{a}	5.33^{d}
0.5	3	0.1	100.00^{a}	10.67^{a}	100.00^{a}	7.73^{a}	100.00^{a}	6.47^{b}	100.00^{a}	10.33^{a}	93.33^{ab}	8.00^{b}
0.5	3	0.2	100.00^{a}	9.27^{b}	100.00^{a}	7.27^{a}	100.00^{a}	7.07^{a}	100.00^{a}	10.60^{a}	100.00^{a}	8.07^{b}
0.5	3	0.3	100.00^{a}	5.53^{c}	93.33^{ab}	5.27^{c}	93.33^{ab}	4.67^{d}	100.00^{a}	5.67^{cd}	86.67^{bc}	4.87^{d}
0.5	3	0.5	93.33^{ab}	5.87^{c}	93.33^{ab}	5.00^{c}	93.33^{ab}	5.20^{c}	100.00^{a}	6.33^{c}	80.00^{c}	5.27^{d}
0.5	3	0.7	53.33^{d}	3.33^{d}	60.00^{cd}	3.27^{d}	66.67^{c}	3.33^{e}	73.33^{b}	3.67^{e}	53.33^{de}	2.20^{e}

*Different letters within a column indicate significant differences at P = 0.05 by Duncan's multiple range test.

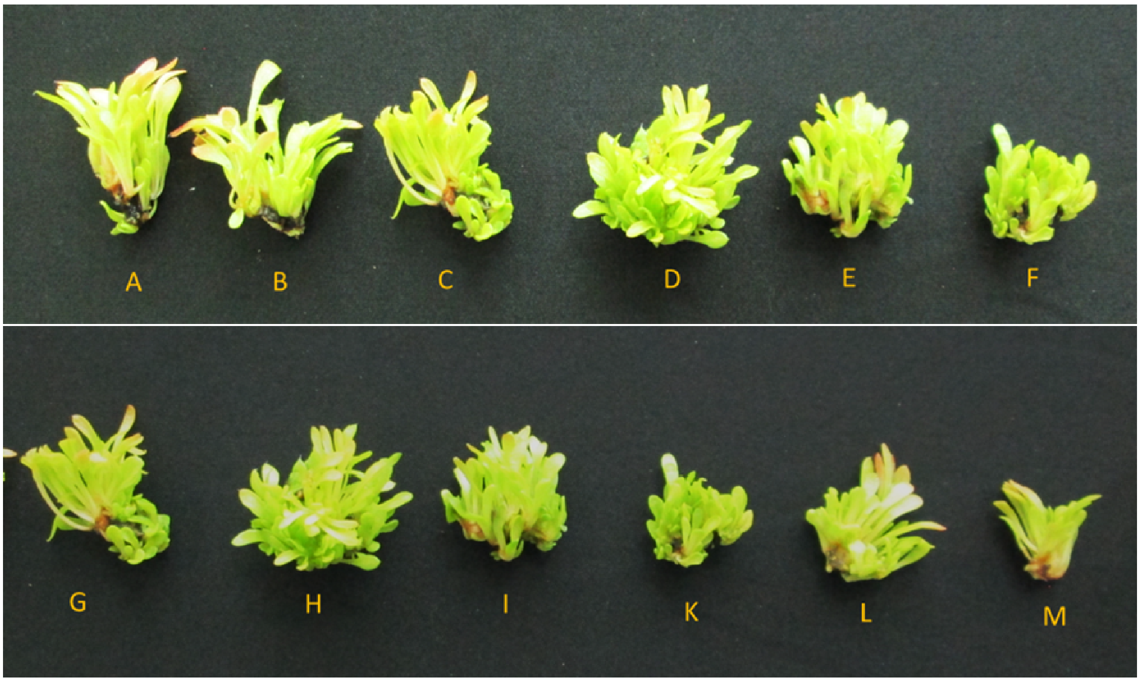

Figure 4: Effect of NAA, KIN and BAP on *in vitro* shoot multiplication. **A**: Treatment with 0.5 mg/l BA và 2 mg/l KIN; **B**: Treatmentwith 0.5 mg/l BA và 2 mg/l KIN và 0.1 mg/l NAA; **C**: Treatment with 0.5 mg/l BA và 2 mg/l KIN và 0.2 mg/l NAA; **D**: Treatment with 0.5 mg/l BA và 2 mg/l KIN và 0.3 mg/l NAA; **E**: NT 0.5 mg/l BA và 2 mg/l KIN và 0.5 mg/l NAA; **F**: Treatment with 0.5

mg/l BA và 2 mg/l KIN và 0.7 mg/l NAA; **G**: Treatment with 0.5 mg/l BA và 3 mg/l KIN; **H**: Treatment with 0.5 mg/l BA và 3 mg/l KIN và 0.1 mg/l NAA; **I**: Treatment with 0.5 mg/l BA và 3 mg/l KIN và 0.2 mg/l NAA; **K**: Treatment with 0.5 mg/l BA và 3 mg/l KIN và 0.3 mg/l NAA; **L**: Treatment with 0.5 mg/l BA và 3 mg/l KIN và 0.5 mg/l NAA; **M**: Treatment with 0.5 mg/l BA và 3 mg/l KIN và 0.7 mg/l NAA.

** Effect of mineral nutrition*

Table 5: Effect of mineral nutrition on *in vitro* shoot multiplication after 35 days culture

Medium	***Old White***		***Rose Pink***		***Blue Violet***		***Light Yellow***		***Cadimi Yellow***	
	Shoot percentage (%)	No. of shoots	Shoot percentage (%)	No. of shoots	Shoot percentage (%)	No. of shoots	Shoot percentage (%)	No. of shoots	Shoot percentage (%)	No. of shoots
2MS	6.67^{b}	0.20^{c}	0.00^{b}	0.00^{c}	13.33^{b}	0.33^{c}	6.67^{b}	0.40^{c}	0.00^{c}	0.00^{c}
MS	100.00^{a}	10.20^{a}	100.00^{a}	7.27^{ab}	100.00^{a}	7.13^{a}	100.00^{a}	10.53^{a}	100.00^{a}	8.60^{a}
1/2MS	100.00^{a}	10.53^{a}	100.00^{a}	7.93^{a}	100.00^{a}	7.27^{a}	100.00^{a}	10.47^{a}	100.00^{a}	8.27^{ab}
3/4MS	100.00^{a}	9.93^{b}	100.00^{a}	7.07^{b}	100.00^{a}	6.73^{ab}	100.00^{a}	10.53^{a}	100.00^{a}	8.07^{ab}
1/4MS	100.00^{a}	10.07^{a}	100.00^{a}	6.67^{b}	100.00^{a}	6.47^{b}	100.00^{a}	9.93^{b}	93.33^{ab}	7.33^{b}

*Different letters within a column indicate significant differences at P = 0.05 by Duncan's multiple range test.

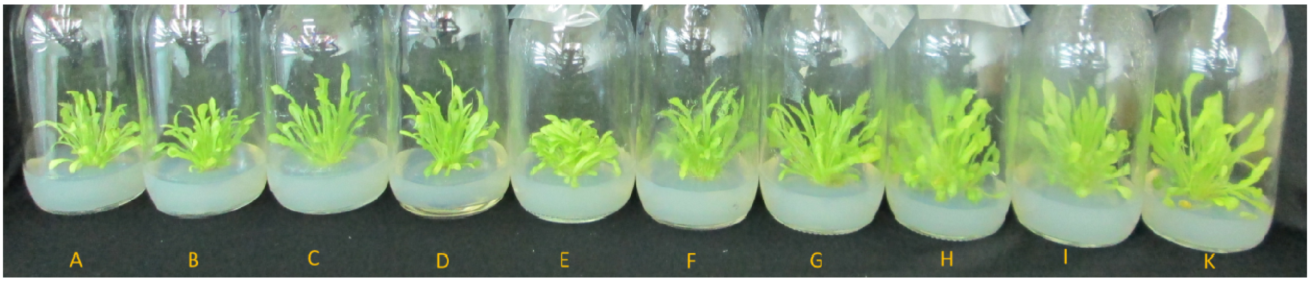

Figure 5: Effect of modified MS medium (reducing NH_4^+ to 75% and replacing $CaCl_2$ with $Ca(NO_3)_2$) on shoot growth and development after 35 days culture. **A**: percentage $NH4^+$: $CaCl_2$ (100: 100); **B**: percentage $NH4^+$: $CaCl_2$ (75: 100); **C**: percentage $NH4^+$: $CaCl_2$ (50: 100); **D**: percentage $NH4^+$: $CaCl_2$ (25: 100); **E**: percentage $NH4^+$: $CaCl_2$ (0: 100); **F**: percentage $NH4^+$: $Ca(NO_3)_2$ (100: 100); **G**: percentage $NH4^+$: $Ca(NO_3)_2$ (75: 100); **H**: percentage $NH4^+$: $Ca(NO_3)_2$ (50: 100); **I**: percentage $NH4^+$: $Ca(NO_3)_2$ (25: 100); **F**: percentage $NH4^+$: $Ca(NO_3)_2$ (0: 100).

3.2.3. Effect of genotypes on in vitro shoot multiplication

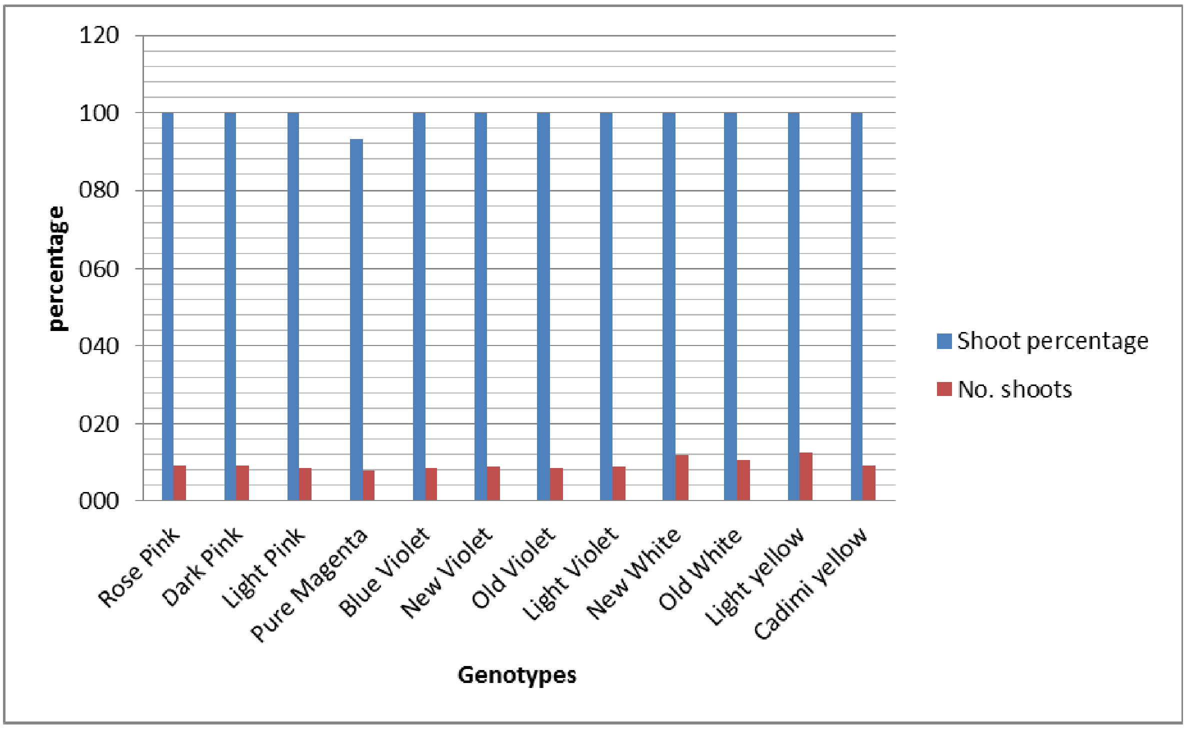

Figure 6: Effect of genotypes on *in vitro* shoot multiplication.

3.2.4. Effect of auxin on in vitro root formation

Figure 7: Effect of combination of NAA and IBA concentration on statice*in vitro* root formation.**A**: control; **B**: 0.5 mg/l NAA and 0.5 mg/l IBA; **C**: 0.5 mg/l NAA and 1.0 mg/l IBA; **C1**: treatment C under the magnifier(4X); **C2**: treatment C under the microscope (10X); **D**: 0.5 mg/l NAA and 2.0 mg/l IBA; **E**: 0.7 mg/l NAA and 0.5 mg/l IBA; **E1**: treatment E under the magnifier (4X); **F**: 0.7 mg/l NAA and 1.0 mg/l IBA; G: 0.7 mg/l NAA and 2 mg/l IBA.

Figure 8: Survival rate of statice grown in greenhouses.**A**: statice rooted *in vitro* (from left to right NAA (mg/l) and IBA mg/l respectively 0.5: 0.5; 0.5: 1; 0.5: 2 and 0.7: 0.5); **B**: Salem after 20 days of culture; **C**: salem after 30 days; **D**: salem after 45 days of culture.

4. CONCLUSIONS

The study results have established the composition and condition for RAPD-PCR reaction of sattice (*Limoniumsinuatum* L.) in Lam Dong. A total of 13 primers RAPD were used to evaluate the genetic diversity of 12 statice genotypes, with a relatively high frequency of polymorphic banding (11.2 bands/primer). Genetic relationships divide 12 genotypes into 4 groups. Thus, statice genotypes in Lam Dong have a high genetic correlation coefficient.

The results of *in vitro* propagation studies have also identified the culture medium, type and concentration of growth regulatorfor shoot multiplication and root formation of all statice varieties in Lam Dong.

REFERENCES

[1] Clarke J.D. (2009). Cetyltrimethyl ammonium bromide (CTAB) DNA miniprepfor plant DNA isolation. *Cold Spring Harbor Protocols* 2009(3): 5177-5178.

[2] Doyle J.J., Doyle J.L. (1990).Isolation of plant DNA from fresh tissue. *Focus* 12: 13-15.

[3] Duncan D. B. (1995). Multiple range and multiple F test. *Biometrics*, 11, 1-42.

[4] Igawa T, Hoshina Y, Mii M (2002). Effcient plant regeneration from cell cultures of ornamental Statice*Limoniumsinuatum*Mill.*In Vitro Cell Dev Plants* 38:157-162.

[5] Jain R, Singh MK, Kishan S, Mahalakshmi, Reddy V, Janakiram T, Prabhat K,Rohit P (2018) Optimization of spacing and nitrogen dose for growth and flowering of statice (*Limoniumsinuatum*). *Ind Jour AgrSci*88(7): 1108-1114.

[6] Mariniello L., Sommella MG, Sorrentino A, Forlani M, and Porta R, (2004). Indentification of *Prunus atmeniaca* cultivars by RAPD and SCAR markers. *Biotechnology Letters*, 24: 749-755.

[7] Nguyen Thi Huyen Trang, Le Thi Thuy Tien (2012). High frequency shoot regeneration of dark blue statice (*Limoniumsinuatum* L. Mill) by combining phytohormones with adenine in *in vitro* culture. *Journal of Biology*, 2012, 34(3SE): 219-226 (*in Vietnamese*).

[8] Morgan ER, Burge GK, Seelye JF, Hopping ME, Grant JE (1998) Production of interspecific hybrids between *Limoniumperezii*(Stapf) Hubb. and*Limoniumsinuatum*(L.) Mill. *Euphytica*102: 109-115.

[9] Murashige T., Skoog F. (1962). A revised medium for rapid growth and bioassays with tobacco tissue culture.*Plant Physiology*, 15, 473-497.

VINATOM-AR 18--15

USING ISOTOPE TECHNIQUES TO EVALUATE THE ABILITY TO ACCUMULATE CO_2 IN THE SOIL OF SOME AGRICULTURAL CULTIVATION MODELS IN THE NORTHERN DELTA

Nguyen Thi Hong Thinh[1], Ha lan Anh[1], Vo Thi Anh[1], Vu Hoai[1], Nguyen Thi Bao My[1], Nguyen Thi Thu Ha[1], Tran Khanh Minh[1] and Tran Minh Tien[2]

[1.] Institute for Nuclear Science and Technology
Hoang Quoc Viet street, Cau Giay district, Ha Noi capital, Vietnam

[2.] Soil and Fertilizers Research Institute,
Dong Ngac, Bac Tu Liem dist., Hanoi, Vietnam

Project information:

- **Code:** ĐTCB.02/16/VKHKTHN
- **Managerial Level:** Ministry
- **Allocated Fund:** 720,000,000 VND
- **Implementation time:** 30 months (Jan 2016- Jun 2018)
- **Contact email:** nhthinh2001@yahoo.com
- **Paper published in related to the project:**

1. Trang K. Trinh, **Thinh T.H. Nguyen**, Tu N. Nguyen, Ta Yeong Wu, Andrew A. Meharg, Minh N. Nguyen, 2017. *Characterization and dissolution properties of phytolith occluded phosphorus in rice straw*. Soil & Tillage Research 171, 19-24.
2. M. N. Nguyen, A. Meharg, M. Carey, S. Dultz, F. Marone, S. B. Cichy, C. T. Tran, G. H. Le, N. T. Mai, **Thinh. T. H. Nguyen.** *Fern, Dicranopteris linearis, derived phytoliths in soil: Morphotypes solubility and content in relation to soil properties*. European Journal of Soil Science, 08 November 2018.
3. **Nguyen Thi Hong Thinh,** Vu Hoai, Ha Lan Anh, Trinh Van Giap, Nguyen Van Vuong. *A procedure of determining carbon-13 composition in soil organic carbon on an Isotope Ratio Mass-Spectrometer*. Nuclear Science and Technology. Vol.8. No.1 (2018), pp.23-28.

Abstract: In this study, Soil organic carbon (SOC) content, some soil properties, and its stable carbon isotopic composition (δ^{13}C) were measured to determine the effect of crops change from maize to rice or vise vera to carbon sequestration in Red River fluvisol soil. In order to better support for the study, the $\square^{13}$C analysis procedure using EA-IRMS system was successfully developed in the Isotope Hydrology Laboratory - Institute for Nuclear Science and Technology. The repeatability of the method is better than 0.3 ‰ and the bias (accuracy) of (0.4 – 0.5) % from standard. The results showed that the amount of C of new plants (rice) contributed to the total soil carbon content of about 9.55 MgC / ha for alluvial soil in Dan Phuong area and 5.24 MgC / ha for gray soil in Dong Anh area when we changed from maize to rice cultivation.

Keywords: *soil organic carbon, δ^{13}C value, rice – maize crop system, isotope ratio mass spectrometer EA- IRMS.*

1. INTRODUCTION

In soil science, soil organic carbon (SOC) plays a very important role in soil structure, soil chemical and physical characteristics and soil fertility (Carter, 2002). In soil-crop ecosystems, SOC storage reflects the net balance between ongoing carbon (C) accumulation resulting from inputs of crop biomass (aboveground, belowground) and/or exogenous organic matter (e.g., manure, straw) and soil C decomposition processes due to microbial oxidation (Tian et al., 2015; Meng et al., 2016)

Stable isotope ratio of $^{13}C/^{12}C$ in SOC ($\delta^{13}C_{SOC}$) - a natural tracer, is given much concern in research areas such as carbon sinks and photosynthetic mechanisms of plants [Baisden et al., 2002], assessing the carbon reservoir turnover times and soil carbon dynamic in agroforestry ecosystems, methods of fixation and storage of carbon dioxide in soils (Accoe et al., 2003, D. Yakir et al., 2000, Garten et al., 2006, Suthisak Saree et al., 2012) or exploring soil mineralization processes (Joann K 2014). Plant species (C3, C4 and CAM plants) differ in their isotopic ^{13}C values due to isotopic discrimination by their photosynthetic enzymes and the regulation of the diffusion resistance of their stomata. C3 plants (rice, wheat, soybean…) have $\delta^{13}C$ average value of -27‰ (-35‰ to -20 ‰), C4 plants (sugarcane, corn ...) have $\delta^{13}C$ average value of -13‰ (-15 to - 7 ‰) (J. Balesdent et al., 1988, Boutton TW et al., 1998). For topsoil calculations, SOM has stable carbon isotopic composition comparable to that of the source plant material and changes in the proportion of C3 and C4 plants will result in a corresponding change in the $\delta^{13}C_{SOM}$. Therefore, $\delta^{13}C$ of SOM can be used to study C turnover in soils in areas where C3 vegetation was replaced by C4 plants or vice versa (Balesdent et al., 1987).

Furthermore, partitioning the contributions of before and after conversion plant types (C3, C4 plant) to the total SOC budget provides a more complete picture of the sustainability of the cultivating land use system, as well as the potential negative implications with regard to nutrient cycling, soil-water relationships, erosion processes, and carbon sequestration. Such information is important to determine impacts of land use on the sustainability of cropping systems, and its feedbacks to future climate changes.

The use of stable C-13 isotope techniques to study above issues is not new to the world but it is still quite new to Vietnam. Therefore, the purpose of this project is: Using isotope techniques to evaluate the ability to accumulate CO_2 in the soil of some agricultural cultivation models in the Northern Delta, Vietnam. The Red River fluvisol soil is one of the main agricultural soils, covering an area of about 600 thousand hectares in Vietnam. This is a type of land that accounts for a large proportion of agricultural land with high C sequestration potential and reduces greenhouse gas CO_2 in agroecosystem.

2. METHOD

2.1. Study site

The experiment was implemented in the cultivated land in the period 2016-2017 at 2 sites: Dan Phuong (21°06’21.0” N, 105°39’45.0” E) and Dong Anh (21°10’19.0”N, 105°47’26.2”E) suburban districts, Hanoi city, Vietnam. This area has been growing two maize crops and one rice crop per year for approximately 10 years.

The experiment site has a monsoon climate with an average annual precipitation of 1721 mm, an average annual temperature of 25.14 °C, atmosphere humidity of 75.58 % and a mean annual sunshine hour of 1207 h. The soil of the experimental site was classified as a Red river alluvial. Rice- rice –maize or maize – rice -maize cropping system was the most important cropping system in the region.

Briefly, rice (Khang Dan 18 variety) and maize (HN88 variety) rotation was planted in plots of 120 m^2 for each with 3 replicates. The experiment included 3 treatments in 2017: (1) initial soil condition (ISC), maize – rice – maize cropping system without plant return; (2) rice – rice – maize cropping system (RRM -NR) without plant return; and (3) rice – rice – maize cropping (RRM - R) with plant return during a 1-year cultivation.

Each cropping season took around 3.5 months. Leaves, stems and roots of maize and rice from the previous crops were ploughed into the soil after harvest. Maize (HN88 variety) was grown with a plant spacing of 25 cm and a row spacing of 75 cm. The chemical fertilizer 16-16-8 (N-P2O5-K2O) was applied for maize at the rate of 500 kg/ha (divided in three times), the 166 kg/ha single fertilizer P2O5 was used 3 days after planting and the single fertilizer K2O was applied 45 days after planting at the rate of 166 kg/ha. Rice seedlings (Khang Dan 18 variety) were transplanted by hand with three plants/hill and a spacing of 20 cm × 25 cm. Fertilizer was applied 3 times with total 416kg/ha chemical fertilizer 16-16-8; broadcast application at the rate of 139 kg/ha 1-3 days after transplanting (DAT), 165 kg/ha at 12-15 DAT and 122 kg/ha at 40-45 DAT. Weed eradication was made at 20 and 50 DAT. Pesticide management of both rice and maize seasons was in accordance with the conventional.

2.2. Sampling

Soil samples were collected at cultivated land at the beginning and before harvesting crops. Soil samples were taken using a core sampler (6 cm i.d.) to a depth of 30 cm and then it was divided into two layers: 0-15 cm and 15 - 30 cm depth. This depth was chosen because it contains most of the root apparatus of rice and maize species. For each crop, three replicates were taken according to a completely randomized experimental design. Each replicate was composed of three subsamples, which were combined. Then, the soil samples were sieved (< 4 mm), visible plant debris were removed, and the soils were then air-dried. On the same date, separate samples (50 mm diameter) of undisturbed soil were taken for a bulk density analysis. The samples are spread on stainless steel trays with the use of a stainless-steel spatula, air-dried at room temperature or dried at 40^{o}C – 50^{o}C in a ventilated oven for two days. Dried soils were homogenized in ceramic mortar and sieved through 1 mm mesh sieve to remove bricks, stones, gravel and roots. Samples were then grounded and sieved through 100 μm mesh sieve; the specimen was dried at 50^{o}C for 24 hours. Finally, samples were subdivided into subsamples for determination pH, soil organic carbon, total N, Total P, total K, and carbon stable isotope components in SOC (^{13}C/^{12}C ratio - $\square^{13}C_{SOC}$).

The plant samples were collected at harvesting time for each crop. About 10 maize plants or 10 rice clusters of each treatment were chosen randomly, rinsed and subdivided into 4 parts: root, stem, leave and seeds. Each plant part was cut into 0.5 -1.0 cm, dried at 40^{o}C - 50^{o}C in a ventilated oven until unchanged weight. Dry mass of each part was determined by weight. The dried plant samples were then grounded and sieved through 100 μm mesh sieve for carbon stable isotope ratio and percent of C.

2.3. Isotope analysis of δ^{13}C in soil and plants by EA-IRMS

Stable carbon isotopic composition - δ^{13}C values (the proportion of ^{13}C with respect to ^{12}C), measured for soil and plant samples were used to determine the contribution of plant carbon source to soil organic carbon. The rice and maize plant samples and those of the soil samples were dried at 60^{o}C, ball-milled, passed though a 100-μm sieve, and fumigated with 12 N HCl overnight to remove carbonates (Ramarine *et al.*, 2011). The δ^{13}C of plant and soil samples was analyzed using isotope ratio mass-spectrometer (IRMS, Micromass GV Instrument, UK) equipped with an elemental analyzer (EA, EuroVector, Italy) at the Isotopes Hydrology Laboratory, Vietnam Institute for Nuclear Sciences and Technology.

The $^{13}C/^{12}C$ isotope ratio is expressed in the delta notation ($\delta^{13}C$) and calculated by the following equation:

$$\delta^{13}C\ (‰) = \left(\frac{R_{\text{sample}}}{R_{\text{standard}}} - 1\right) * 1000 \qquad (1)$$

Where:

R_{sample} is the mole ratio of the $[^{13}C]/[^{12}C]$ in the sample;

R_{standard} is the mole ratio of the $[^{13}C]/[^{12}C]$ in the standard.

The VPDB standard was used. This is Vienna Pee Dee Belemnite supplied by the IAEA in Vienna.

With respect to the different cropping treatments, the δ13C values of the SOM were used to calculate the proportion of new C (f_{new}, i.e., the C derived from current maize/rice residues) and old C ($f_{\text{old}} = 1 - f_{\text{new}}$, soil C present prior to tillage, i.e., C in the initial soil) using a mass balance equation (Balesdent and Mariotti, 1996):

$$f_{\text{new}} = \frac{\delta_{new} - \delta_{old}}{\delta_{\text{veg}} - \delta_{old}} * 100\% \qquad (2)$$

Where δ_{new} represents the $\delta^{13}C$ values of organic C in soil fractions after 1 year of tillage, δ_{old} represents the $\delta^{13}C$ values of organic C in the initial soil, i.e., the soil samples prior to tillage, and δ_{veg} represents the $\delta^{13}C$ values of the mixed samples, including plant materials (maize and/or rice leaves, stems and roots) in both cropping treatment.

2.4. Statistical analysis

Pearson's test allowed us to evaluate correlation coefficient and differences in soil parameter means among tree treatments (soil humidity, bulk density, pH, humic, fulvic, OC, TN, TP, TK and C13 ($\delta^{13}C$) from two soil depths (0–15 and 15–30 cm). All statistical analyses were done with SPSS 20.0.

3. RESULTS AND DISCUSION

1.1 The procedure of determination of $\delta^{13}C$ by EA-IRMS

The procedure included: drying, crushing, sifting and removing carbonate in soil samples before the analysis on the mass spectrometer. The results showed that the fumigation of 12M HCl in 6 hours can completely remove the low carbonate content in soil samples at two depths (0-15cm and 15-30cm, IC ≤ 1%). The developed procedure gained a good repeatability of $\delta^{13}C_{SOC}$ within ± 0.3 ‰. The accuracy of the procedure was checked with analyzing the IAEA-CH-3 cellulose standard.

1.2 Soil property of study area

The average results of main parameters in 0-30 cm soil layer in Dan Phuong and Dong Anh are shown in table 1; 2.

Table 1: The average results of main parameters in Dan Phuong soil

No.	Code	Humidity	Buck density	pH	Humic	Fulvic	OC	TN	TP	TK	C13
		%	(g/cm3)		C (%)	C (%)	C (%)	N (%)	P_2O_5 (%)	K_2O (%)	(‰)
1	CTL 0616 0-15	22.96	1.30	6.08	0.07	0.19	0.66	0.11	0.18	2.19	-24.44
2	CTL 0916 0-15	21.60	1.35	5.32	0.09	0.11	0.68	0.10	0.19	2.47	-24.51
3	CTN 1216 0-15	21.61	1.31	5.09	0.03	0.10	0.60	0.10	0.19	2.41	-24.53
4	CTN 0317 0-15	29.12	1.20	4.76	0.10	0.05	0.63	0.11	0.20	2.48	-24.23
5	CTL 0617 0-15	24.79	1.17	4.86	0.14	0.19	0.71	0.11	0.41	1.54	-24.40
6	CTL 0917 0-15	21.14	1.21	5.30	0.08	0.13	0.75	0.09	0.26	1.85	-24.70
7	CTN 1217 0-15	20.12	1.25	5.56	0.09	0.12	0.72	0.09	0.26	1.90	-24.40
	0-15 cm TB	**23.05**	**1.26**	**5.28**	**0.09**	**0.13**	**0.68**	**0.10**	**0.24**	**2.12**	**-24.46**
	SD	**3.06**	**0.07**	**0.45**	**0.03**	**0.05**	**0.05**	**0.01**	**0.08**	**0.37**	**0.14**
8	CTL 0616 15-30	23.22	1.28	6.46	0.02	0.09	0.38	0.10	0.15	2.58	-22.90
9	CTL 0916 15-30	19.60	1.44	7.48	0.03	0.12	0.39	0.08	0.13	2.41	-22.09
10	CTN 1216 15-	18.41	1.51	7.55	0.02	0.07	0.33	0.06	0.13	2.30	-22.37

	30										
11	CTN 0317 15-30	20.40	1.51	7.09	0.05	0.08	0.33	0.06	0.14	2.73	-21.80
12	CTL 0617 15-30	22.35	1.51	6.69	0.05	0.09	0.37	0.10	0.16	1.52	-22.43
13	CTL 0917 15-30	20.12	1.55	6.69	0.05	0.09	0.38	0.10	0.16	1.52	-22.43
14	CTN 1217 15-30	18.04	1.56	7.40	0.02	0.07	0.36	0.06	0.13	2.25	-22.52
	15-30 cm TB	**20.31**	**1.48**	**7.05**	**0.04**	**0.09**	**0.36**	**0.08**	**0.14**	**2.19**	**-22.36**
	SD	**1.91**	**0.09**	**0.44**	**0.02**	**0.02**	**0.03**	**0.02**	**0.01**	**0.48**	**0.35**

Table 2: The average results of main parameters in Dong Anh soil

No.	**Code**	**Humidity**	**Buck density**	**pH**	**Humic**	**Fulvic**	**OC**	**TN**	**TP**	**TK**	**C13**
		%	(g/cm3)		C (%)	C (%)	C (%)	N (%)	P_2O_5 (%)	K_2O (%)	(‰)
1	CTL 0616 0-15	24.95	1.21	5.32	0.02	0.18	0.58	0.08	0.15	0.17	-24.67
2	CTL 0916 0-15	24.87	1.21	5.83	0.08	0.12	0.59	0.09	0.18	0.18	-24.76
3	CTN 1216 0-15	22.96	1.29	5.72	0.03	0.13	0.45	0.05	0.16	0.16	-24.29
4	CTN 0317 0-15	25.32	1.24	6.17	0.11	0.02	0.60	0.06	0.18	0.15	-24.03
5	CTL 0617 0-15	26.94	1.31	5.86	0.07	0.13	0.56	0.07	0.33	0.13	-24.56
6	CTL 0917 0-15	17.70	1.32	5.46	0.10	0.08	0.74	0.02	0.21	0.13	-25.09
7	CTN 1217 0-15	17.96	1.35	5.52	0.13	0.13	0.73	0.04	0.11	0.16	-27.92
	0-15 cm TB	**22.96**	**1.28**	**5.70**	**0.08**	**0.11**	**0.61**	**0.06**	**0.19**	**0.15**	**-25.05**

	SD	**3.69**	**0.05**	**0.29**	**0.04**	**0.05**	**0.10**	**0.02**	**0.07**	**0.02**	**1.31**
8	CTL 0616 15-30	20.05	1.42	7.48	0.06	0.04	0.22	0.04	0.04	0.40	-21.32
9	CTL 0916 15-30	17.05	1.55	6.46	0.08	0.04	0.19	0.03	0.04	0.25	-21.04
10	CTN 1216 15-30	16.99	1.54	6.16	0.06	0.04	0.29	0.04	0.08	0.16	-21.13
11	CTN 0317 15-30	17.84	1.70	6.36	0.07	0.02	0.28	0.04	0.05	0.24	-22.04
12	CTL 0617 15-30	21.34	1.65	4.32	0.03	0.10	0.25	0.04	0.05	0.20	-22.16
13	CTL 0917 15-30	14.00	1.75	6.80	0.04	0.06	0.31	0.02	0.06	0.14	-22.12
14	CTN 1217 15-30	15.99	1.76	6.65	0.05	0.05	0.29	0.03	0.07	0.13	-22.56
	15-30 cm TB	**17.61**	**1.62**	**6.32**	**0.06**	**0.05**	**0.26**	**0.04**	**0.06**	**0.22**	**-21.77**
	SD	**2.46**	**0.12**	**0.98**	**0.02**	**0.03**	**0.04**	**0.01**	**0.01**	**0.09**	**0.60**

The results showed that the soil in Dan Phuong area has an average annual OC content higher than that of Dong Anh, the value of □^{13}C is also relatively depleted.

1.3 The average values of δ^{13}C and carbon content in plants

The δ^{13}C and C content in rice and maize sample in table 3 showed that cultivated rice plant (C3 plant) and maize plant (C4 plant) have $\delta^{13}C_{VPDB}$ average value of -29.8 ‰ , - 12.5 ‰ , respectively.

Table 3: The average values of δ^{13}C and carbon content in plant samples

Plant type	**Plant parts**	**Dry biomass/1 crop**		**Carbon content/ 1 crop**		**$\delta^{13}C_{VPDB}$**	
		(Mg/ha)	SD	(Mg/ha)	SD	‰	SD
Rice 2016	Stubble+Roots	2.66	0.11	1.10	0.0463	-29.85	0.16
	Stem	5.82	0.33	2.42	0.1374	-29.55	0.18
	leave	2.96	0.07	1.21	0.0270	-29.98	0.17
Rice 2017	Stubble+Roots	2.13	0.15	0.87	0.06	-29.76	0.13
	Stem	5.19	0.41	2.15	0.17	-29.70	0.15
	leave	2.52	0.25	1.03	0.10	-29.83	0.14
Maize 2016	Stubble+Roots	1.56	0.09	0.66	0.04	-12.81	0.21

	Stem	4.21	0.19	1.83	0.08	-12.95	0.19
	leave	3.17	0.19	1.31	0.08	-12.61	0.17
Maize 2017	Stubble+Roots	1.66	0.10	0.69	0.04	-12.50	0.08
	Stem	4.29	0.14	1.81	0.06	-12.47	0.19
	leave	3.28	0.18	1.35	0.07	-12.33	0.24

1.4 Soil organic carbon content and its relation with δ13CSOC

Figure 1 shows the fluctuating carbon content in soil but it tends to increase from June 2016 to September 2019.

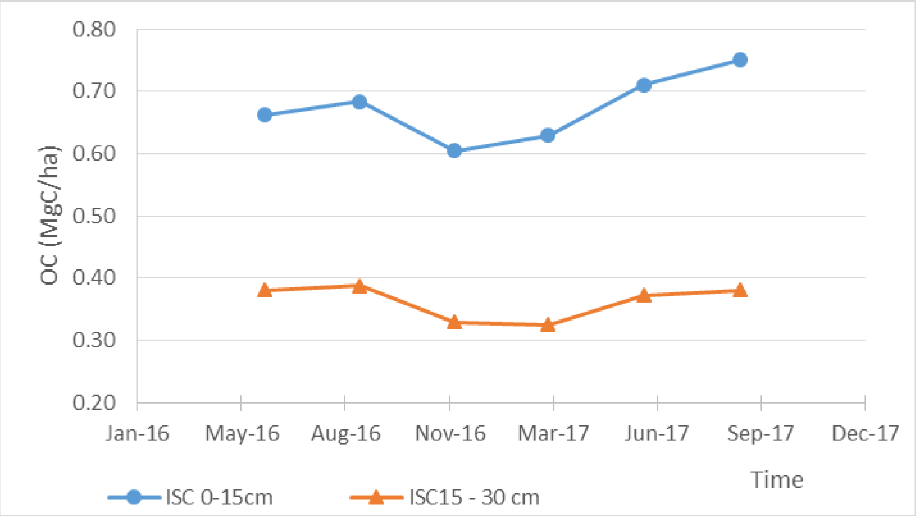

Figure 1: The fluctuating carbon content in Đan Phuong soil

The stable isotope value C-13 in soil samples is closely related to soil C content and divided into 2 ranges corresponding to 2 depths of 0-15 cm and 15 to 20cm (Fig.2)

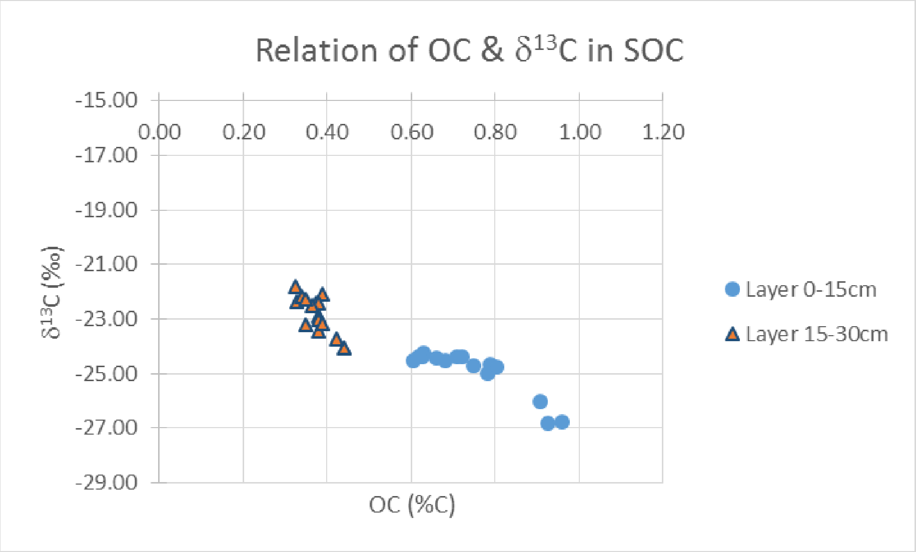

Figure 2: The relation of SOC and δ^{13}C in SOC

1.5 Carbon sequestration potential of rice – maize crop systems

The formula No. 2 was applied to calculate the amount of C accumulated in the 2 soil layers when shifting the 2 maize - 1 rice crops to 2 rice crops in Dan Phuong soil. The results are shown in the following table 4.

Table 4: The accumulated C in the 2 soil layers when shifting the 2 maize - 1 rice crops to 2 rice - 1 corn crops in Dan Phuong an Dong Anh soil

Parameters	**Units**	**Dan Phuong Soil**		**Dong Anh soil**	
		0-15 cm	15-30 cm	0-15 cm	15-30 cm
$\delta^{13}C_{SOMnew}$	‰	-26.78	-23.72	-27.92	-22.56
$\delta^{13}C_{SOM-old}$	‰	-24.40	-22.52	-24.29	-21.13
$\delta^{13}C_R$	‰	-29.79	-29.79	-30.15	-30.15
SOM_{new}	(MgC/ha)	18.27	8.75	14.74	7.74
F	%	44.14	16.46	24.41	21.17
C_{rice} residues	(MgC/ha)	8.065	1.440	3.599	1.638
Total SOM_{new}	(MgC/ha)	9.505		5.238	

According to the above results, the amount of C due to new plants (rice) contributes to the total carbon content in the soil about 9.55 (MgC / ha) in Dan Phuong soil and 5.24 MgC / ha in the East of England at 0-30 cm depth. Most of this plant carbon is concentrated at the 0-15 cm level. Dan Phuong land area is capable of storing C better than Dong Anh area.

4. CONCLUSION

The project has been completed with all the registed contents. The □^{13}C analysis procedure using EA-IRMS system was successfully developed in the Isotope Hydrology Laboratory - Institute for Nuclear Science and Technology. The repeatability of the method is better than 0.3 ‰ and the bias (accuracy) of (0.4 – 0.5) % from standard.

Applying C-13 stable isotope technique in the study of C storage in cropland with 2 rice - 1 corn and 2 corn- 1 rice cultivation models had initial results. In 0-30cm layer, the amount of C of new plants (rice) contributes to the total soil carbon content of about 9.55 MgC / ha for alluvial soil in Dan Phuong area and 5.24 MgC / ha for gray soil in Dong Anh area. Most of this plant carbon is concentrated at the 0-15 cm layer.

Acknowledgement

This work was supported by Ministry of Science and Technology (MOST), Vietnam through the ministerial project code ĐTCB.02/16/VKHKTHN. We would like to express our great appreciation for the finacial support that allowed us to impliment this study.

REFERENCES

[1] Accoe, F., Boeckx, P., Van Cleemput, O. & Hofman, G., 2003. Relationship between soil organic C degradability and the evolution of the δ^{13}C signature in profiles under permanent grassland. *Rapid Communications in Mass Spectrometry*, 17, 2591–2596.

[2] Baisden, W.T., Amundson, R., Cook, A.C., Benner, D.L., 2002. Turnover and storage of C and N in five density fractions from California annual grassland surface soils. Global Biogeochem. Cycles 116, 1117–1122.

[3] Balesdent, J., Mariotti, A., 1996. Measurement of soil organic matter turnover using 13C natural abundance. In: Boutton, T.W., Yamasaki, S.I. (Eds.), Mass Spectrometry of Soils. Marcel Dekker, New York, pp. 83–111.

[4] Boutton TW, Archer SR, Midwood AJ, Zitzer SF, Bol R (1998) $\delta\ ^{13}$C values of soil organic carbon and their use in documenting vegetation change in a subtropical savanna ecosystem. Geoderma 82:5–41.

[5] Carter, M.R.,2002, Soil quality for sustainable land management: organic matter and aggregation interactions that maintain soil functions, Argon, J. 94, 38-47.

[6] D. Yakir, L.da S.L. Sternberg, 2000. The use of stable isotopes to study ecosystem gas exchange. *Oecologia*, 123:297- 311.

[7] Freudenthal, T., Wagner, T., Wenzhofer, F., Zabel, M., Wefer, G., 2001. Early diagenesis of organic matter from sediments of the eastern subtropical Atlantic: evidence from stable nitrogen and carbon isotopes. Geochim. Cosmochim. Acta 65 (11), 1795–1808.

[8] Garten Jr., C.T. & Hanson, P.J., 2006. Measured forest soil C stocks and estimated turnover times along an elevation gradient. *Geoderma*, 136, 342–352.

[9] Joann K. Whalen, Shamim Gul, Vincent Poirier, Sandra F. Yanni, Myrna J. Simpson, et al., 2014. Transforming plant carbon into soil carbon: Process-level controls on carbon sequestration, Can. J. Plant Sci., 94: 1-9.

[10] Mazzilli, S.R., Kemanian, A.R., Ernst, O.R., Jackson, R.B., Piñeiro, G., 2015. Greater humication of belowground than aboveground biomass carbon into particulate soil organic matter in no-till corn and soybean crops. Soil Biol. Biochem. 85, 22–30.

[11] Suthisak Saree, Pancheewan Ponphang-nga, Ed Sarobol, Pitayakorn Limtong and Amnat Chidthaisong, 2012. Soil Carbon Sequestration Affected by Cropping Changes from Upland Maize to Flooded Rice Cultivation, *Journal of Sustainable Energy & Environment*, 3, 147-152.

[12] Tian, K., Zhao, Y., Xu, X., Hai, N., Huang, B., Deng, W., 2015. Effects of long-term fertilization and residue management on soil organic carbon changes in paddy soils of China: a meta-analysis. Agric. Ecosyst. Environ. 204, 40–50.

1.7- Radiation Protection and Radioactive Waste Management

THE STUDY ON PREPARING ABSORBENT OF MESO-POROUS SILICA SBA-15 FROM VIETNAM SODIUM SILICATE FOR RADIOACTIVE CONTAMINATED WASTEWATER TREATMENT

Nguyen Van Chinh[1], Nguyen Ba Tien[1], Le Xuan Huu[1], Vuong Huu Anh[1], Doan Thi Thu Hien[1], Luu Cao Nguyen[1], Nguyen Hoang Lan[1], Duong Dinh Tho[1], Nguyen Dinh Tuyen[2] and Hoang Mai Ha[2]

[1]*Institute for Technology of Radioactive and Rare Elements (ITRRE),*
Vietnam Atomic Energy Institute (VINATOM)

[2]*Institute of Chemistry and Graduate University of Sciences and Technology,*
Vietnam Academy of Science and Technology (VAST)

Project information:

- **Code:** DTCB - 03/17/VCNXH
- **Managerial Level:** Ministry
- **Allocated Fund:** 850,000,000 VND
- **Implementation time:** 24 months (Jan 2017- Dec 2018)
- **Contact email:** chinhitrre@gmail.com
- **Paper published in related to the project:**

1. "***Study on synthesis of mesostructured silica SBA-15 and composite SBA-15/TiO$_2$ nanotube using vietnam sodium silicate for efficient removal of radioactive wastes in aqueous solution***"

Nguyễn Văn Chính[1], Nguyễn Bá Tiến[1], Vương Hữu Anh[1], Đoàn Thị Thu Hiền[1], Cao Đinh Thanh[1], Lê Xuân Hữu[1], Lưu Cao Nguyên[1], Nguyễn Huy Cường[1], Lê Thị Mai Hương[1], Nguyễn Đức Hải[3], Nguyễn Đình Chung[3], Phạm Thái Hưng[3], Hà Phương Long[2,3], Nguyễn Anh Dũng[3], Nguyễn Đình Tuyến[2,3*]

[1]*Institute for Technology of Radioactive and Rare Elements*

[2]*Institute of Chemistry, Vietnam Academy of Science and Technology*

[3]*Graduate University of Science and Technology, Vietnam Academy of Science and Technology*

[4]*Hanoi University of Mining and Geology*

Vietnam Journal of Chemistry, April 2019, 57(2e1,2) 361-367 (In Vietnamese)

2. "***Preparation of mesostructured silica SBA-15 and Fe$_3$O$_4$@SBA-15 using sodium silicate for enhance photocatalytic removal of radioactive uranium (VI) in aqueous solution***"

Phạm Thái Hưng[1], Nguyễn Đức Hải[1], Nguyễn Đình Chung[1], Nguyễn Thị Thu An[2], Hà Phương Long[2], Vũ Duy Hiển[1,2], Nguyễn Ngọc Tuấn[1,2], Ngô Văn Quang[2], Nguyễn Quyết Tiến[1,2], Nguyễn Văn Chính[3], Nguyễn Bá Tiến[3], Cao Đinh Thanh[3], Lê Thị Mai Hương[3], Đỗ Quốc Hùng[4], Nguyễn Đình Tuyến[1,2*]

[1]*Graduate University of Science and Technology, Vietnam Academy of Science and Technology*

[2]*Institute of Chemistry, Vietnam Academy of Science and Technology*

[3]*Institute for Technology of Radioactive and Rare Elements*

[4]*Geological Division ForRadioactive and Rare Elements*

Vietnam Journal of Chemistry, April 2019, 57(2e1,2) 353-360 (In Vietnamese).

3. "***Study on preparation and modification SBA-15 material used for radioactive contaminated waste water treatment from Vietnam glass liquid***"

Nguyễn Văn Chính[1], Lê Thị Mai Hương[1], Ngô Văn Tuyến[1], Vương Hữu Anh[1], Nguyễn Thành Chung[1], Nguyễn Đình Tuyến[2]

[1]*Institute for Technology of Radioactive and Rare Elements, 48 Langha, Dongda, Hanoi Vietnam*

[2]*Institute of Chemistry and Graduate University of Sciences and Technology, Vietnam Academy of Science and Technology*

The Vietnam Conference on Nuclear Science and Technology, 2017, (240) (In Vietnamese)

4. "***Study on adsorption of Th (IV) ion onto mesoporous silica SBA-15 material***"

Nguyễn Văn Chính, Vương Hữu Anh, Lưu Cao Nguyên, Dương Đình Thơ

Institute for Technology of Radioactive and Rare Elements, 48 Langha, Dongda, Hanoi Vietnam

The 5th National Conference on Nuclear Science and Technology for Young Researcher, 2018, (50) (In Vietnamese).

Abstract: Materials of SBA-15 and modified SBA-15 (with Fe_3O_4 and TiO_2) have been synthesized by a new method (short time, low temperature) using cheap materials: Vietnam sodium silicate and sulfuric acid. The SBA-15 material has high surface area (939 m^2/g), average pore diameter of 6.5 nm, wall thickness of 4.1 nm, pore volume of 0,78 cm^3/g.

Materials of SBA-15 and modified composite SBA-15/TiO_2 (mol ratio of Si/Ti = 1) have high adsorption capacity for radioactive ions in solution. The maximum adsorption capacity of bare SBA-15 and modified SBA-15/TiO_2 for U(VI) were 476,19 mg/g and 666,67 mg/g; for Th(IV) were 116,28 mg/g and 222,22 mg/g, respectively.

The experimental results fit well in the Langmuir sorption isotherm model and the kinetic data were described with pseudo-second-order model.

The treatment process of radioactive wastewater released from the processing of uranium ore at the Institute for Technology of Radioactive and Rare Elements (ITRRE) using modified material was shown in laboratory scale.

Keyword: *SBA-15, SBA-15/TiO_2, adsorption, uranium (VI), thorium (IV)*

I. INTRODUCTION

Currently, a large amount of wastewater from the processing of ores containing radioactive elements (U, Th, Ra, ...) is being discharged into the environment but it has not been treated to meet the environmental standards. This wastewater is polluting soil and water in many areas and seriously affecting human health.

Material of SBA-15 has been modified which is high effective compared to the materials of the same type in separating metal ions (Fe, Mn, As, Pb, …) and radioactive ions (U, Th, Ra). The precursor material is low cost Vietnamese sodium silicate, instead of using TEOS - tetraethyl orthosilicate (high cost). Therefore, the study and application of this material to treat radioactive elements (U, Th, Ra , ...) in wastewater in Vietnam will open a new orientation in the treatment of radioactive wastewater today as well as in the future.

In this study, SBA-15 materials were synthesized from Vietnam liquid sodium silicate and sulfuric acid under low temperature conditions (80 ^{0}C) in the laboratory. Using the metal oxides of Fe_3O_4 and TiO_2 with SBA-15 to improve the efficiency of phase separation, adsorption capacity of radioactive ions was studied. Finally, modified processes of SBA-15 materials and the application process of materials SBA-15 to treat wastewater released from uranium ore processing (containing the radioactive elements: U, Th and Ra) were shown in the laboratory scale.

II. EXPERIMENTAL

2.1. Determining sodium silicate module

8 g of P123 was dissolved in 190 mL of distilled water and 37 g sodium silicate (the molar ratio of X:1 (X= 1, 2, 3)), followed by stirring at 40 °C to get a transparent solution. Then 10g of concentrated sulfuric acid was quickly added to the P123 – sodium silicate solution under stirring vigorously. The mixture was stirred for 18 hours. Consequently, the mixture was put into a 1000 mL PP bottle, then hydrothermally treated at 100 °C for 20 hours. The solid products were washed, filtered dried, and calcined under air at 550 °C for 5 hours.

2.2. Determining surfactant P123, F127, Brij 56

The experiments were similarly conducted to what were carried out in the section of 2.1, using the charged surfactants of P123, F127 and Brij 56 with the weights of 8g, 4g and 16g, respectively.

2.3. Determining ratio of sodium silicate/ surfactant

The experiments were similarly conducted to what were carried out in the section of 2.1 with samples of S1, S2, S3 and S4 prepared by changing the sodium silicate/ surfactant mass ratio of 2.9; 3.5; 4.0; 4.5 to determine the optimal ratio of sodium silicate/ surfactant.

2.4. Determining aging temperature

The experiments were similarly conducted to what were carried out in the section of 2.1, but differed in the aging temperatures: 40, 60, 80 and 100 ^{0}C.

2.5. Synthesis of modified SBA-15 materials (with Fe_3O_4 and TiO_2)

➢ **Synthesis of TiO_2**: 292 g of NaOH was dissolved in 630 ml of distilled water and stirred. Then 30 g of TiO_2 evenly distributed in 70 mL ethanol was into solution and stirred vigorously for 30 minutes. TiO_2 was mixed in ultrasonic bath with NaOH 10M for 1 h, then transferred to a teflon-flask for hydrothermal treatment at 150°C for 24 h. The mixture was cooled and neutralized with 800 ml of 1M HCl acid, filtered and washed for pH = 7; the solid product was dried at 120 ^{o}C for 2h, and calcined under air at 300 °C for 3 h.

➢ **Synthesis of modified SBA-15 materials (with Fe_3O_4 and TiO_2)**

Surfactant was dissolved in distilled water, then sodium silicate was slowly added to the solution. Fe_3O_4 or TiO_2 was added into the solution and stirred for 30 minutes. Stirring vigorously and adding quickly concentrated sulfuric acid, the solution was stirred for 18 h. Consequently, the mixture was put into a 1000 mL PP bottle, then hydrothermally treated at 100 °C for 20 h. The solid products were filtered, washed, dried, and calcined under air at 550 °C for 5 h (Fe_3O_4@SBA-15 or SBA-15/TNT).

2.6. Influence of pH to adsorption capacity of materials for U(VI) and Th(IV) ions

5 mg of SBA-15 or modified SBA-15 and 50 mL of uranium or thorium solution at pH of 2 to 8 were put into a 100 mL triangular vase. The triangular vases were horizontally shaken at 120 rpm, 25 ^{o}C for shaking time 24 h. After filtering the solid-liquid phase, the concentrations of U(VI)

or Th(IV) ions were measured by ICP-OES. Adsorption capacity was defined as following formula:

$$q = \frac{C0-C}{m} V \text{ (mg/g)} \quad (1)$$

where: C_0, C is initial concentration and equilibrium concentration of U(VI) or Th(IV) ions, respectively (mg/L), V is volume of solution (L), m is the amount of adsorbent (g).

2.7. Influence of contact time to adsorption capacity of materials for U(VI) and Th(IV) ions

The experiments were similarly conducted to what were carried out in the section of 2.1, using optimal pH in the section of 2.6. The triangular vases were horizontally shaken at contact times of 30 minutes to 24h. Adsorption capacity was defined as formula (1).

2.8. Determining absorption capacity of materials for U(VI)

The experiments were similarly conducted to what were carried out in the section of 2.1, using optimal pH in the section of 2.6, balanced adsorption time in the section of 2.7. Initial concentration of U(VI) was changed from 20mg/l to 300mg/l. Adsorption capacity was defined as formula (1).

2.9. Determining absorption capacity of materials for Th(IV)

The experiments were similarly conducted to what were carried out in the section of 2.1, using optimal pH in the section of 2.6, balanced adsorption time in the section of 2.7. Initial concentration of U(VI) was changed from 10mg/l to 150mg/l. Adsorption capacity was defined as formula (1).

2.10. Determining absorption capacity of materials for Ra(II)

Wastewater released from uranium ore processing at the laboratory was precipitated at pH of 8, then the solid-liquid phase was filtered. After that 50 ml of liquid phase and 5 mg of SBA-15 or modified SBA-15 were put into a 100 mL triangular vase. The triangular vases were horizontally shaken at 120 rpm, 25^oC for shaking time 24h. Followed by filtering the solid-liquid phase. The total activity of α, β of the wastewater before and after adsorption were measured to determine the adsorption capacity of Ra on the materials.

2.11. The treatment process of radioactive wastewater released from the processing of uranium ore

The process was built by batch process at the laboratory scale. Wastewater from laboratory of the Center of Radioactive Ore Processing Technology – Institute for Technology of Radioactive and Rare Elements (ITRRE) was treated according to 2 main stages:

+ **Stage 1**: Precipitation: Wastewater was precipitated at pH of 8 by lime milk of 20% và PAC of 10% and polymer A101 of 0,2% to improve the efficiency of solid-liquid phase separation;

+ **Stage 2**: Using modified SBA-15 material for adsorbtion of the remaining radioactive ions in the waste water.

Concentrations of ions and total activity of α, β in wastewater after each treatment stage were analyzed to check the quality.

III. RESULTS AND DISCUSSION

3.1. Determining sodium silicate module

Figure 3.1 presents the X-ray diffraction patterns of calcined SBA-15 samples prepared with different moduli. It shows that all samples exhibit three well-resolved peaks, which can be indexed as (100), (110) and (200) diffractions of a P6mm hexagonal symmetry, which are typical for of meso-porous material. The peak intensity increases when the module increases, which showed that a higher order structure can be obtained in a higher module. This phenomenon is mainly due to different types of silica agglomeration in different modules. In general, the interaction between poly silicate anion and surfactant facilitates the formation of highly ordered SBA-15 materials.

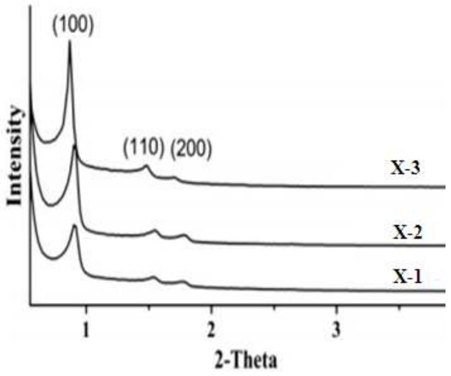

Figure 3.1: XRD patterns of the SBA-15 samples synthesized at different moduli

3.2. Determining surfactant P123, F127, Brij 56

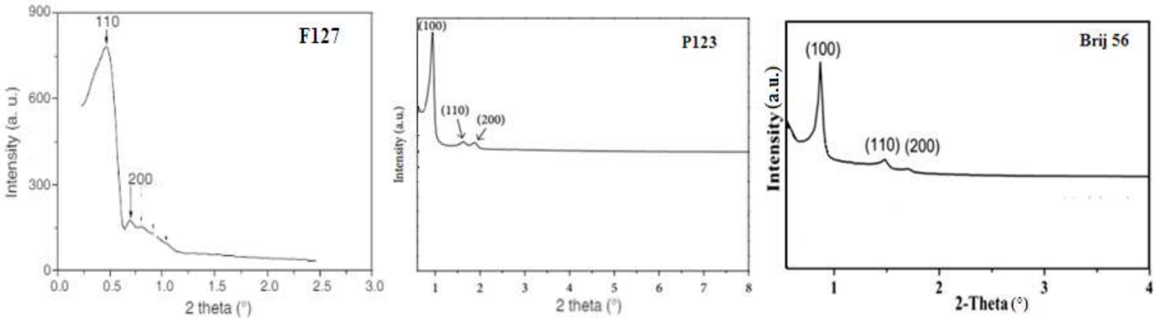

Figure 3.2: XRD patterns of the SBA-15 samples synthesized by F127, P123, Brij 56

XRD patterns of the SBA-15 samples synthesized by F127, P123, Brij 56 were shown in Fig 3.2, materials were synthesized by P123 and Brij 56, which has a strong intensity peak along with two weak intensity peaks, which is typical for a hexagonal structure. However, the XRD pattern of the material synthesized by F127, showed a cube structure.

3.3. Determining ratio of sodium silicate/ surfactant

Figure 3.3 showed that, the reflectance intensity (100) was low and there won't clear reflection (200). The disappearance of these reflections showed that material with a higher sodium silicate/ surfactant ratio has lower order structure than materials with a lower sodium silicate/ surfactant ratio. However, Table 3.1 showed that when sodium silicate/ surfactant ratio increased, the surface area decreased and the wall thickness increased.

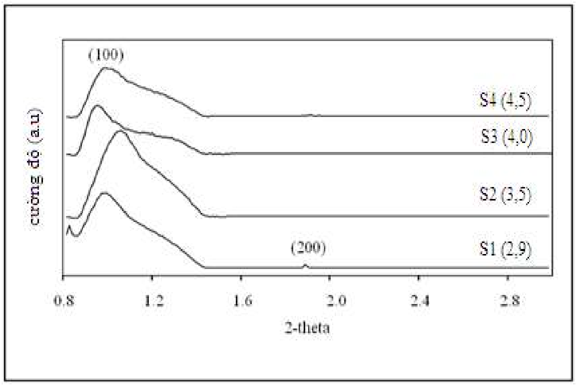

Figure 3.3: XRD patterns of the SBA-15 samples synthesized at various sodium silicate/ surfactant ratio

Table 3.1: Characteristic of SBA-15 materials synthesized at various silicate/ surfactant ratio

Samples	$\mathbf{S_{BET}}$ (m^2/g)	$\mathbf{d_{pore}}$ (nm)	$\mathbf{V_{pore}}$ (cm^3/g)	**W** (nm)
S1 (2,9)	669	4,95	0,5	6,59
S2 (3,5)	536	4,86	0,42	6,62
S3 (4,0)	520	4,57	0,42	6,70
S4 (4,5)	510	4,35	0,35	6,76

3.4. Determining aging temperature

Figure 3.4 showed that samples have diffraction peak (100) with high intensity and sharpness at angle 2θ <1°. This is a typical pattern of meso-porous materials. In addition, XRD pattern also appeared two peaks corresponding to the diffraction (110), (200). They are typical for high order hexagonal structure 2-dimensional P6mm. SBA-15 at 40 °C showed only one peak in this area, indicating 2D P6mm hexagonal structure of material SBA-15 at 40 °C with lower order structure.

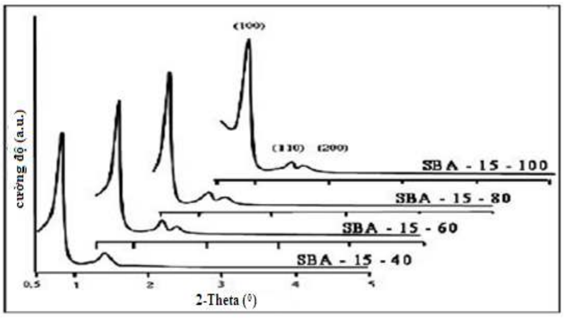

Figure 3.4: XRD patterns of the SBA-15 samples synthesized at various aging temperature

Table 3.2: Characteristic of SBA-15 materials synthesized by various aging temperature

Samples	**Aging temperature**, ^0C	$\mathbf{S_{BET}}$, m^2/g	$\mathbf{d_{pore}}$, nm	**W**, nm	$\mathbf{V_{pore}}$, cm^3/g
SBA-15 – 40	40	488	6,0	3,5	0,579
SBA-15 – 60	60	589	6,4	3,9	0,654
SBA-15 – 80	80	665	8,2	4,0	0,898
SBA-15 – 100	100	649	9,5	2,9	0,912

Table 3.2 showed that when the aging temperature increased from 40 °C to 80 °C, the average diameter pore and overall volume pore increased, leading to the increase of wall thickness W and surface area S_{BET} increase. When aging temperature increased to 100 °C, although diameter pore and overall volume pore Vpore increased, the wall thickness W, surface area S_{BET} decreased.

3. 5. Characterization of SBA-15 and modified SBA-15 materials

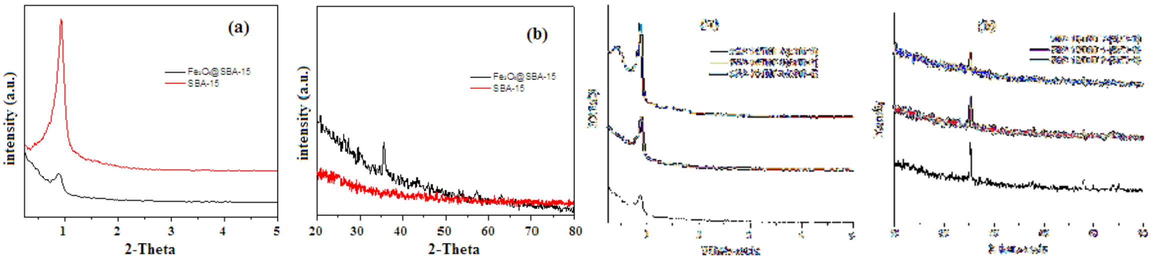

Figure 3.5: XRD patterns of the SBA-15 samples (Fe_3O_4@SBA-15 và SBA-15/TNT)

Figure 3.5 showed that modified SBA-15 samples (with Fe_3O_4 or TiO_2) still have meso-porous structure, and the Fe_3O_4 or TiO_2 were in the structure of materials. This proved that the materials of Fe_3O_4@SBA-15 and composite of SBA-15/TNT were successfully synthesized.

Table 3.3: Characteristic of SBA-15 and modified SBA-15 materials

Materials	**d**$_{\textbf{pore}}$, (nm)	**W**, (nm)	**S**$_{\textbf{BET}}$, (m^2/g)	**V**$_{\textbf{pore}}$, (cm^3/g)
SBA-15	6,5	4,1	939	0,78
Fe_3O_4@SBA-15	14,0	5,4	332	1,00
SBA-15/TNT-2 (Si/Ti = 4)	6,6	4,3	819	1,30
SBA-15/TNT-4 (Si/Ti = 2)	14,8	4,5	491	1,34
SBA-15/TNT-7 (Si/Ti = 1)	14,4	4,9	414	1,37

Table 3.3 showed that SBA-15 and modified SBA-15 materials have large surface areas of 300 - 900 m^2/g, pore diameter of 6 -15 nm. However, testing uranium (VI) adsorption capacity on 4 modified materials (as in the table 3.3) showed that SBA-15/TNT-7 has the highest adsorption capacity, so SBA- 15/TNT-7 was used to study the process of adsorption of radioactive elements in wastewater.

3.6. Influence of pH to adsorption capacity of materials for U(VI) and Th(IV) ions

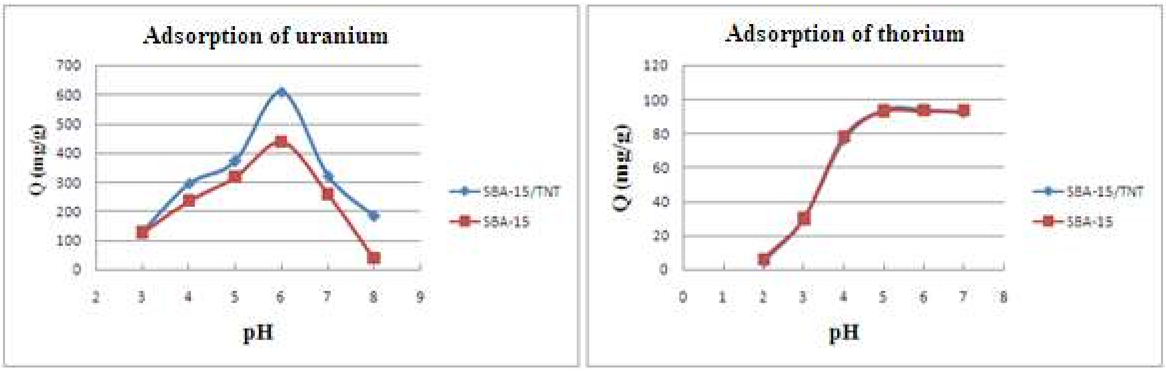

Figure 3.6: Influence of pH on adsorption capacity of materials

Figure 3.6 showed that the optimal pH for U(VI) and Th(IV) adsorption processes were 6 and 5, respectively.

3.7. Influence of contact time to adsorption capacity of materials for U(VI) and Th(IV) ions

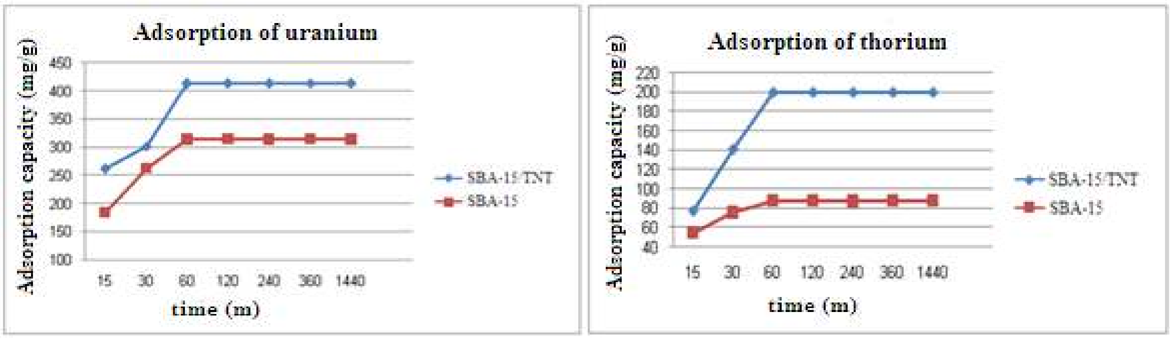

Figure 3.7: Influence of contact time on adsorption capacity of materials

Figure 3.7 showed that adsorption of U(VI) and Th(IV) on SBA-15 and SBA-15/TNT materials reached balance after 60 minutes.

3.8. Determining adsorption capacity of materials for U(VI)

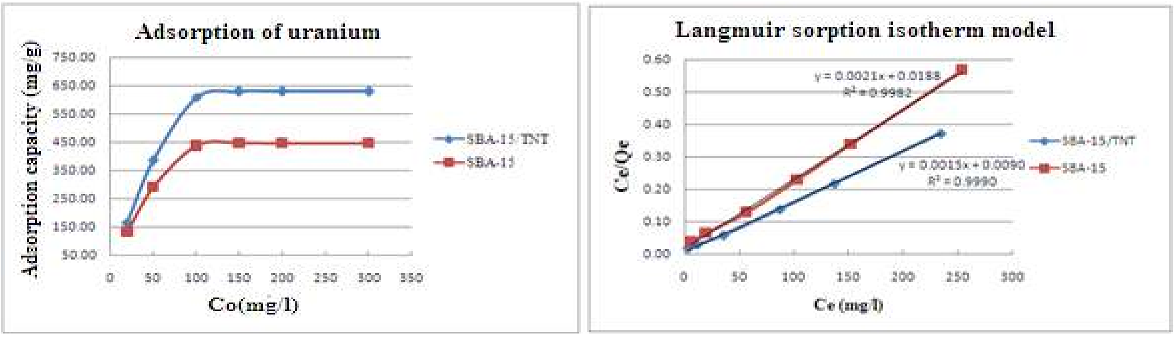

Figure 3.8: Adsorption capacity and Langmuir sorption isotherm model of materials for U(VI)

Figure 3.8 shows that adsorption on SBA-15 and SBA-15/TNT for uranium fit very well to the Langmuir adsorption isotherm model with correlation coefficients of 0,9982 and 0,9990, respectively. From that maximum adsorption capacity on SBA-15 and SBA-15/TNT for uranium were calculated 476,19 (mg/g) and 666,67 (mg/g), respectively.

3.9. Determining adsorption capacity of materials for Th(IV)

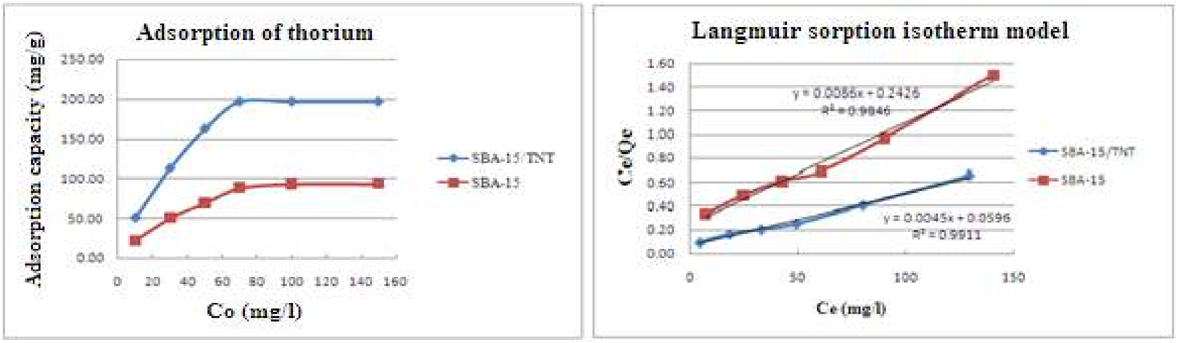

Figure 3.9: Adsorption capacity and Langmuir sorption isotherm model of materials for Th(VI)

Figure 3.9 showed that adsorption on SBA-15 and SBA-15/TNT for thorium fit very well to the Langmuir adsorption isotherm model with correlation coefficients of 0,9846 and 0,9911, respectively. Accordingly, maximum adsorption capacity on SBA-15 and SBA-15/TNT for thorium reached 116,28 (mg/g) and 222,22 (mg/g), respectively.

3. 10. Determining adsorption capacity of materials for Ra(II)

The results of adsorption capacity of Ra (by the method of total radioactivity measurement) on SBA-15 and SBA-15/TNT materials for real wastewater samples (containing mainly Ra) were shown in the Table 3.4.

Table 3.4: Results adsorption capacity on materials for radium

Materials	**pH**	**Volume** (L)	**Adsorbent** (g)	**Time** (m)	**Initial activity** (Bq/l)	**Balance activity** (Bq/l)
SBA-15/TNT	7	0,05	0,005	60	11	0,055
SBA-15	7	0,05	0,005	60	11	0,43

Table 3.4 showed that SBA-15 and SBA-15/TNT materials were able to adsorb well radium in the water. This result is very useful for the calculation and design of a wastewater treatment system for the processing of uranium ore in particular and the processing of ore containing radioactive elements in general.

3.11. The treatment process of radioactive wastewater from the processing of uranium ore

The process of treating wastewater from the processing of uranium ore was built by batch method (scale of 5 L/batch scale), includes the following steps:

Step 1: Precipitation: Wastewater from laboratory of the Center of Radioactive Ore Processing Technology – Institute for Technology of Radioactive and Rare Elements was contained in containers. 5 liters of wastewater were put into a 10 liter container.

+ Using a pH meter to check the pH of waste water before precipitation (input wastewater usually has pH = 1.8 ÷ 2.2)

+ The tank of wastewater was stirred with a stirring speed of about 500 rpm

+ Precipitation: by 250 mL milk of lime 20%

+ Stirring well for 10 minutes, then reducing the stirring speed to 300 rpm and adding 200 mL of PAC solution 10% into the solution

+ After 10 minutes of stirring, adding 60 ml of polymer 0.2% to improve the efficiency of solid-liquid phase separation

+ Waste water was stirred for 5 minutes then stop stirring and taking stirring device out of the container

Step 2: Solid-liquid phase separation: A process of sludge filtration after preliminary precipitation with a cloth filter bag was conducted to collect the solution containing radioactive elements and heavy metal elements that were not precipitated. The waste sludge was moved to the stage of solid waste treatment (cementation);

Step 3: Adsorption by modified SBA-15 materials: 4 liters of solution obtained from step 2 were stirred at a stirring speed of 300 rpm

+ 0,2g modified SBA-15/TNT material was added to the solution and then stirred for 2h.

+ Then stirring and precipitating for 30 minutes

Step 4: Solid-liquid phase separation: Because of easy precipitation of SBA-15 material, after 30 minutes, the solution after adsorption was taken and tested. The adsorbed material was treated as solid waste.

Step 5: The characteristics of wastewater were analyzed by ICP-MS analyzer and total activity α, β measuring device; if the wastewater after radioactive treatment meets QCVN 40: 2011/BTNMT standards, it will be discharged to the environment, if not, it will be returned to adsorption again.

Table 3.5: Results wastewater of characteristics after processing steps

	Unit	Feed	After precipitation	After adsorption	Column B QCVN 40:2011/BTNMT
pH		2,2	7	7	5,5 – 9
Al	mg/l	557,0	<0,06	<0,06	-
Fe	mg/l	1055,0	<0,03	<0,03	5
Cu	mg/l	2,4	<0,01	<0,01	2
Zn	mg/l	132,6	0,3	0,014	3
As	mg/l	1,6	<0,06	<0,06	0,1
Pb	mg/l	<0,01	<0,01	<0,01	0,5
Mg	mg/l	179,0	71,3	3,049	-
Mn	mg/l	368,0	79,3	0,613	1
Ni	mg/l	3,3	<0,01	<0,01	0,5
U	mg/l	94,6	0,6	0,24	-
Th	mg/l	3,2	0,02	0,002	-
Total activity α	Bq/l	1494	1,26	0,066	0,1
Total activity β	Bq/l	1281	9,24	0,58	1,0

Table 3.5 showed that after treatment, the wastewater met column B QCVN 40: 2011/BTNMT standards, allowing to discharge into the environment.

IV. CONCLUSIONS

The results from this work were as follows:

1. Meso-porous silica material SBA-15 was successfully synthesized using Vietnam sodium silicate and sulfuric acid. The quality of SBA-15 produced from this work is as high as the quality of commercial products in the world.

2. The synthesis and modification of SBA-15 materials with Fe_3O_4 and TiO_2 and treating process of wastewater released from the processing of uranium ore with modified SBA-15 material were shown in this study.
3. 03 articles in national journals and 02 scientific reports in conferences were published.
4. Supported for training one PhD in the field of chemistry technology.
5. Adsorption of uranium and thorium on SBA-15 and SBA-15/TNT were studied. The maximum adsorption capacity of uranium on SBA-15 and SBA-15/TNT were 476.19 (mg/g) and 666.67 (mg/g), respectively. The maximum adsorption capacity of thorium on SBA-15 and SBA-15/TNT were 116.28 (mg/g) and 222.22 (mg/g), respectively.

REFERENCES

[1] Nguyen Đinh Tuyen, Le Thi Hoai Nam (2007), "*Research on synthesis of Ti-SBA-15 materials from Vietnam sodium silicate and catalytic properties in α-pinene oxidation reactions*", Vietnam Journal of Chemistry T.45 (5), 565-569.

[2] K C Souza, "*Mesoporous silica–magnetite nanocomposite synthesized by using a neutral surfactant"*, Nanotechnology, 2008.

[3] Mohammad Reza Yaftian, "*Adsorption characteristics of Eu(III) and Th(IV) ions onto modified mesoporous silica SBA-15 materials"*, Journal of the Taiwan Institute of Chemical Engineers, 2015.

[4] Wang Xinghui, Zhu Guiru,Guo Feng, "*Removal of uranium (VI) ion from aqueous solution by SBA-15",* Annals of Nuclear Energy, (2013) 151-157.

[5] Zhao D., Huo Q., Feng J., Chmelka B. F., Stucky G. D., (1998), "*Noionic Triblock and Star Diblock Copolimer and oligomeric Surfactant Syntheses of Highly ordered, Hydrothermally Stable, Mesoporous Silica Structures*", Journal of the American Chemical Society, 120, pp. 6024-6036.

[6] Zhao D., Feng J., Huo Q., Melosh N., Fredrickson G. H., Chmelka B. F., Stucky G. D., (1998), "*Triblock Copolymer Syntheses of Mesoporous Silica with Periodic 50 to 300 Angstrom Pores*", Science, 279, pp. 548-552.

VINATOM-AR 18--17

GEOMETRY CORRECTIONS FOR CYLINDRICAL AND RECTANGULAR NEUTRON MEASURING DEVICES WITH ^{241}AM-BE SOURCE

Nguyen Ngoc Quynh, Bui Thi Anh Duong, Bui Duc Ky, Duong Van Trieu,
Ho Quang Tuan and Tran Thanh Ha.

Institute for Nuclear Science and Technology,
179 Hoang Quoc Viet, Cau Giay, Hanoi

Project information:

- **Code:** CS/18/04-02
- **Managerial Level:** Institute
- **Allocated Fund:** 70,000,000 VND
- **Implementation time:** 12 months (Jan 2018- Dec 2018)
- **Contact email:** *nnquynh.inst@gmail.com*
- **Paper published in related to the project:**

Nguyen Ngoc Quynh et. al., 2018. Geometry Correction Factor for Cylindrical Neutron Devices with ^{241}Am-Be Source. The 5th Conference on Nuclear Science and Technology for Young Researchers*, 2018 (in Vietnamese).*

Abstract: In calibration of neutron sensitive devise, geometry correction need to be performed due to finite size of source and/or devices. Geometry correction factor for device with spherical moderating is well studied but not for other shape of moderating. In this study, geometry correction for cylindrical and rectangular neutron devices with ^{6}LiI(Eu) detector were simulated using MCNP code. The results will be applied for neutron calibration procedure in Institute for Nuclear Science and Technology (INST).

Keywords: *Geometry correction, cylindrical neutron device, rectangular neutron devices, MCNP6*

1. INTRODUCTION

In order to calibrate a neutron measurement device, methods described in the ISO 8259-2 standard [1] implies a number of corrections applied to the device reading. These corrections were summarized in the following equation:

$$M_T = \frac{k}{l^2}.F_L.F(\theta).F_1(l).F_S(l) \qquad (1)$$

where M_T represents the uncorrected reading of device, *k* represents the source-detector characteristic constant, l represents the distance from source center to point of test, F_L represents the linearity correction,$F(\theta)$represents the anisotropy correction, $F_1(l)$ represents the geometry correction, and $F_S(l)$ represents the scatted neutron correction.

Geometry correction factor spherical devices irradiated by point sources, based on Axton's theory and published by Hunt was well-established, and can be calculated by the following equation:

$$F_1(l) = 1 + \delta.\left\{\frac{2l^2}{r_D^2}\left[1 - \left(1 - \frac{r_D^2}{l^2}\right)\right] - 1\right\} \qquad (2)$$

where $\delta = 0.5 \pm 0.1$ represents the neutron effectiveness parameter, $l$represents the distance from source to detector center, and r_D represents the radius of the detector.

However, regarding the non-spherical device (*i.e.* cylindrical devices, rectangular devices), ISO 8529-2 gives only a guidance that the distance l should be greater than twice the diameter of the device. This limitation in the standard is acknowledged but there're few publications addressed this problem [2,3]. In this work, the geometry correction factor for cylindrical and rectangular devices irradiated side-on was simulated by the Monte Carlo code MCNP6 [4].

2. MATERIALS AND METHODS

2.1 Simulation of geometry correction factor

Two source-detector geometries were simulated: isotropic point source and planar rectangular source. The point source was located at various distance, from the detector's surface to 300 cm from the detector. In all simulation, neutron spectrum of ^{241}Am-Be was used and was taken from ISO 8529-1 [5]. The model of cylindrical devices consists of cylindrical moderator and The model of rectangular consists of rectangular moderator. The moderator is polyethylene of 0.95 g/cm^3. At the centre of these moderator, a 4 mm diameter x 4 mm cylindrical ^{6}LiI(Eu) scintillator enriched to 96% of^{6}Li (density of 3.84 g/cm^3). The dimensions of cylindrical and rectangular moderators were presented in table 1 and 2.

Table 1: Dimension of cylindrical moderators

Name	C1	C2	C3	C4	C5	C6	C7
Height (cm)	2,7	4,1	t,2	10,4	16,6	20,7	24,8
Diameter (cm)	3,0	4,6	6,9	11,5	18,4	23,0	27,6

Table 2: Dimension of rectangular moderators

Name	**Width** (cm)	**Length** (cm)	**Height** (cm)	**Name**	**Width** (cm)	**Length** (cm)	**Height** (cm)
H1	10	10	10	H16	15	15	30
H2	10	10	15	H17	15	20	20
H3	10	10	20	H18	15	20	25
H4	10	10	25	H19	15	20	30
H5	10	10	30	H20	20	20	20
H6	10	15	15	H21	20	20	25
H7	10	15	20	H22	20	20	30
H8	10	15	25	H23	20	25	25
H9	10	15	30	H24	20	25	30

H10	10	20	20
H11	10	20	25
H12	10	20	30
H13	15	15	15
H14	15	15	20
H25	20	30	30
H26	25	25	25
H27	25	25	30
H28	25	30	30
H29	30	30	30

Geometry correction factor was determined by ratio of the detector response under plane-parallel condition to the one under divergent condition. Detector response can be calculated via number of reactions (n,α) in ^{6}LiI crystal which was simulated by MCNP6. Number of reactions (n,α) was determined by the follow equation:

$$M = \Phi . n_{Li} . V_{crystal} . \sigma_{(n,\alpha)} \quad (3)$$

where M represents number of reaction (n,α), Φ represents neutron fluence, n_{Li} represents density of ^{6}Li isotope, $V_{crystal}$ represents volume of the crytal and $\sigma_{(n,\alpha)}$ represents cross-section of (n,α) reaction.In MCNP, this quantity can be calculated by using F4 tally and FM card. F4 tally determined neutron fluence in the crystal and others parameters in Eq. (3) were declared in FM card. The ENDF/B-VII [6] neutron cross-section library and S(α,β) thermal neutron cross-section tables were used. In order to reduce of computation time, two variance techniques were used: geometry splitting and source direction bias.

2.2 Calibration of cylindrical and rectangular neutron devices

In order to verify and validation of the calculated geometry correction factor, some neutron devices were calibrated by three methods recommended in ISO 8529-2: generalized method, semi-empirical method and reduced methods. In this work, three Aloka TPS-451C devices and one Ludlum 42-41L were calibrated. The Aloka TPS-451C's moderator has cylindrical shape of 21 cm height and 20 cm diameter. The Ludlum 42-41L's moderator has cubic shape of 10 cm.

3. RESULTS AND DISCUSSIONS

3.1 Geometry correction factor

Geometry correction factor (GCF) for cylindrical and rectangular neutron devices were presented in table 3 and table 4. As expected, the GCF decreases with increasing source-detector's center distance l, as well as toward the value 1 when the distance is much larger than the size of the device.

3.2 Calibration of neutron devices

The calibration of Aloka TPS-451C and Ludlum 42-41L devices with different methods were presented in table 5, figure 1.

Table 5: Correction factor with different methods

Name	Generalized method	Semi-empirical	Reduced method
Aloka 1	0.97 ± 0.06	0.97 ± 0.05	0.93 ± 0.05
Aloka 2	1.01 ± 0.06	0.99 ± 0.05	0.95 ± 0.05

Aloka 3	0.97 ± 0.05	0.98 ± 0.05	0.94 ± 0.05
Ludlum	1.09 ± 0.03	1.11 ± 0.03	1.06 ± 0.02

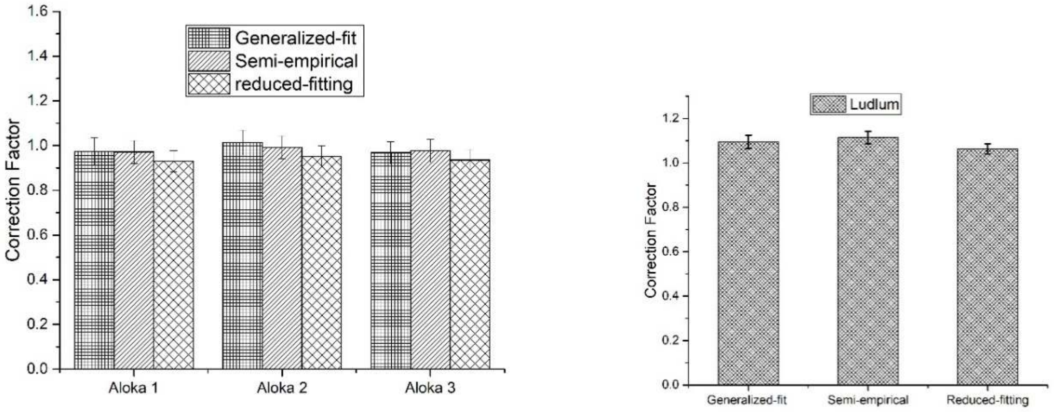

Figure 1: Correction factor with different methods

These correction factors with different methods are consistent within uncertainty. Three methods recommend by ISO 8529-2 can be used to calibration of cylindrical and rectangular neutron devices.

4. CONCLUSIONS

Geometry correction factor for cylindrical and rectangular neutron devices were calculated using the MCNP6 code. These geometry correction factors were successfully applied to calibrate Aloka TPS-451C and Ludlum 42-41L neutron devices. These geometry correction factors can be used to calibrate others devices. It is suggested that the reduced method can be the method of choice to calibrate the neutron devices.

Acknowledgments:

Authors would like to express special thanks to the Nuclear Training Center (NTC – VINATOM) for their help with computer to run the code. This research was supported by the Ministry of Science and Technology, under grants No. CS/1804-02.

REFERENCES

[1] ISO 8529-2, Reference neutron radiations – Part 2: Calibration fundamentals of radiation protection devices related to the basic quantities characterizing the radiation filed, 2000

[2] Pulpal *et. al*., Geometrical correction factor, Radiation Protection Dosimetry, vol. 35, 1991

[3] G.C. Taylor, Geometry corrections for cylindrical neutron area survey meters, Applied Radiation Isotopes, vol. 68, 2010

[4] T. Goorley *et. al.*, Initial MCNP6 release overview – MCNP version 1.0, LA-UR-13-22934, 2013

[5] ISO 8529-1, Reference neutron radiations – Part 1: Characteristics and methods of production, 2000

[6] Colin et. al., Continuous Energy Neutron Cross Section Data Tables Based upon ENDF/B-VII.1, LA-UR-13-20137, 2013

Table 3: Geometry correction factor for cylindrical neutron devices*

C1		C2		C3		C4		C5		C6		C7		C8	
SDD	GF	SDD	GF	SDD	GF	SDD	GF	SDD	GF	SDD	GF	SDD	GF	SDD	GF
1.5	1.3415	2.3	1.4112	3.45	1.4409	5.75	1.4721	9.19	1.4881	11.49	1.4790	13.79	1.4665	16.6	1.4520
1.6	1.2305	2.4	1.3188	3.5	1.4004	5.8	1.4387	9.2	1.4844	11.5	1.4743	13.8	1.4616	16.7	1.4520
1.7	1.1971	2.6	1.2537	4	1.2702	6	1.3815	9.3	1.4506	11.6	1.4516	13.9	1.4445	16.8	1.4311
1.8	1.1749	2.8	1.2207	5	1.1985	6.1	1.3625	9.4	1.4287	11.7	1.4321	14	1.4311	16.9	1.4259
1.9	1.1596	3	1.1954	5.5	1.1781	6.2	1.3440	9.5	1.4173	11.8	1.4214	14.1	1.4221	17	1.4050
2	1.1471	5	1.1160	6	1.1620	6.3	1.3337	9.6	1.4023	11.9	1.4118	14.2	1.4089	17.5	1.3811
2.1	1.1366	6	1.0899	6.5	1.1529	6.5	1.3111	9.7	1.3871	12	1.4016	14.3	1.3977	18	1.3643
2.2	1.1348	7	1.0749	7	1.1354	7	1.2750	9.8	1.3797	12.5	1.3594	14.4	1.3919	18.5	1.3380
2.3	1.1328	8	1.0614	8	1.1230	8	1.2271	9.9	1.3713	13	1.3306	14.5	1.3874	19	1.3243
2.4	1.1195	9	1.0669	9	1.1028	10	1.1804	10	1.3579	14	1.2946	16	1.3138	19.5	1.3133
2.5	1.1152	10	1.0558	10	1.0943	15	1.1164	12	1.2626	15	1.2619	18	1.2625	20	1.2997
2.6	1.1115	20	1.0133	20	1.0511	20	1.0808	20	1.1454	20	1.1839	20	1.2266	25	1.2311
2.7	1.1109	30	1.0269	30	1.0292	30	1.0580	30	1.0888	30	1.1218	30	1.1474	30	1.1756
2.8	1.1074	40	1.0060	40	1.0175	40	1.0448	40	1.0738	40	1.0841	40	1.1108	40	1.1257
2.9	1.0966	50	1.0359	50	1.0230	50	1.0372	50	1.0541	50	1.0672	50	1.0882	50	1.1134
3	1.0978	60	1.0030	60	1.0203	60	1.0278	60	1.0457	60	1.0568	60	1.0737	60	1.0794
5	1.0586	80	1.0096	80	1.0056	80	1.0191	80	1.0334	80	1.0456	80	1.0480	80	1.0750
10	1.0556	100	1.0059	100	1.0146	100	1.0115	100	1.0292	100	1.0308	100	1.0454	100	1.0531
15	1.0269	120	0.9929	120	1.0024	120	1.0133	120	1.0184	120	1.0241	120	1.0314	120	1.0322
20	0.9946	150	0.9918	150	1.0160	150	1.0092	150	1.0166	150	1.0181	150	1.0203	150	1.0419
30	0.9693	200	1.0184	200	0.9994	200	1.0097	200	1.0142	200	1.0145	200	1.0202	200	1.0244
40	1.0032	250	1.0071	250	0.9973	250	1.0119	250	1.0119	250	1.0103	250	1.0191	250	1.0256
50	1.0062	300	0.9897	300	1.0094	300	1.0093	300	1.0082	300	1.0077	300	1.0187	300	1.0159

(SDD: Source-detector distance; GF: geometry correction factor)

Table 4: Geometry correction factor for rectangular neutron devices

H1		**H2**		**H3**		**H4**		**H5**		**H6**		**H7**		**H8**		**H9**		**H10**	
SDD	GF	SDD	GF	SDD	GF	SDD	GF	SDD	GF	SDD	GF	SDD	GF	SDD	GF	SDD	GF	SDD	GF
5.0	1.4645	5	1.2182	5.0	1.1389	5.0	1.1134	5.0	1.0995	7.50	1.8951	7.5	1.7447	7.5	1.6856	7.5	1.6522	10	2.1960
5.2	1.4162	5.2	1.1872	5.2	1.1068	5.2	1.0844	5.2	1.0740	7.6	1.8547	7.6	1.7064	7.6	1.6469	7.6	1.6214	10.1	2.1486
5.4	1.3940	5.6	1.1679	5.6	1.0931	5.6	1.0717	5.6	1.0564	7.8	1.8035	7.8	1.6637	7.7	1.6289	7.7	1.6043	10.2	2.1189
5.6	1.3778	6	1.1633	6	1.0897	6	1.0682	6	1.0566	8	1.7747	8	1.6327	8	1.5816	8	1.5667	10.4	2.0717
5.8	1.3665	8	1.1613	8	1.0993	8	1.0810	8	1.0661	8.5	1.7080	8.5	1.5874	8.5	1.5334	8.5	1.5137	10.6	2.0365
6	1.3590	10	1.1555	10	1.1027	10	1.0861	10	1.0794	9	1.6623	9	1.5462	9	1.4929	9	1.4749	11	1.9738
7	1.3279	15	1.1356	15	1.1027	15	1.0845	15	1.0724	10	1.5932	10	1.4904	10	1.4417	10	1.4253	15	1.6535
8	1.3101	20	1.1101	20	1.0927	20	1.0843	20	1.0664	15	1.3952	15	1.3250	20	1.2275	20	1.2300	18	1.5172
9	1.2886	30	1.0822	30	1.0647	30	1.0596	30	1.0467	20	1.2916	20	1.2451	30	1.1529	30	1.1549	20	1.4522
10	1.2742	40	1.0664	40	1.0535	40	1.0508	40	1.0636	30	1.2032	30	1.1809	40	1.1263	40	1.1143	30	1.2819
20	1.1567	50	1.0498	50	1.0389	50	1.0452	50	1.0359	40	1.1441	40	1.1380	50	1.0929	50	1.0604	40	1.2090
30	1.1073	60	1.0463	60	1.0371	60	1.0370	60	1.0213	50	1.1023	50	1.0913	60	1.0818	60	1.0655	50	1.1661
40	1.0858	70	1.0347	70	1.0252	70	1.0294	70	1.0235	60	1.0919	60	1.0922	70	1.0622	70	1.0706	60	1.1534
50	1.0589	80	1.0314	80	1.0313	80	1.0236	80	1.0235	70	1.0717	70	1.0694	80	1.0537	80	1.0767	70	1.1184
60	1.0497	100	1.0329	100	1.0222	100	1.0228	100	1.0248	80	1.0724	80	1.0577	100	1.0508	100	1.0631	80	1.1134
70	1.0428	120	1.0169	120	1.0237	120	1.0246	120	1.0150	100	1.0510	100	1.0478	120	1.0445	120	1.0393	100	1.0859
80	1.0393	150	1.0155	150	1.0140	150	1.0200	150	1.0072	120	1.0470	120	1.0450	150	1.0379	150	1.0350	120	1.0753
100	1.0260	200	1.0157	200	1.0100	200	1.0074	200	1.0097	150	1.0337	150	1.0292	200	1.0280	200	1.0248	150	1.0537
120	1.0203	250	1.0042	250	1.0077	250	1.0096	250	1.0016	200	1.0272	200	1.0378	250	1.0129	250	1.0083	200	1.0495
150	1.0209	300	1.0101	300	1.0039	300	1.0065	300	1.0061	250	1.0264	250	1.0186	300	1.0210	300	1.0203	250	1.0324
200	1.0150									300	1.0190	300	1.0184					300	1.0318
250	1.0067																		
300	1.0138																		

(SDD: Source-detector distance; GF: geometry correction factor)

Table 4: Geometry correction factor for rectangular neutron devices (cont.)

H11		**H12**		**H13**		**H14**		**H15**		**H16**		**H17**		**H18**		**H19**		**H20**	
SDD	GF	SDD	GF	SDD	GF	SDD	GF	SDD	GF	SDD	GF	SDD	GF	SDD	GF	SDD	GF	SDD	GF
10	2.0923	10	2.0610	7.5	1.5499	7.5	1.4122	7.5	1.3460	7.5	1.3294	10	1.7910	10	1.6992	10	1.6645	10	1.6010
10.1	2.0572	10.1	2.0308	7.6	1.5276	7.6	1.3919	7.6	1.3254	7.6	1.3084	10.1	1.7636	10.1	1.6709	10.1	1.6423	10.1	1.5834
10.2	2.0212	10.2	1.9928	7.7	1.5077	7.7	1.3739	7.7	1.3142	7.7	1.2983	10.2	1.7436	10.2	1.6571	10.2	1.6237	10.3	1.5582
10.4	1.9778	10.4	1.9403	7.8	1.5013	7.8	1.3632	7.8	1.3069	7.8	1.2835	10.4	1.7166	10.4	1.6304	10.4	1.6027	10.5	1.5337
10.6	1.9480	10.6	1.9074	8	1.4782	8	1.3511	8	1.2922	8	1.2752	10.6	1.6943	10.6	1.6142	10.6	1.5834	11	1.5007
11	1.8982	11	1.8628	8.2	1.4628	8.5	1.3221	8.5	1.2671	8.5	1.2504	11	1.6596	11	1.5810	11	1.5471	12	1.4596
15	1.5853	15	1.5654	8.6	1.4361	9	1.3060	9	1.2526	9	1.2396	12	1.5938	12	1.5198	12	1.5027	15	1.3783
18	1.4750	18	1.4433	9	1.4248	10	1.2904	10	1.2382	10	1.2200	15	1.4731	15	1.4229	15	1.3977	18	1.3255
20	1.4095	20	1.4188	10	1.3910	15	1.2260	15	1.2001	15	1.1791	20	1.3665	20	1.3162	20	1.3047	20	1.3087
30	1.2462	30	1.2618	20	1.2267	20	1.1872	20	1.1568	20	1.1574	30	1.2442	30	1.2298	30	1.2096	30	1.2088
40	1.2033	40	1.1844	30	1.1601	30	1.1320	30	1.1303	30	1.1217	40	1.1911	40	1.1783	40	1.1641	40	1.1489
50	1.1519	50	1.1675	40	1.1297	40	1.1098	40	1.0905	40	1.0835	50	1.1595	50	1.1324	50	1.1275	50	1.1398
60	1.1173	60	1.1239	50	1.1020	50	1.0870	50	1.0804	50	1.0712	60	1.1227	60	1.1030	60	1.1164	60	1.1092
70	1.1083	70	1.1124	60	1.0896	60	1.0724	60	1.0576	60	1.0677	70	1.0980	70	1.0814	70	1.0825	70	1.0985
80	1.0714	80	1.0914	70	1.0681	70	1.0611	70	1.0630	70	1.0619	80	1.0834	80	1.0741	80	1.0737	80	1.0879
100	1.0721	100	1.0881	80	1.0686	80	1.0584	80	1.0554	80	1.0611	100	1.0622	100	1.0656	100	1.0662	100	1.0620
120	1.0615	120	1.0600	100	1.0441	100	1.0468	100	1.0386	100	1.0500	120	1.0675	120	1.0574	120	1.0589	120	1.0520
150	1.0570	150	1.0557	120	1.0357	120	1.0383	120	1.0296	120	1.0323	150	1.0442	150	1.0441	150	1.0517	150	1.0470
200	1.0215	200	1.0411	150	1.0330	150	1.0466	150	1.0189	150	1.0320	200	1.0268	200	1.0359	200	1.0571	200	1.0355
250	1.0231	250	1.0230	200	1.0270	200	1.0256	200	1.0165	200	1.0293	250	1.0404	250	1.0122	250	1.0331	250	1.0206
300	1.0467	300	1.0316	250	1.0110	250	1.0173	250	1.0185	250	1.0172	300	1.0230	300	1.0210	300	1.0318	300	1.0225
				300	1.0205	300	1.0183	300	1.0162	300	1.0169								

(SDD: Source-detector distance; GF: geometry correction factor)

Table 4: Geometry correction factor for rectangular neutron devices (cont.)

H21		**H22**		**H23**		**H24**		**H25**		**H26**		**H27**		**H28**		**H29**	
SDD	GF	SDD	GF	SDD	GF	SDD	GF	SDD	GF	SDD	GF	SDD	GF	SDD	GF	SDD	GF
10	1.5205	10	1.4838	12.5	1.7317	12.5	1.6812	15	1.8220	12.5	1.6329	12.5	1.5810	15	1.6914	15	1.6472
10.1	1.4991	10.1	1.4632	12.6	1.7120	12.6	1.6656	15.1	1.8193	12.6	1.6175	12.6	1.5663	15.1	1.6846	15.1	1.6384
10.3	1.4760	10.3	1.4430	12.7	1.6960	12.7	1.6525	15.2	1.7900	12.7	1.5986	12.7	1.5430	15.2	1.6649	15.2	1.6105
10.5	1.4606	10.5	1.4238	12.8	1.6896	12.8	1.6425	15.4	1.7809	12.8	1.5927	12.8	1.5329	15.4	1.6536	15.4	1.6045
11	1.4377	11	1.3979	13	1.6605	13	1.6235	15.5	1.7589	13	1.5780	13	1.5185	15.5	1.6434	15.5	1.5972
12	1.3913	12	1.3650	13.5	1.6325	13.5	1.5899	16	1.7291	13.5	1.5404	13.5	1.4915	16	1.6075	16	1.5753
15	1.3172	15	1.3023	14	1.5986	14	1.5605	17	1.6690	14	1.5171	14	1.4695	18	1.5211	18	1.4885
18	1.2750	18	1.2584	15	1.5468	15	1.5077	18	1.6162	15	1.4816	15	1.4429	20	1.4738	20	1.4330
20	1.2681	20	1.2464	20	1.4214	20	1.3816	20	1.5609	20	1.3788	20	1.3265	30	1.3230	30	1.2979
30	1.1719	30	1.1843	30	1.2772	30	1.2591	30	1.3891	30	1.2563	30	1.2308	40	1.2562	40	1.2542
40	1.1424	40	1.1354	40	1.2264	40	1.2137	40	1.2776	40	1.2039	40	1.1899	50	1.2021	50	1.1901
50	1.1121	50	1.1361	50	1.1635	50	1.1719	50	1.2329	50	1.1564	50	1.1442	60	1.1803	60	1.1123
60	1.0897	60	1.1018	60	1.1625	60	1.1486	60	1.1969	60	1.1443	60	1.1254	70	1.1581	70	1.1266
70	1.0963	70	1.0981	70	1.1130	70	1.1152	70	1.1543	70	1.1211	70	1.1191	80	1.1207	80	1.1220
80	1.0764	80	1.0864	80	1.1075	80	1.1047	80	1.1427	80	1.0948	80	1.0979	100	1.1055	100	1.1017
100	1.0594	100	1.0589	100	1.0709	100	1.0836	100	1.1128	100	1.0836	100	1.0779	120	1.0873	120	1.1046
120	1.0468	120	1.0517	120	1.0767	120	1.0681	120	1.0815	120	1.0771	120	1.0658	150	1.0737	150	1.0584
150	1.0323	150	1.0333	150	1.0688	150	1.0496	150	1.0719	150	1.0633	150	1.0625	200	1.0512	200	1.0535
200	1.0289	200	1.0392	200	1.0348	200	1.0373	200	1.0429	200	1.0474	200	1.0320	250	1.0518	250	1.0263
250	1.0255	250	1.0169	250	1.0368	250	1.0422	250	1.0471	250	1.0450	250	1.0293	300	1.0217	300	1.0275
300	1.0255	300	1.0177	300	1.0295	300	1.0225	300	1.0451	300	1.0237	300	1.0244				

(SDD: Source-detector distance; GF: geometry correction factor)

STUDY ON THE STANDARDIZATION OF SOME SAMPLE GEOMETRIES USING MONTE CARLO SIMULATION FOR LOW BACKGROUND GAMMA SPECTRUM ANALYSIS METHOD

Phan Quang Trung, Nguyen Van Phuc, Vo Thi Mong Tham, Nguyen Minh Dao,
Nguyen Thi Huong Lan and Le Xuan Thang.

Dalat Nuclear Research Institute
01 Nguyen Tu Luc Street, Dalat, Lam Dong province

Project information:

- **Code:** CS /18/01-03
- **Managerial Level:** Institute
- **Allocated Fund:** 65,000,000 VND
- **Implementation time:** 12 months (Jan 2018- Dec 2018)
- **Contact email:** trungnri@yahoo.com.vn
- **Paper published in related to the project:**

Phan Quang Trung, 2018. Study on the standardization of some sample geometries using Monte Carlo simulation for low background gamma spectrum analysis method. *The 5th Vietnam Conference on Nuclear Science and Technology for Young Researchers.* Hanoi, Vietnam October 2018 (in Vietnamese).

Abstract: The efficiency of a low background gamma HPGe spectrometer is a significant factor in determination of the specific radioactivity of environmental samples. Since the diversity of environmental samples, the varieties in geometry and density are not satisfied by standard sources in laboratory. So, by using Monte Carlo method in GEANT4 and MCNP simulation softwares, the efficiencies of a low background gamma spectrometer with HPGe detector for several kinds of geometries and densities of environmental samples are estimated. In this study, GEANT4 and MCNP softwares are used to simulate and standardize some geometries of environmental samples for measurement on low background gamma spectrometry system.

Keywords: *Gamma spectrometry, efficiency calibration, environmental samples, Geant4, Monte Carlo simulation.*

1. INTRODUCTION

The efficiency of detector is a significant factor to determine the radioactivity in sample accurately. The efficiency of detector depends on density of samples, geometry and thickness of samples. Most of laboratories determine the radioactivity in samples by analyzing a known-radioactivity in standard sources in same geometry. Current standard sources cannot meet the requirement for the diversity of environment samples. Therefore, the efficiencies of detector for some kinds of geometry of environment samples are needed to be standardized by Monte Carlo simulation.

2. METHOD AND EXPERIMENT

The efficiencies of detector HPGe for some kinds of geometry which were used for determination of environment samples are studied by Monte Carlo simulation as well as experiment methods. The accuracy of the*Input file* is tested by comparison of the detector's efficiencies resulted from experimental calculation with Monte Carlo simulation. The efficiencies of detector HPGe are simulated in regard to measurement geometries including column geometry, Marinelli geometry while changing the radius, the thickness and density of samples. There are some facilities in the study:

2.1. Equipment

HPGe Detector: GMX30P4

Standard sources:

- Point sources including 8 sources of which radioactivity are ratified by U.S.NRC
- Disk source: (radius of 3.65cm, thickness of 2cm), its radioactivity is ratified by IAEA.

The efficiency of experiment method is calculated by following formula:

$$\varepsilon = \frac{Cps}{A_0 I_\gamma e^{-\lambda t}} \qquad 1.1$$

Where ε*is the efficiency of detector at energy level E,*

Cps:counts per second at consider energy level E(count/second),

A_0*is the radioactivity of standard source at the time of production (Bq),*

$I_\gamma(E)$ *is the intensity of gamma emission energy level E (%),*

$\lambda$is decay constant (s^{-1}), $\lambda=ln2/T_{1/2}$, $T_{1/2}$is half-life of consider radionuclide (s),

$t = T_1 - T_2$is the time from sample preparation to measurement (s).

Uncertainty of efficiency is calculated by following formula:

$$d\varepsilon = \sqrt{\left(\frac{\varepsilon}{A}\right)^2 dA^2 + \left(\frac{\varepsilon}{N}\right)^2 dN^2 + \left(\frac{\varepsilon}{I_\gamma}\right.} \qquad 1.2$$

2.2. GEANT4 and MCNP5 Softwares

The GEANT4 simulation software is developed by CERN and used as the Monte Carlo simulation toolkit. The package can calculate detector's response to the passage of particles, propagating each particle step by step and taking into account all physic effects, including secondary particle production.

The efficiency of detector is calculated in Monte Carlo simulation method by following formula:

$$\varepsilon_{abs} = \varepsilon_{\text{int}}\left(\frac{\Omega}{4\pi}\right) \qquad 1.3$$

where

$$\varepsilon_{\text{int}} = \frac{N}{N_0} \qquad 1.4$$

With $\varepsilon_{abs}$is absolutely efficiency,

$\varepsilon_{int}$is intrinsic efficiency,

Ωisthe solid angle, $\Omega = 2\pi(1-\cos\theta)$,

$\theta$is distribution angle (degree),

N is the number of pulses recorded in photopeak,

$N_0$is the number of radiation quanta emitted by source.

The uncertainty$\delta\varepsilon/\varepsilon$ (%) is calculated by following formula:

$$\frac{\delta\varepsilon}{\varepsilon} = \frac{\sqrt{N}}{N} \qquad 1.5$$

*WhereN*is the photons that are emitted by source which lose the energy in the active area of detector.

3. RESULTS AND DISCUSSION

The results showed that the relative uncertainties of intrinsic efficiency and simulation efficiency for standard sources are less than 10%.

Table 2.1: The efficiency of detector for point source by experiment and simulation methods

Radionuclides	Energy (keV)	Intrinsic efficiency	Simulation efficiency	Relative uncertainty TN/G4 (%)
Ba-133	81.00	0.01108	0.01177	6.2
Cd-109	88.00	0.01236	0.01217	1.5
Co-57	122.06	0.01346	0.01231	8.5
Co-57	136.47	0.01284	0.01199	6.6
Ba-133	276.40	0.00651	0.00714	9.7
Ba-133	302.85	0.00599	0.00649	8.4
Ba-133	356.01	0.00526	0.00553	5.2
Ba-133	383.85	0.00485	0.00509	4.9
Cs-137	661.66	0.00290	0.00303	4.5
Co-60	1173.20	0.00187	0.00182	2.5
Co-60	1332.50	0.00169	0.00161	4.3

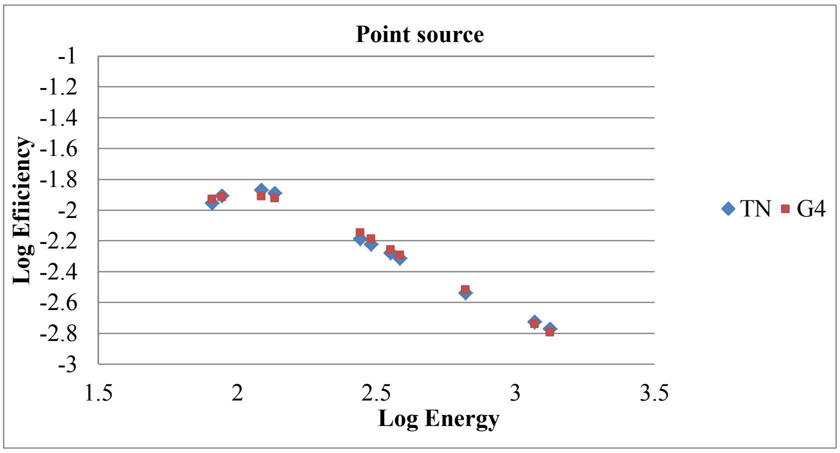

Figure 2.1:.Efficiency linear by experiment and simulation

After testing the accuracy of Input file, the dependence of detector's efficiency on changing of column geometry was simulated: radius from 0.5cm – 5cm; thickness from 1cm to 5cm and density from 0.6g/cm^3 to 2.4g/cm^3. This showed that detector's efficiencies decrease by the increasing of radius, thickness or density of samples. This decreasing is apparent at low energy peak (lower 295 keV).

Furthermore, this study investigated and suggested an optimal sample geometry which has radius of 3.5cm and thickness ranging from 4 – 5 cm.

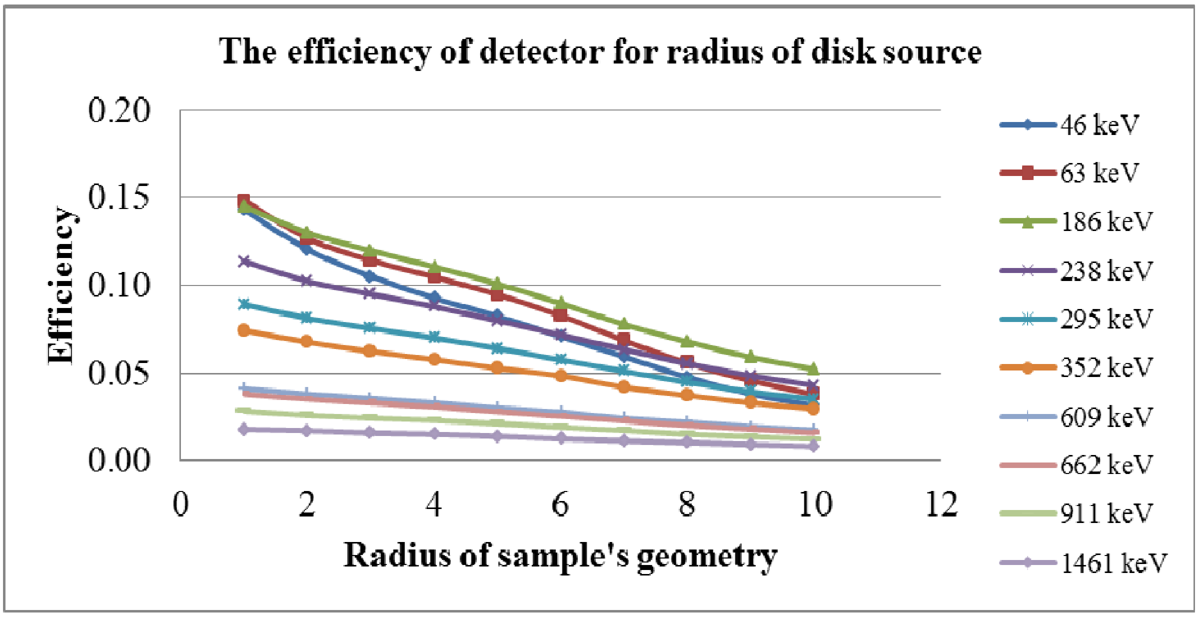

Figure 2.2: The variation of detector efficiencies by changing of radius of sample's geometry (sample thickness: 2cm and density: 2g/cm^3)

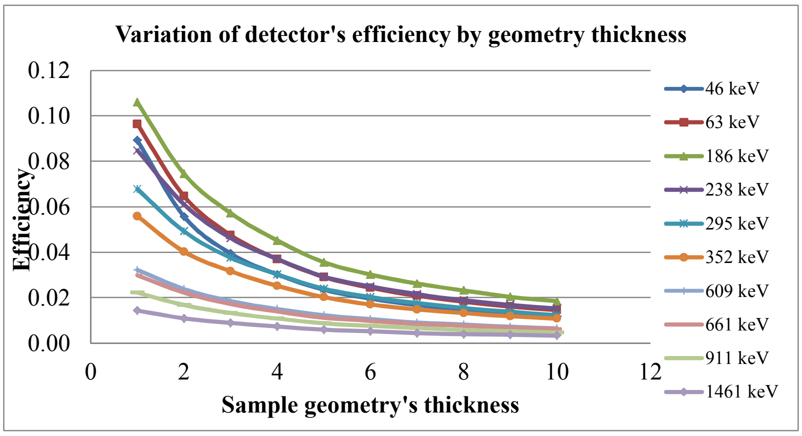

Figure 2.3: Variation of detector’s efficiency by sample geometry’s thickness

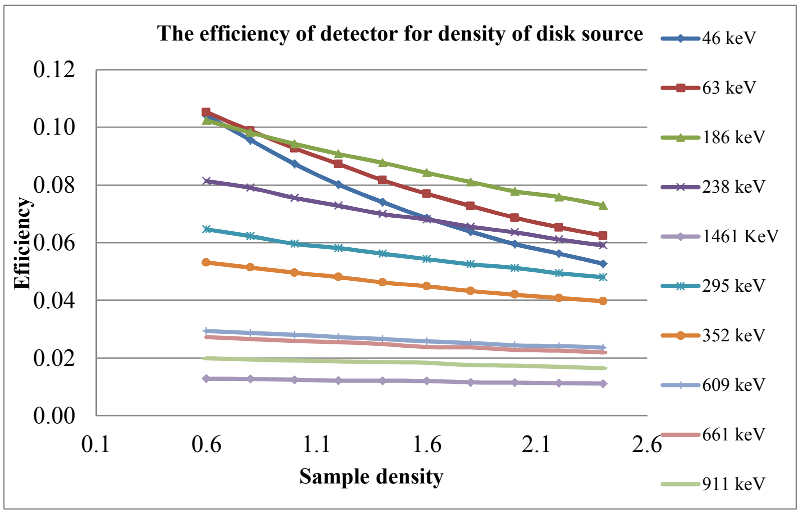

Figure 2.4: Variation of detector’s efficiency by sample density

In this study, the linear of detector’s efficiency for Marinelli beaker was established. This study suggested an optimal sample density for Marinelli beaker geometry ranging from 0.6g/cm^{3}to 2.4g/cm^3. Then, the mathematical functions of efficiencies linear were constructed for each geometry as well as the mathematical functions for the decreasing of efficiencies by radius, thickness or density of sample.

4. CONCLUSIONS

The study has implemented fully the registration subjects. Based on the simulation and experimental data, different types of sample's geometry were simulated by changing the radius, thickness and density of samples. The linear of detector's efficiencies for some sample geometries are established. Through this study, the optimal geometry's thickness for disk source is estimated.

REFERENCES

[1] Şahin D, Ünlü K, Modeling a gamma spectroscopy system and predicting spectra with Geant-4, J RadioanalNuclChem 282:167–172, 2009.

[2] Chuanlei Liu1, Kurt Ungar1, Dylan Pierce2, Ian Hoffman1, Weihua Zhang1, Detection efficiency calculations using Geant4 for a broad-energy germanium gamma spectrometer, J RadioanalNuclChem 312:471–478 DOI 10.1007/s10967-017-5239-5, 2017.

[3] M. Korun, A.Likar and T. Vidmar, Monte-Carlo calculation of the spatialdependence of the coaxial HPGe detector efficiency for point sources, Nuclear Instruments and Methods in Physics Research A, 1997.

[4] McNamara AL, Heijnis H, Fierro D, Reinhard MI, The determination of the efficiency of a Compton suppressed HPGe detector using Monte Carlo simulations, J Environ Radioact 106:1–7, 2012.

[5] Szentmiklosi L, Belgya T, Maroti B, Kis Z, Characterization of HPGe gamma spectrometers by geant4 Monte Carlo simulations, J RadioanalNuclChem 300:553–558, 2014.

[6] Haase G, Tait D, Wiechen, A determination of full energy peak efficiency for cylindrical volume sources by the use of a point source standard in gamma spectrometry, NuclInstr Methods Phys Res A361:240–244, 1995.

[7] G. Giubrone, J. Ortiz, S. Gallardo, S. Martorell, M.C. Bas, Calculation of coincidence summing correction factors for HPGe detector using GEANT4, Journal of Environmental Radioactivity, Volumes 158–159, July 2016, Pages 114–118, 1995.

[8] Zhonglu Wang, Bernd Kahn, and John D. Valentine, Member, IEEE, Efficiency calculation and coincidence summing correction for germanium detectors by Monte Carlo Simulation, Ieee transactions on nuclear science, Vol. 49, No. 4, August 2002.

[9] Optimization of geometric parameters for Marinelli beaker to maximize the detection efficiency of an HPGe detector, Nuclear Instruments and Methods in Physics Research Section A: Accelerators, Spectrometers, Detectors and Associated Equipment, Volume 610, Issue 3, Pages 718–723, 11 November 2009.

[10] Geant4 users guide for application deverlopers, Version geant4.9.3, Geant4 Collaboration, 2009.

[11] Geant4 Collaboration, Physics Reference Manual, Version geant 4.9.4, 2010.

1.8- Radiation Technology

STUDY ON THE EFFECTS OF COBALT 60 GAMMA RADIATION ON GROWTH OF HAIRY ROOTS IN SACRED FIG *FICUS RELIGIOSA* L. BY *AGROBACTERIUM RHIZOGENES*TR7

Ha Thi Ngoc Trinh, Doan Pham Ngoc Nga and Cao Thi Bang Giang

Center for Nuclear Techniques, Ho Chi Minh City

Project information:

- **Code:** CS/18/02-01
- **Managerial Level:** Institute
- **Allocated Fund:** 90,000,000 VND
- **Implementation time:** 12 months (Jan 2018- Dec 2018)
- **Contact email:** ngoctrinhhathi@gmail.com
- **Paper published in related to the project:**

Ha Thi Ngoc Trinh, Doan Pham Ngoc Nga, Cao Thi Bang Giang, 2018. Study on induction of hairy roots in sacred figFicus religiosa L. byAgrobacterium rhizogenes TR7. *The 11th Scientific Conference of University of Science*, Viet Nam National University Ho Chi Minh City, November 2018 (In Vietnamese).

Abstract: This study was carried out to induce the hairy roots of *Ficus religiosa* Lusing *Agrobacterium rhizogenes* TR7 to investigate suitable medium for growth of hairy roots and to evaluate the growth of hairy roots under effect of Co-60gamma rays at different doses. The results indicated that among of three materials (leaves, leaf stalk and inter node) infiltrated by *A. rhizogenes* TR7, leaves were the best appropriate materials to the bacteria genetic transformation with success induction after 30 minutes of infection and five days of co-cultivation at 66.67 ± 7.64 %. The hairy roots from *A. rhizogenes* TR7 was confirmed by PCR method using *rol*B, *rol*C gene and *vir*D gene. Hairy roots with highest growth index reach at (22.00 ± 1.074) after 4 weeks in MS medium with 2 % sucrose. Hairy roots were treated with gamma irradiation at doses of 0, 10, 20, 30, and 40 Gy. Co-60 gamma radiation made a significant decline in survival rate, fresh and dry weight in comparison with control. However, at dose of 30 Gy dry weight marginally increased at(22.25 ± 1.38%) higher than control (15.04 ± 0.71%). Whereas at 20 Gy the highest total phenolic content recorded 36.72 mg GAE/g DW higher 1.44 times than the control.

Keyword: *Agrobacterium rhizogenes*TR7*,* hairy roots*, Ficus religiosa* L., gamma radiation.

1. INTRODUCTION

Ficus religiosa L. (family Moraceae), commonly known as Bodhi tree is native to India where it has great ethno-medicinal importance since time immemorial. It has 50 diverse medicinal applications, from various parts of the plant such as bark, bark decoction, leaves and tender shoots, leaf juice, leaf decoction, dried fruit, fruit, seeds and latex [1].The plant was reported to have wide spectrum of activities such as anticancer, antioxidant, antidiabetic, antimicrobial, anthelmintic, antiulcer, antiasthmatic and antineurode generation.

Hairy root culture, also called transformed root culture, is a type of plant tissue culture that is used to study plant metabolic processes or to produce valuable secondary metabolites. In nature, hairy roots are induced by soil bacterium named *A. rhizogenes* that can be infected into plant roots. Hairy roots are morphologically different from normal roots which are much more branched and have much lateral meristematic growth, hairy roots are easy to culture in artificial media without hormone [2]; genetic and biochemical stability. Hairy roots system has been developed for more than 100 plant species. However, for many medicinally and economically important plants, hairy root cultures have not developed yet; *F. religiosa* L. is among of them.

Gamma irradiation is one of the environmental stresses that has considered as a rapid and new method to change the qualitative and quantitative characteristics of plants for several years. Low-dose ionizing irradiation can affect on cell growth, germination rate and enzyme activity as well as stress resistance [3]. Bioactive compounds also can be promoted under proper dose of radiation.

Hence, this was firstly carried out to induce the hairy roots of *F. religiosa* L.using *A. rhizogenes,* then to investigate suitable medium to growth of hairy roots and finally to investigate the effect of different doses of gamma radiation on growth and accumulation of phenolic compound of *F. religiosa* L. hairy roots.

2. EXPERIMENTAL

2.1. Materials

Plant materials: The shoot tip of *F. religiosa* were collected from a 55 to 60 year old *F. religiosa* mother plants that were grown on the campus of Lam Te pagoda (Ho Chi Minh City).

*A. Rhizogenes*strain and culture condition: The strains of *A. rhizogenes* TR7was used for transformation provided by Department of Genetic technology, Institute of Tropical Biology. *A. rhizogenes* TR7 was subcultured in NB medium, pH 7.0.

2.2.Methods

2.2.1. In vitro culture F. religiosa L.

The explants were washed thoroughly under running tap water for 15 minutes and soaked in *a liquid soap solution* for about 5 minutes, followed by rinsing with sterilized distilled water. Then, the surface of the shoots were sterilized with 70% aqueous ethanol, 1 % NaOCl and finally washed with sterilized distilled water 4 times in a laminar air flow chamber.

The surface sterilized explants were cut into 1-1.5 cm length containing a single node with an axillary bud or a shoot tip with an apical bud. The explants were placed vertically on the culture medium. The new shoots induced from the *in vitro* continuedbeing used as an explants for adventitious shoot regeneration

2.2.2. Plant transformation

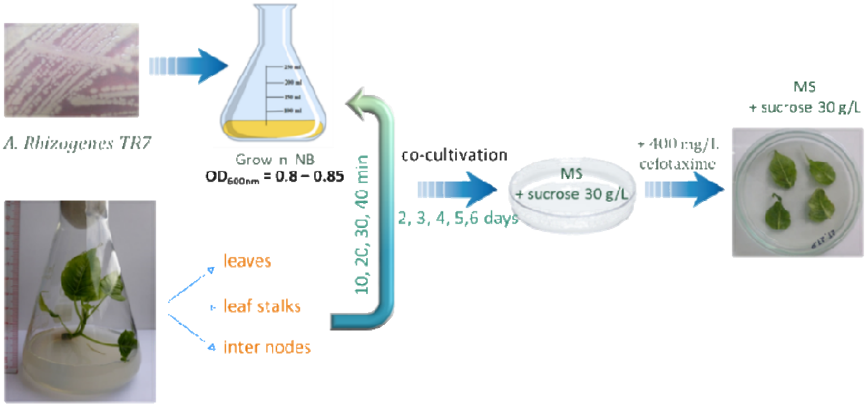

Figure 1: Plant transformation process

The strain was cultured in liquid NB mediumOD ≈0.8-0.85 for infection. Leaves, leaf stalks and inter nodes were chosen from 2.5-month-old sterile *F. religiosa* plants for use as explants.

The explants were submerged in the *A. rhizogenes* suspension medium for 10, 20, 30 or 40 minutes. Then, we put the explants on sterile filter paper to remove surface moisture and excess bacteria and then co-culture them on MS medium (supplemented with 3 % sucrose, 8 g/L agar, pH 5.8) in darkness, at 25 °C for 2, 3, 4, 5 or 6 days. After the co-cultivation period, the explants were transferred onto MS media plate supplemented with 400 mg/L cefotaxime and 3 % sucrose. Hairy roots appeared after 3 - 4 weeks at wounded positions of explants, cut into 1 cm long sections and cultured and maintained on MS media supplemented with 250 mg/L cefotaxime and 3% sucrose.

2.2.3. DNA extraction and PCR amplification

The genomic DNA of *F. religiosa*was isolated from the putative hairy roots lines and wild type (negative control) using the ISOLATE II Plant Kit. The plasmid from *A. rhizogenes* TR7 was used as the positive control which was isolated by QIAGEN kit.

Transformants were screened for the presence of *rol*A, *rol*C genes and absence of *vir*D gene using the sequence specific primers (Table 1).

Table 1: Primers used for PCR analysis

Gene	**primer**	**primer sequence (5'→3')**	**Predicted amplicon size (bp)**
*Rol*B	*Rol*BF *Rol*BR	GCTCTTGCAGTGCTAGATTT GAAGGTGCAAGCTACCTCTC	780
*Rol*C	*Rol*CF *Rol*CR	CTCCTGACATCAAACTCGTC TGCTTCGAGTTATGGGTACA	540
*Vir*D	*Rol*BF *Rol*BR	ATGTCGCAAGGACGTAAGCCC GGAGTCTTTCAGCATGGAGCA	450

2.2.4.Samples irradiation

Samples of *F. religiosa*hairy roots were divided into five groups: control (non-irradiated, 0 Gy), and samples irradiated with different doses (10, 20, 30 and 40 Gy). Irradiation of *F. religiosa*hairy roots were conducted in Nuclear ResearchInstitute. The source of gamma rays was Cobalt 60

3. Results and discussion

3.1. Effect of sterilization conditions on percent response of explants and frequency of contamination

To study the effect of sterilization conditions on percent response as well as on percent contamination, the surface of the explants were sterilized with 70% aqueous ethanol for 1 or 2 minutes, combined with dipped in 1% NaOCl for 3, 5 or 7 minutes

The results showed that the treatment of 70 % ethanol for 1 minute and 1 % NaOCl for 7 minutes had percent sterile sample reached 76.67 ± 8.61%; the percent response of explants reached 97.50 ± 5.0 %, which was the optimal sterilization condition

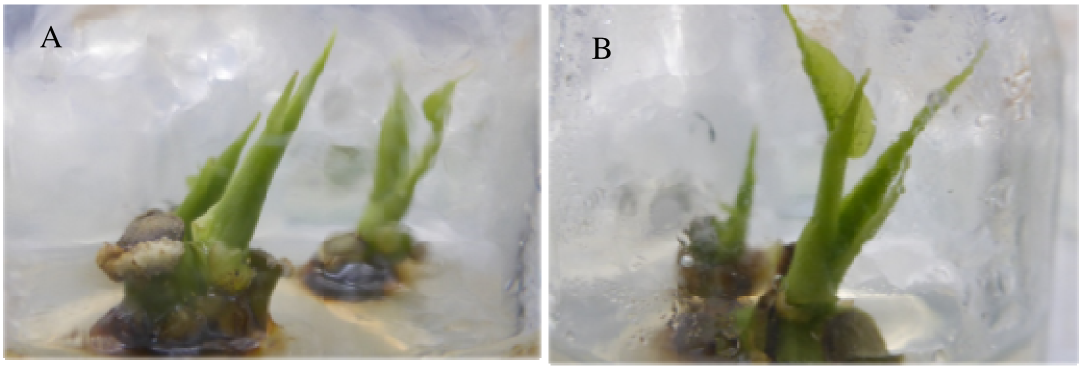

Figure 2: In vitro regeneration of F. religiosa from nodal (A) and shoot tip (B) in 2 weeks of culture

3.2. Effect of materials, infection time and co-cultivation period on hairy roots induction

3.2.1. Effect of materials

In oder to determined the suitable explantfor hairy roots induction, leaves, leaf stalks and inter nodes were submerged in the *A. rhizogenes* suspension medium for 20 minutes, co-cultivation for 3 days. Control sampleswere submerged in sterilized distilled water.

From the results were showed in Table 1 we found that leaves were the best appropriate material to the bacteria genetic transformation 32.00 ± 4.0 %. While for inter nodes were the next 16.00 ± 2.0 %, no hairy roots were induced on leaf stalks.

Table 2: Influence of various explants on hairy roots induction

	Materials	Number of hairy roots (hairy root/explant)	Induction rate (%)	Appearance time (day)
Transfor-mation	Leaves	2.27 ± 0.05^{a}	32.00 ± 4.0^{a}	26.0 ± 2.0^{a}
	Leaf stalks	-	-	-
	Inter nodes	1.70 ± 0.11^{b}	16.00 ± 2.0^{b}	21.00 ± 2.0^{b}
Control	Leaves	-	-	-
	Leaf stalks	-	-	-
	Inter nodes	-	-	-

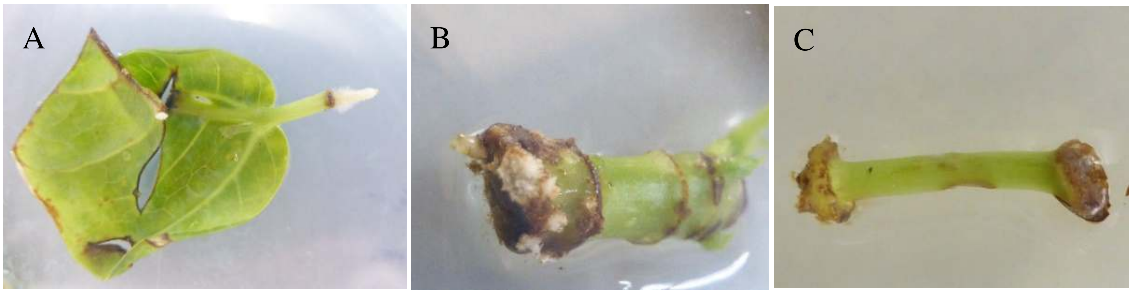

Figure 3: Hairy roots Induced on Leaves (A), Inter nodes (B) and Leaf stalks (C)

3.2.2. Effect of infection time

Further optimization was carried out by changing the infection time.Among of all the materials, leaves were the best one for transformation of gene by *A. rhizogenes*in vitro. The leaves were given by random cuts with sterilized scalpel. These wounded leaves were then dipped in bacterial suspension with infection time from 10 minutes to 40 minutes, in 3 days of co-cultivation.

The results were provided in Table 3. During this study, in wide range of infection time, 30 minutes was the most effective time and to get the maximum transformation efficiency at 44.00 ± 6.00 %.

Table 3: Transformation frequencies obtained with different infection time

Infection Time (minute)	Number of hairy roots (hairy root/explant)	Induction rate (%)	Appearance time (date)
10	2.10 ± 0.21^{a}	15.33 ± 1.15^{c}	25.53 ± 1.53^{a}
20	2.02 ± 0.09^{a}	36.67 ± 5.03^{b}	27.33 ± 2.52^{a}
30	2.20 ± 0.16^{a}	44.00 ± 6.00^{a}	26.67 ± 2.08^{a}
40	2.21 ± 0.45^{a}	21.33 ± 4.16^{c}	28.00 ± 1.73^{a}

3.2.3. Effect of co-cultivation period

The maximum transformation efficiency at 66.67 ± 7.64 % was achieved after 5 days of co-cultivation (Table 4). Longer period of co-cultivation were unsuitable, particularly for *in vitro* explants, many of explants decreased survival ratio because of uncontrollable overgrowth of bacteria.

Table 4: Influence of co-cultivation period on hairy roots induction

Co-cultivation (date)	Number of hairy roots (hairy root/explant)	Induction rate (%)	Appearance time (day)
2	2.08 ± 0.31^{a}	40.83 ± 3.82^{c}	30.33 ± 4.16^{a}
3	2.22 ± 0.26^{a}	51.67 ± 8.04^{bc}	29.67 ± 3.06^{a}
4	1.92 ± 0.49^{a}	59.17 ± 8.04^{ab}	26.67 ± 8.02^{a}
5	1.97 ± 0.44^{a}	66.67 ± 7.64^{a}	28.33 ± 4.16^{a}
6	1.94 ± 0.34^{a}	52.50 ± 9.01^{abc}	29.33 ± 2.52^{a}

3.3. Identification of genetic transformation by PCR

Beside these morphological characterizations, identification of the transformation status of the hairy roots was completed by a molecular analysis. In our study, *A. rhizogenes*DNA plasmid, DNA of hairy roots and normal roots were analysed by PCR.

An amplification signal at 780 and 540 bp for *rol*B and *rol*C fragments, respectively, was observed in transgenic hairy roots (Figure 4.A, B). No amplification signal was detected for *vir*D2 gene in the same sample (Figure 4.C), indicating the absence of residual bacteria. Those were a proof for the successful genetic transformation.

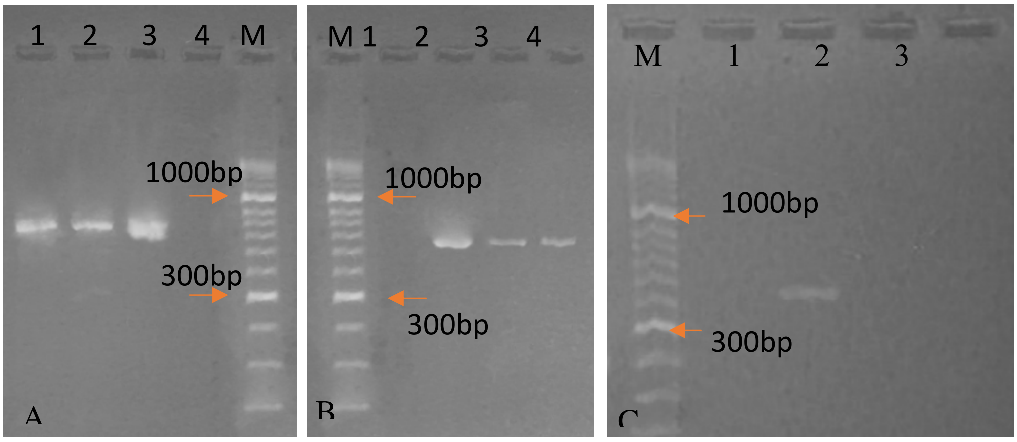

Figure 4: Confirmation of transformation by PCR. A.PCR amplification of *rol*B gene (780bp). Lane 1, 2: Hairy root sample; Lane 3: *A. rhizogenes* plasmid DNA (positive control); Lane 4: non-transformed roots (negative control).B.PCR amplification of *rol*C gene. (540 bp). Lane 1: non-transformed roots (negative control); Lane 2: *A. rhizogenes* plasmid DNA (positive control); Lane 3, 4: Hairy root sample.C.PCR amplification of *vir*D gene. (450 bp). Lane 1: non-transformed roots (negative control); Lane 2: *A. rhizogenes* plasmid DNA (positive control); Lane 3, 4: Hairy root sample.

3.4.1. Influence of medium type

Composition of plant culture media is an important parameter for both growth and specialized metabolite production. Here, the effects of culture media on the growth were evaluated using three different culture media: Murashige and Skoog (MS) [4], Woody Plant Medium (WPM) [5]and Gamborg B5 (B5) [6].

Figure 5: The hairy roots culture development on B5, WPM and MS medium (left to right)

The results showed that after 28 days of cultivation, among of the three tested culture media, MS was the best for root growth with growth index at 17.27 ± 0.82, then were WPM and B5 with growth index reaching 13.25 ± 0.70 and 11.29 ± 0.45 respectively (Figure 5).

3.4.2. Influence of level of sucrose

Hairy roots are heterotrophically-grown culture generally*in vitro* cultures.Hence sugar carbon source has to be provided during cultivation to ensure normal growth and metabolite production. However, high sugar concentration could result in an osmotic stress that can affect plant growth.

Here sucrose source at five different levels were tested: 0, 10, 20, 30 and 40 g/L. The obtained data showed that MS medium supplemented with 20 mg/L sucrose was the best medium for hairy roots growth with growth index 22.00 ± 1.074 after 28 days of cultivation. In this study, increasing sucrose level beyond 20 g/L resulted in detrimental impact on growth (Figure 6)

Figure 6: The hairy roots culture development on MS medium supplemented with 0, 10, 20, 30 and 40 g/L (left to right)

3.5. Effect of cobalt-60 radiation on growth and total phenolic content of hairy roots

The results showed that survival rate, fresh and dry weight decreased with increasing dose of irradiation from 10 to 40 Gy (Table 5). Significant differences were found in the total phenolic content of hairy roots at different doses.The total phenolic content was found to be highest at 20 Gy reached 36.72 mg GAE/g DW that increase 1.44 fold compared to the control at 25.54 mg GAE/g DWand 30 Gy was found to be the lowest total phenolic content reached 23.21 mg GAE/g DW (Figure 7)

Table 5: Effect of different doses of gamma irradiation on the growth parameters of hairy root

Dose (Gy)	Survival rate (%)	Fresh weight(g)	Growth index	Dry weight (%)
0	100.00 ± 0.0	0.362 ± 0.051^{a}	18.25 ± 1.39^{a}	15.04 ± 0.71^{b}
10	86.67 ± 13.33	0.284 ± 0.030^{b}	12.66 ± 1.19^{b}	14.05 ± 2.59^{b}
20	55.56 ± 10.18	0.184 ± 0.041^{c}	7.59 ± 1.18^{c}	14.13 ± 2.03^{b}
30	31.11 ± 10.18	0.161 ± 0.041^{c}	7.96 ± 2.51^{c}	22.25 ± 1.38^{a}
40	0.00 ± 0.0	-	-	-

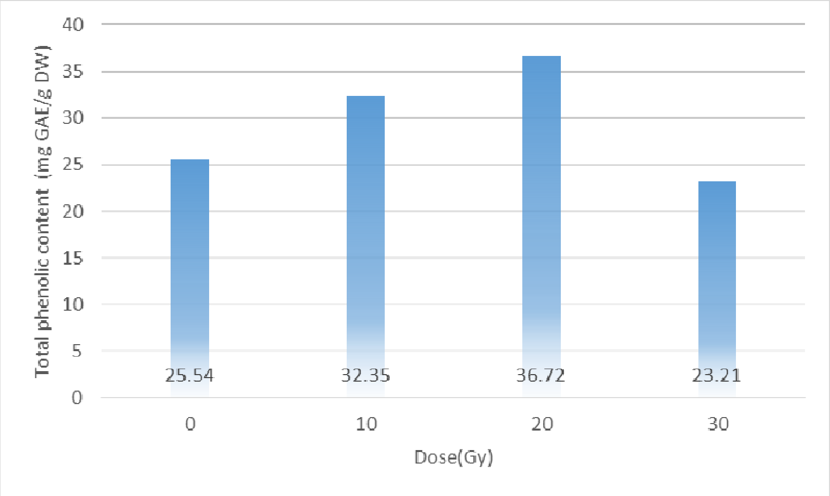

Figure 7: Effect of different doses of gamma irradiation on total phenolic content

4. CONCLUSIONS

During process in vitro culture, sterilization is the most important step in preparation of explants. The results showed that treatment of 70 % ethanol for 1 minute and 1 % NaOCl for 7 minutes were the optimal sterilization conditions.The best conditions for transformation included the use of leaves with 30 minutes of infection and five days of co-cultivation. MS medium with supplemented 2 % sucrose was suitable for the growth of hairy roots.

Our results showed that gamma radiation effected on the growth rate and morphological characterizations of hairy roots. It is noteworthy in this study that under gamma conditions the phenolic contents increased of 1.44 fold at 20 Gy reached 36.72 mg GAE/g DW.

In the future, both the hairy roots cultivation of *F. religiosa* gamma radiation using as a elicitor that will enable extraction of secondary metabolites serving for medicinal properties such as phenolic compounds.

REFERENCES

[1] Vivek D. Rathod, Digambar N. Ware2, Shibu Pillai3 et al. Antiarthritic activity of ethanolic extract of ficus religiosa leaves in fca induced arthritis in rats. *World Journal of Pharmaceutical Research*. 2018,Volume 7, Issue 2, 778-789 ().

[2] Vrishali V. Korde, Snehal S. Dhas and Neha A. Gurave. Hairy Root Culture: A Promising Approach in Biotransformation. *Asian Journal of Plant Science and Research*. 2016, 6(4), 6-11.

[3] Ashouri Sheikhi A, Hassanpour H, Jonoubi P et al. The Effect of Gamma Irradiation on In vitro Total Phenolic Content and Antioxidant Activity of Ferula gummosa Bioss. *Journal of Medicinal Plants*. 2016, 15(59), 122-131.

[4] Murashige, T.; Skoog, F.. A revised medium for rapid growth and bioassay with tobacco tissue culture.*Physiol. Plant*.1962, 15, 473–497.

[5] Lloyd, G.; McCown, B.. Commercially-feasible micropropagation of Mountain Laurel, Kalmia latifolia,by shoot tip culture. *Int. Plant Prop. Soc.* 1981, 30, 421–427.

[6] Gamborg, O.L.; Miller, R.A.; Ojima, K.. Nutrient requirements of suspension cultures of soybean root cells.*Exp. Cell Res*.1968, 50, 151–158.

STUDY ON PREPARATION OF SILVER NANOPARTICLE/DIATOMITE NANOCOMPOSITE BY ELECTRON BEAM IRRADIATION METHOD FOR TREATMENT OF PATHOGENOUS BACRERIA IN CULTURE WATER OF TRA CATFISH

Truong Thi Hanh, Nguyen Thi Thu, Le Anh Quoc and Nguyen Quoc Hien.

Research and Development Center for Radiation Technology, Vietnam Atomic Energy Institute,
202A, 11 Street, Linh Xuan Ward, Thu duc District, Ho Chi Minh City

Project information:

- **Code:** CS/18/07-01
- **Managerial Level:** Institute
- **Allocated Fund:** 80,000,000 VND
- **Implementation time:** 12 months (Jan 2018- Dec 2018)
- **Contact email:** Vinagamma@ vinagamma.com.vn; Truongthihanh05@yahoo.com
- **Paper published in related to the project:**

1. Trương Thi Hanh et al., Synthesis and Characterization of Silver/Diatomite nanocomposite by Electron Beam irradiation, *Radiation Physics and Chemistry* 139, 141-146, 2017.

2. Truong Thi Hanh, et al., Preparation of silver nano/diatomite nanocomposite by electron beam irradiation method. *Vietnam Conference on Nuclear Science and Technology 12*, Nha Trang, Vietnam, 2-4 August 2017 (in Vietnamese).

3. Truong Thi Hanh, Nguyen Thi Thu, Le Anh Quoc (young staff), Investigation of characterizations of silve nanoparticles/diatomite nanocomposite prepared by electron beam irradiation method. *The 5th Vietnam Conference on Nuclear Science and Technology for Young Researchers.* Hanoi, Vietnam October 2018 (in Vietnamese).

Abstract: Electron beam (EB) irradiation of suspension including $AgNO_3$/chitosan solution and diatomite (DA) to synthesize nanocomposite of silver nanoparticles (AgNPs)/DA was investigated. The Ag^+ ions of $AgNO_3$ precursor were reduced to Ag^0 atoms and aggregated on DA. The AgNPs were identified by UV-Vis spectra with peak maxima around 417-422 nm. Nanocomposites – AgNPs/DA were characterized by TEM images in which the AgNPs were spherical with an average diameter of 5-9 nm corresponding to absorbed doses from 5 to 25 kGy. Energy dispersive X-ray (EDX) spectra for DA and AgNPs/DA nanocomposites confirmed the presence of elemental compounds in DA and AgNPs. The antibacterial activity of the AgNPs/diatomite nanocomposite against *E. coli* as well as the infectious pathogens for Tra catfish such as *Aeromonas hydrophila* and *Edwardsiella ictaluri* were tested.

1. INTRODUCTION

Recently, nanoparticles and nanocomposites have been potentially applied in various fields such as nanodevices, biomedicine, cosmetic, filter aid in food, photocatalysis and antibacterial treatment in environment…[1, 2]. Further, new properties have been achieved through improvements in physical, chemical interactions and biological effects [3]. The development of advanced nanomaterials by combination of macromolecules with inorganic particles has become one of the most innovative research areas [4]. These nano materials display featured characterizations by synergistic effects resulting from interactions between inorganic nanoparticles and organic components [5]. Because of their effective antimicrobial properties and low toxicity toward animal cells, silver nanoparticles (AgNPs) have become one of the most commonly used nanomaterials in consumer products [6]. Especially, AgNPs-decorated porous silica such as ceramic, montmorillonite, zeolite, diatomite… have been used in purpose of water purification such as bactericide, antifouling agent, catalyst and decontaminant… [7]. Nanocomposite contains AgNPs which have a broad spectrum of antimicrobial activities including multi-drug resistant bacteria was studied by several scientists [8, 9]. At present, AgNPs were considered as a “green” decontaminant against the bacteria in the aquatic environment such as *Lactococcus garvieae*, *Streptococuss iniaea*… which were isolated from diseased rainbow trout in culture ponds [10]. The size and the morphology of metal nanoparticles as AgNPs were stabilized by chitosan, an antibacterial polysaccharide, will be suitable for purpose using nanoparticle as bactericide [11]. Preparation of nanocomposite as AgNPs/chitosan and AgNPs/silica in ceramic, diatomite or zeolite for controlling infectious agents in the environment has been necessary to substitution for the use of toxic chemicals [12]. Irradiation by electron beam (EB) or γ-rays was also reported by experts to be effective and attractive method to prepare nanocomposite. The advantage of radiolytic reduction method, over the other methods, is possibility to obtain a homogeneous distribution of synthesized AgNPs within polymer matrix as well as to control their size by changing the experimental conditions [11]. The obtained material is clean and sterilized at the same time, which is important to use nanocomposite as a decontaminant.

In this study, nanocomposite of AgNPs/DA was prepared by irradiation method in which the ions (Ag^+) adsorbed on silica in DA were reduced by the solvated electrons and $^\bullet H$ radicals from radiolysis water process. Continuous reduction of the Ag^+ ions causes the aggregation into AgNPs cluster on DA for formation of AgNPs/DA nanocomposite.

2. METHODS

2.1. Preparation of AgNPs-chitosan/diatomite nanocomposite by EB radiolytic reduction method

Process of preparation of AgNPs/DA nanocomposite by EB irradiation of DA/$AgNO_3$ suspension:

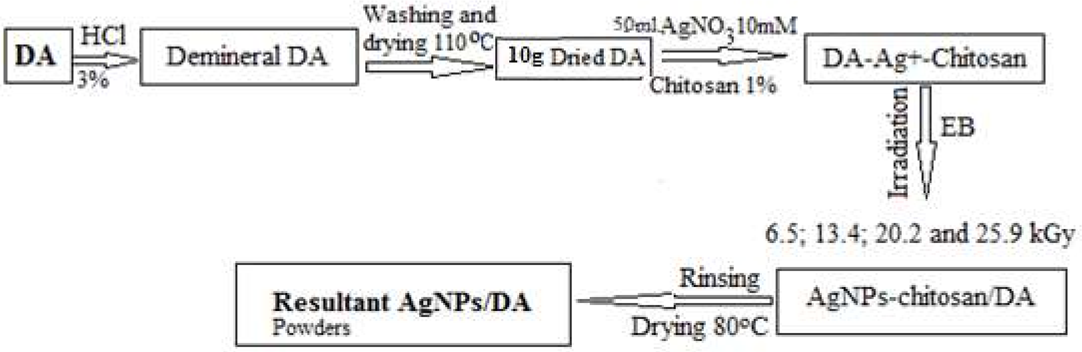

2.2. *Characteristics of AgNPs-chitosan/diatomite nanocomposite*

The UV-vis spectra of the colloidal AgNPs were recorded on a Jasco V-630 spectrophotometer in the range from 200-600 nm after the solution was diluted 20 times with distilled water. EDX spectra were carried out on a SEM-EDX instrument – SEM S4800 (Hitachi) combined with a H7593 (Horiba) X-ray analyzer. Transmission electron microscopy (TEM) images were performed with a JEOL, JEM-1400 electron microscope at an accelerated voltage of 100 kV. The content of AgNPs in AgNPs/diatomite nanocomposite was evaluated by inductively coupled plasma atomic emission spectroscopy (ICP-AES).

2.3. Antibacterial efficacy of AgNPs/DA nanocomposite

The antibacterial activity of the resultant AgNPs/DA nanocomposite against *E. coli* (ATCC 6538) was evaluated using spread-plate method on LB agar Petri plate, while *Edwardsiella ictaluri* and *Aeromonas hydrophila* were cultured on Brain Heart Infusion Agar (BHIA) medium. And then the bacterial suspension as 0.5 McFarland standard at 10^8 (CFU/ml) was adjusted and diluted to 10^3-10^4 (CFU/ml) bacteria. Next, AgNPs/DA nanocomposite was introduced in bacterial suspension with ratio of 0.2 g nanocomposite/10 ml bacterial suspension, then mixture was shaken and incubated for 3 and 24 hours. After interaction between bacteria and AgNPs in nanocomposite, 0.1 ml liquid was spread on LB agar plates, then incubated at 30°C for 24 h. Percent reduction of bacteria was evaluated by the counts of survival colonies on agar plates of sterilized water (control) and experimental samples at 0, 3 and 24 hours, respectively.

3. RESULTS AND DISCUSSION

3.1. Preparation of AgNPs/DA nanocomposite

Firstly, diatomite was treated with 1% hydrochloric acid (v/v) in order to reduce mineral then washed and dried at 110°C before stirring with $AgNO_3$/chitosan solution. And then, the aqueous ammonia was used as base to adjust the pH of suspension to 5-6. Caliskan et al (2011) reported that the pHzpc (isoelectric point) of diatomite was ~ 4 so the diatomite surface may be negatively charged above pHzpc [13]. The electrophilic silver ions (Ag^+) were adsorbed on the surface and embedded in amorphous silicon dioxide (SiO_2) with the nucleophilic oxide groups (SiO—) by stirring formation of suspension before irradiation [14]. The solvated electrons (e^-_{aq}) with E^o (H_2O/e^-_{aq} = - 2.87 V_{NHE} and $^{\bullet}H$ radicals with E^o (H^+/ $^{\bullet}H$) = - 2.3 V_{NHE} that were generated by water radiolysis can reduce adsorbed Ag^+ ions to Ag atoms by irradiation effects in suspension solution ($E^o(Ag^+/Ag)$ = - 1.8 V). Continuous reduction of the Ag^+ ions causes the aggregation into AgNPs cluster (E^o (Ag^+_n/Ag_n) = 0.79 V_{NHE}) [15]. Moreover, in chitosan solution, the radiolytic $^{\bullet}OH$ groups from irradiated water coordinate with chitosan by hydrogen abstraction to form macromolecule free radicals ($R^{\bullet}_1$). At a slight acid medium pH 5-6, hydronium ion H_3O^+ represents an important scavenger for solvated electrons e^-_{aq} which are converted to $^{\bullet}H$ radicals ($k = 2.3 \times 10^7$ $m^3.mol^{-1}.s^{-1}$). These radicals also contribute to reduction of Ag^+ in chitosan solution to Ag^0, so the value of total reduction yield (G_{red}) is unchanged and close to maximal reduction yield ($G_{red.max}$) in theory [9]. In this study, the reaction mechanism for the reduction of adsorbed Ag^+ on silica (SiO_2) in suspension of $AgNO_3$/chitosan/DA by electron irradiation can be proposed as follows:

$$Ag^+ \quad + \quad (SiO—) \quad \rightarrow \quad Si\text{-}O{\bullet}{\bullet}{\bullet}Ag^+ \qquad (1)$$

$$H_2O\ (EB) \quad \rightarrow \quad {}^{\bullet}OH + e^-_{aq} + {}^{\bullet}H + H_2O_2 + H_2 + \ldots \qquad (2)$$

$$e^-_{aq} + H_3O^+ \quad \rightarrow \quad {}^{\bullet}H + H_2O \qquad k = 2.3 \times 10^7\ m^3.mol^{-1}.s^{-1} \qquad (3)$$

$$Si\text{-}O{\bullet}{\bullet}{\bullet}Ag^+ \quad + \quad e^-_{aq}\ ({}^{\bullet}H) \quad \rightarrow \quad Si\text{-}O{\bullet}{\bullet}{\bullet}Ag^0 \qquad (4)$$

$$R(chitosan) \quad + \quad {}^{\bullet}OH\ ({}^{\bullet}H) \quad \rightarrow \quad R^{\bullet}_1\ \text{(H abstraction)} \quad + \quad H_2O\ (H_2) \qquad (5)$$

$$Si\text{-}O{\bullet}{\bullet}{\bullet}Ag^+ \quad + \quad R^{\bullet}_1 \quad \rightarrow \quad Si\text{-}O{\bullet}{\bullet}{\bullet}Ag^0R_1 \qquad (6)$$

$$nSi\text{-}O{\bullet}{\bullet}{\bullet}Ag^0R_1 \quad \rightarrow \quad Si\text{-}O{\bullet}{\bullet}{\bullet}Ag_2R_2 \quad \rightarrow \quad Si\text{-}O{\bullet}{\bullet}{\bullet}Ag_nR_n \qquad (7)$$

The binding of silver clusters with chitosan as well as with silica surface of diatomite are achieved through the Ag—O—Si bonds. Besides, the protonated amine groups ($R—NH_3^+$) of chitosan in acidic medium can stabilize silver clusters by electrostatics repulsions [11].

UV-Vis spectrophotometry technique was applied to confirm the formation of AgNPs in the irradiated solution by EB. The AgNPs colloidal solutions depicted peak maxima (λ_{max}) of UV spectra in the range from 415- 422 nm as presented spectra in Fig. 1. The absorbance intensities increased with EB doses from 6.5 to 20.2 kGy. Above 20.2 kGy (25.9 kGy), the absorbance changed insignificantly. Therefore, the dose of 20.2 kGy was optimal for complete conversion of the 10 mM $AgNO_3$ to AgNPs in suspension with the ratio of $DA/Ag^+ = 1:5$ (/w/v, g/ml).

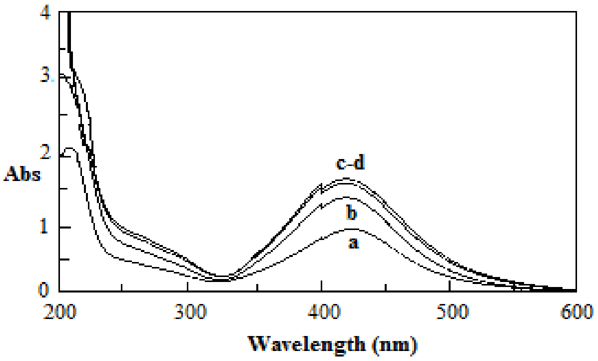

Figure 1: UV-Vis spectra of colloidal AgNPs from 10mM $AgNO_3$/DA suspension diluted 20 times corresponding to absorbed doses of: (a) 6.5 kGy, (b) 13.4 kGy, (c) 20.2 kGy and (d) 25.9 kGy

1.2. Characterizations of AgNPs/DA nanocomposite

Figure 2 shows SEM images of DA and AgNPs/DA samples. The image revealed the blank porous structure of DA in Fig. 2a. On the other hand, the morphology of AgNPs/DA indicated that the particles were loaded into pores of DA which could be attributed to the presence of silver nano (Fig. 2c).

The elemental compositions of DA are determined by EDX spectrum in Fig. 2b including peaks of O, Na, Al and Si at 0.5, 1.1, 1.5 and 1.8 keV, respectively The EDX spectrum of AgNPs/DA nanocomposite

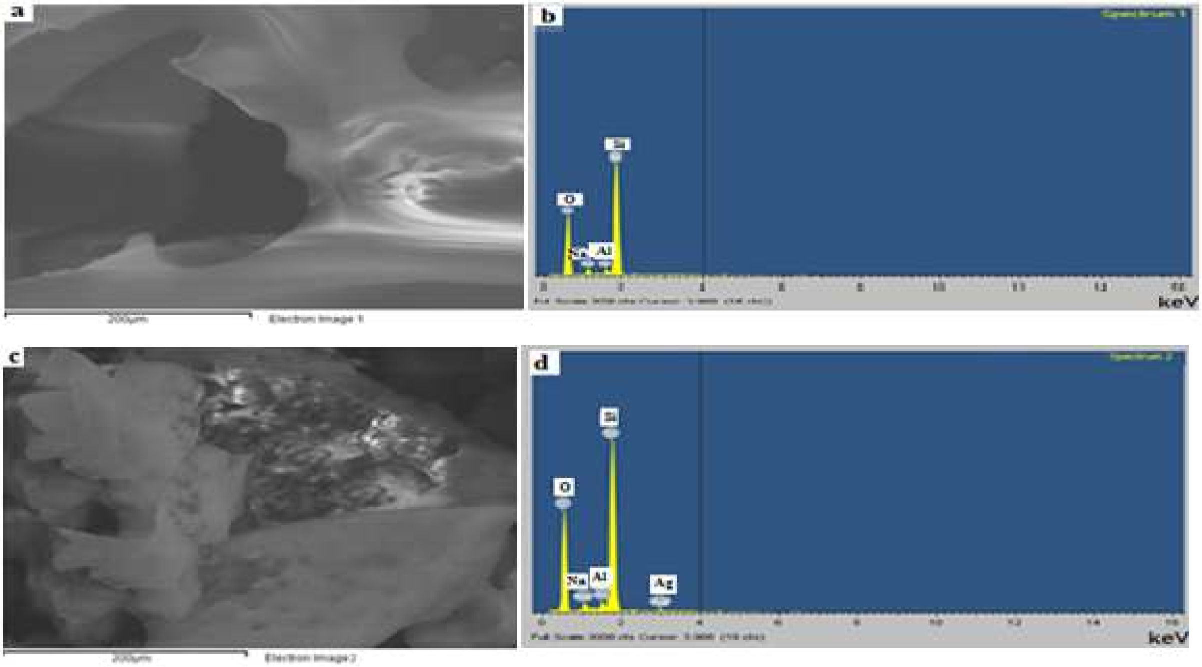

Figure 2: SEM images and EDX spectra respectively for the diatomite (a, b) and AgNPs/DA nanocomposite (c, d) at the dose of 20.2 kG y

depicted a new peak of Ag at 3 keV besides similar elements to component of DA (Fig. 2d).

The absorbed dose plays an important role in formation and growth of AgNPs by EB-irradiation in which Ag^+ ions in $AgNO_3$/chitosan/DA suspension were reduced to Ag^0 and simultaneously immobilized on diatomite. The silver nanoparticles grow in size with an increase in the absorbed dose, at the same parameters such as the beam energy, beam current and concentration of the precursor. This means that density of the hydrated electrons (e^{-}_{aq}) and hydrogen radicals ($^{\bullet}H$) increased at a high dose, so the reduction and aggregation of silver nanoparticles at a high dose is superior to that at a low dose [16]. The TEM images of nanocomposites - AgNPs/DA were formed from 10mM $AgNO_3$ at different EB-irradiation doses were shown in Fig 3. The results that the AgNPs with spherical morphology are well dispersed without aggregation on the surface of diatomite. The average diameters of AgNPs are determined from TEM images to be 5.5 ± 1.0 nm; 6.9 ± 1.2 nm; 9.3 ± 1.3 nm and 8.9 ± 1.0 nm at the doses of 6.5; 13.4; 20.2 and 25.9 kGy, respectively. At high irradiation dose, the amounts of chitosan chains increase by degraded irradiation, the more chitosan chains there are, the more they inhibit the aggregation of the silver nanoparticles. The dispersion of AgNPs in DA matrix through silica avoiding their aggregration, so small sized AgNPs with a typical diameter <10 nm were formed [17].

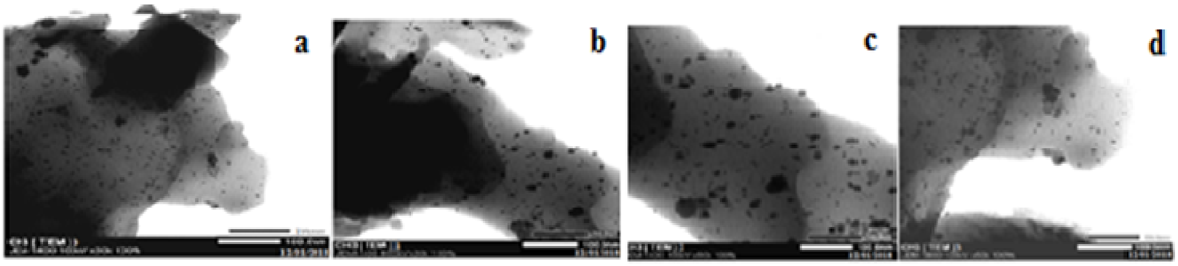

Figure 3: TEM images of AgNPs in nanocomposites at absorbed doses of a) 6.5; b) 13.4; 20.2 and 25.9 kGy.

1.3. Antibacterial efficacy of AgNPs/DA nanocomposite

Fig.4. shows the test results for antibacterial efficacy against *E. coli* of samples, namely the LB control and the AgNPs/DA nanocomposite at various concentrations of bacteria. The control specimens showed the overgrowth of bacteria on the LB nutrient substrate (Fig.4O). However, the bacterial counts decreased remarkably after a contact time of 3 hours with the nanocomposite of AgNPs/DA. The inhibitory effect of AgNPs/DA depends on the CFU of bacteria used in the experiments. The total reduction of 100% *E. coli* ($<10^6$) was determined to be 5 μg/ml of AgNPs/DA (Fig. 4a, b, c, d).

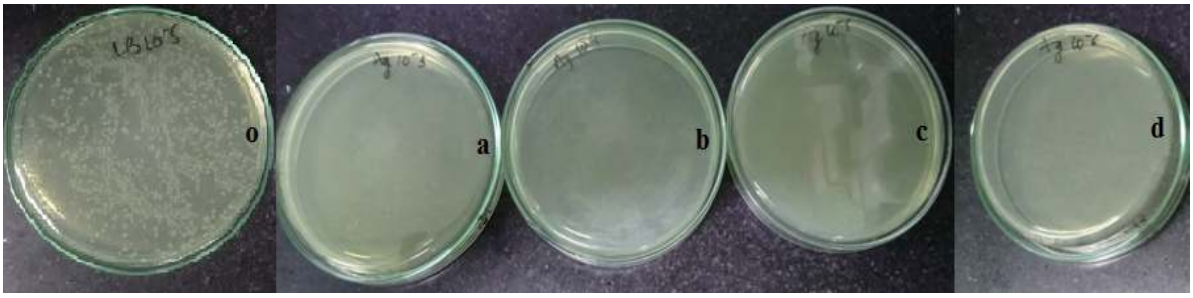

Figure 4: Photographs of antibacterial test results against *E. coli:* Sterilized water (o); AgNPs/DA nanocomposite with bacteria CFU/ml of 10^3 (a); 10^4 (b); 10^5 (c); 10^6 (d)

In aquaculture, one of the big challenges was infection disease control caused by virus, bacteria, fungus and parasites. Traditionally, the antibiotic was used to oppose bacterial infections in aquaculture. However, the frequent use of antibiotic causes the antibiotic resistant of strains such as *Aeromonas salmonicida, Photobacterium damselae, Yersinia ruckeri, Listeria sp, Vibrio sp, Pseudomonas sp* and *Edwardsiella sp…* [18]. Another alternative can control important pathogens from fishes, mollusks, and crustaceans which have been studied by several scientists, namely silver nanoparticles [18, 19].

According to nanocomposite experts, the silica matrix structure acts a convenient carrier for incorporating with metal nanoparticles as AgNPs by dispersion of discrete silver nanoparticles throughout silica and limitation for release of AgNPs, resulting in long-term antibacterial efficacy [17]. In this study, nanocomposite containing AgNPs immobilized on DA was tested to determine its antibacterial activity against contaminative *Aeromonas hydrophila* and *Edwardsiella ictaluri* bacteria for catfish (*Pangasianodon hypophthalmus*) in Vietnam. The experiment was carried by incubation of bacteria with AgNPs/DA for 3h and 24h. The test results showed that no bacteria survived on BHIA plates cultured bacteria which were incubated with AgNPs/DA containing 0.13% AgNPs at concentration of 26 µg/ml media. However, bacteria were unreduced on the control samples with sterilized water (ĐC - Fig. 5). Vaseeharan et al. (2011) reported AgNPs at 75 µg/ml inhibited the total growth of *Vibrio harveyi*, a pathogenous agent for penaeid shrimps [20]. These studies made a successful attempt to demonstrate the ability of AgNPs as well as AgNPs composite on controlling aquaculture diseases. These small sized-AgNPs possess large surface areas, enabling them to have large contact areas with the bacterial cells, leading on the increase in permeability of cell membranes and disturbance of respiration. Moreover, the aerobic environments of the antibacterial tests allow for the partial surface oxidation of the AgNPs, resulting in generating Ag^+ ions that can disrupt ATP (adenosine triphosphate) production to inhibit the phosphate adsorption of bacterial protein [1]. Therefore, silver nanoparticles - silica composite is a promising candidate has been used as antibacterial, antifungal and antiviral agents.

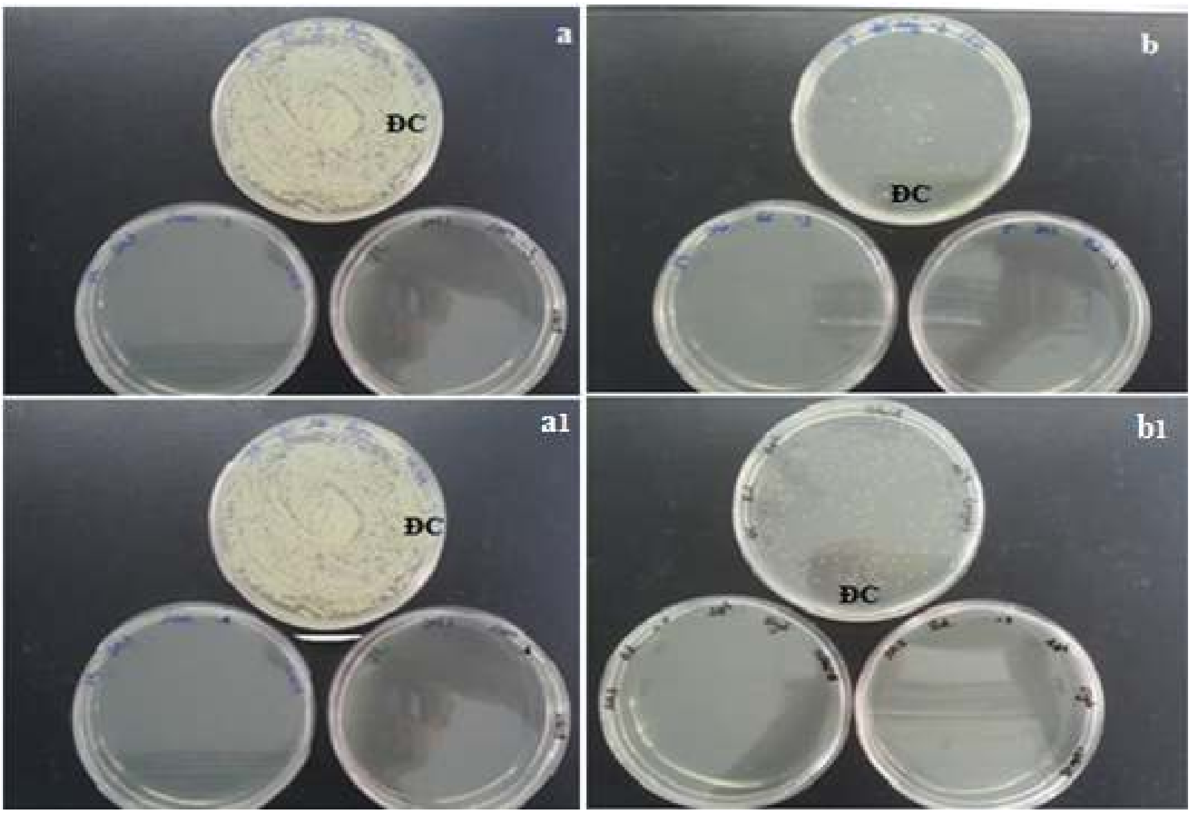

Figure 5: Photographs of antibacterial test results of AgNPs/DA against *Aeromonas hydrophila* at conc. 10^3(a) - 10^4 CFU/ml (a_1) and *Edwardsiella ictaluri* at conc. 10^3(b) - 10^4 CFU/ml (b_1).

2. CONCLUSIONS

The silver ions were reduced to atoms by EB irradiation and simultaneously deposited on the diatomite by *in situ* synthesis. The AgNPs in DA were confirmed by the SEM and TEM images, EDX spectra. The average diameter of AgNPs in nanocomposite <10 nm were formed from 1-10 mM $AgNO_3$ precursor in DA under an electron beam irradiation of 10 MeV energy and beam current of 1.5 mA. The AgNPs/DA nanocomposite exhibited good antibacterial activity against *E. coli* as well as *Aeromonas hydrophila* and *Edwardsiella ictaluri.* The inhibition of microbial growth due to surface contact with the AgNPs/DA nanocomposite demonstrated that material functionalized with AgNPs has excellent antimicrobial properties. Further assays of the activity of AgNPs/DA on bacteria *in vivo* with pathogens for Tra catfish in aquaculture will be tested with the next study.

REFERENCES

[1] C.M. Jone, E.M.V. Hoek, A review of the antibacterial effects of silver nanomaterials and potential implications for human health and the environment, J. Nanopart. Res. 12, 1531-1551, 2010.

[2] Baker, A. Pradhan, L. Pakstis, D.J. Pochan, S.I. Shah, S.I., Synthesis and antibacterial properties of silver nanoparticles, J. Sci. Technol. 5 (2), 244-249, 2005.

[3] F. Hussain, M. Hojjati, M. Okamoto, R.E. Gorga, R.E., Polymer-matrix nanocomposites, processing, manufacturing and application: An overview. J. Compos. Mater. 40, 1511-1575, 2006.

[4] I.Y. Jeon, J.B. Baek, Nanocomposites derived from polymers and inorganic nanoparticles, Materials 3, 3654-3674, 2010.

[5] A.M.El Nahrawy, A.B. Abou Hammad, G. Turky, M.M.M. Elnasharty, A.M. Youssef, Synthesis and characterization of hydrid chitosan-calcium silicate nanocomposite prepared using sol-gel method, Int. J. Adv. Eng. Technol. Comput. Sci. 2 (1), 9-14, 2015.

[6] M.J. Firdhouse, P. Lalitha, Biosynthesis of silver nanoparticles and its applications. J. Nanotechnol. 2015, Article ID 829526, 18 pages.

[7] Y. Lv, H. Liu, Z. Wang, S. Liu, L. Hao, Y. Sang, D. Liu , J. Wang, R.I. Boughton, Silver nanoparticle-decorated porous ceramic composite for water treatment. J. Membr. Sci. 331, 50-56, 2009.

[8] M.K. Rai, S.D. Deshmukh, A.P. Ingle, A.K. Gade, A.K., Silver nanoparticles: the powerful nanoweapon against multidrug-resistant bacteria, J. Appl. Microbiol. 112, 841-852, 2012.

[9] T.T. Hanh, N.T. Thu, N.Q. Hien, P.N. An, T.T.K Loan, P.T. Hoa, P.T., Preparation of silver nanoparticles fabrics against multidrug-resistant bacteria, Rad. Phys. Chem. 121, 87-92, 2016.

[10] M. Raissy, M. Ansari, *In vitro* antimicrobial effect of silver nanoparticles on *Latococcus garvieae* and *Streptococcus iniae*, Afri. J. Microbiol. Res. 5(25), 4442-4445, 2011.

[11] P. Chen, L. Song, Y. Liu, Y. Fang, Synthesis of silver nanoparticles by γ-rays irradiation in acetic water solution containg chitosan. Radiat. Phys. Chem. 76, 1165-1168, 2007.

[12] S. Vijayakumar, B. Vaseeharan, B. Malaikozhundan, N. Gobi, S. Ravichandran S. Karthi, B. Ashokkumar, N. Sivakumar, A novel antimicrobial therapy for the control of *Aeromonas hydrophila* infection in aquaculture using marine polysaccharide coated gold nanoparticle, *Microbial Pathogenesis,* 110, 140-151, 2017.

[13] N. Caliskan, A.R. Kul, S. Alkan, E.G. Sogut, I. Alacabey, Adsorption of zinc (II) on diatomite and manganese-oxide-modified diatomite: A kinetic and equilibrium study. J. Hazard. Mater. 193, 27-36, 2011.

[14] D. Lawless, S. Kapoor, P. Kennepohl, D. Meisel, N. Serpone, Reduction and aggregation of silver ions at the surface of colloidal silica, J. Phys. Chem. 98(38), 9619-9625, 1994.

[15] T. Linnert, P. Mulvaney, A. Henglein, H. Weller H., Long-lived nonmetallic silver clusters in aqueous solution: preparation and photolysis. J. Am. Chem. Soc. 112, 4657- 4664, 1990.

[16] H.S. Kang, B. Kim, J.H. Park, W. K. Kim, Y.H. Koo, H.B. Bae, C. Park, B.C. Lee, Size Control Technology of Silver Nanoparticles Using Electron Beam Irradiation. Bull. Korean Chem. Soc. 34, 3899-3902, 2013.

[17] S. Egger, R.P. Lehmann, M.J. Height, M.J. Loessner, M. Schuppler, Antimicrobial properties of a novel silver-silica nanocomposite. Appl. Environ. Microbiol. 75(9), 2973-2976, 2009.

[18] J.C.M Márquez, A.H. Partida, M. Carmen, M. Dosta, J.C. Mejía, J.A.B., Martínez, J.A.B., Silver nanoparticles applications (APNPS) in aquaculture, Int. J. Fish. Aquat. Stud. 6(2), 05-11, 2018.

[19] Swain, P., Nayak, S.K., Sasmal, A., Behera, T., Barik, S.K. , Swain, S.K., Antimicrobial activity of metal based nanoparticles against microbes associated with diseases in aquaculture. World J. Microbiol. Biotechnol. 30(9), 2491-2502, 2014.

[20] B. Vaseeharan, P. Ramasamy, J.C. Chen, Antibacterial activity of silver nanoparticles AgNPs) synthesized by tea leaf extracts against pathogenic *Vibrio harveyi* and its protective efficacy on juvenile *Feneropenaeus indicus*", Lett. Appl. Microbiol. 50(4), 352–356, 2010.

1.9- Radiochemistry and Materials Science

STUDY AND APPLICATION OF ISOTOPE DILUTION TECHNIQUE IN COMBINATION WITH INTERNAL STANDARDIZATION AND EXTERNAL CALIBRATION TECHNIQUES TO PRECISELY DETERMINE THE CONTENT OF RARE EARTH ELEMENTS BY ICP-MS

Cao Dong Vu, Nguyen Giang, Truong Duc Toan, Do Tam Nhan, Vo Tran Quang Thai, Nguyen Le Anh and Nguyen Viet Duc.

Dalat Nuclear Research Institute,
01 Nguyen Tu Luc, Ward 8, Dalat, Lam Dong province

Project information:

- **Code:** CS/18/01-02
- **Managerial Level:** Institute
- **Allocated Fund:** 80,000,000 VND
- **Implementation time:** 18 months (Jan 2018- Jun 2019)
- **Contact email:** caodongvu1@yahoo.com
- **Paper published in related to the project:**

1. Cao Dong Vu*, Truong Duc Toan, Nguyen Dang Khanh, Do Tam Nhan, Vo Tran Quang Thai, Nguyen Le Anh, Nguyen Viet Duc, Nguyen Giang, Nguyen Trong Ngo (2018) Use of isotope dilution technique for determination of Ce, Sm and Yb abundances in geological sample by ICP-MS. *Dalat University Annual Science conference*, Dec. 2018, pp: 28-44 (in Vietnamese).
2. C. D. Vu*, T. D. Toan, N. D. Khanh, D. T. Nhan, V. T. Q. Thai, N. L. Anh, N. V. Duc, N. Giang, N. T. Ngo (2019) Use of isotope dilution method for determination of Ce, Sm and Yb abundances in geological sample by ICP-MS. *Dalat University Journal of Science* 9 (2), pp: 68-83 (in Vietnamese).
3. Cao Dong Vu*, Truong Duc Toan, Nguyen Dang Khanh, Nguyen Giang and Nguyen Trong Ngo (2019) Simultaneously application of internal standardization, external calibration and isotope dilution methods to determine of REE concentration in geological sample by ICP-MS. *Vietnam Conference on Nuclear Science and Technology - VINANST 13*, August 2019, Quang Ninh (in Vietnamese).

Abstract: In this study, three analytical methods of: (1) Internal Standardization - IS; (2) External Calibration - EC; and (3) Isotope Dilution – ID, were simultaneously studied and applied to precisely determine fourteen rare earth elements (REEs) in three geological reference materials: BHVO-2, BCR-2 and NIST 2711a by ICP-MS. Calibration experiments in ID technique such as concentration calibration and relative isotopic abundance calibration for spike solutions were carried out. In addition, mass spectral interferences, mass fractionation in ICP-MS were also investigated, corrected and discussed. High accuracy (< 10%) and reproducibility (< 5%) were obtained for all measurements. The procedure proposed by this work is applicable to most sample forms such as sediment, biology, archaeology, meteorite, etc., although sample digestion and dilution factor are different for each type of sample.

Keywords: *ICP-MS; Internal standardization (IS); External calibration (EC); Isotope dilution (ID); Rare earth elements (REEs); Mass spectral interference.*

I. INTRODUCTION

In nature, rare earth element (REE) is a group of 15 elements from La to Lu (in which, Promethium - Pm is radioactive element), mass number is from 57 to 71 in the Mendeleev periodic table [1]. According to the International Union of Pure and Applied Chemistry (IUPAC) [2], elements of Sc and Y are also considered to belong to the REE group, however, in this study Sc and Y are not included. The important characteristic of this element group is that all elements have similar chemical and physical properties [3].

The ICP-MS method, a modern analytical method with high sensitivity and accuracy, is widely applied in many laboratories around the world. In particular, 14 REEs can be determined by ICP-MS simultaneously with the same accuracy and precise, which is very important in the study of specific objects [4]. At the present time, ICP-MS is considered as one of the optimal solutions in trace (ppb) and ultra trace (ppt) analysis and is widely used in investigating of many objects such as meteorite, geology, environment, etc., particularly in the evaluation and validation for Certified Reference Materials (CRMs) [5, 6].

In this study, three analytical methods: (1) Internal standardization; (2) External calibration; and (3) Isotope dilution were applied simultaneously to determine the precise content of 14 REEs rare earth elements in three geological CRMs: BHVO-2, BCR-2 and NIST 2711a by using ICP-MS. The experiments for calibration in ID technique such as the calibration of the content and the relative isotope abundances of spike solutions have been carried out experimentally. In addition, dilution factor (DF), recovery factor (R) and mass interference in ICP-MS were also investigated, corrected and discussed.

II. MATERIAL AND METHOD

II.1. Sample, standard, chemical, equipment and tool

II.1.1. Sample: To study for application of an analytical technique or method, CRMs are often used. In this study, three CRMs were selected: (1) BHVO-2, Basalt, Hawaiian Volcanic Observatory; (2) BCR-2, Basalt, Columbia River; and (3) NIST 2711a, Montana II Soil. In particular, BHVO-2 and BCR-2 are geological standard samples with basalt rock matrix, provided by Department of United States Geological Survey (USGS), and NIST 2711a is with soil matrix, given by the National Institute of Standards & Technology (NIST).

II.1.2. Standard and spike solutions

- Multi-element standard solution REE, Sc and Y, 10 mg/L and single standard solutions of In, 10 mg/L; Pr, Sm, Gd, Tb and Tl, 1000 mg/L (SPEX; Edison, NJ, USA); Standard solutions for single element of Ba, Ce and Nd, 1000 mg/L (Kanto Chemical Co., Inc., Japan) were applied.

- Spike solution were prepared from stable isotope standard (oxide powder), enriched with isotopes of ^{142}Ce (83 - 92%), ^{149}Sm (91 - 97%) and ^{171}Yb (87 - 95%) by the Oak Ridge National Laboratory (ORNL, USA).

II.1.3. Chemical, equipment and tool

- Super pure deionized water (MilliQ, 18 mΩ); HF acid (48%, Merck, Germany), $HClO_4$ (70%, VWR chemicals, France), HNO_3 (65%, Charlau, Spain) and HCl (37%, Charlau, Spain) were used in sample digestion and preparation of measured solutions.

- ICP-MS NexION 300X PerkinElmer device, including ICP – Inductively coupled plasma: high-level heat source providing ion (+); MS - Mass spectrometry; quadrupole spectrum scanner; Control software and spectrum analyzer of NexION 300X version 1.5.

- 7 mL, 15 mL Teflon PFA container ($-200 \div +260^{o}C$, VWR, Savillex, USA).

II.2. Experimental

II.2.1. Sample digestion

The spike solutions, enriched with isotopes of ^{142}Ce (7 ppm), ^{149}Sm (2 ppm) and ^{171}Yb (0.2 ppm) were accurately weighed and added to a clean Teflon container and then dried in 100^{o}C until dryness (~ 1 h). After being cooled to room temperature, weigh a sample of 15 mg (or 20 mg or 30 mg, depending on the experiment) into a Teflon container with a mixture of: 230 µL HF acid, 48% (raio of 15 µL/1 mg sample), 115 µL HNO_3 acid, 65% (raio of 7.5 µL/1 mg sample) and 115 µL $HClO_4$ acid, 70% (raio of 7.5 µL/1 mg sample). Figure 1 shows a detailed digestion procedure of the geological sample by acid mixture in Teflon container used in this study. A procedure blank (PB) was prepared in the same way in order to correct the possible contaminations from the chemical used in the process. A sample volume of about 10, 15 and 20% of the sample stock solution was used to prepare the measured solution, corresponding to the dilution factor (DF) of 3000, 4000 and 5000 times from initial solid sample.

II.2.2. Method of analysis

Two elements of In and Tl were used as internal standard to adjust the instrument drift and the matrix effect during measurement time [7]. Linear interpolation was used in the range of 115 (In) to 205 (Tl) to calibrate the measuring signals for Ba and REEs; The content of Ce, Sm, Yb, representing to the light rare earth group - LREE, medium rare earth group – MREE and heavy rare earth group – HREE, respectively, was determined by both methods: (1) isotope dilution method, using spike solutions with enriched isotopes of ^{142}Ce, ^{149}Sm and ^{171}Yb; and (2) external calibration method. While, the concentration of REE elements (except Ce, Sm and Yb) was determined by EC method [5, 6, 8].

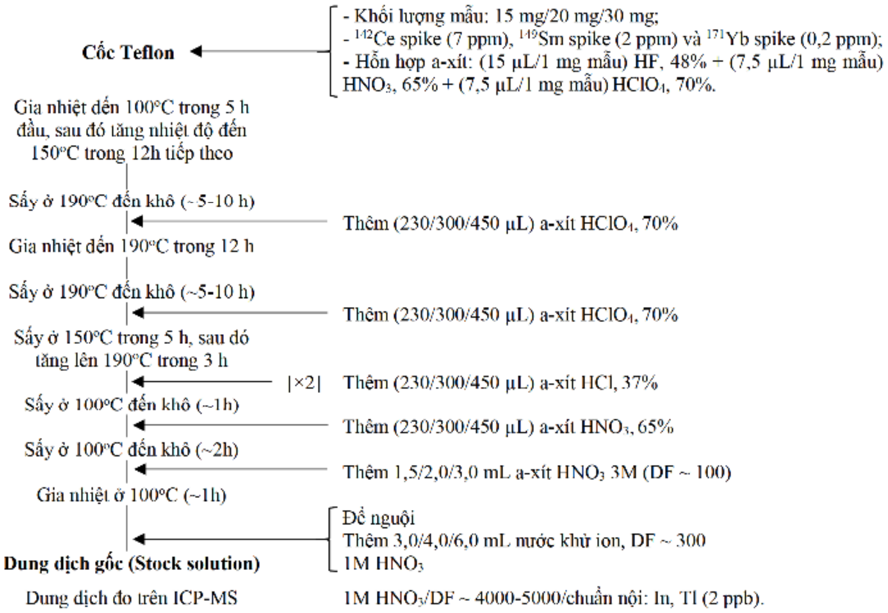

Figure 1: Digestion procedure of geological sample with a mixture of acid in Teflon container

Recovery factor (R) for 3 REE groups was calculated by analytical data obtained from ID and EC methods for 3 elements of Ce, Sm and Yb. Analysis of the remaining REE elements was corrected for the amount of sample lost during sample preparation by using R factor for Ce, Sm and Yb [8]. The related calibrations and corrections such as content calibration, relative isotope abundances in spike solutions in ID method; as well as mass inteference and mass fractionation (MF) corrections were also investigated and corrected experimentally. The method of ID and calibration and/or correction experiments in ICP-MS was presented in detail elsewhere [8].

III. RESULTS AND DISCUSSION

III.1. Internal standard

A quantity of 2 ng g^{-1} of In and Tl was mixed into all measuring solutions (sample and standard) to control instrument drift and the matrix effect during measurement time. The results of linear interpolation in the mass range from 115 to 205, used to calibrate the measurement signals of Ba and REE, are given in Figure 2

III.2. Dilution factor (DF) and recovery factor (R)

In general, choosing of DF is based on two factors: (1) the content of the element of interest in the sample so that the count of the mass spectral peak within the optimal range of the device is of $5 \times 10^3 \div 5 \times 10^5$ cps [9]; (2) total matrix content is < 400 mg kg^{-1} [7]. In this study, DF of 3000, 4000 and 5000 were used. From the results given in Figure 3 and Table 1, the effect of matrix to R factor is quite clear, especially for the NIST 2711a. For DF coefficients of 4000 and 5000, recovery coefficient R for three samples (for Ce, Sm and Yb) were perfectly consistent with each other and are in the range of: 94% - 101% (BHVO-2), 90% - 98% (BCR-2) and 78% - 87% (NIST 2711a).

The recovery coefficient R of NIST 2711a is quite low compared to that of other two samples. This is explained not to be related to the DF coefficient but derived from the procedure of sample digestion used in this study is not completely optimal for soil samples. For DF coefficient of 3000, the recovery coefficient R fluctuates across a wide range are completely inconsistent between light rare earth groups (Ce), medium (Sm) and heavy (Yb). (Figure 3). As the result, the optimal DF for geological samples with soil and basalt rock matrix is in the range of 4000 ÷ 5000.

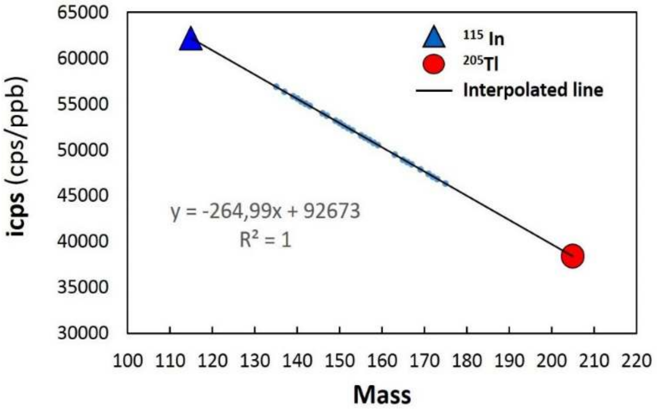

Figure 2: Correlation between the measured signal (icps) and the number of mass

Table 1: Recovery factor (R, %) for different DF dilution factors of: 3000, 4000 and 5000.

CRMs	Ce	*SD*	Sm	*SD*	Yb	*SD*
			DF: 5000			
BHVO-2	96	2	101	3	94	2
BCR-2	95	8	98	8	90	9
NIST 2711a	84	3	87	2	80	3
			DF: 4000			
BHVO-2	94	3	101	2	96	5
BCR-2	95	6	98	8	93	7
NIST 2711a	83	4	84	2	78	3
			DF: 3000			
BHVO-2	93	1	103	3	97	2
BCR-2	93	7	97	10	92	8
NIST 2711a	98	4	83	3	73	3

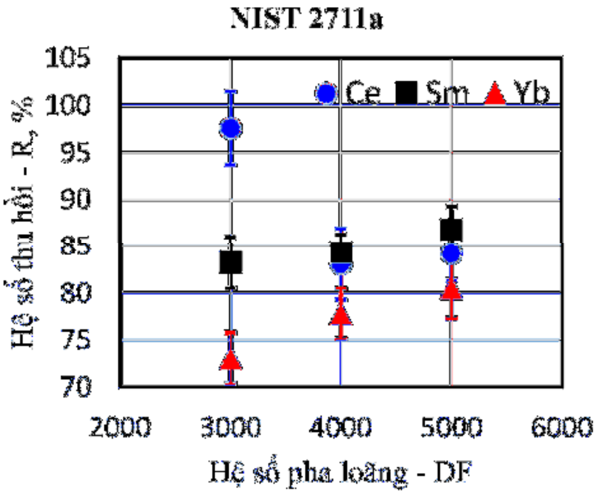

Figure 3: Correlation between DF and R factors for NIST 2711a.

III.3. Mass interference correction by experiment

In mass spectrometry technique using ICP-MS, there are many different effects that may affect the measurement results of the element (or isotope) of interest, one of which is mass spectral interference which are required to be fully identified.

Basically, there are two main types of interfering causing major mass interference: (1) the isotopes of different elements but has the same mass number; (2) in plasma environment, an isotope combined with $^{16}O^{+}$ or $^{16}O^{1}H^{+}$ to form an new ion with the same mass as the isotope of interest. For the first type, the correction method is quite simple by observing another peak without interference of the interfering element and based on the natural isotope abundance of these isotopes we can determine the contribution of the interference isotope to the peak of the element of interest. For the second type, the correction should be carried out experimentally.

Table 2: Results of mass interference survey of LREEs on MREE and HREE

Monitored isotope	Interference species	Interference contribution (%) *BHVO-2*	*BCR-2*	*NIST 2711a*	Used isotope
^{151}Eu	$^{135}Ba^{16}O^{+}$	0.64	3.2	6.1	^{151}Eu
^{153}Eu	$^{137}Ba^{16}O^{+}$	1.2	5.9	10.8	
^{156}Gd	$^{140}Ce^{16}O^{+}$	34	40	57	
^{157}Gd	$^{141}Pr^{16}O^{+}$	8.1	9.4	14.7	^{157}Gd
^{157}Gd	$^{140}Ce^{16}O^{1}H^{+}$	2.8	3.6	6.2	
^{159}Tb	$^{142}Ce^{16}O^{1}H^{+}$	3.5	4.4	8.3	^{159}Tb
^{159}Tb	$^{142}Nd^{16}O^{1}H^{+}$	4.5	4.5	6.5	
^{163}Dy	$^{146}Nd^{16}O^{1}H^{+}$	0.17	0.17	0.27	^{163}Dy
^{163}Dy	$^{147}Sm^{16}O^{+}$	0.17	0.16	0.20	
^{165}Ho	$^{149}Sm^{16}O^{+}$	3.9	3.3	4.0	^{165}Ho
^{166}Er	$^{149}Sm^{16}O^{1}H^{+}$	3.7	2.8	3.4	
^{166}Er	$^{150}Nd^{16}O^{+}$	2.4	2.0	3.0	
^{167}Er	$^{150}Sm^{16}O^{1}H^{+}$	1.1	0.90	1.0	^{167}Er
^{167}Er	$^{150}Nd^{16}O^{1}H^{+}$	0.20	0.10	0.20	
^{169}Tm	$^{152}Sm^{16}O^{1}H^{+}$	0.10	0.10	0.10	
^{171}Yb	$^{155}Gd^{16}O^{+}$	0.87	0.60	0.74	^{171}Yb
^{172}Yb	$^{155}Gd^{16}O^{1}H^{+}$	3.0	2.1	2.8	
^{173}Yb	$^{156}Gd^{16}O^{1}H^{+}$	3.8	2.8	3.6	
^{175}Lu	$^{159}Tb^{16}O^{+}$	2.9	1.9	1.9	^{175}Lu

In this study, we used single standard solutions of Ba, Pr, Ce, Nd, Sm, Gd and Tb to prepare 4 solutions with a content of 20 ppb: [BaPr], [Ce], [Nd] and [SmGdTb]. Then, the sapmples were measured with the analytical samples to calibrate the contribution of the isobaric ions to the peak of interest. Table 2 presents the results of the mass spectrometry survey in three studied samples conducted in this study. From the results obtained in Table 2, the contribution of the isobaric ions from the LREE peaks to the peaks of MREE and HREE is significant (from 0.1%). (^{169}Tm) to 57% (^{156}Gd)) and is different from sample to sample. This means that, in order to have accurate results in REE analysis using ICP-MS, the correction of mass interference is necessary. Moreover, the results are also the basis for selecting the optimal analytical peak for each interested element.

III.4. Analysis of 14 REEs in 03 CRMs using ICP-MS

Tables 3, 4 and 5 present the results of the determination of 14 REEs in three CRMs: BHVO-2, BCR-2 and NIST 2711a using ICP-MS. Analytical results were evaluated, compared with: certified value [10], the recommended value [11, 12] and the information value (*Information*) of the manufacturer; and other values studied and published in international journals by some authors.

Table 3: Analytical results of 14 REEs in BHVO-2

Ele.	This work					Certified value			Literiture value			Bias, %[2]		
	Mean (n=3)	Std. deviation		Unc. (acc.)[1]		G. Plumlee (1998)	SD	RSD, %	A.J.R. Kent et al. (2004)/ID	SD	G. Bayon et al. (2009)/ ICP-MS	G. Plumlee (1998)	A.J.R. Kent et al. (2004)/ID	G. Bayon et al. (2009)/ ICP-MS
	$\mu g\ g^{-1}$	*SD*	*RSD, %*	$\mu g\ g^{-1}$	%									
La	15.5	0.07	0.5	0.4	2.6	15	1	6.7	15.25	0.02	15.2	3.0	1.3	1.6
Ce	37.5	0.20	0.5	1.1	3.0	38	2	5.3	37.84	0.19	37.5	-1.3	-0.9	0.0
Pr	5.41	0.003	0.1	0.14	2.5	-			5.351	0.015	5.31	-	1.1	1.9
Nd	25.0	0.12	0.5	1.0	3.9	25	1.8	7.2	24.39	0.02	24.5	0.1	2.6	2.1
Sm	6.08	0.03	0.4	0.25	4.1	6.2	0.4	6.5	6.03	0.01	6.07	-1.9	0.9	0.2
Eu	2.10	0.02	0.9	0.11	5.0	-			2.036	0.003	2.07	-	2.9	1.3
Gd	6.41	0.09	1.4	0.18	2.8	6.3	0.2	3.2	6.229	0.007	6.24	1.7	2.9	2.7
Tb	0.938	0.008	0.9	0.044	4.7	0.9	0.045	5.0	-		0.94	4.3	-	-0.2
Dy	5.30	0.04	0.7	0.10	1.9	-			5.3	0.009	5.31	-	-0.1	-0.2
Ho	0.983	0.017	1.7	0.057	5.8	1.04	0.04	3.8	-		0.97	**-5.5**	-	1.3
Er	2.54	0.02	0.7	0.11	4.3	-			2.547	0.003	2.54	-	-0.5	-0.2
Tm	0.326	0.004	1.2	0.013	4.0	-			-		0.35	-	-	**-6.8**
Yb	2.01	0.02	1.2	0.13	6.4	2	0.2	10.0	1.955	0.005	2	0.6	2.9	0.6
Lu	0.275	0.005	1.7	0.027	10.0	0.28	0.01	3.6	0.2709	0.0009	0.27	-1.6	1.7	2.0

[1] *Accumulated error is calculated by the formula: SQRT[(SD1)^2+(SD2)^2+(SD3)^2];*

[2] *The relative bias is determined by the formula: [(measured value - compared value)×100/compared value].*

- *Precision:* The repeatability of analytical results was evaluated by relative standard deviation (RSD, 1σ, %) with n = 3. From the stock solution, 03 measurement solutions were diluted with the same DF and measured by ICP-MS. The results were averaged ± SD or/and RSD. The results in Tables 3, 4 and 5 show that the repeatability of the analytical result is less than 2%, except for Tm and Lu in NIST 2711a which is 3.0% and 4.1%, respectively. This shows that the stock solutions and measurement solution have high uniformity; The ICP-MS device used in this study has good stability. In other words, the analytical procedure is applied with good repeatability.

- *Accuracy:* Accuracy is evaluated based on the relative bias (%, the formula noted under Table 3.) between the obtained result and the compared value (certified, recommended, information values and the literature values). From the results obtained in Tables 3 and 4, most values of relative bias of the results for BHVO-2 and BCR-2 are < 5%, except, the results of Ho and Tm in the BHVO-2 sample with a deviation of -5.5% and -6.8%, respectively (Table 3); Nd in the BCR-2 sample (Table 4) with a deviation value of 5.2%.

Table 4: Analytical results of 14 REEs in BCR-2

Ele.	This work					Certified values			Literature values				Bias, %		
	Mean (n=3)	Std. deviation		Unc. (acc.)		G. Plumlee (1998)	SD	RSD, %	A.J.R. Kent et al. (2004)/ID	SD	G. Bayon et al. (2009)/ ICP-MS	SD	G. Plumlee (1998)	A.J.R. Kent et al. (2004)/ID	G. Bayon et al. (2009)/ ICP-MS
	$\mu g\ g^{-1}$	*SD*	*RSD, %*	$\mu g\ g^{-1}$	%										
La	25.4	0.2	0.7	0.6	2.3	25			24.94	0.12	26	0.70	1.7	1.9	-2.2
Ce	52.9	0.2	0.4	1.1	2.0	53	2	3.8	53.52	0.28	55.4	1.20	-0.1	-1.1	-4.4
Pr	6.93	0.03	0.4	0.09	1.3	6.80			6.756	0.045	7.07	0.04	2.0	2.6	-1.9
Nd	29.5	0.2	0.6	0.9	3.2	28			28.71	0.14	29.67	0.12	**5.2**	2.6	-0.7
Sm	6.56	0.05	0.8	0.24	3.6	6.7	0.3	4.5	6.534	0.034	6.76	0.18	-2.0	0.5	-2.9
Eu	2.00	0.00	0.0	0.09	4.7	2.00			1.949	0.011	2.01	0.06	0.1	2.7	-0.4
Gd	7.02	0.08	1.2	0.42	6.0	6.8			6.727	0.04	7.07	0.04	3.3	4.4	-0.7
Tb	1.08	0.01	0.8	0.069	6.4	1.07			-		1.09	0.01	0.6	-	-1.2
Dy	6.47	0.07	1.1	0.26	4.0	-			6.441	0.028	6.58	0.05	-	0.5	-1.6
Ho	1.31	0.01	0.9	0.108	8.3	1.33			-		1.35	0.02	-1.7	-	-3.1
Er	3.73	0.02	0.4	0.09	2.3	-			3.707	0.017	3.77	0.04	-	0.5	-1.2
Tm	0.523	0.007	1.4	0.017	3.3	0.54			-		-		-3.2	-	-
Yb	3.44	0.01	0.3	0.18	5.4	3.5	0.2	5.7	3.348	0.017	3.4	0.07	-1.7	2.7	1.1
Lu	0.510	0.008	1.5	0.039	7.6	0.51			0.4961	0.0022	0.5	0.02	-0.1	2.7	1.9

The note is similar to Table 3

From these data, it is possible to conclude: for geological samples with basalt rock matrix, the results obtained through this study are reliable and in good agreement with validated values and literature values; The REE analytical procedure proposed through this research gives the analytical results with the same accuracy as the laboratories in the world using the same analytical methods.

Table 5: Analytical results of 14 REEs in NIST 2711a

Ele.	This work					Certified values			Bias, %
	Mean (n=3)	**Std. deviation**		**Unc. (acc.)**		A. S. Wise and L. R. Watters Jr. (2009)	SD	RSD, %	A. S. Wise and L. R. Watters Jr. (2009)
	µg g^{-1}	***SD***	***RSD, %***	**µg g^{-1}**	%				
La	38.7	0.01	0.03	1.5	3.8	38	1	2.6	1.9
Ce	73.8	0.92	1.24	4.0	5.4	70			5.5
Pr	8.76	0.063	0.71	0.31	3.6	-			-
Nd	32.3	0.03	0.09	1.4	4.3	29	2	6.9	**11.3**
Sm	6.12	0.04	0.60	0.16	2.7	5.93	0.28	4.7	3.1
Eu	1.08	0.02	1.68	0.06	5.6	1.1	0.2	18.2	-1.6
Gd	5.32	0.01	0.20	0.32	6.1	5			6.3
Tb	0.798	0.005	0.60	0.080	10.0	0.8			-0.2
Dy	4.61	0.00	0.02	0.36	7.7	5			-7.7
Ho	0.927	0.016	1.69	0.087	9.4	-			-
Er	2.81	0.03	1.15	0.24	8.7	-			-
Tm	0.411	0.012	3.00	0.044	**10.6**	-			-
Yb	2.77	0.03	1.04	0.32	**11.6**	3			-7.7
Lu	0.411	0.017	4.07	0.053	**13.0**	0.5			**-17.7**

The note is similar to Table 3

For the NIST SRM 2711a, the obtained results were less accurate than that of the other two samples. Basically, most of the results have a relative bias of < 10%, except for Nd and Lu, with relative bias of 11.3% and 17.7%, respectively. In which, Nd is the reference value defined by a unique method of NIST as INAA [10]. However, the Nd result obtained by this study (32,3 ± 1,4) is consistent with the reference value recommended by NIST (29 ± 2) within the error range.

For Lu, the value given by NIST (0.5) is the information value, determined by INAA and the measurement uncertainty is not evaluated. Therefore, there is no evidences to conclude that our results for Lu are consistent with the value proposed by NIST. From the analysis of NIST 2711a through this study, the discussion in Section III.2 on DF coefficients and the recovery factor R for NIST 2711a and the accuracy assessments allow us to conclude that the sample digestion procedure used in this study is not optimal for soil-based analytical samples. Research is needed to have a better recovery factor (> 90%), thereby improving the repeatability and accuracy of analytical results (<10%).

IV. CONCLUSIONS

A combination of 3 analytical methods: internal standardization, external calibration and isotope dilution was successfully studied and applied in Vietnam for the first time for simultaneous analysis of 14 REEs in basalt stone based geological standard by ICP-MS with very high precision and accuracy. Specifically: achieved repeatability is: < 2% for 2 CRMs with basalt rock matrix BHVO-2 and BCR-2; and < 5% for CRM with soil matrix NIST 2711a. The relative bias of the obtained results is: < 7% for BHVO-2 and BCR-2; and < 12% for NIST 2711a (except for Lu which is 17.7%). The accumulative error of analytical results is ≤ 10%, except for Tm, Yb and Lu in NIST 2711a which are less than 13%.

For the geological samples with basalt rock matrix, REE analytical procedure proposed by this work gives results with the same accuracy as the analysis data from some laboratories in the world which used same analytical method.

This analytical procedure is applicable to most sample forms such as sediment, biology, archeology, meteorite, etc., except for the sample digestion procedure and the dilution factor is different for each type.

REFERENCES

[1] De Laeter J. R., Böhlke J. K., De Bièvre B., Hidaka H., Peiser H. S., Rosman K. J. R., and Taylor P. D. P. (2003) Atomic weights of the elements: Review 2000 (IUPAC Technical Report). *Pure Appl. Chem.* 75 (6), 683-800.

[2] IUPAC - https://iupac.org/.

[3] Evensen N. M., Hamilton P. J. and O'Nions R. K. (1978) Rare-earth abundances in chondritic meteorites. *Geochim. Cosmochim. Acta* 42, 1199-1212.

[4] Shinotsuka K., Hidaka H. and Ebihara M. (1995) Detailed abundances of rare earth elements, thorium and uranium in chondritic meteorites: An ICP-MS study. *Meteoritics* 30, 694-699.

[5] Shirai N., Toktaganov M., Takahashi H., Yokozuka Y., Sekimoto S., Ebihara M. (2015) Multielemental analysis of Korean geological reference samples by INAA, ICP-AES and ICP-MS. *J. Radioanal. Nucl. Chem.* 303, 1367-1374.

[6] Cao D. V., Sucgang R., Tran Q. T., Ho V. D., Shirai N., Ebihara M. (2017) Measurements of Rare Earth Element and Other Element Mass Fractions in Environmental Reference Materials (NIST SRM 1646a, NIST SRM 1400, IAEA-395 and IAEA-450) by INAA, ICP-AES and ICP-MS. *Geostand. Geoanal. Res.* 41 (2), 303-315.

[7] Shinotsuka K. and Ebihara M. (1997) Precise determination of rare earth elements, thorium and uranium in chondritic meteorite by inductively coupled plasma mass spectrometry – a comparative study with radiochemical neutron activation analysis. *Anal. Chim. Acta* 338, 237-246.

[8] C. D. Vu*, T. D. Toan, N. D. Khanh, D. T. Nhan, V. T. Q. Thai, N. L. Anh, N. V. Duc, N. Giang, N. T. Ngo (2019) Use of isotope dilution method for determination of Ce, Sm and Yb abundances in geological sample by ICP-MS. *Dalat University Journal of Science* 9 (2), pp: 68-83 (in Vietnamese).

[9] Vogl J. (2005) Calibration Strategies and Quality Assurance. Inductively Coupled Plasma Mass Spectrometry Handbook (ed. Simon M. N.), Blackwell Publishing Ltd., *CRC Press*, 147-181.

[10] Wise A. S. and Watters L. R., Jr. (2009) Certificate of Analysis NIST SRM 2711a. *NIST.* 1-6.

[11] Plumlee G. (1998a) Certificate of Analysis: Basalt, Hawaiian Volcanic Observatory, BHVO-2. *USGS.* 2 pages.

[12] Plumlee G. (1998b) Certificate of Analysis: Basalt, Columbia River, BCR-2. *USGS.* 3 pages.

[13] Kent A. J. R, Jacobsen B., Peate D. W.,Waight T. E and Baker J. A. (2004) Isotope dilution MC-ICP-MS rare earth element analysis of geochemical reference materials NIST SRM 610, NIST SRM 612, NIST SRM 614, BHVO-2G, BHVO-2, BCR-2G, JB-2, WS-E, W-2, AGV-1 and AGV-2. *Geostand. Geoanal. Res.* 28 (3), 417–429.

[14] Bayon G., Barrat A. J., Etoubleau J., Benoit M., Bollinger C., và Révillon S. (2009) Determination of Rare Earth Elements, Sc, Y, Zr, Ba, Hf and Th in Geological Samples by ICP-MS after Tm Addition and Alkaline Fusion. *Geostand. Geoanal. Res.* 33 (1), 51-62.

USING FRAPCON AND FRAPTRAN SOFTWARE TO EVALUATE CHARACTERISTIC OF NUCLEAR FUEL PELLETS IN NUCLEAR REACTORS

Nguyen Trong Hung, Le ba Thuan, Nguyen Van Tung, Nguyen Thanh Thuy, Cao Duy Minh, Dao Truong Giang, Ha Dinh Khai and Ngo Quang Hien.

Center for Technology of Nuclear Fuel,
Institute for Technology of Radioactive and Rare Elements,
48 Lang Ha, Dong Da, Hanoi

Project information:

- **Code:** DTCB.08/17/VCNXH
- **Managerial Level:** Ministry
- **Allocated Fund:** 600,000,000 VND
- **Implementation time:** 24 months (Jan 2017- Dec 2018)
- **Contact email:** nthungvaec@gmail.com
- **Paper published in related to the project:**

1. Nguyen Trong Hung, Le Ba Thuan, Tran Chi Thanh, Hoang Nhuan, Do Van Khoai, Nguyen Van Tung, Jin-Young Lee, Rajesh Kumar Jyothi, “Modeling the UO2 ex-AUC pellet process and predicting the fuel rod temperature distribution under steady-state operating condition”, *Journal of Nuclear Materials* 504 (2018) 191-197.
2. Nguyen Trong Hung, Nguyen Van Tung, Nguyen Thanh Thuy, Cao Duy Minh, “Predicting behavior of AP-1000 nuclear reactor fuel rod under steady state operating condition by using FRAPCON-4.0 software” *Nuclear Science and Technology*, (Artical in press)
3. Nguyen Van Tung, Nguyen Thanh Thuy, Cao Duy Minh, Nguyen Trong Hùng, “Predicting behavior of AP-1000 nuclear reactor fuel rod under steady state operating condition by using FRAPCON-4.0 software”, *The 5th Conference of Nuclear Science and Technology for Young Researchers,* October 2018, Hanoi, Vietnam.
4. Nguyen Van Tung, Nguyen Thanh Thuy, Nguyen Trong Hung, “Using FRAPCON and FRAPTRAN software to evaluate characteristic of nuclear fuel pellets in nuclear reactors”, *Vietnam Conference of Nuclear Science and Technology 12*, Nha Trang, Khanh Hoa, Vietnam, 2017.

Abstract: This report gave an overview of FRAPCON and FRAPTRAN software including the theoretical basis and computational modeling of the status of the fuel rods in steady operating conditions and the transition state of the reactor.

This paper also reported the results on the predictions of behavior of AP-1000 nuclear reactor fuel rod under steady state operating condition by using FRAPCON-4.0 software and transition state by using FRAPTRAN software. The predictive items were the temperature distribution in the fuel rod, including fuel centerline temperature, fuel pellet surface temperature, gas temperature, cladding inside and outside temperature, oxide surface and bulk coolant temperature; gap conductance and thickness. The predictive items also included deformation of fuel pellets, fission gas release and rod internal pressure, cladding oxidation and hydration. The predictive data suggested the fuel rod behavior in nuclear reactor.

Keywords: *FRAPCON, FRAPTRAN, nuclear fuel ...*

I. INTRODUCTION

In modern nuclear reactors, ceramic fuel in which uranium dioxide (UO_2) is the main material is widely used. Nuclear fuel for heavy water reactors are manufactured from natural uranium. For light water reactor, uranium fuel must be enriched (3-5%).

The quality of UO_2 pellets is assessed based on the ASTM safety standards. In addition, state of UO_2 pellets in operating conditions of the nuclear reactor - one of the important criteria in the process of researching, designing, manufacturing and safety evaluation of UO_2 pellets and nuclear power plants are assessed by the simulation software. FRAPTRAN and FRAPCON are two of many programs that are used to assess the status of nuclear fuel in the reactor at the operational status of nuclear reactors.

The Fuel Rod Analysis Program CONstan (FRAPCON) is a Fortran 90 computer code that calculates the steady-state response of light-water reactor fuel rods during long-term burnup. The code calculates the temperature, pressure, and deformation of a fuel rod as functions of time-dependent fuel rod power and coolant boundary conditions.

The phenomena modeled by the code include: 1) Heat conduction through the fuel and cladding to the coolant; 2) Cladding elastic and plastic deformation; 3) Fuel-cladding mechanical interaction; 4) Fission gas release from the fuel and rod internal pressure;5) Cladding oxidation.

The latest version of FRAPCON has been changed to modernize the FORTRAN language to the most recent standards. Other updates include, an update to plenum temperature model, update to gas properties, the inclusion of the ANS-5.4 (2011) Standard Fission Product Release Model, the ability to model spent fuel storage using the DATING creep models, the ability to use the ANS-5.1 decay heat model to calculate heating after shutdown, and the ability to specify axial coolant conditions.

The Fuel Rod Analysis Program TRAnsient (FRAPTRAN) is a FORTRAN language computer code that calculates the transient performance of light-water reactor fuel rods during reactor transients and hypothetical accidents such as loss-of-coolant accidents, anticipated transients without scram, and reactivity-initiated accidents. FRAPTRAN calculates the temperature and deformation history of a fuel rod as a function of time-dependent fuel rod power and coolant boundary conditions. Although FRAPTRAN can be used in “standalone” mode, it is often used in conjunction with, or with input from, other codes.

The phenomena modeled by FRAPTRAN include: 1) Heat conduction; 2) Heat transfer from cladding to coolant; 3) Elastic-plastic fuel and cladding deformation; 4) Cladding oxidation; 5) Fission gas release; 6) Fuel rod gas pressure.

The latest version of FRAPTRAN updates material properties, incorporates improvements to the ballooning model and the high temperature steam oxidation models. New modeling capability has been added to model axial zoning of gadolinia content. Other new capabilities include increased time steps and axial nodes, and the inclusion of Optimized ZIRLO cladding.

II. USING FRAPCON AND FRAPTRAN SOFTWARE EVALUATION CHARACTERIZED NUCLEAR FUEL PELLETS IN NUCLEAR REACTORS

2.1. Description of AP-1000 fuel rod design

The AP-1000 fuel rods consist of cylindrical, ceramic pellets of slightly enriched uranium dioxide (UO_2). These pellets are contained in cold-worked and stress-relieved ZIRLO tubing, which is plugged and seal-welded at the ends to encapsulate the fuel. ZIRLO is an advanced zirconium-based alloy. The UO_2 pellets are slightly dished to better accommodate thermal expansion and fuel swelling, and to increase the void volume for fission product release. The void volume will also accommodate the differential thermal expansion between the clad and the fuel as the pellet density increases in response to irradiation. An AP-1000 fuel rod comprises the following parts: Upper plug, cladding, lower plug, fuel pellets and a spring (Table 1, Fig.1).

Table 1: Main parameters of AP-1000 fuel rod

Parameter	Value
Number of fuel rods in fuel assembly	264
Rod array	17x17
Fuel rods pitch, mm	12.6
Fuel	UO_2
Fuel density, kg/m^3	95.5
Cladding material	$ZIRLO^{TM}$
Total fuel rod length, mm	4267.2
Total active fuel height, cold state, mm	3657.6
Outer diameter of fuel cladding, mm	9.5
Cladd thickness, mm	0.57
Diameter gap, mm	0.0825
Outer diameter of fuel pellet, mm	8.2
Fuel pellet height, mm	9.8
Average linear power, kW/m	18.76
Peak linear power for normal operation, W/cm	48.86
Enrichment U^{235} (maximum value), %	4.50

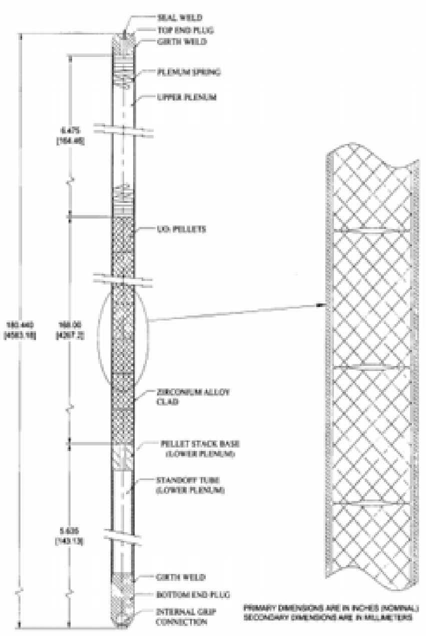

Figure 1: Configuration of AP1000 fuel rod.

2.2. Modeling method

The AP-1000 fuel rod has been modeled using FRAPCON and FRAPTRAN code based on the design parameters, reference data in the operation of AP-1000 reactor. The dimensions for AP-1000 fuel rod were from design data. The fuel rod was divided into 24 time steps (50 days/1 time step), 17 (fuel) radial boundaries and 9 (equal-length) axial nodes (Fig.2). The axial and radial nodes are numbered from bottom to top of total active fuel height and from the fuel rod centerline to the cladding outside surface, respectively.

Main parameters of the boundary conditions were given in Table 2. Calculations were performed for 3 fuel cycles; the length of each cycle was 351 effective full power days.

Table 2: Main parameters of the boundary conditions

Parameter	Value
The rod initial fill pressure, in Mpa	2.35
Coolant system pressure, in Mpa	15.5
Coolant inlet temperature,in K	552.6
Mass flux of coolant, in kg/(s.m^2)	3466
Linear heat generation rate,in kW/m 1st cycle 2nd cycle 3rd cycle	 18.4 20.3 20.2

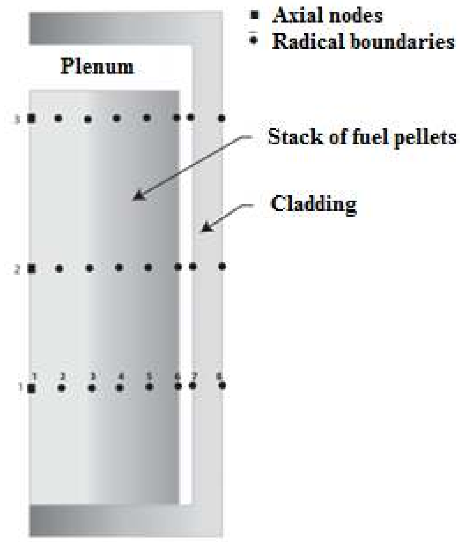

Figure 2: Fuel rod nodalization.

The temperature distribution throughout the fuel and coolant was calculated at each axial node. A schematic of the temperature distribution at an arbitrary axial node might be found in the document [4].

III. RESULTS AND DISCUSSION

3.1. Predicted behavior of nuclear fuel rod under steady state operating condition

3.1.1. Predicted fuel rod temperature distribution predictions as a function of burnup

Table 3 summarized the prediction of the fuel rod temperature distribution calculated by FRAPCON-4.0 code. The image of thermal behavior of fuel rod was shown in Fig.3.

Table 3: Results of the thermal calculations

Axial node		Temperature, in K					
		T_{fc}	T_{fs}	T_{ci}	T_{co}	T_{ox}	T_b
Node 1	Maximum	1098.4	775.2	595.1	577.7	576.7	562.7
	Nominal	1058.9	727.7	593.8	576.7	576.3	562.6
Node 2	Maximum	1345.4	851.2	618.5	592.0	588.7	567.1
	Nominal	1322.6	738.4	615.4	589.4	587.9	567.0
Node 3	Maximum	1400.4	861.8	627.7	600.1	595.1	572.6
	Nominal	1362.8	731.3	624.0	596.6	594.4	572.3
Node 4	Maximum	1393.7	863.9	634.0	606.6	600.3	578.0
	Nominal	1358.8	732.8	629.3	602.2	599.4	577.6
Node 5	Maximum	1383.1	863.7	639.0	612.6	604.9	583.3
	Nominal	1342.9	735.0	633.7	607.4	603.9	582.8
Node 6	Maximum	1363.4	863.5	644.6	618.8	609.4	588.3
	Nominal	1328.2	737.5	638.0	612.4	608.1	587.7
Node 7	Maximum	1357.7	866.3	650.3	625.0	613.8	593.1
	Nominal	1324.0	738.3	642.7	617.5	612.5	592.4
Node 8	Maximum	1309.8	856.9	651.8	628.6	616.5	597.6
	Nominal	1278.9	747.1	643.9	620.6	615.2	596.7

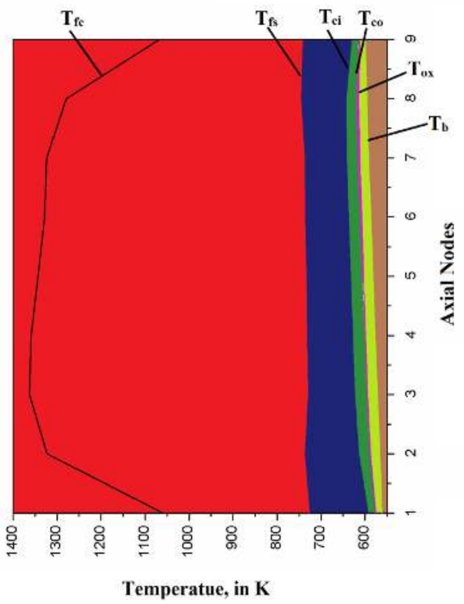

Figure 3: Image of thermal ehavior of fuel rod.

Node 9	Maximum	1107.5	799.1	637.3	620.9	614.2	601.0
	Nominal	1067.3	743.3	631.5	615.5	612.6	600.1
Rod fuel nominal	Maximum	1306.6	766.7	633.1	609.1	602.2	582.6
	Nominal	1271.6	736.8	628.0	604.3	601.1	582.1

The predictive data showed that the centerline temperature (T_{fc}) reaches its maximum of 1400.4 K, lower than the limit value of the AP-1000 designed nuclear reactor fuel rod of T_{fc}(max.) = 2866.3 K (for prevention of centerline melt). The maximum of average fuel centerline temperature was 1306.6K. The fuel centerline temperature at the bottom (node 9) and top (node 1) of the fuel rod was lower than that at the center (from node 2 to node 8) of the fuel rod. The reason for this is the distribution of neutron flux in the core of the reactor varies depending on the operation and control of the reactor. Also for this reason, the deformation of fuel pellets along the fuel rods axis also varies according to the location of the fuel pellets.

The temperature difference between the fuel centerline and fuel pellet surface temperature (ΔT) was predicted. The maximum temperature difference was 711K at node 3 and node 4, but at the top and end of the fuel column, the temperature difference was lower, about 385 K, for 4.1 mm of radius of pellets. The reason is also the distribution of neutron flux in the core of the reactor varies depending on the operation and control of the reactor. At each node positions, temperature difference increased with the operating time. Thus, the thermal conductivity of the fuel pellets increased with operating time.

The heat transfer from the fuel surface to the inside cladding depends on the thermal conductivity of the gap. The thermal conductance and the thickness change of the gap were shown in Fig.4. The obtained results showed that gap conductance was very high; its maximum calculated by the code was approximate 90 kW/(m^2.K) and the fuel clad gap was closure due to creeping down of cladding and swelling of the fuel pellet solid fission product; the gap thickness calculated by the code was 2.6 µm during 3 cycles.

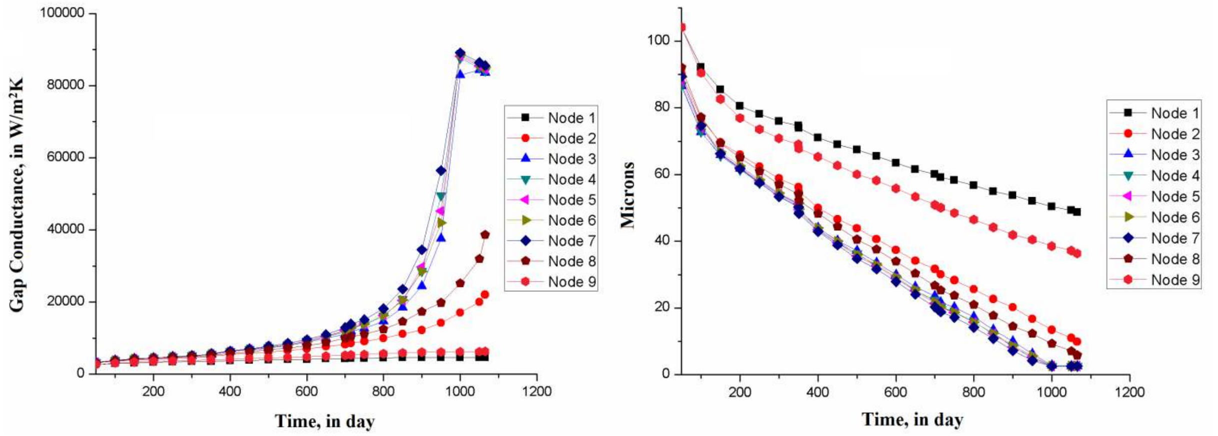

Figure 4: Predicted gap conductance and gap thickness during 3 cycles.

The maxima of the average cladding outside surface (T_{co}), oxide surface (T_{ox}) and bulk coolant (T_b) temperature were 609.1K, 602.2K and 582.6K, respectively. The T_b value was close to average coolant temperature in core of 617K; this denoted that the cooling system always ensures the requirements for the operation.

3.1.2. Predicted deformation of fuel pellets

The results of deformation of fuel pellets were given in Fig. 5 (nominal value), including: Fuel stack axial extension, fuel swelling, fuel densification, fuel relocation and fuel thermal expansion.

After about 100 days of first cycle (burn-up about 5 to 10 GWd/tU), the re-sintering effect has the greatest effect on the deformation of the ceramic. The ceramic shrinkage was about 9 µm, which reduced the length of the fuel column. After that, the effect of this phenomenon no longer occurred.

The fuel pellets were deformed due to the influence of temperature, irradiation, and reactor operating conditions.The results showed that during three cycles of operation, maximum fuel stack axial extension was 49.42 mm and the fuel clad gap was closure (see part 3.1). However, the rise of the fuel column and the disappearance of the capsule gap remain within the design limits of the AP-1000.

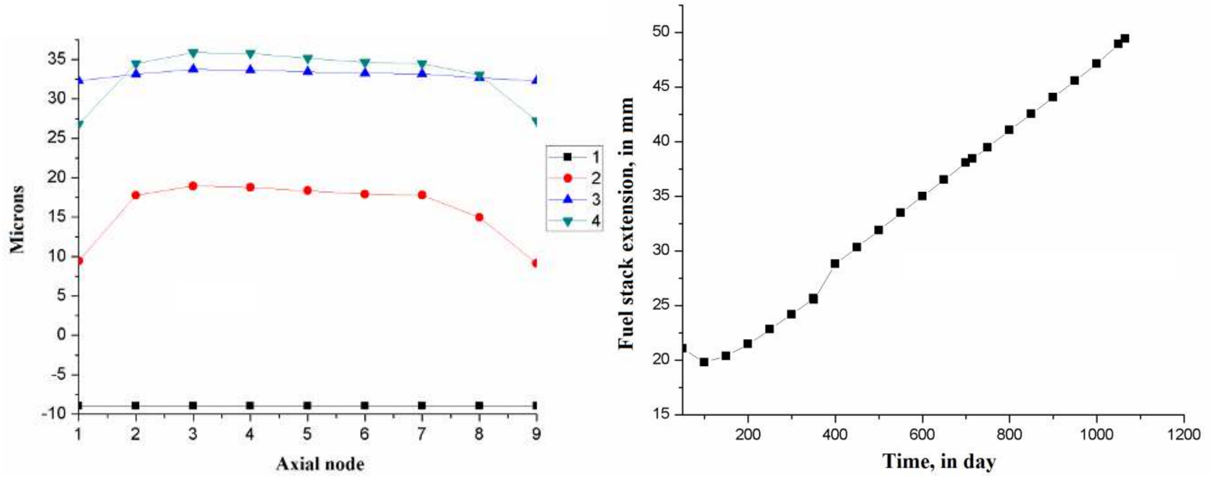

Figure 5: Deformation of fuel pellets.

3.1.3. Predicted fission gas release and rod internal pressure

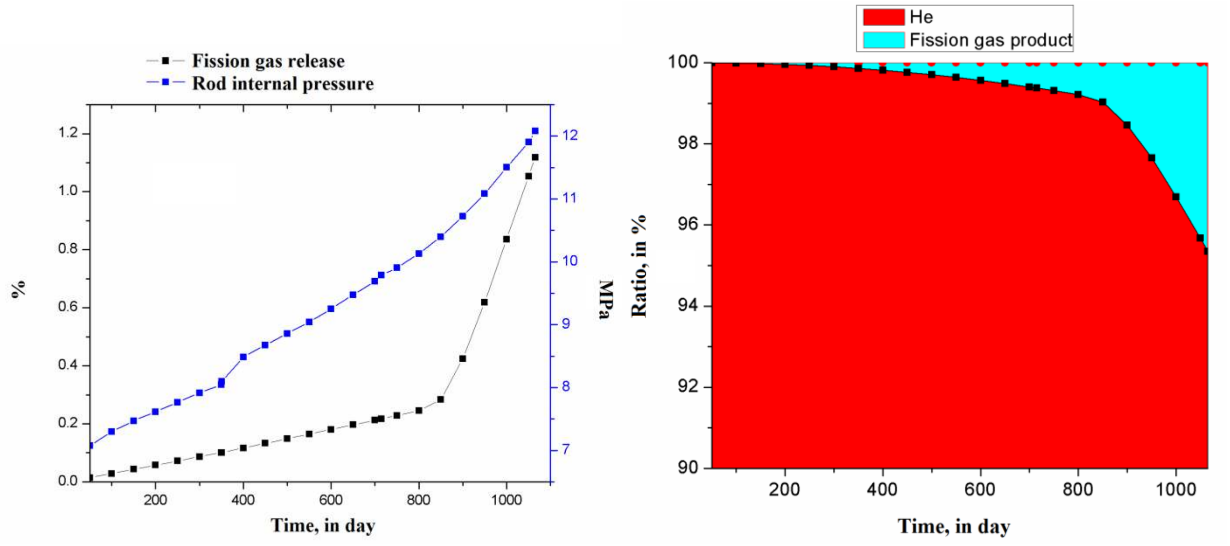

Figure 6: Fission gas release and rod internal pressure.

Fission gas release (FGR) and rod internal pressure (Pi) have a major impact on mechanical properties of fuel rod. Fission gas release can cause fuel swelling, pressure build up (xenon, krypton), pellet-cladding mechanical interaction, stress corrosion cracking, etc. As a result, the excessive fission gas release can cause the rod pressure to rise beyond system pressure and lead to fuel damage. Thus, rod pressure need to be limited by safety criteria and must be calculated for the design evaluation.

Maximum fission gas release of fuel rod (FGR) was 1.12 % at the end of 3rd cycle. Thus, almost all fission products were stored in pottery (in porous holes). Maximum rod internal pressure was 12.08 Mpa during three cycles of operation and lower than the limit values (16.2 MPa). The calculation results of FGR and internal pressure showed the guarantee of design in order to protect the fuel against cladding lift-off. These results were lower than the limit values, ensuring to prevent the diametric gap between the fuel and the cladding during steady state operation, which causes ballooning phenomenon affecting the coolant flow or the local overheating of the cladding.

3.1.4. Predicted cladding oxidation and hydration

The results of oxide thickness and hydrogen concentration of cladding were given in Fig. 7 (nominal value). Oxidation and hydriding under normal operating conditions of reactor directly influence fuel performance, not only during normal operation, but also during transients and accidents. Cladding corrosion reduces the effective thickness of the cladding, decreases the effective thermal conductivity of the cladding and thus increases the cladding and fuel temperatures and also reduces effective cladding-to-coolant heat transfer. Hydrogen absorption by the cladding and subsequent formation of hydrides may lead to cladding embrittlement. These phenomena are in creasingly important at higher exposures. So, the analyses have to show ability to protect the fuel against any type of cladding corrosion induced failure.

The results of surface corrosion and cladding hydration calculation showed that maximum oxide thickness was 36.13 µm and maximum hydrogen concentration was 347.29 ppm during three cycles and lower than the limit values (100 µm and 600 ppm respectively). As such, the cladding rod was ensuring safety during the operation of the nuclear reactor.

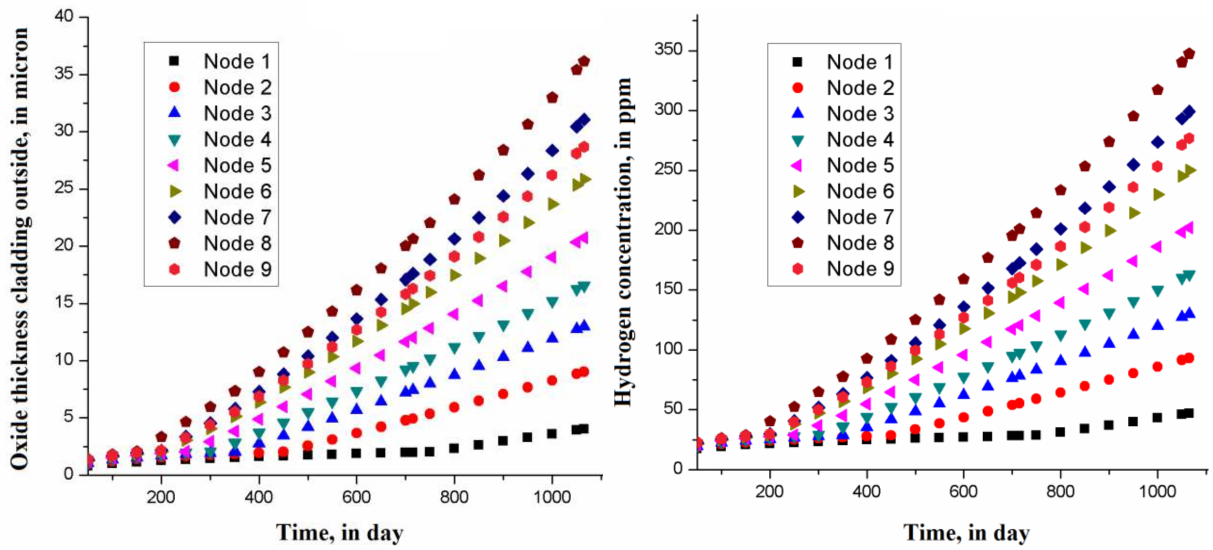

Figure 7: Cladding oxide thickness and hydrogen concentration.

3.2. Predicted behavior of nuclear fuel rod under transition operating condition

3.2.1. Predicted behavior of nuclear fuel rod under LOCA accident condition

The results of calculating the centerline of the fuel rod were shown in Fig.8. The results showed that in a very short time, the fuel rod center temperature increased dramatically (about 600K to 800K depending on the axial position). The maximum fuel centerline temperature about 2252K did not exceed the 2813K safety limited. Thus, no fuel melting phenomenon occurred.

The maximum fuel enthalpy was 370 kJ/kg, lower than safety value limited of 830 kJ/kg (Fig.9). The maximum fuel enthalpy increase was 67 cal/g, lower than limited safety value of 200 cal/g.

The results of calculating the oxide layer thickness on the fuel rod cladding were shown in Fig.10. The results showed that, surface inside cladding had an additional layer of oxide on the surface of the fuel rod shell with a thickness of about 3 µm. The surface oxide thickness increased from 3 to 5 µm depending on the axial position of the nodes. The maximum oxide thickness was about 81 µm, equivalent to about 14.21% of the thickness of the fuel cladding, 18% lower than the limited safety value. Thus, the oxidation of the fel rod cladding due to the effect of the coolant does not damage the fuel rod cladding.

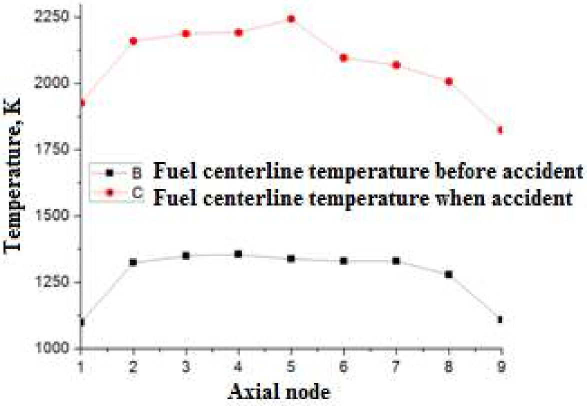

Figure 8: Fuel centerline temperature.

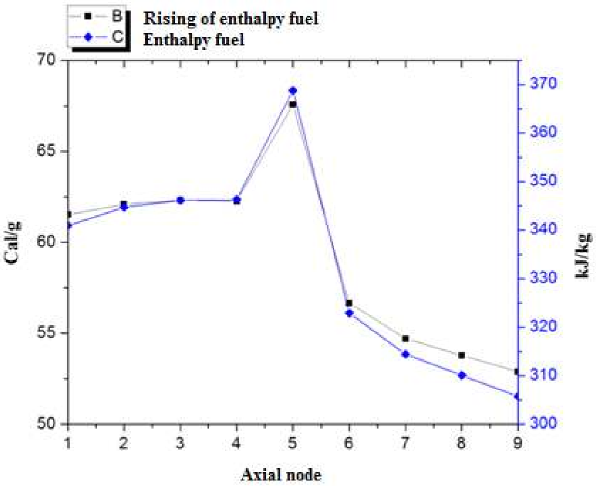

Figure 9: Enthalpy fuel.

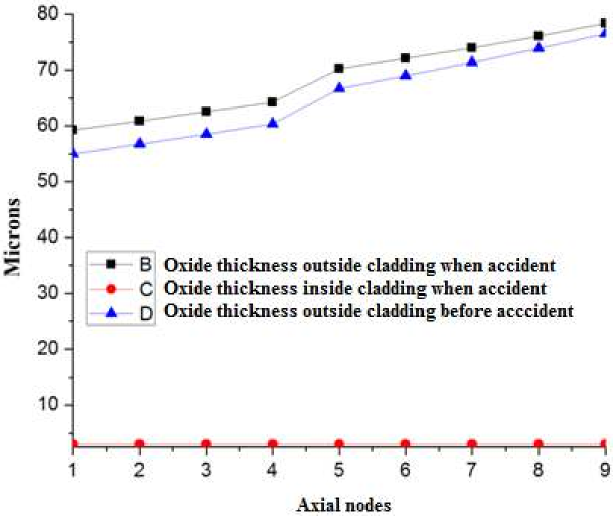

Figure 10: Cladding oxide thickness.

3.2.2. Predicted behavior of nuclear fuel rod under RIA accident condition

Fig. 11 has shown the results of calculating the centerline of the fuel rod. The results showed that in a very short time, the fuel rod center temperature increased dramatically (about 800K to 1150K depending on the axial position). The maximum fuel centerline temperature about 2483K did not exceed the 2813K safety limited. Thus, no fuel melting phenomenon occurred.

The maximum fuel enthalpy was 408 kJ/kg, lower than safety value limited of 830 kJ/kg (Fig.12). The maximum fuel enthalpy increase was 81 cal/g, lower than limited safety value of 200 cal/g.

The results of calculating the oxide layer thickness on the fuel rod cladding were shown in Fig.13. The results showed that an additional layer on the surface of the fuel rod shell with a thickness of about 3 µm was generated. The surface oxide thickness increased from 14 to 40 µm depending on the axial positions of the nodes. The maximum oxide thickness was about 98 µm, equivalent to about 17.19% of the thickness of the fuel cladding, 18% lower than the limited safety value. Thus, the oxidation of the fuel rod cladding due to the effect of the coolant did not damage the fuel rod cladding.

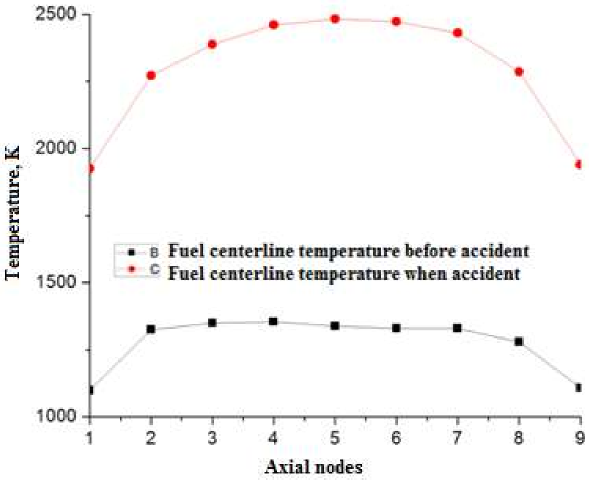

Figure 11: Fuel centerline temperature.

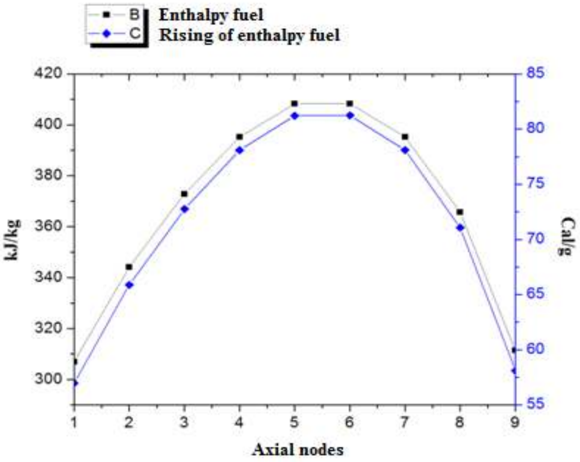

Figure 12: Enthalpy fuel.

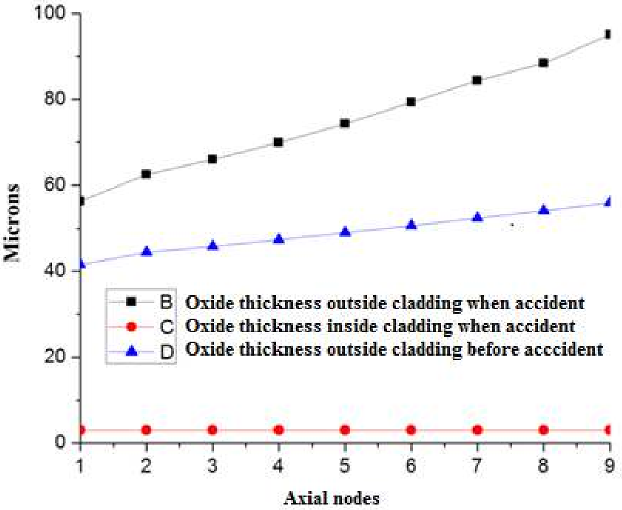

Figure 13: Cladding oxide thickness.

IV. CONCLUSIONS

The work has achieved the aims as follows:

- Overview of FRAPCON and FRAPTRAN software includes the theoretical basis and computational modeling of the status of the fuel rods in stable operating conditions and the transition state of the reactor.
- Predicting behaviors of AP-1000 nuclear reactor fuel rod under steady state operating condition by using FRAPCON-4.0 software and under transition state by using FRAPTRAN software (LOCA and RIA accident conditions) was investigated.
- The project products consisted of 01 final reports, 01 published paper on Journal of Nuclear Materials 504 (2018) 191-197, 01 published paper on Journal of science and technology (in Vietnamese), 01 presentation in the 12nd National Conference of Nuclear Science and Technology (Nha-Trang 4-6 Aug., 2017), 01 presentation in the 5nd Conference of Nuclear Science and Technology for Young Reseacher.

REFERENCES

Vietnamese documents

[1] Nguyễn Trọng Hùng và cộng sự *"Tìm hiểu phần mềm FRAPCON và FRAPTRAN đánh giá đặc trưng thanh nhiên liệu trong lò phản ứng hạt nhân"* BCTK 2017.

[2] Trần Đại Phúc và cộng sự, *"Nghiên cứu ảnh hưởng của quá trình vận hành đến tính chất của nhiên liệu và vỏ thanh nhiên liệu trong lò phản ứng VVER-1000"*, BCKH 2014.

Enghlish documents

[3] Geelhood, K.J., and W. G. Luscher , "*FRAPCON-4.0: A Computer Code for the Calculation of Steady-State, Thermal-Mechanical Behavior of Oxide Fuel Rods for High Burnup*", NUREG/CR-7022, Vol. 1, Rev. 1. PNNL-19418, Vol. 1, Rev. 1, Pacific Northwest National Laboratory, Richland, WA.

[4] Geelhood, K.J., and W.G. Luscher, 2015. *FRAPCON-4.0 Integral Assessment*, NUREG/CR-7022, Vol. 2 Rev. 1, PNNL-19418 Vol. 2 Rev. 1, Pacific Northwest National Laboratory, Richland WA.

[5] Geelhood, K.J., W.G. Luscher, and J.M. Cuta. 2014. *FRAPTRAN-1.5: A Computer Code for the Transient Analysis of Oxide Fuel Rods*, NUREG/CR-7023 ,Vol. 1 Rev.1, PNNL-19400, Vol. 1 Rev. 1, Pacific Northwest National Laboratory, Richland, WA.

[6] Geelhood, K.J., W.G. Luscher, J. M. Cuta, "*FRAPTRAN-1.5: Integral Assessment*" NUREG/CR-7023, Vol. 2 Rev.1 PNNL-19400, Vol. 2 Rev.1, Pacific Northwest National Laboratory, Richland, WA.

[7] Luscher, W.G., and K.J. Geelhood. 2014. *Material Property Correlations: Comparisons between FRAPCON-3.5, FRAPTRAN-1.5, and MATPRO*, NUREG/CR-7024 Rev.1, PNNL-19417 Rev.1, Pacific Northwest National Laboratory, Richland, WA.

[8] Manzel, R., and C.T. Walker. 2000. "High Burnup Fuel Microstructure and Its Effect on Fuel Rod Performance," *LWR Fuel Performance Meeting*, Park City, UT.

[9] U.S. Nuclear Regulatory Commission, 2007. *Standard Review Plan for the Review of Safety Analysis Reports for Nuclear Power Plants: LWR Edition: Section 4.2: Fuel System Design, Revision 3.* NUREG-0800, U.S. Nuclear Regulatory Commission, Washington D.C.

[10] Sagrado, I.C., I. Vallejo, and L.E. Herranz. 2013. *Analysis of Experimental RIA Scenarios: CIEMAT Contribution to the OECD RIA International Benchmark*, DFN/SN-02/OP-13, CIEMAT, Madrid, Spain.

[11] Shestopalov, A., K. Lioutov, L. Yegorova, G. Abyshov, and K. Mikitiouk. 1999. *Modification of USNRC's FRAP-T6 Fuel Rod Transient Code for High Burnup VVER Fuel*, NUREG/IA-0164 U.S. Nuclear Regulatory Commission, Washington, D.C.

[12] Nuclear Energy Agency Organisation for Ecomomic Co-operation and Development, 2010, "Nuclear fuel behaviour under reactivity-initiated accident (RIA) conditions", ISBN 978-92-64-99113-2.

[13] Tero Manngard, Jan-Olof Stengard, "Evaluation of the Halden IFA-650 loss-of-coolant accident experiments 5, 6 and 7", Report number: 2014:19 ISNN: 2000-0456.

[14] IAEA-TECDOC-CD-1709, "Fuel behavior and modelling under severe transient and loss of coolant accident (LOCA) conditions", Proceedings of a technical meeting held in Mito, Japan, 18 – 21 October 2011

STUDY ON MAGNETIC SEPARATION METHOD WITH LOW CONTENT ZINC ORE AT CHO DIEN MINE, CHO DON DISTRICT, BAC KAN PROVINCE TO PRODUCE INDUSTRIAL FINE ORE

Duong Van Su, Truong Thi Ai, Bui Ba Duy, Tran Van Son, Nguyen Hong Ha, Luong Manh Hung, Nguyen Van Tien, Pham Thi Thuy Ngan, Vu Khac Tuan, Le Quang Thai and Le Thi Mai Huong.

Center for Radioactive Ore Processing Technology,
Institute for Technology of Radioactive and Rare Elements,
48 Lang Ha, Dong Da, Hanoi

Project Information

- **Code:** DTCB 14/17/VCNXH
- **Managerial level:** Ministry
- **Allocated Fund:** 750,000,000 VND
- **Implementation Time:** 19 month (June 2017 – Dec 2018)
- **Contact Email:** sudung1991@gmail.com
- **Papers published in relation to the project:**

1. Duong Van Su, Truong Thi Ai, Bui Ba Duy, Nguyen Hong Ha. Summary of material composition of zinc oxide ore with low zinc content, rich in iron and magnesium at A mine - Technology difficulties and orientations. *The 4th National Conference On Mineral Processing Science And Technology*, Hanoi 2018 (in Vietnamese).
2. Duong Van Su, Truong Thi Ai, Bui Ba Duy, Nguyen Hong Ha, Tran Van Son, Pham Thi Thuy Ngan. Zinc oxide ore separation technology has low zinc content at Cho Dien mine, Cho Don district, Bac Kan province. *Science and mine industry magazine*, No. 6, Hanoi 2018 (in Vietnamese).

Abstract: Cho Dien mine is a multi – metal ore mine. Ores exist mainly in two forms: zinc sulfide, zinc oxide. Zinc oxide form is divided into two types: brown zinc oxide ore and black zinc oxide ore.

Two types of zinc oxide ore have common properties: highly weathered ore; largely proportional fine particles; high iron content; low zinc content; non-magnetic iron minerals; disseminated rock, non-ore and ore particles with fine to very fine dimensions.

Brown zinc oxide ore: zinc minerals are mostly calamine. Besides, this ore contains a lot of clay mineral and rock. This ore is easy for separation. Using methods of gravity separation, the magnetization process by heating, wet magnetic separation, the recovery yields reached: 79,94% with fine zinc ore (zinc content of 25,35%) and 64,68% with fine iron ore (TFe content of 62,86%).

Black zinc oxide ore: Useful and non-useful minerals are diverse and complex, closely symbiotic relationships together. Zinc mineral is mostly chalcophanite. Manganese element almost does not exist as an independent mineral, but exist in the composition of zinc minerals, occupying the position of zinc in the chalcophanite mineral crystal structure. This ore is very difficult for enrichment. It can not be processed if traditional separation methods were used.

Keywords: *zinc oxide, refine ore, gravity separation, magnetic separation.*

I. INTRODUCTION

1.1. The objectives of project

The main objective of this work is suggesting one procedure of the zinc ore magnetic separation technique in order to meet producing demands of Thai Nguyen Iron and Steel Join Stock Corporation (TISCO) and producing the fine ores with the quantity and quality as follows:

+ 30 kg Refined zinc with content of Zn ≥ 25% (by the weight) and recovery of Zn ≥ 70% (by the weight); content of TFe ≤ 8% (by the weight); content of ≤ 3% (by the weight)

+ 50 kg Refined iron with content of Fe ≥ 60% (by the weight) and recovery of Fe ≥ 55% (by the weight); content of TFe ≤ 3% (by the weight); content of Pb ≤ 1% (by the weight)

1.2. Materials

The research sample is zinc oxide ore from Cho Dien mine. Zinc oxide form is divided into two types: brown zinc oxide ore and black zinc oxide ore. In fact, these two types of ores have very different properties.

1.2.1. Black zinc oxide ore

The research sample has low zinc content, high iron content (5.43% Zn; 35.30% TFe) and they are distributed without rule. Zinc minerals are diverse and complex, mainly chalcophanite $ZnMn_3O_7(H_2O)_3$ and a small amount of calamine, smitsonite, zincite, hydrozincite minerals. Iron minerals existing mainly in non-magnetic form are goethite. A small amount of iron minerals existing in weak magnetic form is hematite.

Ore is strongly weathered, in which fine particle accounts for a high proportion. The beneficial minerals have a strong bond with most of companion impurity minerals. The fine to very fine particles of ore minerals and rock particles are disseminated.

Manganese element almost does not exist as an independent mineral, but exist in the composition of zinc minerals, occupying the position of zinc in the chalcophanite mineral crystal structure. The content of manganese is about three times as much as that of zinc is. If minerals are classified according to useful content, chalcophanite minerals are manganese minerals. Therefore, the black color of ore is the typical color of manganese minerals. Manganese is a dark metal – therefore, if the magnetization process by heating is applied, chalcophanite also becomes a magnetic mineral. Appling magnetic separation after that is not effective.

The results of orientation studies showed that black zinc oxide ore is particularly difficult to enrich. In the framework of this work, it can be said that: black zinc oxide ore can not be processed if traditional separation methods were used.

From now on, brown zinc oxide ore was selected as the research object of this work.

1.2.2. Brown zinc oxide ore

The research sample has a low zinc content and distribution rule. The distribution of zinc is directly proportional to particle size, the iron content is relatively high and the iron distribution has no rule (8.01% Zn; 25.76% TFe). Zinc minerals exist in three main forms, mainly calamine $Zn_4Si_2O_7(OH)_2(H_2O)$ and a small amount of smitsonite and chalcophanite. Iron minerals existing mainly in non-magnetic form are goethite. A small amount of iron minerals existing in weak magnetic form is hematite.

Ore is strongly weathered, in which recovery yield of fine particles is high. Fine to very fine particles of ore minerals and rock particles are disseminated.

There are many clay minerals and rock in this ore. It is quite easy for separation of this ore. Brown color is the typical color of clay minerals and rock.

Based on results of researching of separation methods, it can be said that brown zinc oxide ore is relatively easy for separation.

1.3. The processing equipment and the main enrichment equipment used in the research.

The main equipment of the project was shown in Table 1

Table 1: The main equipment of the project

No	Main equipment	
1	*Trammel screen, shaking, washing and spiral classifier (Vietnamese)* Capacity, kg/h: 150,0 1) Trammel screen, shaking, washing Tumbling drum dimension, mm: 380 x 620 Rotating screen dimension, D x L, mm: 380 x 580 Screen hole dimension, mm: 10 Rotating speed , rpm: 0 - 120 Electric motor power, kW: 0.75 2) Spiral classifier Spiral diameter, mm: 150 Spiral length, mm: 1.200 Number of spiral core: 01 Electric motor power, kW: 0.55	
2	*Multi-gravity separator (English)* Separator drum, rpm: 280 Water consumption, lpm: 0-10 Ore sludge flow, lpm: 0 - 7 Separator drum tilting angle: 0-10 degree Power, kW: 0.75 Capacity, kg/h: 50.0	

3	*Electric resistance furnace SX2-5-1.200 (Chinese)* Heating element dimension BxLxH, mm: 120x300x200 Maximum temperature, degree of Celsius : 1.200 Power consumption, Kw: 5.0 Capacity: 4.5 Kg/batch	
4	*Mixer-Magnetic separator system* Capacity, l/h: 280.0 1) Mixer (Vietnamese): Mixing tank volume, l: 150 Mixer speed, rpm: 75 Electric motor power, kW: 0,75 2) Wet magnetic separator (Vietnamese) Separating drum dimension DxL, mm: 330x220 Drum rotating speed, rpm: 60 Magnetic intensity, gauss: 600; 900; 1.200 Electric motor power, kW: 0.35	

II. EXPERIMENTAL

2.1. Reasons for milling method and equipment selection

1) Brown zinc oxide ore is a relatively complex multi-metal ore. Iron content is high (25,71%), zinc and manganese content is low (8.01% Zn; 3.32% Mn). Other elements exist in many different minerals with insignificant-contents.

2) Zinc minerals exist in three main forms, mainly calamine $Zn_4Si_2O_7(OH)_2(H_2O)$ and a small amount of smitsonite and chalcophanite.

3) Iron minerals existing mainly in non-magnetic form are goethite. A small amount of iron minerals existing in weak magnetic form is hematite. It is appropriate when applying the magnetization process by heating combining the low magnetism flux density-wet magnetic method for this ore.

4) There are many clay minerals and rock in this ore. Therefore, ore is relatively easy to separate and gravity separation method can be applied for the ore.

5) Fine to very fine particles of useful and non-useful minerals and rock particles are disseminated, 0.2 – 0.05 mm

6) Yields for -0.2 mm; -0.075 mm; -0.035 mm particle sizes are very high: 37.57%; 32.56%; 24.45%. This indicated that brown zinc oxide ore were strongly weathered. The first step in

technology are trammel screening, shaking, ball grinding, vibrating screen and spiral classifier to separate the primary particles, avoiding over-crushing phenomenon. The results of orientation experiments on trammel, shaking equipments are very effective. With optimal experimental conditions, -0.2 mm particle size was separated with yield of more than 38%.

7) Zinc recovery yield according to particle size has no rule. Distribution of zinc content has a rule, which is proportional to the particle size. Distribution of iron content is almost homogeneous with all particle sizes. This typical property showed that it is possible to use the particle size to sort out the zinc element.

8) With orientation experiments on multi-gravity separator, sludge concentrating table, hydrocyclone, with particle size of -0.2 mm, multi-gravity separator showed better efficiency compared to sludge concentrating table, hydrocyclone. Therefore, the multi-gravity separation device was selected as the main separator.

9) Iron minerals and zinc minerals have high density from 3.3 g/cm^3 to 5.7 g/cm^3. Impurity minerals and rock have smaller density of 2.5 g/cm^3. Therefore, it is possible to use gravity separation method, specifically multi-gravity separator to separate the majority of impurity minerals and rock right after steps of trammel screening, shaking.

10) The results of magnetization heating process were very high. Almost of non-magnetic iron minerals and weak magnetic iron minerals were transfer to strongly magnetic iron minerals of magnetite. The reductive agent used for magnetization heating process is activated carbon (HTV) with optimal conditions, such as: coal mixing ratio of 8%, heating temperature of 730 degree of Celsius, heating time of 90 minutes.

11) The results of orientation magnetic separation experiments for ore after heating process have indicated that it only can apply wet magnetic separation method for this ore with low-intensity, from 600 gauss to 1200 gauss.

12) Middling ores of steps of magnetic separation, multi-gravity separation should be combined together and then wet grinded in ball milling equipment to decrease particle size to -0.1 mm to break down the bonds between minerals, then middling ores were sent back to the previous separation steps to increase recovery yields of zinc and iron ore.

2.2. Suggestion of separation technological procedure for brown zinc oxide ore

Based on the researching frame work, researching contents and results from experiments of separation methods, a technological procedure of separation for brown zinc oxide ore was presented as in Fig. 1.

All steps of separation for brown zinc oxide ore were described in Table 2

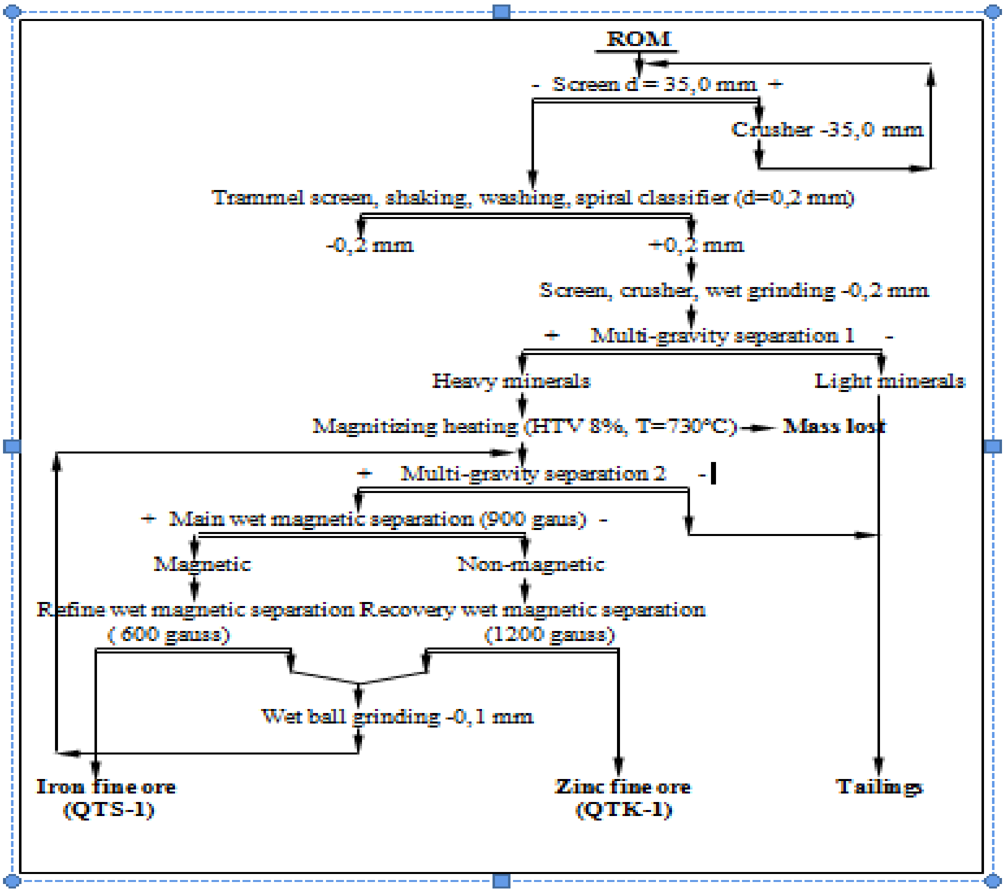

Figure 1: The diagram of optimal technological procedure of separation for brown zinc oxide ore

Table 2: Parameters for the stages of separation process for brown zinc oxide ore

No	**Separation steps**	**Parameters for Separation process**		
		Technological conditions	Unit	
1	Trammel screen, shaking, washing spiral classifier	Solid/liquid in tumbling drum	-	1.0/1.2
		Water consumption for rotating screen and vibrating screen	m^3/tone	6.5
		Water pressure for rotating screen and vibrating screen	at	2.0 – 2.5
		Shaking-trammel time	minute	6
		Rotating speed	rpm	65
2	Multi-gravity separation 1	Solid concentration in input ore sludge	%	20.0
		Rotating speed	rpm	250

		Separator drum tilting angle	^{o}	3.0
3	The magnetization process by heating	HTV Coal mixing ratio	%	8.0
		Heating temperature	^{o}C	730 ^{0}C
		Heating time	minute	90
4	Multi-gravity separation 2	Solid concentration in input ore sludge	%	20.0
		Rotating speed	rpm	250
		Separator drum tilting angle	^{o}	3.0
5	Main wet magnetic separation	Field intensity	gauss	900
		Solid concentration in input ore sludge	%	25.0
6	Refine wet magnetic separation	Field intensity	gauss	600
		Solid concentration in input ore sludge	%	25.0
7	Recovery wet magnetic separation	Field intensity	gauss	1200
		Solid concentration in input ore sludge	%	25.0

Enrichment steps in technological procedure were listed as follows:

1. ROM (Run of mine) with D_{max} = 125 mm was screened and crushed reasonably to -35 mm particle size, then it was put into the trammel screen, shaking, washing and spiral classifier to separate the primary fine particle. Ore was crushed and optimally classified to 2 types of particle size: -0.2 mm and +0.2 mm
2. +0.2 mm size particles were crushed, screened, wet ball grinded properly to -0.2 mm size particles. Then grinded particles were mixed together with -0.2 mm primary particles to form a product named -0.2 mm assorted product.
3. Using gravity concentration (multi gravity separator), -0.2 mm assorted product were separated assorted product -0.2 mm. Two types of groups were produced: heavy mineral group and light mineral group. Light mineral group was removed as waste ore (meeting requirements applied for waste). As a result, almost rock and light mineral were discharged.
4. Using magnetization process by heating for heavy mineral product of process of multi-gravity separation 1 in order to transfer non-magnetic iron minerals and weakly magnetic iron minerals into strongly magnetic iron mineral of magnetite. The reductive agent used was HTV activated carbon with optimal conditions: coal mixing ratio of 8% (by weight), heating temperature of 730 degree of Celsius, heating time of 90 minutes.
5. Using multi-gravity separator (step of multi-gravity separation 2) to separate HTV and a part of impurity minerals out of ore after the heating process.

6. Using wet magnetic separation method with field intensity H = 900 gauss to separate ore after magnetization heating process, 2 types of product were obtained: magnetic and non-magnetic products. Magnetic product was crude iron refined ore. Non-magnetic product was crude zinc refined ore.
7. Refining step of crude iron refined ore and crude zinc refined ore.

+ The crude zinc refined ore was separated on wet magnetic separator with field intensity H = 1200 gauss. The final product is zinc refined ore (QTK-1)

+ The crude iron refined ore was separated on wet magnetic separation with field intensity H = 600 gauss. The final product is iron refined ore (QTS-1)

8. Middling products of all milling steps were mixed together, followed by wet grinding in ball milling equipment to decrease the particle size to -0,1 mm in order to break down the bonds between minerals, then middling ores were sent back to the multi-gravity separator 2 to increase recovery yields of zinc and iron ore.

III. RESULTS AND DISCUSSION

The results of separation process for brown zinc oxide ore were shown in Table 3

Table 3: The experimental results of separation process for brown zinc oxide ore

No	Separation steps and products	Yield, %	Content, %		Recovery, %	
1	Trammel screen, shaking, washing and spiral classifier					
1.1	Particle size +0,2 mm	53.79	11.70	25.02	78.54	52.35
1.2	Particle size -0,2 mm	46.21	3.72	26.51	21.46	47,65
Inlet ore		100.00	8.01	25.71	100.00	100.00
2	Multi-gravity separation 1					
2.1	Heavy minerals total 1	64.04	11.12	29.85	88.87	74.36
2.2	Light minerals total 1 (tailings 1)	35.96	2.48	18.33	11.13	25.64
Inlet ore		100.00	8.01	25.71	100.00	100.00
3	Magnetization process by heating					
3.1	Product after heating	55.29	12.87	34.58	88.87	74.36
3.2	Mass Lost	8.75	0.00	0.00	0.00	0.00
Inlet ore		64.04	11.12	29.85	88.87	74.36
4	Multi-gravity separation 2					
4.1	Heavy minerals total 2	62.56	13.27	33.81	103.66	82.26

4.2	Light minerals total 2 (tailings 2)	3.58	3.10	19.50	1.39	2.72
Inlet ore		66.14	12.72	33.03	105.04	84.98
5	Main wet magnetic separation 900 gauss					
5.1	Magnetic product	27.94	2.70	61.13	9.40	66.44
5.2	Non-magnetic product	34.62	21.81	11.75	94.25	15.82
Inlet ore		62.56	13.27	33.81	103.66	82.26
6	Recovery wet magnetic separation 1200 gauss					
6.1	Refined zinc (QTK-1)	25.26	25.35	7.09	79.94	6.96
6.2	Middling 1	9.36	12.25	24.33	14.31	8.86
Inlet ore		34.62	21.81	11.75	94.25	15.82
7	Refine wet magnetic separation 600 gauss					
7.1	Refined iron (QTS-1)	26.45	2.30	62.86	7.58	64.68
7.2	Middling 2	1.49	9.80	30.47	1.82	1.77
Inlet ore		27.94	2.70	61.13	9.40	66.44
8	Total tailings (Tailings 1 + Tailings 2)	39.54	2.53	18.44	12.48	28.36
ROM		100.00	8.01	25.71	100.00	100.00

IV. CONCLUSIONS

4.1. Conclusions

1. There are two types of zinc oxide ore in the Cho Dien mine: brown zinc oxide ore and black zinc oxide ore. These two types of ore have very different mineral composition.
2. With black zinc oxide ore, the results of orientation studies showed that:
   - Black zinc oxide ore is particularly difficult to separate
   - If traditional separation methods are applied, it will not separate this kind of ore.
3. Brown zinc oxide ore is relatively easy to separate. The optimal parameters for separation procedure of this ore were shown in Fig.1
4. In researching scale of this work,
   - 36.0 kg Refined zinc ore (QTK-1) with βZn = 25.35% ; εZn = 79.94% and βTFe = 7.09% (by the weight)
   - 52.0 kg Refined iron (QTS-1) with βTFe = 62.86% ; εTFe = 64.68% and βZn = 2.30% (by the weight)
   -

4.2. Suggestions

1. In industrial production, with zinc ore products of type 1, zinc content should be in the range of 20.0 - 22.0% (by the weight) not only for increasing the yield of zinc recovery, but also for avoiding resource loss and still meeting the requirements of quality for production.
2. With the black zinc oxide ore, it is necessary to study comprehensively the technology, in which traditional mechanical enrichment methods such as gravity separation, magnetization heating process and magnetic separation or flotation combine with the chemical separation methods (hydrometallurgy) as well as separation methods by temperature to find the most suitable and economical technology, recovering maximum useful mineral resources.
3. It is necessary to study at semi-industrial scale, in order to assess the stability and calculate economic efficiency with the suggested milling technology layout.

REFERENCES

[1] Báo cáo "*Kết quả công tác thăm dò tỉ mỉ các mỏ quặng ôxit và sunfua chi kẽm Chợ Điền Bắc Thái*". Cục địa chất, năm 1984.

[2] Nguyễn Văn Thái - Báo cáo "*Nghiên cứu xác lập công nghệ tuyển quặng kẽm chì ôxit từ quặng nghèo*". Công ty Kim loại màu Thái Nguyên, năm 2002.

[3] Báo cáo "*Tổng hợp quặng ôxit mỏ Chợ Điền - Bắc Kạn Thái Nguyên".* Công ty TNHH NN MTV KLM Thái nguyên, 2006.

[4] Nguyễn Văn Minh - Báo cáo "*Nghiên cứu công nghệ tuyển quặng sắt nghèo không từ tính (sắt nâu) vùng Văn Bàn - Lào Cai bằng phương pháp nung từ hóa nhằm tận thu tài nguyên", Viện Khoa học và công nghệ mỏ, Vinacomin.*

[5] Trần Thị Hiến - Báo cáo *"Nghiên cứu công nghệ tuyển quặng ôxit kẽm (dưới 10%) mỏ Chợ Điền phục vụ yêu cầu sản xuất bột kẽm"* - Viện Khoa học công nghệ mỏ - luyện kim, năm 2007.

[6] Bùi Tiến Hải - Báo cáo *"Nghiên cứu công nghệ tuyển thu hồi các kim loại thiếc, sắt trong đới mũ sắt khu Lũng Cháy và Suối Teo mỏ kẽm chì Chợ Điền"* - Công ty Cổ phần Kim loại màu Thái Nguyên, năm 2016.

EVALUATION OF THE RESULTS OF PREVIOUS RESEARCH PROJECTS AND ADDITIONAL RESEARCH ON URANIUM SANDSTONE ORE PROCESSING TECHNOLOGY TO ESTABLISH ECONOMIC AND TECHNICAL DATA

Than Van Lien, Tran The Dinh, Pham Minh Tuan, Nguyen QuocHoan, Ha Dinh Khai, Tran Van Son, Nguyen Thi Hong Ha, Le Quang Thai, Nguyen Thi Thuy Ngan and Le Thi Hong Ha.

Center for Radioactive Ore Processing,
Institute for Technology of Radioactive and Rare Elements,
48 Lang Ha, Dong Da, Hanoi.

Project information:

- **Code:** DTCB.04/16/VCNXH
- **Managerial Level:** Ministry
- **Allocated Fund:** 700,000,000 VND
- **Implementation time:** 30 months (Jan 2016- Jun 2018)
- **Contact email:** tvlien59@yahoo.com.vn
- **Paper published in related to the project:**

1. Than Van Lien, Tran The Dinh, Nguyen Dinh Van, Nguyen Ba Tien, Nguyen Thi Kim Dung, 2017. Pilot Study on Uranium Recovery from Vietnam low grade uranium sandstone ores by the heap leaching method. *ALTA 2017, Uranium – REE Proceedings, ALTA metallurgical Services Publications*, Perth – Australia, ISBN: 978-0-9925094-9-1.

2. T.K.D. NGUYEN, T.S. DOAN, V.L. THAN. Removal of uranium and thorium from uranium and rare earth ores processing case study of QA/QC on environmental analysis. *International Symposium on Uranium Raw Material for the Nuclear Fuel Cycle: Exploration, Mining, Production, Supply and Demand, Economics and Environmental Issues*, URAM 2018, 25–29 June 2018 Vienna, Austria; Book of Abstracts and Extended Abstracts

3. Than Van Lien, Le Ba Thuan, Nguyen DucThanh. The extraction of Thorium from Vietnam Monazite ore processing. *Journal of East China University of Technology, Special Edition of ECUT Journal*, 2016, ISSN1674-3504, CN36-1300/N

4. Tran The Dinh, Than Van Lien, Pham Thi Thuy Ngan, 2017. Study on Palua – Parong uranium sandstone ore treatment by heap leaching method. *Journal of Science and Technology, Ministry of Science and Technology*, (ISSN 1859 - 4794), 1B/2017, pp. 48-52.

5. Tran The Dinh, Than Van Lien, Pham Minh Tuan, Le Quang Thai, Vu Khac Tuan, Pham Thi Thuy Ngan, Le Hong Ha, Nguyen Hong Ha, Truong Thi Ai, Nguyen Quoc Hoan, Ha Dinh Khai, 2017. Study onPalua - Parong uranium sandstone ore treatment by agitation method. *Journal of Science and Technology, Ministry of Science and Technology,* (ISSN 1859 - 4794), 1B/2017, pp.38-42.

6. Than Van Lien, Tran The Dinh, Pham Minh Tuan, Le Quang Thai, Vu Khac Tuan, Pham Thi Thuy Ngan, Le Hong Ha, Nguyen Hong Ha, Truong Thi Ai, Nguyen Quoc Hoan, Ha Dinh Khai, 2017. The results of research projects on treatment of Nong Son Basin Uranium ores and proposal the research directions. *Workshop proceeding of Vietnam Conference of Nuclear Science and Technology 12*, Nha - Trang, 2 - 4 August, 2017.

7. Pham Thi Thuy Ngan, Than Van Lien, Tran The Dinh, 2016. Study on Technology for Thanh My uranium ore treatment by agitation method. *Workshop proceeding of The 4th Conference of Nuclear Science and Technology for Young Young scientist*, Hanoi, October, 2016.

Abstract: This report synthesizes and evaluates the results of research projects on the Nong Son basin (Quang Nam province) uranium ores treatment and presents additional research results on the treatment of uranium ores withcontentU_3O_8> 0.2% by agitation leaching method,treatment of leaching solution by solvent extraction method, and propose the next research direction in the field of uranium ore processing. Based on the research results, heap leaching method is selected as suitable method for Nong Son basin sandstone orestreatment.The main parameters for heap leaching process are: ore size ≤ 1cm, the concentration of H_2SO_4 is 75 g/L, acid H_2SO_4 concentration of the irrigation solution 50 – 75 g/L, spraying flow rate 10-30 L/m^2.h, the consumption of acid 38-40 kg/ore ton, the consumption of MnO_2 is 4 kg/ore ton, the maximum height of the ore bed is 6 m, the leaching time depends on the mass of the ore bed. The leaching solution is enriched and purified by ion exchange method using the Amberrlite IRA-420, GSS300. Precipitation of technical uranium by MgO in two phases, phase 1 at pH = 3.8-4.0 and phase 2 at pH 7.0-7.2. The uranium leaching efficiency was ≥ 80%.For the plant with operating capacity of 100 tons U/year, estimated technical uranium price is about 60USD/kg.

The results ofadditional researchshow thatthe irrigation rate of 30 L/m^2.h is optimal, when Nong Son basin uranium ore istreated by heap leaching method.

The effects of main parameters on uranium leaching efficiecy for treatment of uranium ore containingU of 1.188% and Fe of 2.154% by agitation methodwas studied. Under leaching conditions of ore particle size ≤75µm; acid consumption of 40 kg/ton of ore, MnO_2 consumption of 2 kg/ton of ore, leaching time 18 h, the uranium leaching efficiency reaches (94 ± 3)%.

The influence of various factors affecting the solvent process, such as contact time, solvent concentration, dilution factor, etc. on uranium extraction was investigated using Tri-Octyl Amine (TOA), 5% n-decanol, kerosinwith 4 stages of extraction sequential extraction, scrubbing and 3 stages of stripping;uranium extration efficiencywas≥ 95%.

Keywords: *Uranium ore, heap leaching, agitation leaching.*

I. INTRODUCTION

Up to now, the research projects related to uranium ore processing in our country have had a history of more than 40 years, from the first experiments to analyze the chemical composition and identification of the ability to extract uranium from Lao Caiapatite ore and Nam Xe rare earth, which were conducted at the Hanoi University of Science and Technology from 1968 until the study of Nong Son basin uranium ores processing, conducted at the Institute for Technology of Radioactive and Rare Elements. These works have systematically studied all types of uranium ore in Vietnam.

Particularly, there have been over 25 research projects at all levels, including 4 state-level, 17 ministerial-level and 7 Institute -level research works onNong Son basin uranium ores, treatment. Therefore, the comprehensive assessment of theseobtained research results is very neccesary. This review is intended to:

- Evaluate the achieved results;
- Identify what is or is not done to propose the next research direction.

This report synthesizes, evaluates and analyzes the results of researches on the Nong Son basin uranium ores processing. From there, the successes and limitations of the researches were identified and further research direction in the coming years was proposed to serve the assessment of uranium resources as the master of technology and to develop the options for efficient use of this resource.

In addition, the report also presents the results of uranium extraction from uranium ore containing U_3O_8 more than 0.2% by agitation leaching method, study on permeability of uranium ore and U recovery from leaching liqour by solvent extraction method using Tri-Octyl Amine (TOA).

II. EXPERIMENTAL

2.1. Material, chemical and equipment

- Uranium sandstone ores from Palua – Parong area of QuangNam province – the central part of Vietnam was used in this study. The chemical compositions of ore are shown in Table 2.1.

- Chemicals: H_2SO_4, HC*l*, NaOH, NH_4Cl, Na_2CO_3, NaCl,TriOctyl Amine TOA ($C_{24}H_{51}N$, IP2028 solvent, Kerosene), n-decanol 98%, Uranyl nitrate,$BaCl_2$, ion exchange resin maked GS300.

Table 2.1: Chemical composition of research ore

Elements	Content, %	Elements	Content, %
Al	9.32	Sr	0.0123
Si	46.2	Li	0.0013
K	3.56	Na	2.0
Ca	0.53	Mg	0.0632
Ti	0.2123	Mo	0.0013
V	0.0504	Ba	0.1276
Cr	0.0052	Zr	0.0035
Mn	0.0091	Th	0.0049
Fe	2.154	U	1.188

Equipment: HoaPhat (Vietnam) jaw crusher, Chinese jaw crusher, pH meter, magnetic stirrers

- PVC column system: D= 0.105m, H = 1.0m;
- PVC column system: D = 0.2m, H = 2.0m;

2.2. Leaching procedure

Fig.1 shows the type of laboratory leaching apparatus used for constant pH leach tests. A 1000 mL baffled glass beaker is leach vessel for 500 g ore samples. A variable speed electric agitator unit (0.1 hp)5 is used to drive the impeller. The pH is measured by a combination electrode, and a platinum-calomel electrode configuration is used to determine the oxidation potential.The pH is adjusted to the target level by adding 1:1 sulfuric acid. The pH is monitored continuously and controlled at the desired level by adding more acid.The oxidation potential is controlled by adding an oxidant MnO_2. The progress of the leach is followed by withdrawing 20-40 mL slurry samples at appropriate intervals. Immediately after each sample is taken, it is filtered and washed with five 20-40 mL volumes of acidified (approximately pH2.0) water.All products are measured and analysed so that a complete material balance can be made for each test.

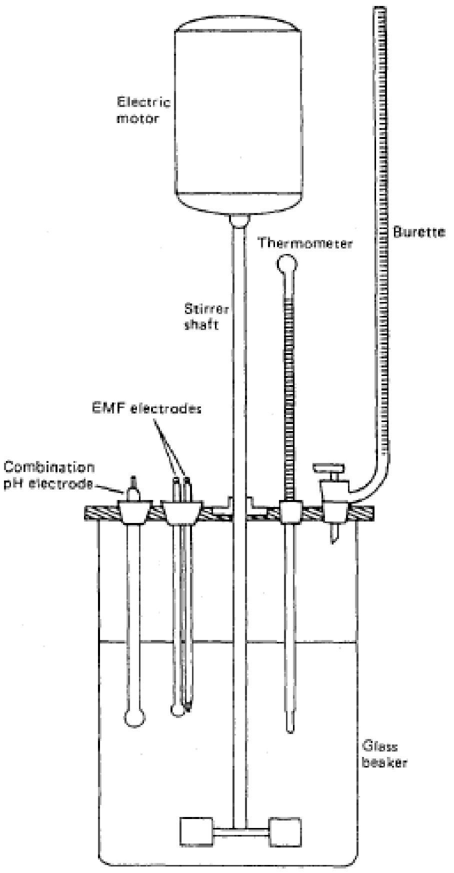

Figure 1: Apparatus for acid leach tests.

2.3. Laboratory tests of uranium recovery by solvent extraction

A 50 mL aliquot of leach liquor is shaken with an equal volume of solvent for 5s in a 250 mL separating funnel. The two layers are allowed to separate. The aqueous phase is analysed for uranium. The equilibration is repeated for times of 30, 45, 60, 90, 120, 150 and 180 s using fresh aliquots of aqueous solution and solvent for each equilibration time.

2.4. Analytical techniques

Uranium concentration in leach liquor and in eluate solutions was determined using David-Gray titration method. Other dissolved metals in solution were quantified by InductivelyCoupledPlasma Mass Spectrometry (Agilent 7500, USA).The particle size measurement was conducted with a MALVERN Laser particle size analyzer.

III. RESULTS AND DISCUSSION

3.1. The main results of the research projects on Nongson Basin uranium ore treatment

3.1.1. Thesystem of data on a lithology, mineral compositions, chemical compositions of KheHoa - Khe Cao, Pa Lua - Pa Rong, Dong Nam Giang and An Diem uranium ore deposits was collected intheresearch projects.

Uranium deposits in Nongson Basin are rather low grade and relatively small in extent as compared to present worldwide commercial practice.

Uranium ore in Nong Son Basin is sandstone with different levels of weathered: non-weathered, weathered and semi-weathered (mainlynon-weathered). The main minerals of sandstone ore are quartz (SiO_2), albite ($NaAlSi_3O_8$), glauconite($(K,Na)(Fe^{+3},Al,Mg)_2(Si,Al)_4O_{10}(OH)_2$), calcite ($CaCO_3$), kaolinite ($Al_2Si_2O_5(OH)_4$), sericite ($K_2O.3Al_2O_3.6SiO_2.2H_2O$), illite ($(K,H_3O)Al_2Si_3AlO_{10}(OH)_2$),siderite ($FeCO_3$) and sphene ($CaO.SiO_2.TiO_2$). The mineral containing uranium is mainly nasturan ($(U,Th)O_2.(O_{0.5\text{-}3})UO_3.xPbO$).

The average U_3O_8content in the ore is about 0.05%. The most abundant impurities are Si, Al, Fe, alkali and alkaline earths. The V and Mo contents in sandstone are negligible. The presence of UO_2 in the ore suggests that an oxidant is required. As carbonates in Palua-Parong uranium ore are low (les than 3%), sulfuric acid was chosen for treatment. Furthermore, PbO concentration of this ore is also low and it thus would not inhibit leaching due to the formation of $PbSO_4$.

3.1.2. The parameters of the leaching process for Nongson Basin uranium deposits treatment by using three leached methods: agitation leaching, strong acid pugging and curing and heap leaching were studied and identified.

Ore leaching by agitation method:

Effect of parameters such asparticlesize, pH, leaching time, oxidation consumption (using different oxidants MnO_2, H_2O_2, $KClO_3$), temperature on uranium leaching efficiency were studied.

From obtained experimental data, the optimum conditions for Nongson Basinuraniumdepositsleaching by agitation method were determined as follows: particle size:<75 µm, liquid/solid ratio of 1:1 (vol./wt.), leaching time from 8 h – 24 h upon every deposit, agitation rate: 200 rpm, oxidation reduction potential level of 500 mV (requeired 2 – 4 kg of oxidant/ton of ore), pH 1 (Acid consumption from 25 – 45 kg/ton of ore), temperature30^{o}C. Under the selected optimum condition, the uranium leaching efficiency is reached95 - 97%.

The parameters of the leaching are depended on the type of ore (weathered, semi-weathered and non-weathered) and on each ore deposits (Pa Lua - Pa Rong, KheHoa - He Cao, An Diem And South East Ben Giang).The results showed that when treatment of uranium ore in Tabhing area, the leaching conditions must be stronger than that in KheHoa - Khe Cao and Pa Lua - Pa Rong area. In order to achieve higher uranium removal efficiency, the pH = 0.9 and the leaching time must be up to 14h; the acid consumption is also higher.

Strong acid pugging andcuring:

Effect of parameters such as curing time, washing flow rate, sulfuric acid consumption on efficiency of non-weathered and semi-weathered uranium ore leaching…were studied.

Based on experimental results, the appropriate conditions for operation are as follows: size of ore particles <1 cm, curing duration 2 -3 days, oxidant 3 - 4 kg/tonne of ore, leaching time depend on ore mass, acid consumption 30 -31.5 kg/tonne of ore. The leaching efficiency is reached more than 83%.

Heap leaching:

The effect of parameters such as particlesize, sulfuric acid concentration of spray solution….temperature on uranium leaching efficiency was studied.

Based on experimental results, the appropriate conditions for operation are as follows: Ore size < 1 cm, agglomeration: ratio 20 kg acid H_2SO_4/ton of ore,acid consumption (total): 35 - 38 kg/ton of ore, oxidation MnO_2: 4 kg/ton, concentration of H_2SO_4: 50 g/L,rate of spraying acid solution: 15-20 l/m^2.h, U leaching efficiency > 80%.

3.1.3. The comparison of agitation, strong acid pugging and curing and heap leaching methodswasconducted.

The comparison of main leaching parameters for the three methods:agitation, strong acid pugging and curing and heap leaching was studied.

Table 1: The comparison of three leaching methods

Leaching method	Ore particle size, cm	H_2SO_4consumption, kg/tonne ore	MnO_2addition, kg/tonne ore	Curing time, d	Uranium extraction efficiency, %
Agitation	≤ 0.0074	50.1	4	-	95.3
Strong acid pugging and curing	≤ 1	31.5	4	2	83.5
Heap leaching	≤ 1	40.0	4	-	80.5

The experimental results show that Palua-Parong uranium ores can be treated by all three methods with the uranium leaching efficiency reaching >80%. The uranium leachingefficiency using an agitation method was better than by the others, but the H_2SO_4 consumption for this method was also higher.

Technological disadvantages of the agitation method in comparison with the two other methods include: consumption of more energy for crushing and grinding uranium sandstone ores to particle size $\leq$ 75 µm, and the need for a solid-liquid separation process.Uranium losses due to incomplete washing can further reduce the operating profits.

The strong acid pugging and curing method has the industrial disadvantage in comparison with heap leaching, that it is necessary to mix the ore with concentrated acid, consuming energy and requiring investment in the mixing equipment. By comparison, heap leaching is an advantageous technology in offering a relatively low capital cost for recovering uranium from low grade ores, without a mixing stage. This method was thus proposed as the most suitable method for uranium sandstone ore from the Nong Son Basin area.

3.1.4. Solid – liquid seperation process in the case of using agitation leaching method was studied

- To separate solid-liquid phases of leaching solution, following methods were used: sedimentation, centrifugation, and filtration. In some cases, the coagation agents were used such as FA.920 with the amount of 100g -168 g/ton of ore and sedimentation rate of 0.35m/h; washing speed of 900kg/m^2.h. Efficiency of filterationreached 99.29%.
- The uranium content in leaching solution is 0.1 g/L to 1 g/L

3.1.5. The concentration and purification of uranium leaching solution by ionexchange and solvent extractionwasinvestigated

In order to clarify the leaching solution, the ion exchange process was applied with ion exchange resins Amberlite 420 and GS300 and using column ion – exchange tests with the conditions as following:

- pH of leaching solution: 1.6 – 1.8 (pH of leaching solution was adjusted by NaOH).
- Feed solution temperature: 25^0C.
- Flow rates of adsorption - 5 bed volum (BV/h) (Retention time in resin bed = 5 min).

After the adsorption period was completed, the residual feed solution was washed from the resin bed by passing deionized water through at the rate of about 5 BV/h until pH of effluent was about 3.5.

Elution - regeneration: uranium was eluted from the resin bed by passing eluant (mixture of 0.9 M NaCl and 0.1 M HCl) through at a rate of 2.5 BV/h (Retention time in resin bed = 10 min.). The concentration of uranium and iron of elution - solution was 8.5 g/L and 0.75 g/L, respectively.

In the same experimental conditions, uranium loading of Amberlite IRA-420 resin is higher than that of INDION GS300 resin. At pH = 1.6, the uranium loading capacity of INDION GS300 was approximately 85% that of Amberlite IRA-420 resin.

3.1.6. Precipitation of yellowcake productwasconducted

The eluted solution obtained from ion exchange process was used to precipitate yellowcake product. Although the iron was largely eliminated from the ion exchange process due to the anionite resin usage, the concentration of iron was still too high (0.75g/l) to directly precipitate because the product would not meet the standard on iron content.

Therefore, it was needed to have a neutralization stage to get the pH to about 3.8 in order to remove more iron before precipitating product.

In terms of precipitation agent, MgOwas selected. The precipitation conditions were as follows: pH = 7.0-7.2 and temperature 60^0C.

3.1.7. The flow sheet for Nong Son Basin uranium oretreatment were selected

n the basis of the technical evaluation of experimental parameters at larger scale for the leaching methods described previously, and from the analysis of the advantages of the heap leaching method, the flow sheet given in Fig.2 was selected for technological treatment of Palua - Parong low grade uranium sandstone ores.

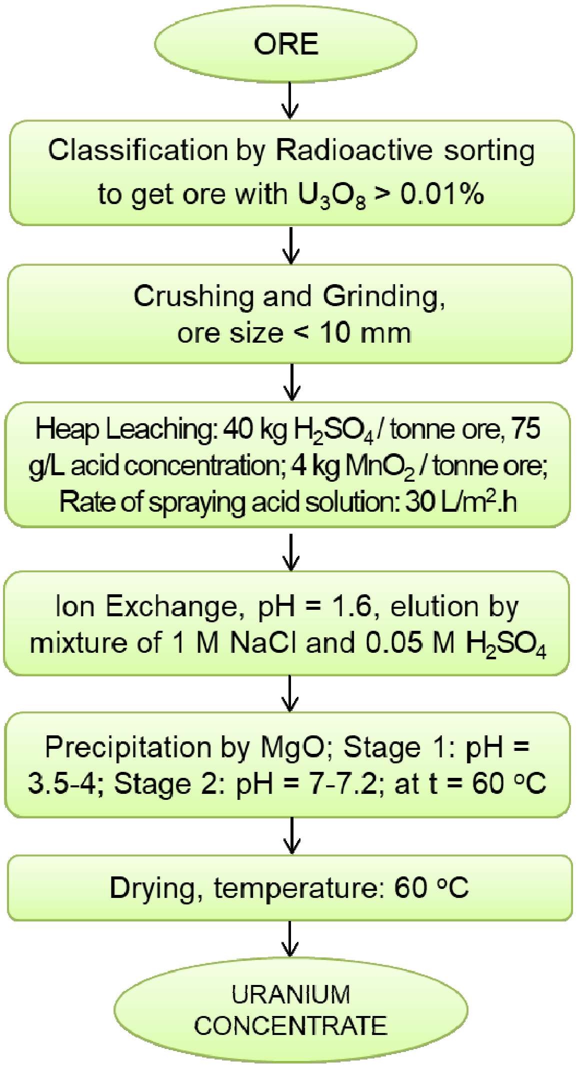

Figure 2: The proposed flowsheet diagram for Palua-Parong uranium ore treatment by heap leaching

3.2. Results of additional research

3.2.1. Study on identification of water retention capacity of uranium ore

The water retention capacity of bother non – weathered and semi – weathered uranium ores were studied. Experimental results showed that the water retention capacity of the ore depends on ore size and the type of the ore.From experimental results, a mathematical model that demonstrated the relationship between the water retention capacity of the ore and ore particle size was established.

For non-weathered ore: $y = 42.181^{e}-0.8447x$

and for semi-weathered ore: $\mathbf{y = 41.473^{e} - 0.7268x}$

Where y: The water retention capacityof ore and x: ore particle size

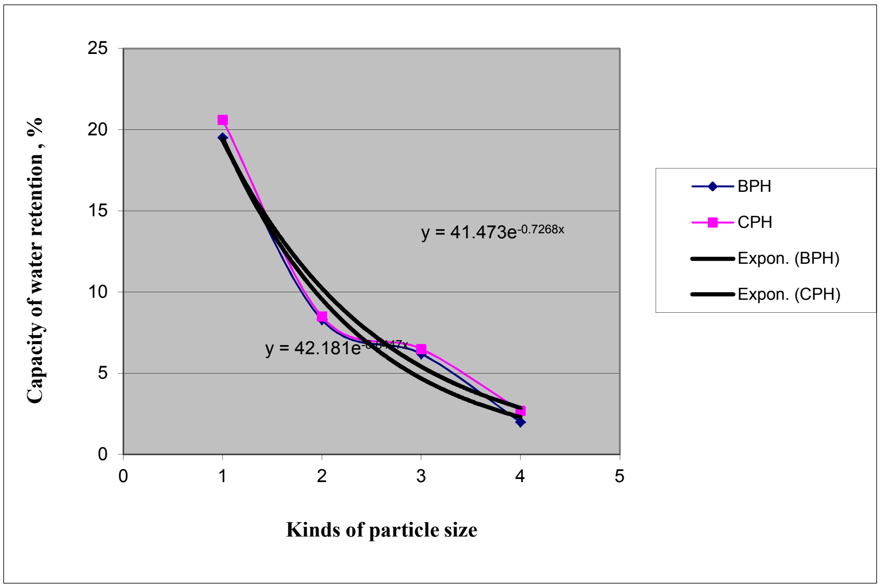

Figure 3: Relation of water retention capacity and ore particle size

3.2.2. Study the effect of of irrigation flow rate on leaching uranium efficiency when using heap leaching method

The effect of irrigation flow rate on leaching uranium efficiency for weathering agglomerated uranium ore and for agglomerated of fine-grained part of weathering uranium ore as well as for semi – weathered orewere studied. The results are shown in fig.4, 5, 6, 7.The results showed that for both types of ore, the appropriate irrigation flow rate was 30 L / m2.h.

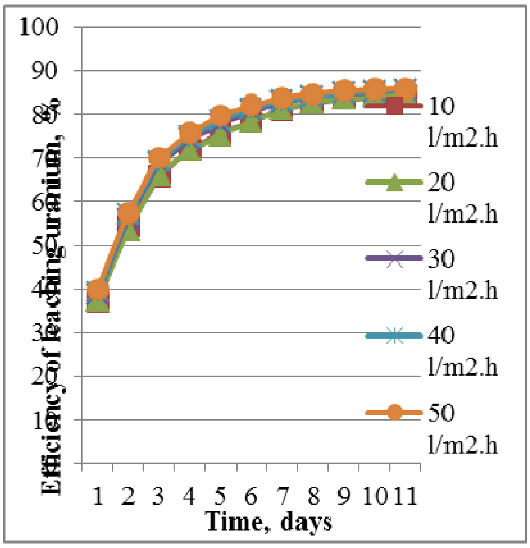

Figure 4: The effect of irrigation flow rate on leaching uranium efficiency for weathering agglomerated uranium ore

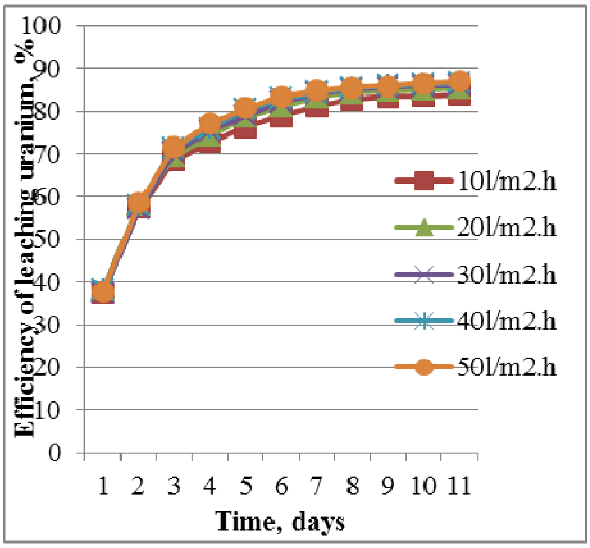

Figure 5: The effect of irrigation flow rate on leaching uranium efficiency for agglomerated of fine-grained part of weathering uranium ore

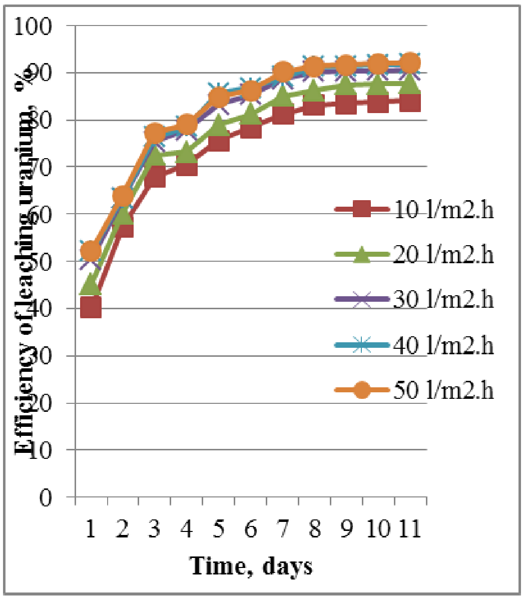

Figure 6: The effect of irrigation flow rate on leaching uranium efficiency for semi -weathering agglomerated uranium ore

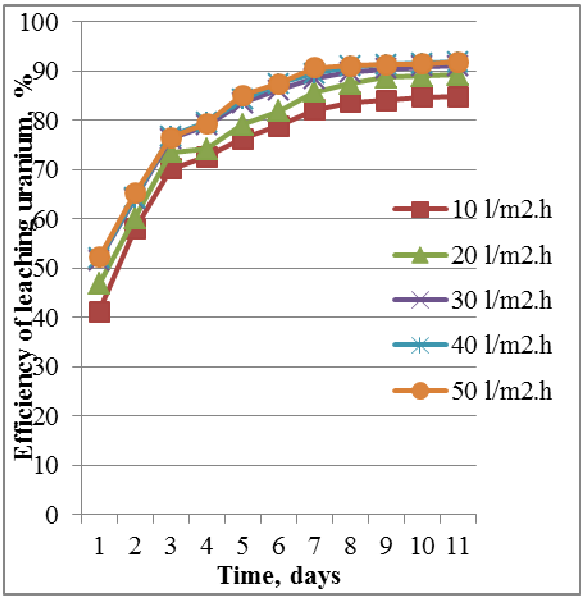

Figure 7: The effect of irrigation flow rate on leaching uranium efficiency for agglomerated of fine-grained part of semi - weathering uranium ore

3.2.3. The results of treatment uranium ore containing U_3O_8 of 1.188% by agitation method.

The experimental results were shown in fig.8,9,10,11.

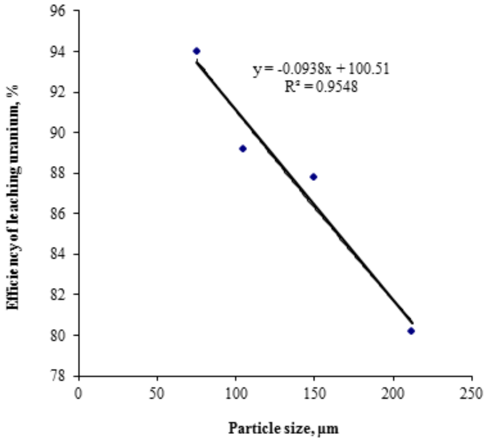

Figure 8: Effect of particle size on leaching uranium efficiency

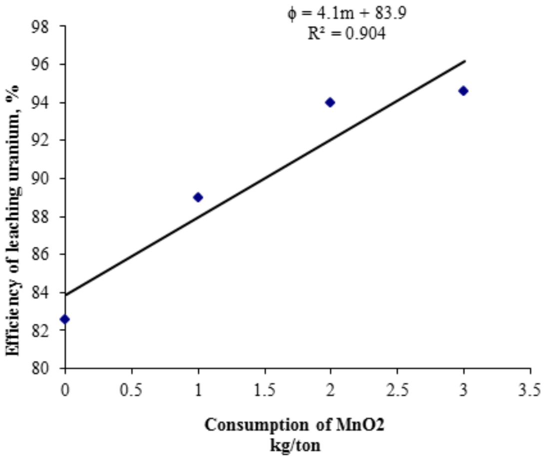

Figure 9: Effect of consumption of MnO_2 on leaching uranium efficiency

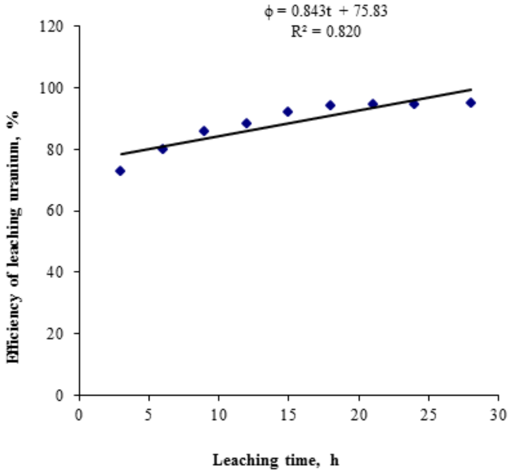

Figure 10: Effect of leaching time on leaching uranium efficiency

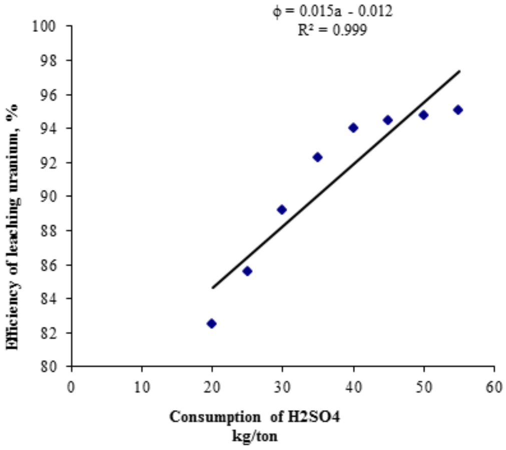

Figure 11: Effect of consumption of H_2SO_4 on leaching uranium efficiency

Based on experimental results, the suitable parameters of the leaching process were indentified and they are as follows: Particle size ≤75µm; consumption of sulfuric acid H_2SO_4: 40 kg/tonne of ore; consumption of MnO_2oxidant: 2 kg/tonne ore; leaching time: 18 h; the uranium leaching efficiency is (94 ± 3)%.

3.2.4. The research results of urranium extraction from leaching liqour by solvent extraction method using TOA

Effect of parameters such as shaking time, pH, SO_4^{2-} concentration, aqueous and organic ratio on uranium extraction efficiency were studied. The results were shown in fig.12, 13,14.

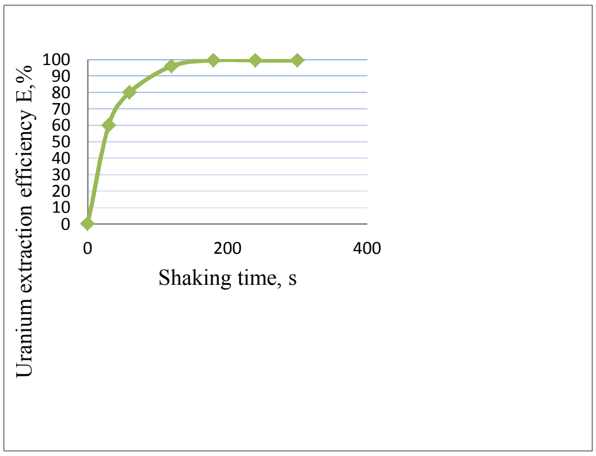

Figure 12: Effect of shaking time upon uranium extraction efficiency (Solvent conc.of 5% TOA, 5% n-decanol in kerosene)

+ Effect of acid concentration:

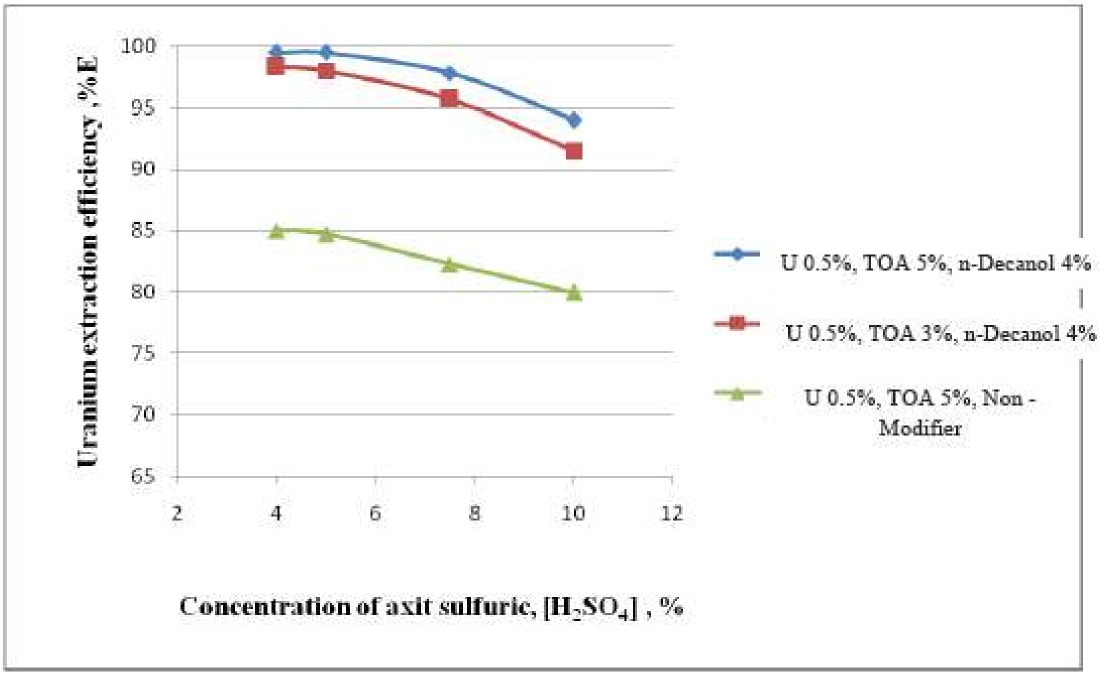

Figure 13: Effect of pH on uranium extraction efficiency

+ Effect of SO_4^{2-}concentraion in aqueous phase:

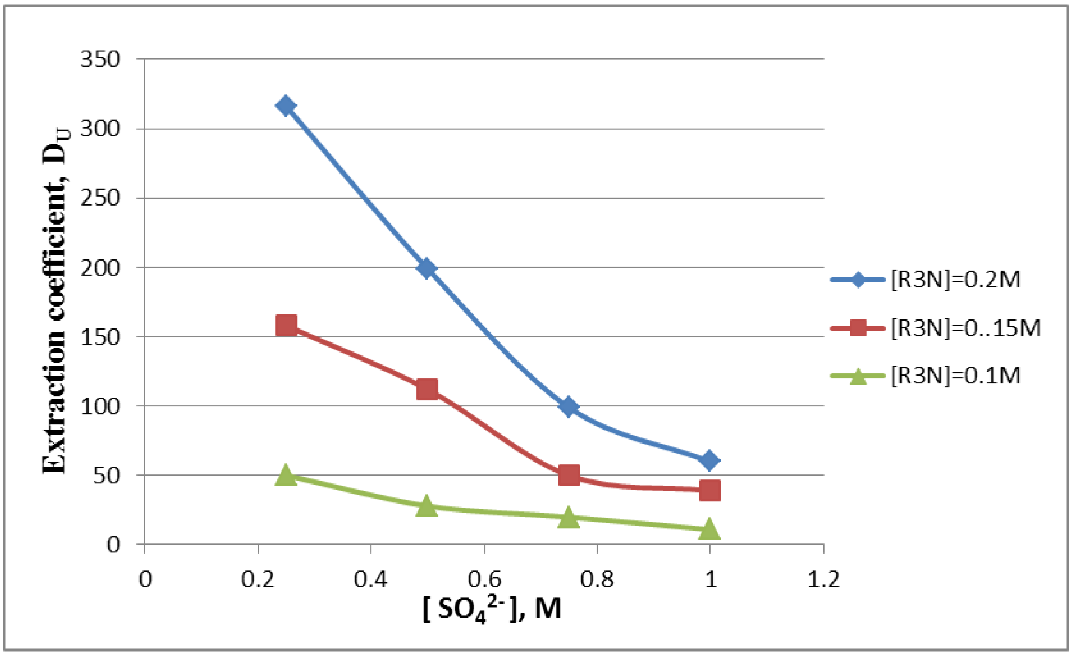

Figure 14: Effect of SO_4^{2-} concentration on uranium solvent process

Effect of V_{aq}/V_o ratio

Effect of aqueous (Vaq) and organic (Vo) phases ratio on uranium extraction.

Effect of aqueous (Vaq) and organic (Vo) phases ratio on uranium extraction is shown in Figure 6. The experimental results show that, the uranium extraction efficiency is decreased with increasing Vaq / Voratio.However, when U content and acidity in the solution are low, the extraction efficiency is still over 90%, so the extraction of uranium from the solution with low uranium content is effective when applying the Vaq / Vo phase ratio > 1.

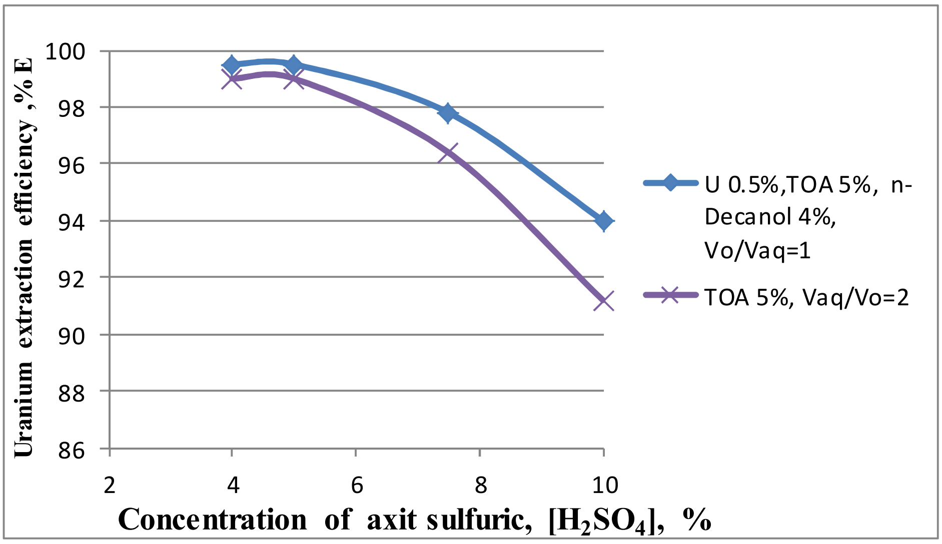

Figure 15: Effect of aqueous and organic ratio on uranium extraction efficiency

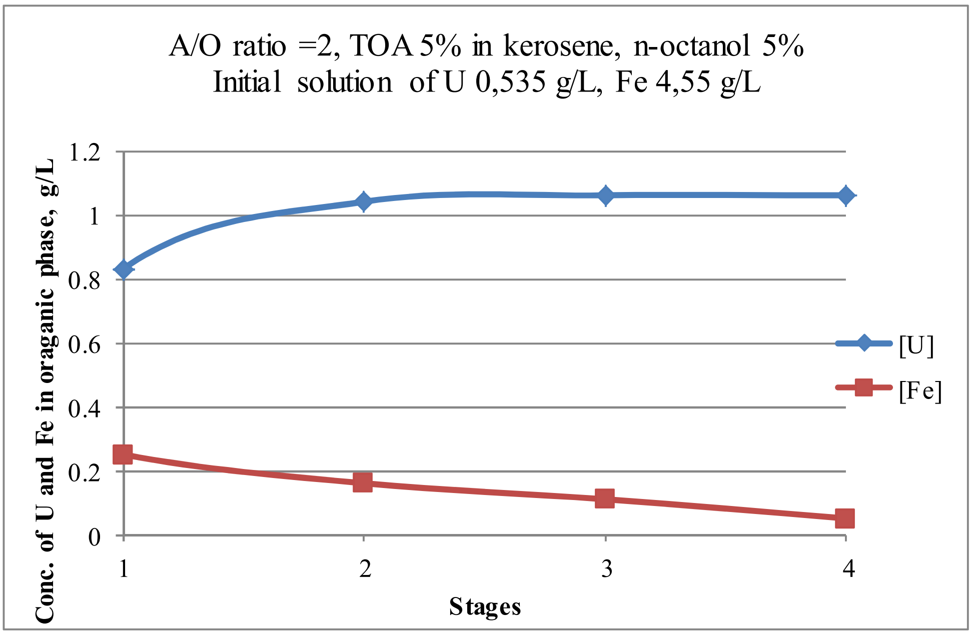

Figure 16: The efficiency of Uranium and Iron extractions

Continuous solvent extraction

A diagram of the continuous uranium reclamation process is shown in Fig.17.

Based on the factors affecting the extracting process, 4 - stages of extraction and 3 - stages of stripping were used.Initial uranium solution with the main components [U] = 0.535 g / L, [Fe] = 4.55 g / L, pH = 1.

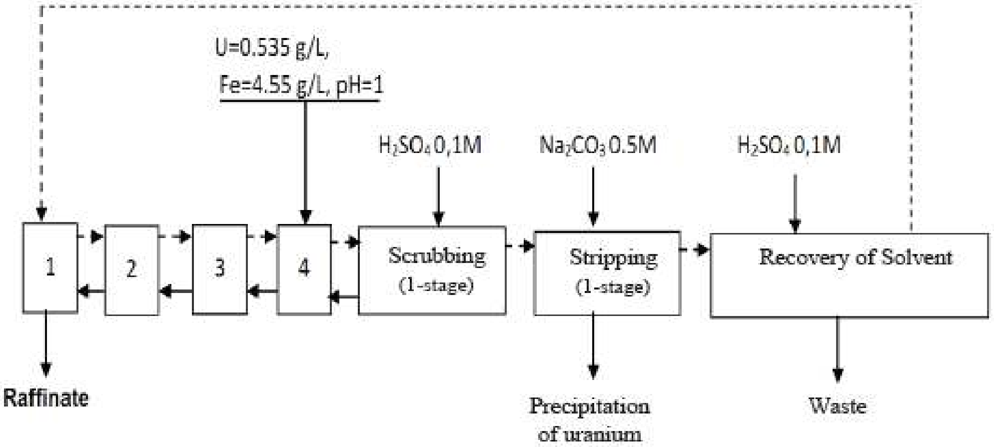

Figure 17: Diagram of 4 stages counter-current extraction process

The experimental results show that, solvent extraction process consists of 4 stages extraction, aqueous/organic ratio = 4/1 in the case of extraction and aqueous/organic ratio = ¼ in the case of stripping, the uranium extraction efficiency is reached 99,3%.The coefficient of uraniumenrichment is 13.12 times.

3.3. Proposed direction for research in the field of radioactive ore processing

- To study the technology for uranium extraction from new uranium occurrences and new uranium deposits which discovered by uranium exploration activitiesin order to serve the assessment of uranium resources at a reliable level and developing uranium extraction technology.
- To study and complete the technology for uranium extraction from different types of sandstone ores in the Nong Son basin at pilot scale.
- Todeeplystudy all stages of uranium ore treatment technology, especially the heap leaching methodfor uranium low grade treatment (continuous ion exchange, solvent extraction in pulp…)
- To study the application of software in the uranium ores processing in order to reduce the cost and time of experimental research.
- To research, design, fabrication and testing of equipment such as radioactive floatation equipment, ion exchange system, continuous extraction system, etc on pilot scale.
- To study the economic and technical efficiency of uranium ores treatment on pilot scale and assessment the uranium resource in Nong Son area.
- To evaluate the thorium potential and research on the recovery of thorium from different ore sources in Vietnam.
- To participate in cooperation research project of radioactive ore processing in IAEA framework.

CONCLUSIONS

The work being done in this project achieved the aims as follows.

The reviewing, analyzing and evaluating the results of previous research projects, concerning Nong Son Basin uranium ore processing were completed.

The research, which was carried out in the area of Nongson Basin uranium ore treatment achieved the following results:

- Obtained data of research projects contributed to the assessment of uranium resources in Vietnam;
- A series of data on petrology, mineral compositions, chemical compositions, uranium distribution in ore, ...of Nongson Basin uranium deposits were obtained;
- A system of relatively complete data of all stages of technology for uranium ore treatment at the laboratory scale and at the post-laboratory scale was obtained;
- A number of technological processes for uranium extraction from Pa Lua - Pa Rong, KheHoa - Khe Cao, An Diem,and South East Ben Giang uranium deposits (agitation, mixing and curing, heap leaching methods) on laboratoty scale and pilot scale were developed and tested;
- Some specialized equipment for uranium ore processing technology (heap leaching system, ion exchange system, equiment for uranium ore agglomeration,…) were designed and manufactured;
- The technology of heap leaching was selected and proposed as only suitable technological process for Pa Lua - Pa Rong ore processing;
- The entire uranium production technology was successfully tested to obtain yellowcake product from the Pa Lua sandstone in pilot scale (capacity> 20 tons / batch). The cost of yellow cake was approximately estimated of $60 / kg;

- The research direction in the field of radioactive ore processing was proposed.
- Additional research contents were completed. The effect of parameters such as ore particle size, leaching time, acid consumption, oxidant consumption on uranium leaching efficiency was investigated.
- The project products consisted of 01 accepted overviewing reports, 02 report papers in processding of International conferences, 02 published paper on journal of science and tachnology (in Vietnamese), 01 solvent extraction procedures for uranium extraction from leaching solution, 01 presentation in the 12nd National Conference of Nuclear Science and Technology (Nha-Trang 4-6 Aug., 2017),01 doctor thesis and 01 completed master thesis with the support from this project in the aspect of scientific content.

REFERENCES

Vietnamese documents

[1] Thai Ba Cau, Research on uranium production process and its byproducts from Tien An graphite ore, State-level scientific and technological project, 50B-02-01, 1986-1990.

[2] Than Van Lien (2013), Technological sampling of uranium receivers, Final report on scientific and technological tasks of State level 2012, Hanoi.

[3] Cao Hung Thai (2001), Research on the improvement of technical uranium processing technology from Pa Lui An Diem ore, Ministerial-level scientific research report, Institute of Atomic Energy Research - Institute of Atomic Energy Vietnam, Hanoi.

[4] Cao Dinh Thanh (1995), Complete the technological process of uranium ore hydration equipment and study the possibility of purification to direct nuclear purity from hydrated solution. Water, Institute of Radioactive Technology - Institute of Atomic Energy Vietnam, Hanoi.

[5] Le Quang Thai (2011), Finalize the process of testing technology and equipment for uranium from Pa Lua ore mine by mixing and ion extrusion technology, Final Report on Ministry Science and Technology , Institute of Radiation Technology, Vietnam Atomic Energy Commission, Hanoi.

[6] Le Quang Thai (2015), research and design of sandstone ore pilot in Pa Lua - Pa Rong area, Ministry of Science and Technology, Vietnam National Institute of Atomic Energy, Hanoi.

[7] Do Quy Son (2006), Reviewing and evaluating the results of R & D activities on nuclear fuel in Vietnam, Ministry of Science and Technology, Institute of Atomic Energy Research Institute Vietnam, Hanoi.

Enghlish documents

[8] Edwards CR, Oliver AJ. Uranium processing: a review of current methods and technology, JOM., 2000;52:12–20.

[9] IAEA, Manual on Laboratory Testing for Uranium Ores Processing, Austria, 1990.

[10] Merritt R.C., The Extractive Metallurgy of Uranium, First printing, Library of Congress Catalog Card No. 71-157076, , USA, 1971.

[11] D.C. Seidel, Laboratory Procedures for hydrometallurgical Processing and waste – Management Experienments, United States department of the interior.

[12] World Uranium Mining 2016. http://www.world-nuclear.org/(accessed 9 Mar.2018).

STUDY ON SET-UP STATISTICAL MODEL TO OPTIMISE THE AGGLOMERATION PROCESS FOR APPLICATIONS IN HEAP LEACHING OF URANIUM ORE

Tran The Dinh, Than Van Lien, Pham Minh Tuan, Pham Thi Thuy Ngan and Le Thi Hong Ha.

Institute for Technology of Radioactive and Rare Elements
48 Lang Ha, Dong Da, Hanoi

Project information:

- **Code:** CS/18/03-01
- **Managerial Level:** Institute
- **Allocated Fund:** 90,000,000 VND
- **Implementation time:** 12 months (Jan 2018- Dec 2018)
- **Contact email:** tranthedinh0802@hotmail.com
- **Paper published in related to the project:**

1. Tran The Dinh, Than Van Lien, Pham Van Thiem, 2019. Study on set-up statistical model to optimize the agglomeration process for applications in heap leaching of uranium ore. *Vietnam Journal of Science and Technology*, (ISSN 1859 – 4794), 3B/2019, p. 48-52 (In Vietnamese).
2. Tran The Dinh, Than Van Lien, Pham Thi Thuy Ngan, Le Thi Hong Ha, 2018. Study on set-up statistical model to optimize the agglomeration process for applications in heap leaching of uranium ore. *The 5th Conference of Nuclear Science and Technology for Young Researchers,* October 2018, Hanoi, Vietnam.

Abstract: The project has studied and developed the agglomeration method for low - grade uranium ore by combining two techniques of mixing – curing and percolation leaching in heap leaching method. From the research results, the authors have selected the appropriate factors effecting agglomeration process for weathered and semi-weathered ores: H_2SO_4 consumption, H_2SO_4 concentration and moisture of ore. Next, set-up statistical model to optimize the agglomeration process for uranium ore in Pa Lua - Pa Rong area from experimental data in heap leaching for weathered and semi-weathered uranium ores has been carried out. The research of the project contributes to the development and application of the heap leaching method for Vietnamese uranium ore using the agglomeration process of input ore to improve the permeability of ore, increase the stability of heap, improve the efficiency of uranium recovery and finally minimize the uranium content in ore tailing.

Keywords: *Uranium ore, agglomeration process, statistical model, heap leaching.*

I. INTRODUCTION

The agglomeration process, commonly applied to the treating process of fine-particles and clay ore. The factors that influence the agglomerate process are ore particle characteristics before agglomeration, acid concentration and acid consumption, ore moisture, etc. [13.23].

The agglomeration is a process fine particles are attached to the coarser particles or bonded together to form coarser particles during the agglomeration by mixing the ore with water, leaching agent and an agglomerating agent (binder). Permeability (permeability coefficient) is one of the most important parameters in heap leaching.It is the particle bed's ability to allow water to flow through voids. The permeability coefficient can be determined in the laboratory using falling head permeability test, and constant head permeability test. Agglomeration equipment mixes the ore with water, leaching agent and an agglomerating agent.

The goal of agglomeration process is making particles larger, more uniform, able to withstand compressing force but having good permeability to ensure the washing process is not restricted by clogging. Ore particles must be stable in acid leaching environments and the achieved uranium recovery efficiency must be acceptable.

The agglomerated ore is heaped and leached by the heap leaching method. In this way, the initial acid solution is mixed well with the ore particles, furthermore the reaction products of minerals and acid and hydration to make fine particles adhesive to larger particles to form aggregated particles relatively equal to increase significantly uranium recovery efficiency [11].

From the above analysis, the goal of the project is to set-up a model of agglomeration process for heap leaching of uranium ore which can be applied to calculate the scale changing and control well agglomeration process, aiming to build a comprehensively technological process for processing of uranium ore.

II. EXPERIMENTALS

2.1. Materials, chemicals and equipments

- Uranium ore in Pa Lua - Pa Rong area (Quang Nam) was taken and processed to the appropriate size or the treatment process using heap leaching method. The ores used in research experiments are weathered and semi-weathered ore.
- Chemicals were used: 98% H_2SO_4 acid (Technical, Vietnam) and 85% MnO_2 (Technical, Vietnam).
- Beside on agglomerator equipment, other equipments and tools also were used such as Hoa Phat jaw crusher (Vietnam), Chinese jaw crusher, shaft threshing machine, disc fastener, crusher, sample mixer (US), containers, ducts, solution pumps with speed regulators No.7553-75 (Cole-Parmer-USA), pH meter 540 GLP (WTW-Germany), redox oxidation meter, ...
- The process was implemented by ore heap leaching. The technological parameters for testing experiments on the PVC column system were as follows: D_ column = 0.075 m, H = 0.37 m; v = 0,105 m, H = 1,0 m; D_ column = 0.2 m, H = 2.0 m.

2.2. Method of study

- Surveying the agglomeration process;
- Heap leaching of agglomerated uranium ore;
- Set-up statistical model of the agglomeration process for uranium ore in Pa Lua - Pa Rong area;
- Testing the statistical model.

III. RESULTS AND DISCUSSION

3.1. Determination of permeability of Pa Lua - Pa Rong uranium ore.

For the heap leaching process, the permeability and water retention capacity of ore were the decisive factors for the whole process, so it is important to determine the physical characteristics of ore depending on different particle sizes. The particle size and permeability of ore have a great influence on water retention capacity of the ore

Using automatic calculation techniques by Add Trendline tool in Microsoft Excel, the experimental relations of water retention capacity depending on different particle sizes have been shown in Table 3.1 and Figure 3.1.

With semi-weathered ore: $y_{semi\text{-}weathered} = 39.72\ e^{-0.71x}$ [3.1]

and weathered ore: $y_{weathered} = 36.55\ e^{-0.63x}$ [3.2]

From the above experimental results about water retention capacity of each particle size, combined with weight ratio of each particle size in the experimental samples, water retention capacity of each sample can be preliminarily calculated and determined (see in Table 3.2, 3.3)

3.2. Set-up statistical model to optimise the agglomeration process for application of heap leaching of uranium ore

There are many factors that affect the agglomeration process of uranium ore including: characteristics of ore, particle size, binder used for agglomeration process, consumption of binder, binder concentration; rotation speed of agglomerator, ...

The following section presents the study results of the agglomeration process of Pa Lua - Pa Rong uranium ore, focusing on studying the effects of binder consumption and concentration (herein, used binder was sulfuric acid), the moisture of ore on the permeability (permeability coefficient k) of ore. The binder in agglomeration process enhances the bonding of particles by chemical or physical ways, which is resistant to acidic environments. For acidic environment, sulfuric acid is often used as a binder. The advantage of using concentrated sulfuric acid during the agglomeration process is to pre-distribute the solution to ore body. This often increases initial reaction rate and leaching efficiency. At that time, the initial acid solution was mixed well with ore particles, furthermore the reaction products of minerals and acid and hydration to make fine particles adhesive to larger particles to form aggregated particles relatively equal.

3.2.1. The effect of some factors in weathered ore agglomeration process on the permeability (permeability coefficient k) of ore

a. The effect of acid consumption in agglomeration process on the permeability (permeability coefficient k) of ore

Weighing 10 kg of processed ore (0,0309 % U), adding 85% MnO_2 (4 kg/ton), then mixing well. The experiments were carried out with varying consumptions of acid: 10, 15, 20 kg H_2SO_4/ton of ore; acid concentration 250 g/l; ore moisture of 8%.

After completing agglomeration process, the experiments were carried out under pressure condition, the water level in the pressure gauge was $\Delta H = 25$ cm, the height of ore column $l = 15$ cm, the area of sample section $\omega = \pi.4^2$ (cm^2) ($R = 2$ cm). The relation between flow and permeability coefficient k was showed by the following formula: $Q = k.\Delta H.\omega / l$.

The results showed that with acid consumption of 20 kg/ton of ore (for the agglomeration stage), the highest permeability coefficient k was achieved 0.0003 cm/s (Table 3.4).

b. The effect of acid concentration for agglomeration process on the permeability (permeability coefficient k) of ore

The results showed that with acid concentration of 300 g/l, the highest permeability coefficient k of 0.00044 cm/s was achieved (Table 3.5).

c. The effect of ore heap moisture for agglomeration process on the permeability (permeability coefficient k) of ore

The results showed that with the ore moisture of 10%, the highest permeability coefficient k of 0.00046 cm/s was achieved (Table 3.6). At this value, the ore heap was wetted out, the phenomenon of pasty didn't occur and the particles size was equal.

3.2.2. The effect of some factors in semi-weathered ore agglomeration process on the permeability (permeability coefficient k) of ore

a. The effect of acid consumption for agglomeration process on the permeability (permeability coefficient k) of ore

Weighing 10 kg of processed ore (0,0905 % U), adding 85% MnO_2 (4 kg/ton), then mixing well. The experiments were carried out with varying consumptions of acid: 10, 15, 20 kg H_2SO_4/ton of ore; acid concentration 250 g/l; ore moisture of 8%.

The results showed that with acid consumption of 20 kg/ton of ore (for the agglomeration stage), the highest permeability coefficient k of 0.01967 cm/s was achieved (Table 3.7).

b. The effect of acid concentration for agglomeration process on the permeability (permeability coefficient k) of ore

The results showed that with acid concentration of 250 g/l, the highest permeability coefficient k of 0.01672 cm/s was achieved (Table 3.8).

c. The effect of ore heap moisture for agglomeration process on the permeability (permeability coefficient k) of ore

The results showed that with the ore moisture of 8%, the highest permeability coefficient k of 0.01788 cm/s was achieved (Table 3.9).

3.2.3. Set-up statistical model of agglomeration process for uranium ore in Pa Lua - Pa Rong area

a. For weathered uranium ore

Problem: The permeability (permeability coefficient k) of ore in heap leaching process of weathered uranium ore depends on the following factors: Z_1 - acid concentration, g/l; Z_2 - acid consumption, kg/ton of ore; Z_3 - moisture, % in agglomeration stage.

For the purpose of studying the effects of three factors: H_2SO_4 acid concentration, H_2SO_4 acid consumption and moisture of ore heap, the number of experiments need to be done: $N = 2^3 = 8$ experiments.

Through the calculation steps, the regression equation was found to describe correctly experimental data as follows: $\hat{y} = 0,00028 + 0,00009^* x_1 + 0,00010^* x_3$.

From the regression equation above, the coefficients of b_0, b_1, b_2, b_3 were plus showing that it is necessary to increase the values of the optimization parameters of z_1, z_2 and z_3. Thereby, if continuing to increase acid concentrations and ore moistures, the permeability of ore will increase However, this was because of following reasons:

- Because consumption of acid and acid concentration affect the size distribution of particles formed when agglomerating ore. According to research works at the ITRRE, uranium absorption of ion exchange resin can be reduced by up to 30% or more when concentration of iron, silicon, sulfate were 9-10 g/l; 2 g/l; 100-120g/l respectively (adsorption of uranium reduced from 62-63 g/l to 42-44 g/l of resin) [1,2,5]. Therefore, it is necessary to select the appropriate acid concentration to avoid unnecessary acid consumption.
- The moisture depends on types of ores and composition of ore particles. When the moisture is low, it is difficult to supply solution for the ore heap. On the other hand, when there is

an excess of leaching solution, the phenomenon of particles remaining together occurs, affecting the heap leaching process. Therefore, it is necessary to select the appropriate moisture to the ore heap will be wetted out, the phenomenon of pasty didn't occur and paticle size was equal that do not affect the heap leaching process later.

b. For semi-weathered uranium ore

Problem: The permeability (permeability coefficient k) of ore in heap leaching process of weathered uranium ore depends on the following factors: Z_1 - acid concentration, g/l; Z_2 - acid consumption, kg/ton of ore; Z_3 - moisture, % in agglomeration stage.

For the purpose of surveying three influencing factors: H_2SO_4 acid concentration, H_2SO_4 acid consumption and moisture of ore heap, the number of experiments need to be done: $N = 2^3 = 8$ experiments.

Through the calculation steps, the regression equation was found to describe correctly experimental data as follows: $\hat{y} = 0{,}01742 + 0{,}00104^* x_1 + 0{,}00031^* x_2 + 0{,}00035^* x_3$.

Thus, based on the experimental results and published documents, the parameters for agglomeration stage were selected as follows: acid concentration of 250 g/l H_2SO_4, acid consumption of 20 kg H_2SO_4 /ton of ore and ore moisture of 8% for the highest permeability (permeability coefficient k) in order to be suitable for heap leaching process of sandstone uranium ore in Pa Lua - Pa Rong area, as well as the later process.

3.3. Testing the model on agglomerate equipment with capacity of 50 kg / hour

a. For weathered uranium ore

The experiments were carried out on the agglomerating equipment with capacity of 50 kg/hour and adjustable rotary speed. The experiments were conducted as follows: Weighing 100kg of processed ore to particles size <1cm (95%), adding 5% MnO_2 (4kg/ton), then mixing well. Conducting experiments with a rotary speed of 15 rounds per minute; 20kg/ton of acid consumption (only for agglomeration stage); Acid concentration of 300g/l, moisture of ore 10%.

The results of the permeability coefficient k of ore were presented in table 3.16.

Table 3.16: Testing the statistical model for weathered uranium ore

Ore	Flow rate (ml/s)	Permeability coefficient k (cm/s)
Weathered	1.46389	0.01748

After completing the agglomeration, taking 50 kg and proceeding to heap leaching of agglomerated uranium ore on the column. The result showed that the uranium recovery efficiency of 88.9% was achieved (see Figure 3.2).

b. For semi-weathered uranium ore

The experiments were carried out on the agglomerating equipment with capacity of 50 kg/hour and adjustable rotary speed. The experiments were conducted as follows: Weighing 100kg of processed ore to particles size <1cm (95%), adding 5% MnO_2 (4kg/ton), then mixing well. Conducting experiments with a rotary speed of 15 rounds per minute; 20kg/ton of acid consumption (only for agglomeration stage); Acid concentration of 250g/l, moisture of ore 8%.

The results of the permeability coefficient k of ore were presented in table 3.17.

Table 3.17: Testing the statistical model for semi-weathered uranium ore

Ore	Flow rate (ml/s)	Permeability coefficient k (cm/s)
Semi-weathered	1.46389	0.01748

After completing the agglomeration, taking 50 kg and proceeding to heap leaching of agglomerated uranium ore on the column. The result showed that the uranium recovery efficiency of 90.2% was achieved (see Figure 3.3).

Through empirical data, it has been shown that the first step regression equation was suitable for the experiments of agglomeration process of uranium ore, demonstrating the permeability (permeability coefficient k) of ore in the heap leaching process of uranium ore in Pa Lua - Pa Rong area depends on the factors: acidity; acid consumption, and moisture of ore.

The testing results showed that the permeability (permeability coefficient k) of ore and the efficiency of uranium recovery for each type of ore changed insignificantly when conducting experiments in the laboratory scale.

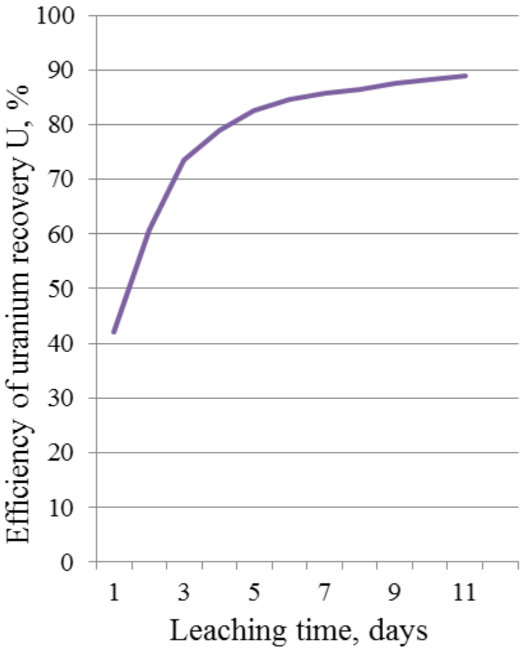

Figure 3.2: Testing the statistical mode for weathered uranium ore

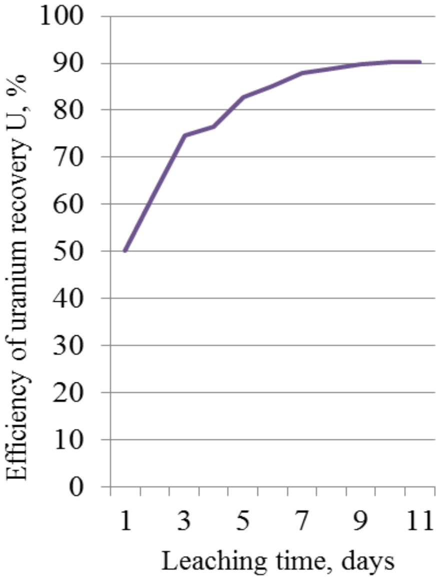

Figure 3.3: Testing the statistical model for semi-weathered uranium ore

*** Remark on the advantages and disadvantages of the two leaching methods on technological regime, quality of the solution:**

The experiments were are conducted for uranium ore in two options: *Non- agglomerated and agglomerated ores with heap leaching method*. The comparison results of process parameters were shown in Table 3.18 below

Table 3.18: Comparison of leaching process parameters for non- agglomerated and agglomerated ores by heap leaching method

Parameters	Non-agglomerated	Agglomerated
Original particle sizes, mm	≤ 10 (95 %)	≤ 10 (95 %)
Acid consumption of H_2SO_4, kg/ton of ore	50	40
Consumption of oxidant MnO_2, kg/ton of ore	4	4
Time of leaching, day	15	11
Uranium concentration in solution after leaching, g/l	0.7-11	0.8-1.4
Concentration of Fe in solution after leaching, g/l	8-11	8-10
Efficiency of uranium recovery, %	80.2	85.7

IV. CONCLUSION

1. From the experimental results, it is possible to predetermine some parameters for specific ores as follows: The volume of stored fluid solution was changed much, about 17-23% compared to ore layer volume.

The quantitative values of empirical relationship between water retention capacity and different particle sizes have been determined:

- For semi-weathered ore: $\mathbf{y= 39{,}72\ e^{-0{,}71x}}$

and For weathered ore: $\mathbf{y= 36{,}55\ e^{-0{,}63x}}$

The water retention capacity of ore between calculation value and actual value has the error of 1.4 - 9.9%.

The permeability coefficient for semi-weathered ore changed in the range: 0,01393 – 0,01967 (cm/s) and weathered ore changed in the range: 0,00009 – 0,00046 (cm/s) depending on particle sizes of ore.

2. The parameters affecting the agglomeration process of Pa Lua - Pa Rong uranium ore were studied and selected, using the binder agent of H_2SO_4 acid, as follows:

- For weathered ore: Acid consumption of 20 kg H_2SO_4/ton ore, acid concentration of 300 g/l, ore moisture of 10%.
- For semi-weathered ore: Acid consumption of 20 kg H_2SO_4/ton ore, acid concentration 250 g/l, ore moisture of 8%.

Through empirical data, a full first step regression equation was found to be consistent with the experiment for uranium ore agglomeration process, showing the the permeability (permeability coefficient k) of ore in the process of heap leaching for uranium ore in Pa Lua – Pa Rong area depends on the factors in the agglomerate stage. The following results as follow:

- Weathered ore: $\hat{y} = 0{,}00028 + 0{,}00009^{*} x_1 + 0{,}00010^{*} x_3$
- Semi-weathered ore: $\hat{y} = 0{,}01742 + 0{,}00104^{*} x_1 + 0{,}00031^{*} x_2 + 0{,}00035^{*} x_3$.

3. Testing the model experiment has been carried out on agglomerate equipment with capacity of 50 kg / hour for each type of weathered ore and semi-weathered ore:

- For weathered ore: Acid consumption of 20 kg H_2SO_4/ton ore, acid concentration of 300 g/l, ore moisture of 10%, rotary time of 10 minutes and rotary speed of 15 r/m.

- For semi-weathered ore: Acid consumption of 20 kg H_2SO_4/ton ore, acid concentration 250 g/l, ore moisture of 8%, rotary time of 10 minutes and rotary speed of 15 r/m.

Through empirical data, it has been shown that the first step regression equation is suitable for the experiment of uranium ore agglomeration process. The results showed that the permeability (permeability coefficient k) of ore and uranium recovery efficiency has changed insignificantly compared to the leaching in the laboratory.

4. In addition, experiments were also conducted compared to non-agglomerated ores, at 10 kg/batch scale. The results showed that the process of leaching for agglomerated uranium ore compared to the process of heap leaching for non-agglomerated uranium ore have the following advantages: better permeability; higher uranium recovery efficiency, lower acid consumption, no clogging, limited dust when wet ore was directly loaded into the column and tank; while the quality of the solution after the leaching hasn't changed much compared to the case of non-agglomerate ore. However, this process also has the disadvantage, as follows: higher the cost because of the agglomerator operation, taking longer time because uranium ore agglomeration stage must to be conducted before leaching.

REFERENCES

[1] Thân Văn Liên (2016), *Nghiên cứu cải tiến công nghệ xử lý quặng urani nghèo bằng phương pháp hòa tách thấm sử dụng quá trình agglomerat hóa quặng đầu vào*, Đề tài KHCN cấp Bộ, Viện CNXH - Viện NLNTVN.

[2] Phạm Quang Minh (2009), *Mô hình hóa quá trình hòa tách thấm quặng urani và ứng dụng để tính toán chuyển quy mô*, Luận án Tiến sỹ kỹ thuật, chuyên ngành quá trình và thiết bị công nghệ hóa học – Đại học Bách khoa Hà Nội.

[3] Lê Đức Ngọc (2011), *Nhập môn Xử lý số liệu và Kế hoạch hoá thực nghiệm*, Khoa Hoá học - Đại học Quốc gia Hà Nội.

[4] Cao Hùng Thái (2003), *Nghiên cứu xử lý quặng cát kết khu vực Pà Lừa với quy mô 2 tấn quặng/mẻ để thu sản phẩm urani kỹ thuật*, Đề tài KH&CN cấp Bộ, Viện CNXH - Viện NLNTVN.

[5] Adirek Janwong (2012), *The agglomeration of nickel laterite ore, Department of Metallurgical Engineering* - The University of Utah.

[6] Ataollah Nosrati, et al (2012), *Improving nickel laterite agglomerate strength for enhanced heap leaching,* Ian Wark Research Institute, University of South Australia, Mawson Lakes, SA 5095, Australia.

[7] Bouffard, S.C. (2008), "Agglomeration for heap leaching: Equipment design, agglomerate quality control, and impact on the heap leaching process", *Minerals Engineering 21*, 1115-1125.

[8] D.G. Dixon, L.L. Hendrix (1993), "A Mathematical Model for Heap Leaching of One or More Solid Reactants from Porous Ore Particles", *Metallurgical Transaction B*, Vol.24B, p.1087-1101.

[9] Emerence Hoummady, et al (2016*),* "Evolution of Structural and Physical Properties of Uranium-Ore Agglomerates During Heap Leaching", *Conference ALTA 2016*, At Perth, Australia

[10] Nikhil Dhawan, et al (2013), “Crushed ore agglomeration and its control for heap leach operations”, *Minerals Engineering,* 41, Complete, pg.53-70.

[11] Nneoma Ogbonna (2006), *Mathematical Modelling of Agglomerate Scale Phenomena in Heap Bioleaching*, Thesis presented for the degree of Masters in Applied Science in the Department of Chemical Engineering University of Cape Town.

[12] Thien Vethosodsakda (2012), *Evaluation of crushed ore agglomeration, liquid retention capacity, and colunm leaching*, Master of Science, Department of Metallurgical Engineering - The University of Utah.

STUDY ON MAGNESIUM PRODUCTION FROM THANH HOA DOLOMITE IN PIDGEON-TYPE REACTOR

Ngo Xuan Hung, Tran Xuan Vinh, Tran Duy Hai, Nguyen Huu Phuc,
Nguyen Huu Duc and Vu Thi Phuoc.

Institute for Technology of Radioactive and Rare Elements,
48 Lang Ha, Dong Da, Hanoi

Project information:

- **Code:** CS/18/03-04
- **Managerial Level:** Institute
- **Allocated Fund:** 80,000,000 VND
- **Implementation time:** 12 months (Jan 2018- Dec 2018)
- **Contact email:** manhhunghanoi@gmail.com
- **Paper published in related to the project:**

Ngo Xuan Hung. Hoan nguyen magie kim loai tu quang dolomit Thanh Hoa bang quy trinh Pidgeo. *Journal of Vinalab*. No.13 (Nov. 2018), pp. 6-11 (In Vietnamese).

Abstract: Magnesium is a light metal that is used in chemical and metallurgical industries. Dolomite, which is abundant in Vietnam, is the source for magnesium production. However, there is no research on the production of magnesium from the dolomite source in Vietnam so far. This work studies the production process of Magnesium from the dolomite source in Thanh Hoa, Vietnam, using the Pidgeon method with ferrosilicon as the reducing agent. The major composition of Thanh Hoa dolomite is $CaCO_3$ (Ca, Mg)CO_3. The content of MgO in dolomite is 23.0%; of CaO is 34.0%. Afer being calcined at 1000 ^oC for 5 hours to reduce CO_2 and water vapor, the contents of MgO and CaO increased up to 37.0% and 54.0%, respectively. Dolomite was then milled with ferrosilicon, thoroughly mixed, and briquetted. The dolomite briquettes were heated at 1000 – 1300 ^oC in a tube retort under vacuum condition for 4 hours to reduce MgO. The highest reduction efficiency was 84% when the ferrosilicon to dolomite ratio was 30%. The purities of magnesium after reduction and after refining were 94,3% and 98.7%, respectively.

Keywords: *Magnesium; dolomite; Pidegon; reduction; reduction efficiency.*

I. INTRODUCTION

Approximately, 80% of the world demand for magnesium is currently supplied by China and nearly 95% of primary magnesium output of China is produced using Pidgeon process mainly due to low labor and energy costs and environmental friendliness. The main scope of this research is to product magnesium metal from Thanh Hoa dolomite ore in the Pidgeon-type reactor.

II. EXPERIMENTALS

In the Pidgeon Process, magnesium metal was produced from dolomite under vacuum and high temperature conditions using ferrosilicon as a reducing agent. In this process, the finely crushed dolomite was feed into kilns to be calcined. Then, the calcined dolomite was pulverized in a mill prior to mixing with fine ferrosilicon particles. After mixing, the mixture of fine calcined dolomite and ferrosilicon were briquetted. Briquettes were put in the reduction furnace and then calcined. The reduction operation was a process of releasing magnesium as the vapor form, which condensed in the cooled end of the retort outside furnace wall. Finally, the magnesium was taken off the sleeves. The reactions of the whole Pidgeon process are as follows:

$$(CaCO_3.MgCO_3)_{(s)} + Heat = (CaO.MgO)_{(s)} + 2CO_{2(g)}$$

$$2(CaO.MgO)_{(s)} + Si(Fe) = 2Mg_{(g)} + Ca_2SiO_4 + Fe$$

The mass loss was measured and sample was taken and analyzed (Table 1)

Table 1: Chemical composition of dolomite and calcined dolomite

	Dolomite, % by weight	**Calcined dolomite , % by weight**
MgO	23.0	37.0
CaO	33.0	54.0

The ferrosilicon and calcined dolomite were accurately weighed (about 300 g in total with 30% FeSi), mixed and pulverized to 74μm in a ball mill. Then the mixture was pressed to produce briquettes of 18 mm in diameter and 25 mm in thickness using a hydraulic press with applied pressure of 30 MPa. The weight of the briquettes was then recorded prior to being put inside the retort.

The reduction process was shown in Figure 1. The system was made of 316 stainless steel tube and housed inside an electrically heated furnace.

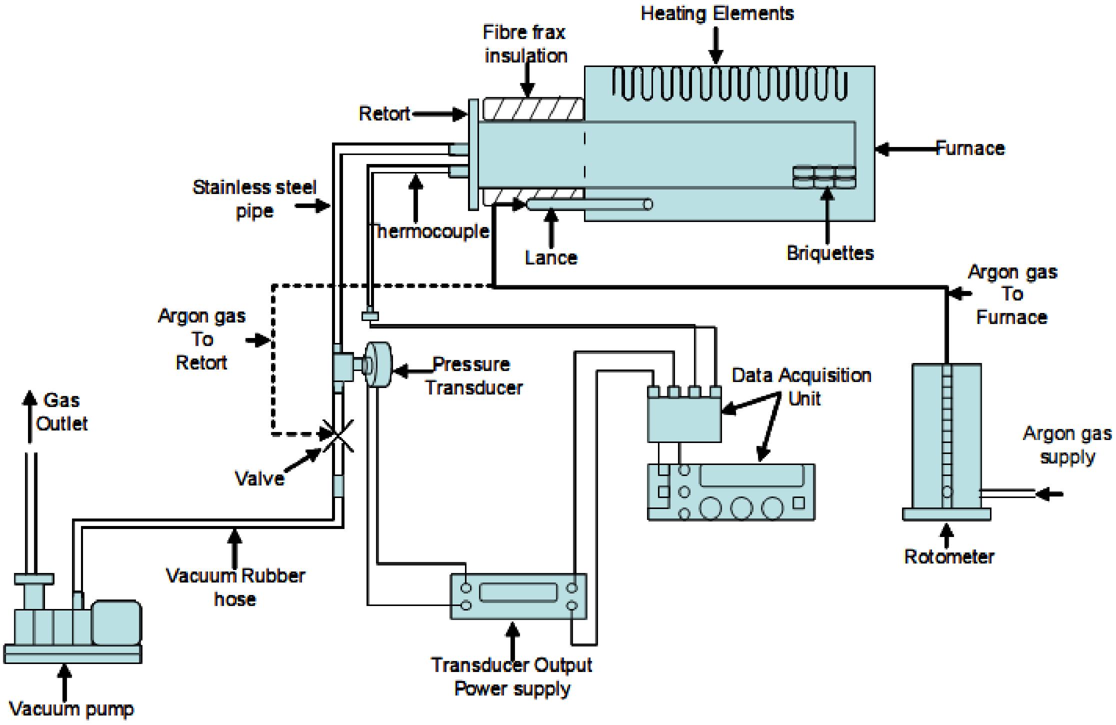

Figure 1: The diagram of experimental system

The retort contained a gas outlet, which was connected to a vacuum system. This system consisted of a vacuum pump, pressure transducer, pressure and temperature readouts, a shut-off valve and argon purge line. The thermocouple was used to measure and control the temperature.

After sealing, the retort was pressure-tested by applying vacuum of 500-700 Pa, switching off the vacuum pump. The retort was heated up to 700 °C over a hour period, followed by degassing any residual moisture and/or carbon dioxide that could have been present in the reactants, then the temperature was increased to 1150 °C over a three-hour period. The furnace was switched off, and the system pressure was brought up to just above atmospheric by flowing argon into the retort. Finally, the facility was allowed to cool down to near room temperature before opening the retort and collecting the products.

III. RESULTS AND DISCUSSION

After reduction, magnesium was collected and analyzed. Magnesium reduction yield was calculated based on the mass of magnesium content in briquette residua (slag) and calcined dolomite. The equation for calculation of magnesium reduction yield was as follows:

(Magnesium in feed – Magnesium in briquette residua) / Magnesium in feed (100%)

Where:

*Magnesium in feed = calcined dolomite mass * % Mg in calcined dolomite (by the weight)*

*Magnesium in briquette residua = Briquette residua mass * % Mg in Briquette residua (by the weight)*

Figure 2 has shown the effect of ferrosilicon contents on magnesium reduction yield when reduction temperature was 1200 °C. The maximum of magnesium reduction yield was 84 % and magnesium grade was 94.3 % in the experiment (with 30% ferrosilicon added). The reduction yield increased when ferrosilicon ratio increased. However, if there is too much ferrosilicon added, $MgSiO_3$ will be created and magnesium reduction yield will be decreased.

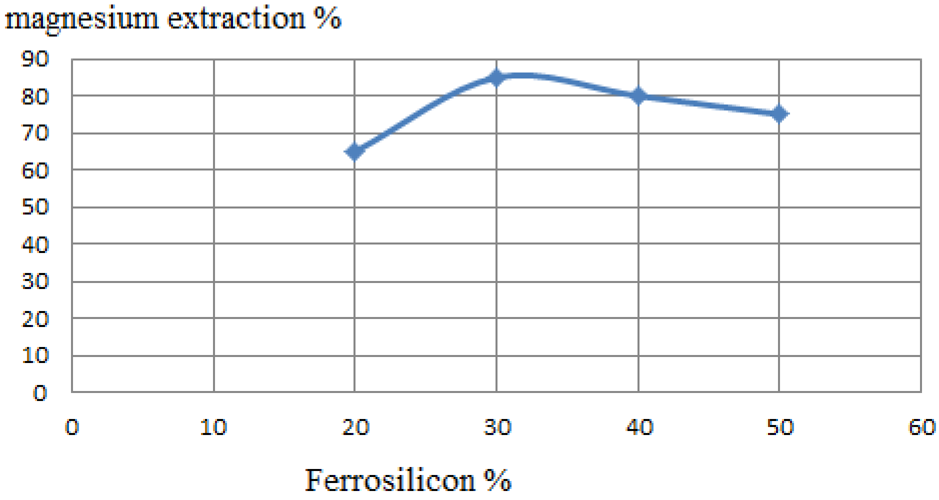

Figure 2: Effect of ferrosilicon contents on magnesium reduction yield

Figure 3 has shown the effect of reduction temperature on magnesium reduction yield with 30% ferrosilicon added. The performance increased from 70% at 1000 °C to 84% at 1200 °C and then remained when increasing temperature. The reduction reaction can occur when the temperature was less than 1000 °C, but reduction process was really effective when the reduction temperature was more than boiling temperature of magnesium (1080 °C).

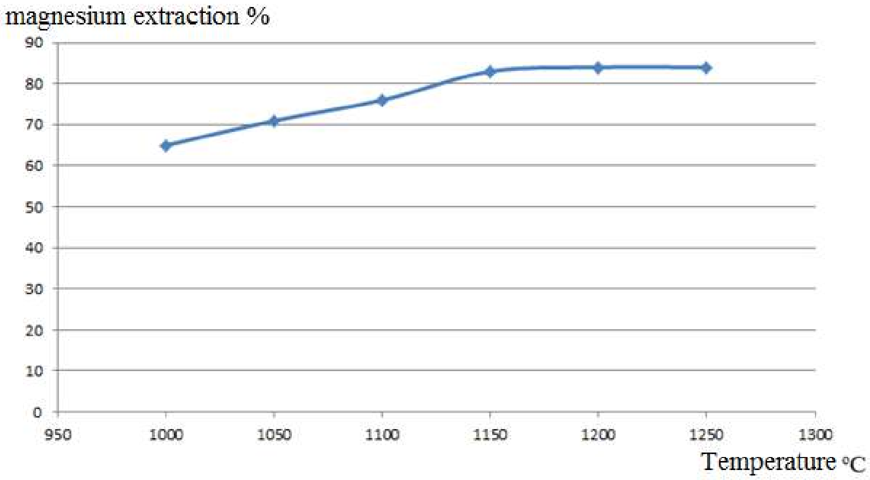

Figure 3: Effect of temperature on magnesium production yield

Finally, magnesium was refined with $MgCl_2$. The magnesium purity reached 98.7%.

IV. CONCLUSION

Using the Pidgeon method with ferrosilicon as the reducing agent is suitable to produce magnesium from Thanh Hoa dolomite ore. The reduction process was performed at 1200 ^{o}C for 3 hours. The maximum of magnesium production yield is 84% and magnesium content is 94,3% with 30% ferrosilicon added. The purity of magnesium after reduction was 94,3%, and after refining with $MgCl_2$ magnesium purity reached 98.7%.

REFERENCES

[1] https://www.nonstopsystems.com/radio/pdf-hell/article-magnesium-prod-history.pdf *History of magnesium production*

[2] Professor Geoffrey Brooks and Ms Winny Wulandari,High Temperature Processing Group, April 2009 “*New Processes For Magnesium Production”*

[3] George J. Simandl, British Columbia Ministry of Energy, Mines and Petroleum Resources, Victoria, BC, Canada,Baymag Inc, Calgary, Alberta, Canada, Jana Simandl, Department of Chemical Engineering, McGill University, Montreal, Que, Canada, Suzanne Paradis, Geological Survey of Canada, Sidney, BC, Canada *“Magnesium - Raw Materials, Metal Extraction and Economics -Global Picture*”

[4] B. Mehrabi1, M. Abdellatif 2 and F. Masoudi3 * *f_masoudi@sbu.ac.ir,* Received: December 2010 Accepted: April 20111 Geology Department, Tehran Tarbiat Moallem University, Tehran, Iran, 2 Mintek Co., Randburg, 2125, South Africa, 3 Faculty of Earth Sciences, Shahid Beheshti University, Tehran, Iran.“*Magnesium production from ASIAN ABE-GARM of dolomite in Pidgeon- type reaction*”.

[5] http://rruff.geo.arizona.edu/doclib/hom/magnesite.pdf *Handbook of Mineralogy Magnesite.*

[6] Handbook of Mineralogy. (PDF) . Retrieved on 2011-10-10” *Dolomite*.”

STUDY ON SYNTHESIS AND CHARACTERISTICS OF LANTHANUM-DOPED Pb($Zr_{1-x}Ti_x$)O_3 CERAMICS BY HYDROTHERMAL METHOD

Nguyen Thanh Thuy, Nguyen Van Tung, Nguyen Trong Hung, Cao Duy Minh,
Dao Truong Giang, Ha Dinh Khai and Ngo Quang Hien.

Institute for Technology of Radioactive and Rare Elements,
48 Lang Ha, Dong Da, Hanoi

Project information:

- **Code:** CS/18/03-02
- **Managerial level:** Institute
- **Allocated Fund:** 80,000,000 VND
- **Implementation time:** 12 months (Jan 2018-Dec 2018)
- **Contact email:** ntthuy.k51a@gmail.com
- **Paper published un related to the projet:**

Nguyen Thanh Thuy, Nguyen Van Tung, Nguyen Trong Hung, Cao Duy Minh, "Study on the hydrothermal synthesis of lanthanum-modified lead zirconate titanate powders" *The 5th Vietnam Conference on Nuclear Science and Technology for Young Researchers.* Hanoi, Vietnam October 2018 (in Vietnamese).

Abstract: Lanthanum-doped lead zirconate titanate (PLZT) powders were synthesized using the hydrothermal method. The influence of pH, reaction temperature and time, lanthanum concentration on the formation and characteristics of PLZT were investigated. Obtained powders were investigated using X-ray diffraction analysis (XRD), scanning electron microscopy (SEM) techniques and a dielectric analyzer. The results showed that $Pb_{1-x}La_x(Zr_{0.65}Ti_{0.35})O_3$ with x= 0.0 – 0.1 were well formed under conditions: pH≥13 , reaction time of 12hrs, reaction temperature of 180°C. Dielectric constant of PLZT is higher than PZT. The grain size of the PLZT is found to be 1–3.5μm.

Keywords: *PLZT, PZT, lanthanum, hydrothermal.*

I. INTRODUCTION

Lead, zirconium, titanium oxide - $PbZr_xTi_{1-x}O_3$ (PZT) is a solid solution of $PbTiO_3$ and $PbZrO_3$ [5,11]. In the perovskite family, it is the most important material in the industry. Depending on the purpose of use, PZT-based materials are doped by some elements such as rare earths, Mn, Fe, Cr, Sb, Zn…. to enhance their properties [1,2]. PZT doped with specific amount of La has been shown to be useful in many applications such as memories (DRAM and FRAM), infrared detectors, electro-optic devices and surface acoustic wave devices and so forth [4]. Modification of the PZT system by the addition of lanthanum has a marked beneficial effect on several of the basic properties of the material such as decreased coercive field, increased dielectric constant, increased mechanical compliance, and enhanced optical transparency [7]. Therefore, the doped PZT-lanthanum is an attractive object for both basic and applied research.

The common methods used for the preparation of PZT and doped PZT powders are solid phase reaction, sol-gel, hydrothermal [4,8-12]. There are also methods such as co-precipitation, microwave [1,2,13]. Hydrothermal is one of the most popular methods to prepare PZT as well as other ceramic materials [4] because of its advantages such as simple operation, easy to implement, low reaction temperature (around 200^oC). It is also a superior method of low production cost due to energy and environmental considerations. Moreover, it is a simple method to prepare powders of single crystal with little post-treatments and good sinterability [9]. It is also a useful method for preparing nano-size ceramic materials.

In Vietnam, PZT doped rare earth elements were researched but a few results have been published [1-4]. Therefore, in this study PZT doped lanthanum by hydrothermal method was investigated. The effect of the reactant preparation, pH, and temperature and time reaction on the PLZT forming was indicated. The effect of La doping on the dielectric and the crystallization of PLZT ceramics has been explored and reported in this research.

II. EXPERIMENTS

Each experiment was calculated to obtain 0.01 mol (about 3g) PLZT as form $Pb_{1-x}La_x(Zr_{0,65}Ti_{0,35})O_3$ (x=0, 0.025, 0.05, 0.10 or lanthanum concentration in the function of Pb is 0, 2.5, 5.0, 10.0%mol respectively). High-purity chemicals of $ZrOCl_2.8H_2O$ (≥98%, German), $TiCl_3$ (15% in HCl media, German), $Pb(NO_3)_2$ (99%,China) La_2O_3 (99,99 – Vietnam), HNO_3 and KOH (PA, China) were used as starting materials. $La(NO_3)_3$ 0.1M solution was obtained from La_2O_3 and HNO_3 5M solution. Two routes to prepare the reactant mixtures before hydrothermal process in an autoclave were applied in this study.

The first route is individual precipitation. As the first step, $Pb(NO_3)_2$ was dissolved into 25 ml de-ionized water and KOH 3M was slowly added until the precipitation to obtain a precipitate of lead. $ZrOCl_2.8H_2O$ was dissolved in 25 ml de-ionized water in another beaker. $TiCl_3$ and $LaCl_3$ solutions were added into this beaker, with stirring (200rpm), to get a mixture solution of Zr^{4+}, Ti^{3+} and La^{3+}. KOH 3M was slowly added into this mixture solution to get a precipitate of zirconium, titanium and lanthanum. Then, two beakers were mixed with sintering (300rpm). Finally, pH of the mixture was adjusted by using KOH 3M.

The second route is co-precipitation. $ZrOCl_2.8H_2O$ and $Pb(NO_3)_2$ were dissolved separately in two beakers. $TiCl_3$ was added into the ZrO^{2+} solution and $LaCl_3$ was added into the Pb^{2+} solution. Then, the ZrO^{2+}/Ti^{3+} mixture was slowly poured with sintering (300rpm) into the beaker which contains the Pb^{2+}/La^{3+} mixture. Finally, pH of the mixture was adjusted by using KOH 3M.

Each reactant mixture was poured into an autoclave after 15 minutes stirring. The hydrothermal reaction was carried out at the temperature of 150 to 180^oC in 12 to 48 hours. The obtained precipitate after hydrothermal process was filtered and washed with distilled water for several times to remove Cl^-, NO_3^- and K^+. The final products were obtained by drying the precipitate at 80^oC in 24 hours.

Phase composition was analyzed by XRD (SIEMENS D5005). Morphology and particle size were analyzed by SEM (JEOL, JSM-IT100LV) and a size analyzer (PARTICA LA-950V2). For dielectric measurements, PLZT powders were pressed into discs (diameter ~12 mm, ~1 mm thick). Dielectric constant (ε) and dissipation factor (tanδ) were measured using an impedance analyzer (Autolab 30) in the frequency range 100Hz - 1 MHz at room temperature.

III. RESULTS AND DISCUSSION

3.1. Effect of the preparation of reactant mixtures on the PLZT forming

Because of variety of the starting chemicals, the mixing of starting material plays an important role in the formation and purity of final product. The presence of Cl^- (from $ZrOCl_2.8H_2O$

and $TiCl_3$) and Pb^{2+} (from $Pb(NO_3)_2$) lead to create $PbCl_2$ precipitate (reaction (1)) during mixing process. In this study, two routes to prepare the reactant mixtures (mentioned at paragraph II) were applied at pH of 13 and La of 10% mol (x=0.1). The hydrothermal process was occurred at 180^{o}C for 48hours.

XRD patterns in Fig.1 showed that $Pb_{0.9}La_{0.1}(Zr_{0,65}Ti_{0,35})O_3$ – PLZT crystal is formed in both precipitation routes. But pure PLZT crystal is formed only in case of co-precipitation. There are some impurities: ZrO_2, PbO exited in case of individual precipitation. In both cases the presence of $PbCl_2$ cannot be detected. This can be explained by reaction (2): $PbCl_2$ was converted to $Pb(OH)_2$ during pH adjustment by KOH solution. In fact, the solubility product constants (K_{sp}) of $PbCl_2$ and $Pb(OH)_2$ are $1.7x10^{-4}$ and $1.42x10^{-20}$ respectively. Thus, the co-precipitation method is a better route to prepare pure PLZT powders.

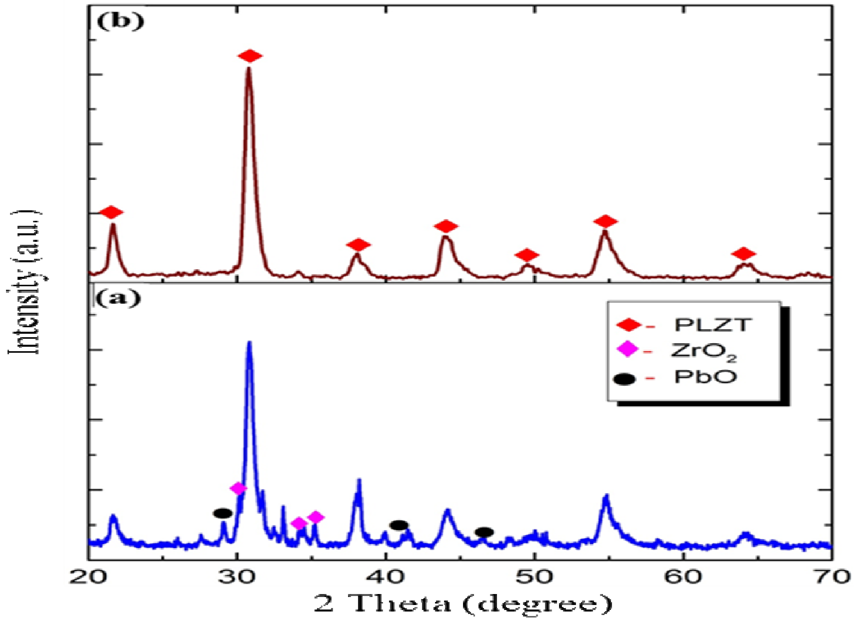

Figure 1: XRD patterns of materials obtained from individual precipitation (a) and co-precipitation (b).

3.2. Effect of pH on the PLZT forming

Because of very important role on the crystallization of PLZT, pH of reactant mixture before hydrothermal process was adjusted in range of 11 to 13. Each sample was treated at temperature of 1 80^{o}C in 48hours and lanthanum concentration of 10%mol.

It can be seen that Fig. 2 exhibits some peaks of ZrO_2, $PbZrO_3$ and $Pb_3(CO_3)_3(OH)_2$ in case of pH of 11 and 12. There are not any peaks of PLZT at these conditions. It means that pH below 12 is not enough for the crystallization or forming of PLZT phase. Meanwhile, pure PLZT crystal is formed at pH of 13. Thus, pH≥13 is necessary to obtain pure PLZT powders.

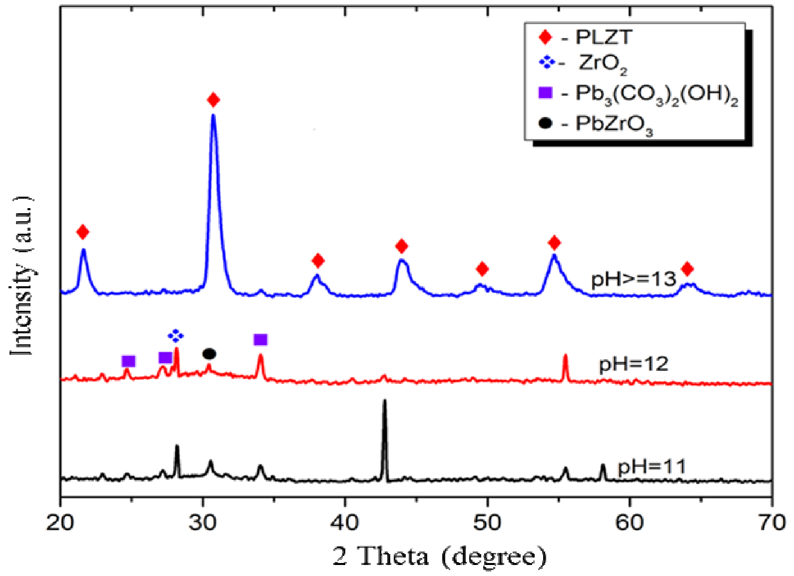

Figure 2: XRD patterns of materials obtained at different pH.

The important role of the pH adjusting of reactant mixture before hydrothermal can be explained through the following reaction mechanism [4,9]:

$$Pb^{2+} + Cl^{-} = PbCl_2 \quad (1)$$

$$PbCl_2 + 2OH^{-} = Pb(OH)_2 + 2Cl^{-} \quad (2)$$

$$Pb^{2+} + 2KOH^{-} = Pb(OH)_2 + 2K^{+} \quad (3)$$

$$Ti^{3+} + 2OH^{-} + ½ O_2 + H_2O = Ti(OH)_4 \quad (4)$$

$$Zr^{4+} + 4OH^{-} = Zr(OH)_4 \quad (5)$$

$$La^{3+} + OH^{-} = La(OH)_3 \quad (6)$$

$$(1-x)Pb(OH)_2 + 0{,}35Ti(OH)_4 + 0{,}65Zr(OH)_4 + xLa(OH)_3 = Pb_{1-x}La_x(Zr_{0,65}Ti_{0,35})O_{3+x/2} + (3+x/2)H_2O \quad (7)$$

First is the forming of $Pb(OH)_2$, $Ti(OH)_4$, $ZrO(OH)_2$, $La(OH)_3$ (3)-(6). These reactions occurred during the pH adjustment process using KOH 3M. Next, at the high pressure and temperature condition of reactor, $Pb(OH)_2$, $Ti(OH)_4$, $Zr(OH)_4$, $La(OH)_3$ participated in reaction and formed PZT material (7).

3.3. Effect of reaction time and temperature

Reaction time and temperature have an important role in hydrothermal process. Abothu [13] has successfully synthesized PZT under hydrothermal condition at 138°C in 2.5h with the presence of microwave in during hydrothermal process. In this study, the hydrothermal reaction was conducted at temperature of 150 and 180°C in 12 to 48 hours. La concentration was 10%mol and pH was 13.

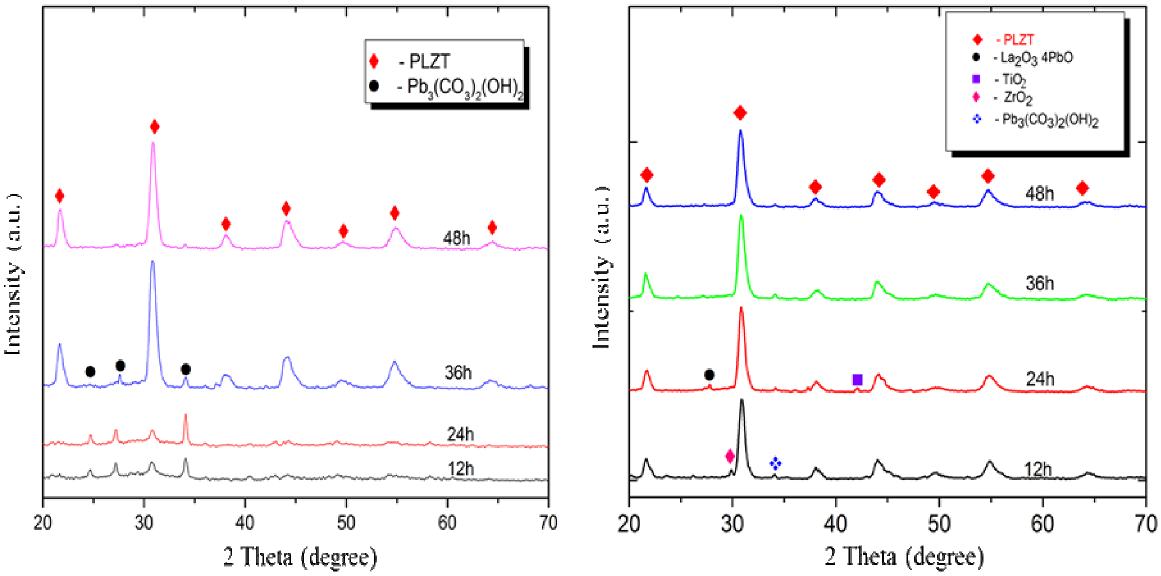

Figure 3: XRD patterns of materials obtained at 150°C (left), 180°C (right).

Fig.3 (left) shows that PLZT is formed at temperature 150°C in 36 hours, but it remained a small amount of ($Pb_3(CO_3)_3(OH)_2$). Pure phase of PLZT created in reaction time of 48hours. During the reaction time of 12 to 24hours, no peaks for PLZT are found. At this condition, only typical peaks for $Pb_3(CO_3)_3(OH)_2$ exist. At 180°C, the typical peaks of PLZT appeared in 12 hours (Fig.3 (right)). However, the hydrothermal reaction is not completely, remaining some impurities with small content such as $Pb_3(CO_3)_2(OH)_2$, TiO_2, ZrO_2, La_2O_34PbO. Pure phase of PLZT is formed when the reaction time is over 36hours. Thus, the reaction temperature and time affect the formation as well as purity of PLZT crystal.

3.4. Effect of La concentration on dielectric constant and practice size

La concentration was adjusted from 0 to 10% mol to estimate the influence on characteristics of material. The hydrothermal process was conducted at 180°C in 48hrs.

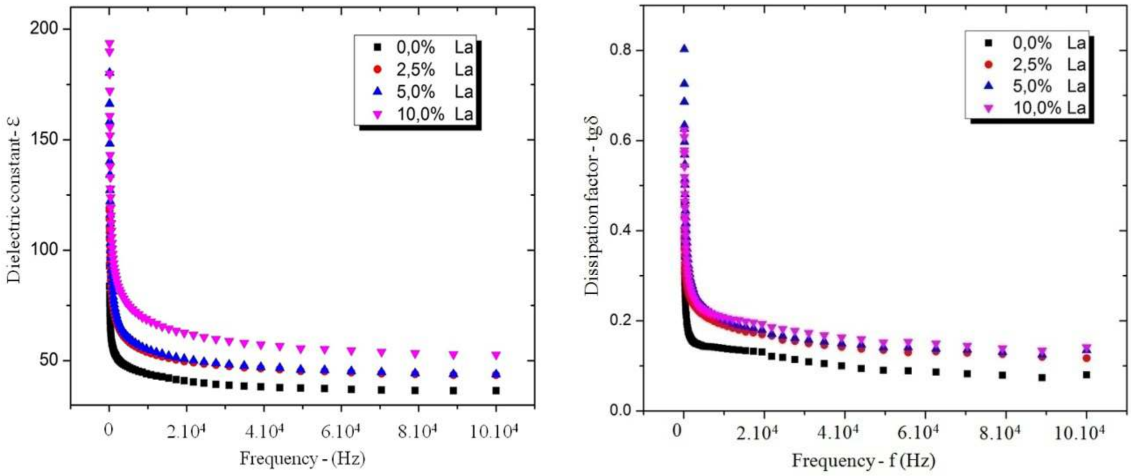

Figure 4: Dielectric constant (left) and dissipation factor (right) of PLZT in the presence of various concentrations of lanthanum.

Fig.4 (left) shows that the dielectric constant and dissipation factor increase proportionally to lanthanum concentration. The dielectric constant PLZT at 100Hz with La concentration of 0, 2.5, 5 and 10%mol are 93, 150, 180 and 193 respectively. Therefore, lanthanum improved significantly the dielectric constant of doped PZT in comparison to PZT. The increase of dielectric constant can be explained as a result of vacancies facilitating domain boundary motion, which in turn allows the relaxation of internal stresses and results in more efficient poling.

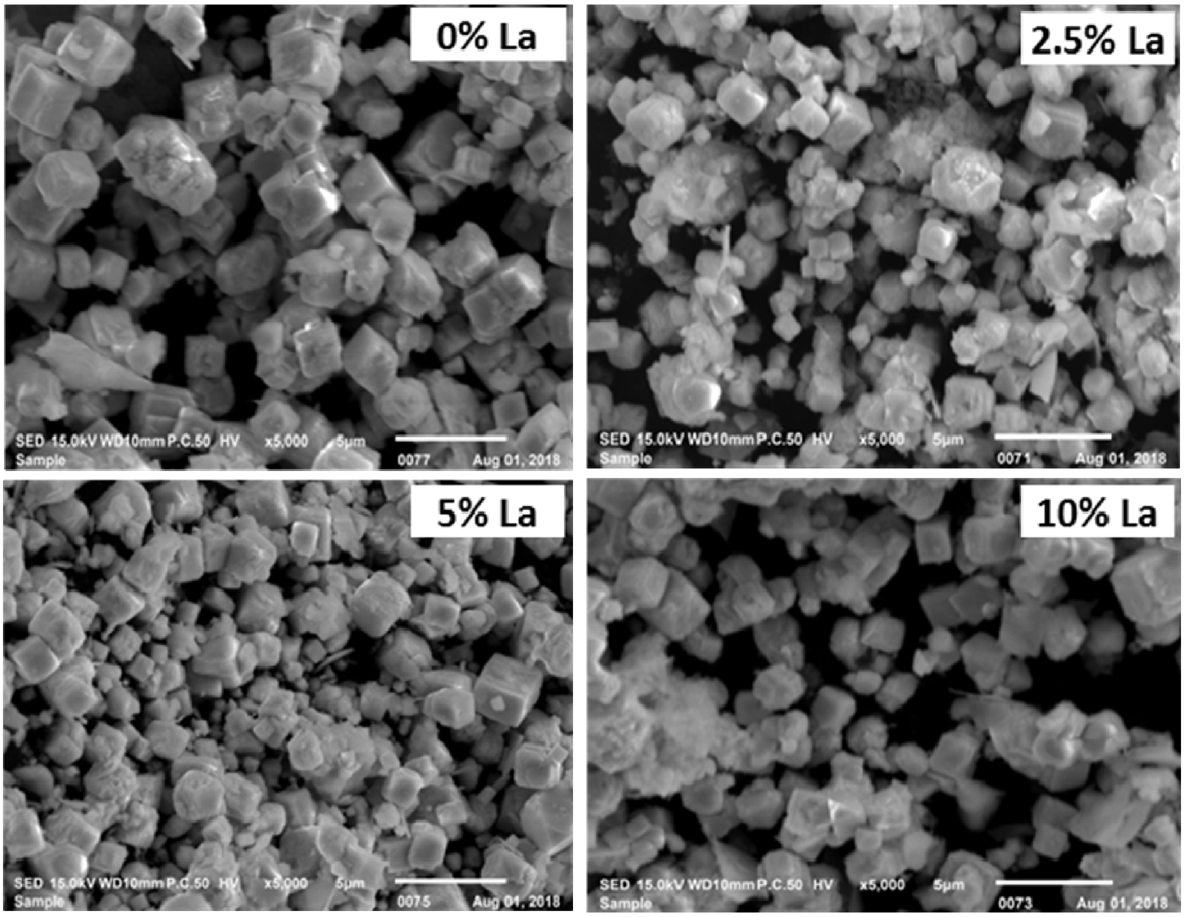

Figure 5: SEM images of PLZT in the presence of various concentrations of lanthanum.

Fig.5 shows that all samples have a clear grain boundary grains. The grain size of the PLZT is found to be 1–3.5μm. The results from size analyzer show the decrease of medium grain size with the increase in La concentration in the sample (3.5 μm with 0% to 2.9μm with 10%mol La). Due to the decrease in grain size, the fraction of dipoles at its interface also increases. The increase in number of dipoles and the lattice strain result in increase in the ferroelectric and piezoelectric properties or dielectric constant [5].

IV. CONCLUSIONS

PZT doped La with $Pb_{1-x}La_x(Zr_{0,65}Ti_{0,35})O_3$ formula was successful prepared by hydrothermal method. The effect of precipitation method, pH, lanthanum concentration, temperature and time reaction were also investigated. Pure PLZT phase was formed when pH ≥ 13; the reaction time was higher than 36 hours at $180^{o}C$ or higher than 48 hours at $150^{o}C$. The grain size of the obtained material was smaller than 3.5μm, the dielectric constant increased proportional to the La concentration. The dielectric constant of PLZT was 193 at 1 kHz in case of La 10% mol in comparison to 93 of PZT.

REFERENCES

[1] Phan Dinh Gio, "Study on the physical characteristics of two and three components ferroelectric ceramics based on PZT doped by La, Mn, Fe", Doctoral thesis, 2007.

[2] Than Trong Huy, "Study on the fabrication and characteristics of piezoelectric ceramics $[(1-x)Pb(Zr,Ti)O_3 + xPb(Mn_{1/3}Nb_{2/3})O_3]$ x = 0 ÷ 12%mol (PZT-PMnN) doped by La", Doctoral thesis, 2014.

[3] Thanh Thuy Nguyen et al., "Elaboration and dielectric property of modified PZT/epoxy nanocomposites", Polymer Composites 37 (2016) 455-461

[4] Nguyen Xuan Hoan et al., "Study on synthesis of the lead zirconate titanate powder by the hydrothermal method", Vietnam Journal of Science and Technology 48 (2A), (2010) 414-418

[5] P. Kour et al., "Enhanced ferroelectric and piezoelectric properties in La-modified PZT", Ceramics Applied Physics A (2016) 122:591.

[6] H.D.Sharma et al., "Effect of rare earth ions on the structural parameters of modified PLZT ceramics (5/65/35)", Journal of Materials Science Letters 15 (1996) 1424-1426.

[7] A. R. James et al., "Chemical synthesis, structural, thermo-physical and electrical property characterization of PLZT ceramics", Journal of Alloys and Compounds 496 (2010) 624–627.

[8] Irinela et al., "Ferroelectric ceramics by sol-gel methods and applications: a reviews", J. Sol-gel Science 64 (2012) 571-611.

[9] Yao-Jung Lee et al, "Phase-formation mechanism for hydrothermally synthesizing lanthanum-modified lead zirconate titanate powders", Journal of Crystal Growth 178 (1997) 335-344.

[10] D. Lui, H. Zhang, W. Cai, X. Wu, L. Zhao, " Synthesis of PZT nanocrystalline powder by a modified sol-gel process using zirconium oxynitrate as zirconium source", Materials Chemistry and Physics 51 (1997) 186-189.

[11] T. Lamcharfi et al., "Dielectric and relaxation studies in hydrothermal processed PLZT ceramics", M. J. Condensed Matter 6, No.1, 2005.

[12] S. N. Shannigrahi et al., "Structural, electrical and piezoelectric properties of rare-earths doped PZT ceramics", Indian Journal of Pure & Applied Physics 37 (1999) 359-362.

[13] Isaac Robin Abothu et al., Processing of $Pb(Zr_{0.52}Ti_{0.48})O_3$ (PZT) ceramics from microwave and conventional hydrothermal powders, Materials Research Bulletin 34 No9 (1999) 1411–1419.

2. IAEA TC PROJECTS AND RESEARCH CONTRACTS

2.1 - LIST OF VIE PROJECTS 2018

(Implemented by VINATOM)

Code	Project Title	Start year	Finish Year	Budjet (Euro)	Field code	Project Counterpart	Institution
VIE9018	Promoting the Reactor Safety Development Program for Enhancing National Capability in Reactor Safety Research - Phase II	2018	2019	130,770.00	10	**Trần Chí Thành**	VINATOM

2.2 - LIST OF INT PROJECTS AND NON-RCA PROJECT 2018

(Implemented by VINATOM)

Code	Project Title	Start year	Finish Year	Budjet (Euro)	Field code	Project Counterpart	Institution
INT2014	Supporting Member States to Evaluate Nuclear Reactor Technology for Near-Term Deployment	2012	2019 (Tentative)	834,529.72	6	**Trần Chí Thành**	VINATOM
INT2019	Deploying Technology and Management of Sustainable Uranium Extraction Projects	2016	2020 (Tentative)	1,362,599.91	7	**Hoàng Nhuận**	ITRRE
RAS2018	Supporting Decision Making for Nuclear Power Planning and Development - Phase III	2016	2020 (Tentative)	833,564.95	5	**Trần Chí Thành**	VINATOM
RAS2019	Conducting the Comprehensive Management and Recovery of Radioactive and Associated Mineral Resources	2016	2020 (Tentative)	419,999.96	7	**Hoàng Nhuận**	ITRRE

2.3 - LIST OF FNCA PROJECTS 2018

(Participated by VINATOM and other Vietnam organizations)

Field	Project Title	Project Coordinator
Research Reactor Utilization Development	Research Reactor Network	**Dr. Duong Van Dong** Director, Center for Research and Production of Radioisotope, Nuclear Research Institute (NRI) Vietnam Atomic Energy Institute (VINATOM)
	Neutron Activation Analysis	**Dr. Ho Manh Dung** Deputy Director, Center for Nuclear Techniques (CNT), Vietnam Atomic Energy Institute (VINATOM)
Radiation Utilization Development (Agricultural/ Healthcare /Industrial/ Environmental Utilization)	Mutation Breeding	**Prof. Le Huy Ham** Chairman of Science Council, Agricultural Genetics Institute (AGI) Ministry of of Agriculture and Rural Development (MARD)
	Radiation Oncology	**Dr. Bui Cong Toan** General Radiotherapy Department, National Cancer Hospital (K Hospital)
	Radiation Processing and Polymer Modification for Agricultural, Environmental and Medical Applications Project	**Dr. Nguyen Ngoc Duy** Head of Research and Development Department, Research and Development Center for Radiation Technology (VINAGAMMA), Vietnam Atomic Energy Institute (VINATOM)
	Research on Climate Change using Nuclear and Isotopic Techniques	**Dr. NGUYEN Trong Ngo** Deputy Director, Nuclear Research Institute (NRI), Vietnam Atomic Energy Institute (VINATOM)
Nuclear Safety Strengthening	Radiation Safety and Radioactive Waste Management	**Dr. Pham Quang Minh** Director, Department for Planning and R&D Management, Vietnam Atomic Energy Institute (VINATOM)

Nuclear Infrastructure Strengthening	Nuclear Security and Safeguard	**Ms. Bui Thi Thuy Anh** National Liasion Assistant (NLA) Director, International Cooperation Division Vietnam Agency for Radiation and Nuclear Safety (VARANS)

2.4 - LIST OF RAS PROJECTS 2018

(Participated by VINATOM and other Vietnam organizations)

Code	Title	Year of approval	Budget (EUR)	Project Type	Project Coordinators
RAS5070	Developing Bioenergy Crops to Optimize Marginal Land Productivity through Mutation Breeding and Related Techniques (RCA)	2014	760,235.52	RCA	**Le Huy Ham** Agricultural Genetics Institute
RAS5077	Promoting the Application of Mutation Techniques and Related Biotechnologies for the Development of Green Crop Varieties (RCA)	2016	610,392.96	RCA	**Le Huy Ham** Agricultural Genetics Institute
RAS5081	Enhancing Food Safety and Supporting Regional Authentication of Foodstuffs through Implementation of Nuclear Techniques	2018	568,965.16	RCA	**Nguyen Thi Hong Thinh** Institute for Nuclear Science & Technology
RAS5084	Assessing and Improving Soil and Water Quality to Minimize Land Degradation and Enhance Crop Productivity Using Nuclear Techniques (RCA)	2018	449,111.01	RCA	**Nguyen Thi Hương Lan** Nuclear Research Institute
RAS6083	Improving Patient Care and Enhancing Government Parties Capacity in Nuclear Medicine programmes in the RCA Region (RCA)	2016	678,063.78	RCA	**Mai Trong Khoa** Nuclear Medicine and Oncology Center Bach Mai Hospital
RAS6085	Enhancing Stereotactic Body Radiation Therapy for Frequent Cancers in the RCA Region (RCA)	2016	594,159.19	RCA	**Bui Quang Bieu** Central Military Hospital 108

RAS6086	Strengthening Cancer Management Programmes in Government Parties through Collaboration with National and Regional Radiation Oncology Societies	2018	551,137.50	RCA	**Mai Trong Khoa** Nuclear Medicine and Oncology Center Bach Mai Hospital
RAS6087	Enhancing Medical Physics Services to Develop Government Parties through Regional Leadership in Standards and Education and Training Support	2018	400,525.00	RCA	**Tran Ngoc Toan** Vice President Vietnam Atomic Energy Institute
RAS7028	Enhancing Regional Capabilities for Marine Radioactivity Monitoring and Assessment of the Potential Impact of Radioactive Releases from Nuclear Facilities in Asia-Pacific Marine Ecosystems (RCA)	2016	790,222.85	RCA	**Nguyen Van Phuc** Nuclear Research Institute, VINATOM
RAS7029	Assessing the Impact of Urban Air Particulate Matter on Air Quality (RCA)	2016	366,699.91	RCA	**Vuong Thu Bac** Institute for Nuclear Science and Technology, VINATOM
RAS7030	Assessing Deep Groundwater Resources for Sustainable Management through the Utilization of Isotopic Techniques (RCA)	2016	658,233.08	RCA	**Nguyen Kien Chinh** Center for Nuclear Techniques, VINATOM

2.5 - LIST OF NATIONAL COORDINATOR AND TOPICAL GROUP MEMBER, ASIAN NUCLEAR SAFETY NETWORK (ANSN) 2018

(Implemented by VINATOM)

Topic	National Coordinator	Topical Group Member	Institution
Asian Nuclear Safety Network (ANSN)	**Tran Ngoc Toan**		Department of International Cooperation, VINATOM
Regulatory Infrastructure (RITG)		**Cao Hong Lan**	Department of International Cooperation, VINATOM
Education and Training (ETTG)		**Nguyen Hao Quang**	VINATOM
Sitting (STG)		**Pham Ngoc Dong**	Nuclear Training Centre, VINATOM
Safety Assessment (SATG)		**Tran Thanh Tram**	Nuclear Education and Training Center, VINATOM
Radioactive Waste Management (RWMTG)		**Bui Dang Hanh**	Department of International Cooperation, VINATOM
Emergency Preparedness and Response (EPRTG)		**Vuong Thu Bac**	Institute for Nuclear Science and Technology, VINATOM
Safety Management of Research Reactor (SMRRTG)		**Luong Ba Vien**	Dalat Nuclear Research Institute, VINATOM
Communication (CTG)		**Hoang Sy Than**	Department of International Cooperation, VINATOM
Self-Assessment Coordination Group (SACG)		**Cao Hong Lan**	Department of International Cooperation, VINATOM

VIỆN NĂNG LƯỢNG NGUYÊN TỬ VIỆT NAM

The ANNUAL REPORT for 2018

VIETNAM ATOMIC ENERGY INSTITUTE

The ANNUAL REPORT for 2018

Responsible for publishing: **MSc. Võ Tuấn Hải**
Editor and Copy Editor: Nguyen Minh Chau
Cover Designer: Dang Nguyen Vu

SCIENCE AND TECHNICS PUBLISHING HOUSE
70 Tran Hung Dao Street - Hanoi
Tel: 024 3942 2443 Fax: 024 3822 0658
Website: http://nxbkhkt.com.vn Email: nxbkhkt@hn.vnn.vn

BRANCH OFFICE
28 Dong Khoi - District 1 - Ho Chi Minh City Tel: 028 3852 5062

Quantity: 100 copies, size 20.5 x 29 cm, at Tuan Viet Commerce printing Co., Ltd..
Address: La Thach hamlet, Phuong Dinh commune, Dan Phuong district, Ha Noi city
Publishing license No: ... 018/CXBIPH/1-112/KHKT.
Publishing decision No: ... /QĐ-NXBKHKT, date ....
Printing completed and copies deposited in 2018.
ISBN: ...

NHÀ XUẤT BẢN KHOA HỌC VÀ KỸ THUẬT
Địa chỉ: Số 70 Trần Hưng Đạo - Hoàn Kiếm - Hà Nội
Điện thoại: 024.39423172 - 024.38220686
Fax: 84.24.8220658   Email: nxbkhkt@hn.vnn.vn
Website: https://nxbkhkt.com.vn

217191H00
ISBN: 978-604-67-1023-3
9 786046 710233
SÁCH KHÔNG BÁN